"Advanced Materials for PEM-Based Fuel Cell Systems"

DOE Award Number: DE-FC36-01GO11086

FINAL REPORT

Period Covered: 10/1/01 – 3/31/05

Recipient Organization:
James E. McGrath, University Distinguished Professor of Chemistry
Macromolecules and Interfaces Institute
Department of Chemistry
Virginia Tech (0344)
2108 Hahn Hall
Blacksburg, VA 24061
Phone: 540-231-5976; Fax: 540-231-8517
jmcgrath@vt.edu

DOE Contact Information:
Jill Jonkouski
Program Manager
U.S. Department of Energy
Office of Program and Project Management-PMO
9800 S. Cass Avenue
Argonne, IL 60439-4899
Tel: (630)-252-2657

Patents

1. J.E. McGrath, M. Hickner, F. Wang, and Y.S. Kim, "Ion-Conducting Sulfonated Polymeric Materials," (2002), Patent Number WO0225764.
2. J.E. McGrath and M. Hickner, "Sulfonated Polymer Composition for Forming Fuel Cell Electrodes," (2003), Patent Number WO03082956.
3. W. Harrison, H. Ghassemi, T.A. Zawodzinski, and J.E. McGrath, "Multiblock Copolymers Containing Hydrophilic-Hydrophobic Segments for Proton Exchange Membrane Fuel Cells," (2005), Patent Number WO2005053060.

Table of Contents

Summary and Discussion of Accomplishments and Goals

Proton exchange membrane fuel cells (PEMFCs) are quickly becoming attractive alternative energy sources for transportation, stationary power, and small electronics due to the increasing cost and environmental hazards of traditional fossil fuels. Two main classes of PEMFCs include hydrogen/air or hydrogen/oxygen fuel cells and direct methanol fuel cells (DMFCs). The current benchmark membrane for both types of PEMFCs is Nafion, a perfluorinated sulfonated copolymer made by DuPont. Nafion copolymers exhibit good thermal and chemical stability, as well as very high proton conductivity under hydrated conditions at temperatures below 80 °C. However, application of these membranes is limited due to their high methanol permeability and loss of conductivity at high temperatures and low relative humidities. These deficiencies have led to the search for improved materials for proton exchange membranes. Potential PEMs should have good thermal, hydrolytic, and oxidative stability, high proton conductivity, selective permeability, and mechanical durability over long periods of time. Poly(arylene ether)s, polyimides, polybenzimidazoles, and polyphenylenes are among the most widely investigated candidates for PEMs. Poly(arylene ether)s are a promising class of proton exchange membranes due to their excellent thermal and chemical stability and high glass transition temperatures. High proton conductivity can be achieved through post-sulfonation of poly(arylene ether) materials, but this most often results in very high water sorption or even water solubility.

Our research has shown that directly polymerized poly(arylene ether) copolymers show important advantages over traditional post-sulfonated systems and also address the concerns with Nafion membranes. These properties were evaluated and correlated with morphology, structure-property relationships, and states of water in the membranes. Further improvements in properties were achieved through incorporation of inorganic fillers, such as phosphotungstic acid and zirconium hydrogen phosphate. Block copolymers were also studied due to the possibility to achieve a desired combination of homopolymer properties as well as the unique morphologies that are possible with block copolymers. Bezoyl substituted poly(p-phenylene) blocks were combined with poly(arylene ether) blocks to merge the structural rigidity of the poly(p-phenylene) with the ductility and high protonic conductivity of the poly(arylene ether)s.

As evidenced by our many refereed publications and preprints, the research that we have conducted over the past several years has made a valuable and significant contribution to the literature and to the state of understanding of proton exchange membranes. Our early efforts at scale-up have suggested that the directly polymerized disulfonated poly(arylene ether sulfone) copolymers are commercially viable alternatives for proton exchange membranes.

A new process for bipolar plates was developed and is described. An important single domain PEMFC model was developed and is documented in herein.

Synthesis and Characterization of Disulfonated Poly(arylene ether sulfone)

Random Copolymers

Wholly aromatic random poly(arylene ether sulfone) – poly(arylene ether disulfonated sulfone) copolymers (BPSH, where H defines the mole percent of disulfonic acid units) were prepared by direct polymerization [1], which contain a controlled balance of hydrophobic and hydrophilic ion conducting sites, as shown in Figure 1. These materials are the basis of new PEM systems for fuel cells.

Scheme 1. Direct copolymerization of pre-sulfonated monomers

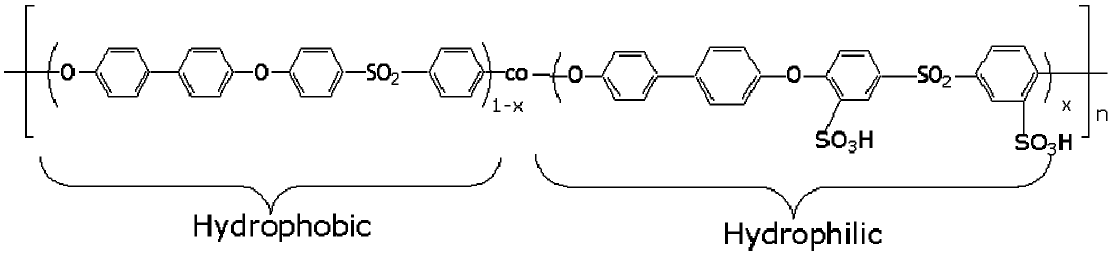

The synthetic scheme for the preparation of these copolymers is briefly shown in Scheme 2, which involves nucleophilic aromatic substitution step polymerization of 4,4’-dichlorodiphenyl sulfone biphenol and a controlled amount of the sulfonated analog referred to SDCDPS.

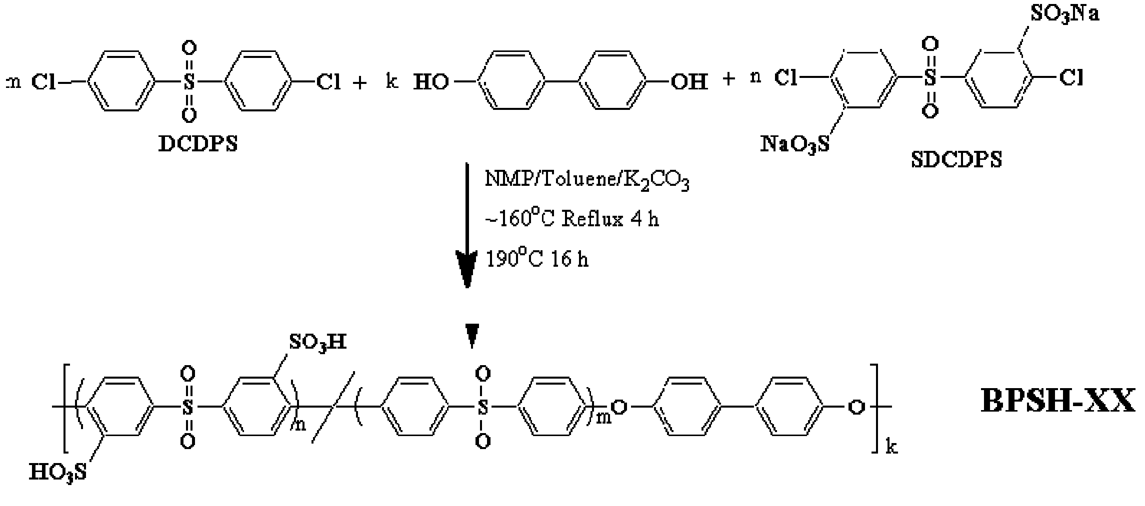

Scheme 2. Wholly aromatic random (statistical) poly(arylene ether sulfone) / poly(arylene ether disulfonated sulfone) copolymers via direct copolymerization

The resulting direct copolymerization has several advantages, including the precise control of ionic concentration during synthesis, well-defined ion conductors, relatively high proton conductivity as illustrated later, enhanced stability due to the positions of the sulfonic acid moieties, the ability to tailor chemistry for coordination, which permits elevated temperature utilization, and the ease of preparing very high molecular weight durable copolymers. The effect of sulfonation and water uptake on conductivity is illustrated in Figure 3.

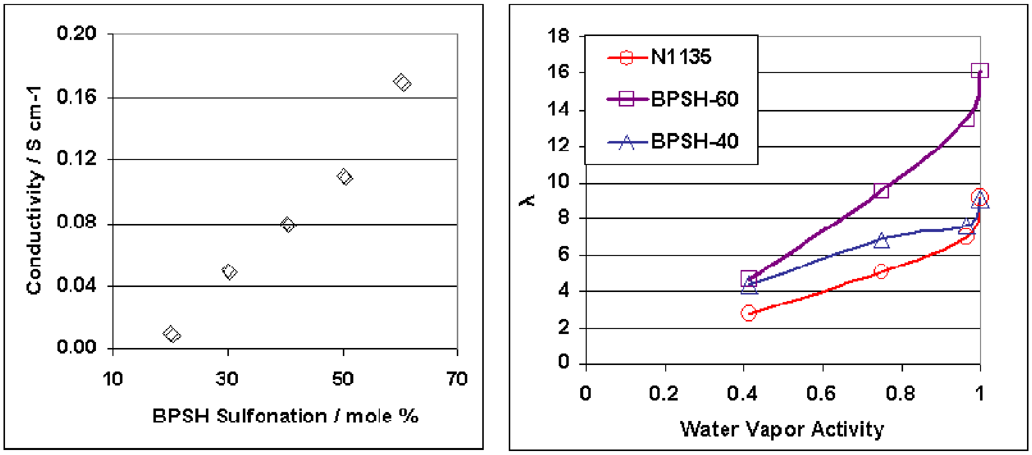

30°C in liquid water **30°C in water vapor**

Figure 3. Effect of sulfonation and water uptake on conductivity

Very significant conductivities can be obtained, which match or exceed state-of-the-art Nafion-type materials. The possible variations in the molecular structure are very broad and are illustrated in Figure 4.

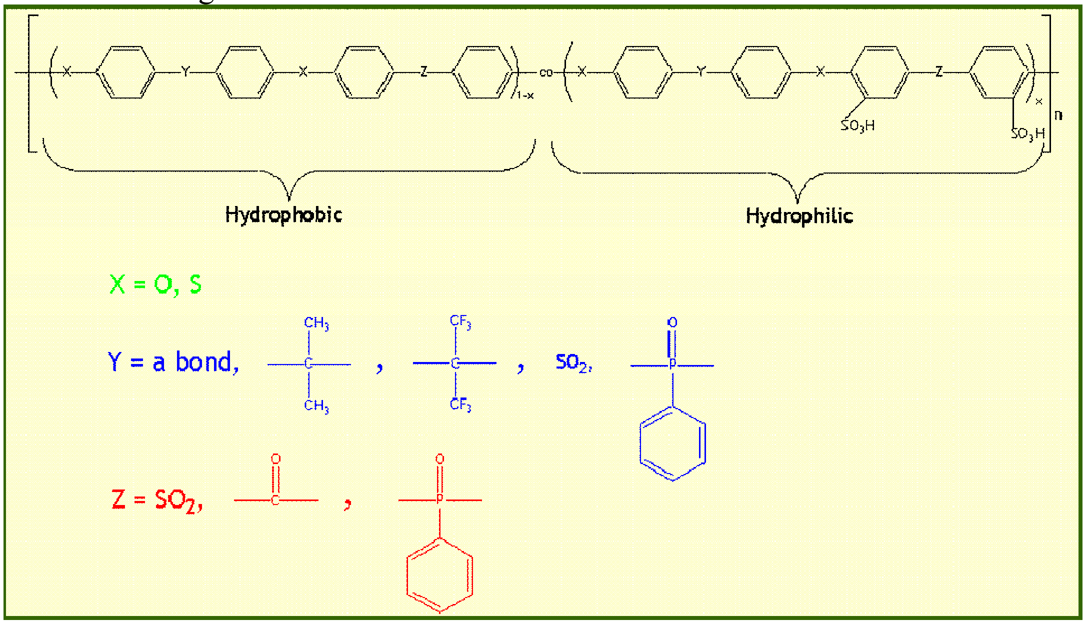

Figure 4. Proton exchange membranes (PEM) and composite electrodes for fuel cells.

Thus, arylene ether sulfides are possible, as well as the arylene ethers, ketones, phenyl phosphine oxides, and partially fluorinated structures that show evidence of self-assembling, allowing surface concentration to be defined by fluorinated species are also possible. Controlled morphologies can be generated that have shown stability for over 1000 hours at 120ºC. The optimal combination of conductivity, mechanical strength, and limited water sorption are observed in the range of 35-45 mol% disulfonation. Direct methanol fuel cells also show a reduction of methanol crossover of >3-4 fold.

The polyarylene ether sulfones are the materials of choice and as indicated in Figure 2, many have investigated post sulfonation reactions to produce the top structure. However, it is less well defined in our view, less acidic (which leads to lower conductivities), and is less thermally stable. We have chosen to sulfonate the monomer, as indicated in Quarterly Report One, to produce structures analogous to the lower repeat units on Figure 2.

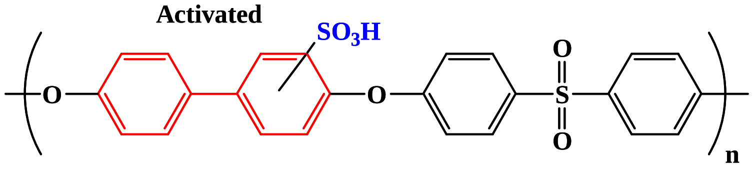

- **Post sulfonation occurs on the most reactive, but least stable, position**
- **High electron density leads to relatively easy desulfonation**

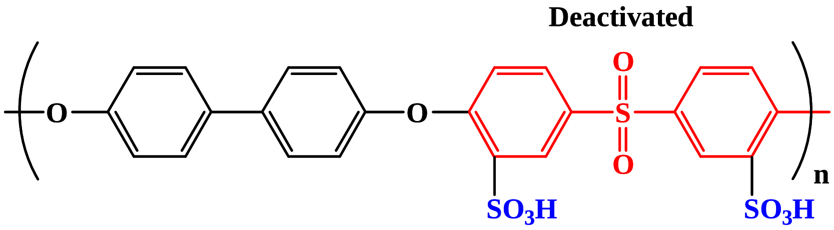

- **Monomer sulfonation on the deactivated position, then direct copolymerization**
- **Enhanced stability due to low electron density**

Figure 2. Comparison of Polymeric –SO_3H Group Stability from Post Monomer Sulfonation Methods

The shorthand nomenclature that has been developed is based upon the ratio of hydrophobic to hydrophilic moieties – or more precisely the fraction of the hydrophilic ion-conducting moieties incorporation into the copolymer. As indicated in Figure 3, our shorthand nomenclature has been to call these copolymers BPSH-systems, where the X refers to the molar fraction of the disulfonic acid moiety. For example, it could be 30% or 40%.

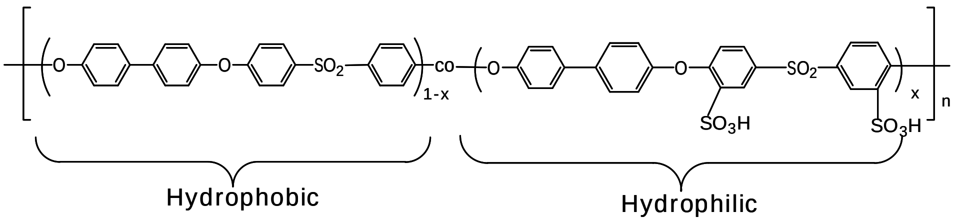

➢Biphenyl Sulfone: H Form (BPSH)
➢x = molar fraction of disulfonic acid unit, e.g., 30, 40, etc.

Figure 3. Wholly Aromatic Random (Statistical) Poly(arylene ether sulfone) / Poly(arylene ether disulfonated sulfone) Copolymers Via Direct Copolymerization (BPSH-x)

Thermal characterization has continued and weight loss as a function of temperature for these copolymers at different compositions in shown in Figure 2.

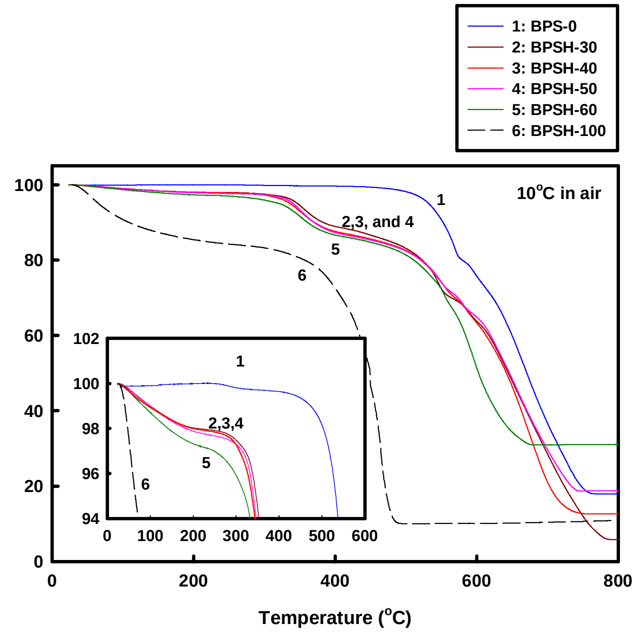

TGA thermogram

Copolymer	$T_{d\ onset}$ (°C)	% water at 250°C[a]
BPS-0	522	0
BPSH-30	336	2.1
BPSH-35	334	2.1
BPSH-40	333	2.2
BPSH-50	329	2.4
BPSH-60	323	3.0
BPSH-100	428[b]	15.7

[a] After vacuum drying at 90°C for 12hr

[b] broad transition

Figure 2. Effect of Composition on the Thermal Decomposition Temperature of BPSH-xx Copolymer

The copolymers from BPSH-30 to BPSH-50 have essentially no weight loss until 300ºC and compares favorably with Nafion 1135, whose TGA weight loss behavior is shown in Figure 3.

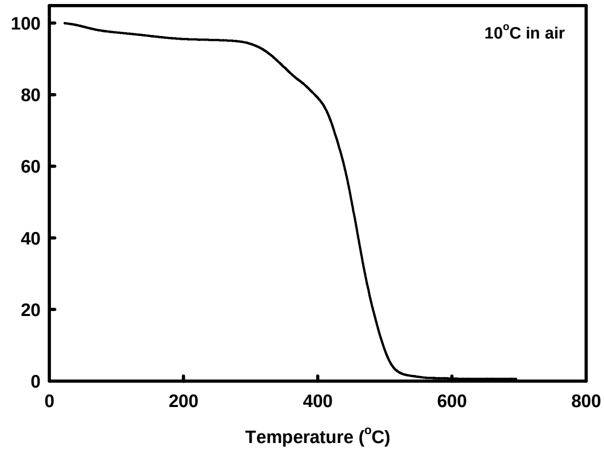

$T_{d\ onset}$:313 °C

% water at 250ºC: 4.7

Figure 3. Thermal Decomposition Temperature of Nafion-1135

Electrical measurements have employed impedance spectroscopy based on the design obtained from LANL a high pressure cell, which permits measurements at 100% relative humidity at temperatures as high as 140-150ºC (described in the Second Quarterly Report), and the membrane electrode assemblies (MEAs)as utilized in fuel cell test stands. The MEAs were either hot pressed on to commercially available Nafion electrodes, or with the novel BPSH copolymer electrodes. During the last period, considerable additional information has been obtained on the important parameter of acidification treatment. Indeed, a manuscript has recently been submitted to the Journal of Polymer Science-Physics to illustrate these results. Additional work has continued on alternate members of the poly(arylene ether) family, as indicated in Figure 4.

Thus, in addition to the wholly aromatic poly(arylene ether sulfone)s, we are also investigating sulfur analogs, as well as partially fluorinated or phosphine oxide containing high performance PEMs. Some interesting results with the fluorinated moieties have already been observed, as summarized in Figure 5.

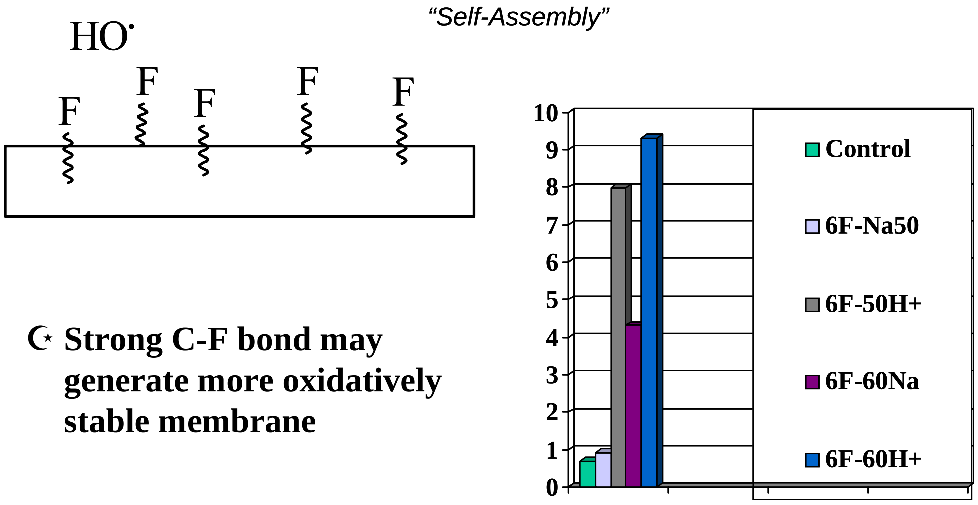

- **Strong C-F bond may generate more oxidatively stable membrane**

Figure 5. Fluorine-Surface Enrichment with Increasing Sulfonation (ESCA)

If one solvent-casts films from these PEM-containing systems, they appear to self-assemble, generating a highly fluorinated surface, which may be more oxidation resistant while at the same time having interior enrichment in the sulfonic acid moiety. This can be illustrated by careful examination of Figure 5, particular for the 60% copolymer sample. Further efforts along these lines to verify this are in progress. The high pressure cell (see Second Quarterly Report) has allowed for the measurement of proton conductivity of the BPSH copolymers as a function of temperature and data on 3 compositions (BPSH 30, 35 and 40),which are illustrated in Figure 6. The important points here are that the Method 2 which involves boiling the membranes at 100ºC, followed by careful neutralization always produces higher conductivity than the analogous treatment at room temperature. We think we have gained some further understanding as to why this is the case, but it could be quite important, as indicated in Figure 6.

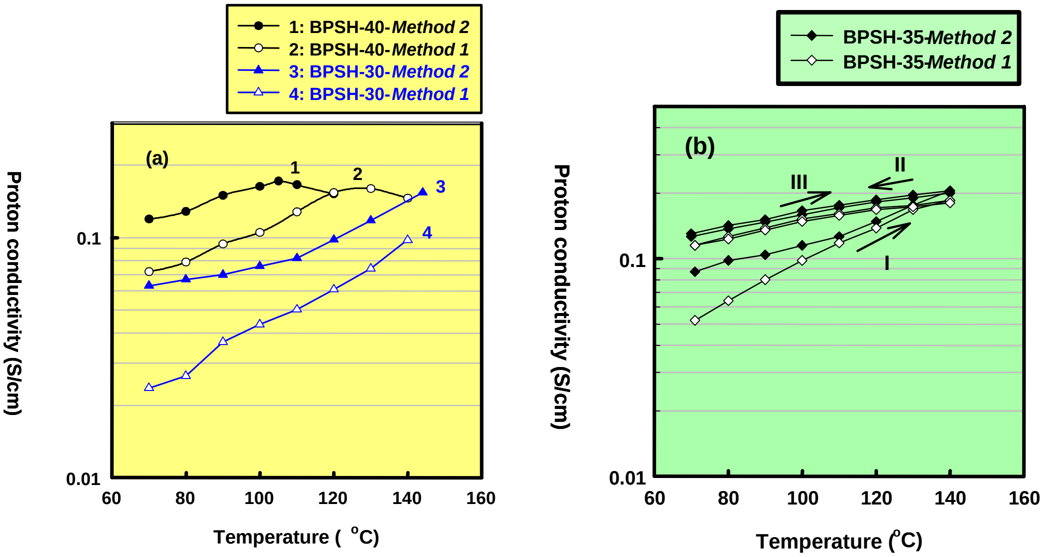

Figure 6. Proton Conductivity of S/cm BPSH 30, 35, and 40 as a Function of Temperature (70-140°C) and Acidification Method

The hysteresis is quite small once elevated temperatures have been measured. This can be seen by the apparent thermal reversibility of BPSH-35. The differing treatment influence the morphology, as shown in Figure 7. There is clearly a more "open" structure generated in BPSH-40 when the membranes are acidified by the boiling treatment. In contrast (Figure 8), the copolymer composition of BPSH-35 is much less affected by the variation in the temperature of acidification. Consequently, it also shows less mechanical deformation after treatment at 140ºC.

Sample treatment: drying at 100ºC for 12 hours, then samples were allowed to equilibrate by exposure to 50% relative humidity at 30ºC for 2 hours, then imaged immediately in relative humidity of about 40%. Scan size: 500nm; Z-range: 10º

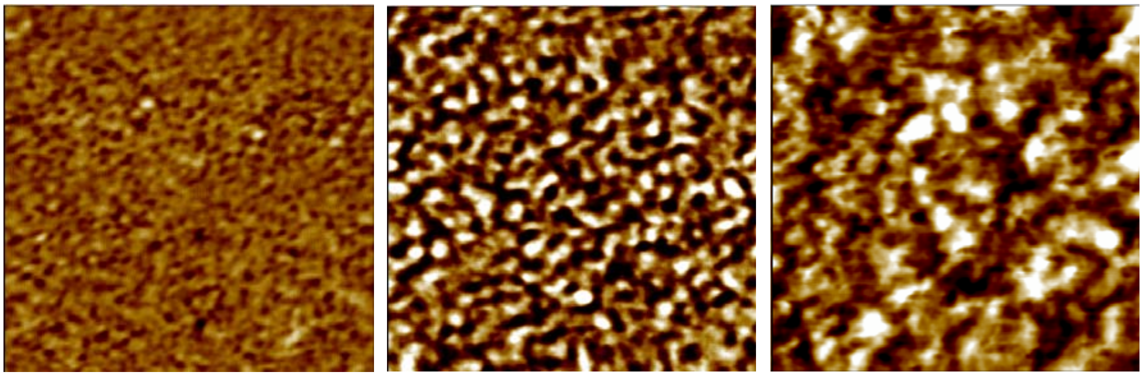

after *Method 1*

after *Method 2*

after high temperature exposure (140ºC max.)

Figure 7. BPSH-40 TM-AFM Phase Images

Sample treatment: drying at 100°C for 12 hours, then samples were allowed to equilibrate by exposure to 50% relative humidity at 30°C for 2 hours, then imaged immediately in relative humidity of about 40%. Scan size: 500nm; Z-range: 10°

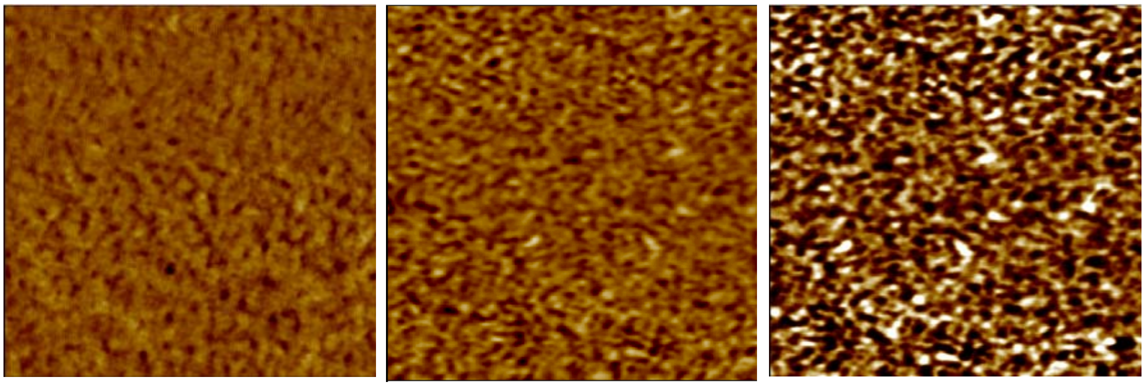

after *Method 1*

after *Method 2*

after high temperature exposure (140°C max.)

Figure 8. BPSH-35 TM-AFM Phase Images

States of Water in Proton Exchange Membranes

We have begun to investigate the details of the water molecular structure of the membrane. For example, in Figure 9 Hodge, et. al reported that one could indicate three possible different states of water: so-called free-water, bound but freezable water, and bound non-freezable water. An ideal differential scanning calorimetry (DSC) thermogram is indicated where one can illustrate the melting behavior of the bound water as expected at 0°C (over an interval). In contrast, the free water melts rather sharply, as anticipated, at 0°C. The water that is essentially soluble in the membrane itself serves as a plasticizer for the PEM copolymer. We've investigated this using our new pressure DSC instrumentation, which allows us to prepare samples at different percent

- Three State of Water
- ***Nonfreezing water***

  water that is strongly bound
  to sulfonic acid groups

2. ***Freezable bound water***

   water that weakly bound
   to the polymer chain

- ***Free water***

  water that has the same phase
  transitions as bulk water

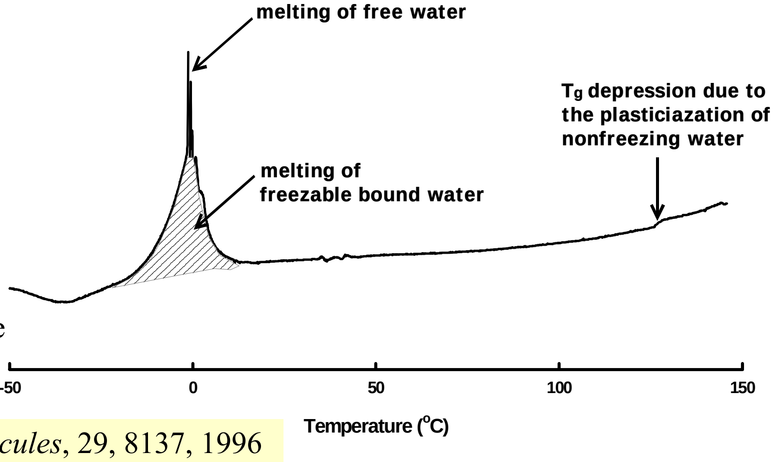

Ref. Hodge, R.M. *et.al. Macromolecules*, 29, 8137, 1996

Figure 9. Three States of Water and Their Effect on DSC Thermogram

humidities, cap the pans and then investigate the thermal behavior. Thus examining Figure 10, one may compare the behavior of the DSC profile for both BPSH-40 and the Nafion control. One concludes that all three types of water can be identified – water that is soluble in the membrane which plasticizes material reduces its Tg, bound but freezable water that produces a broad transition around 0ºC, and free water that produces a very sharp melting behavior.

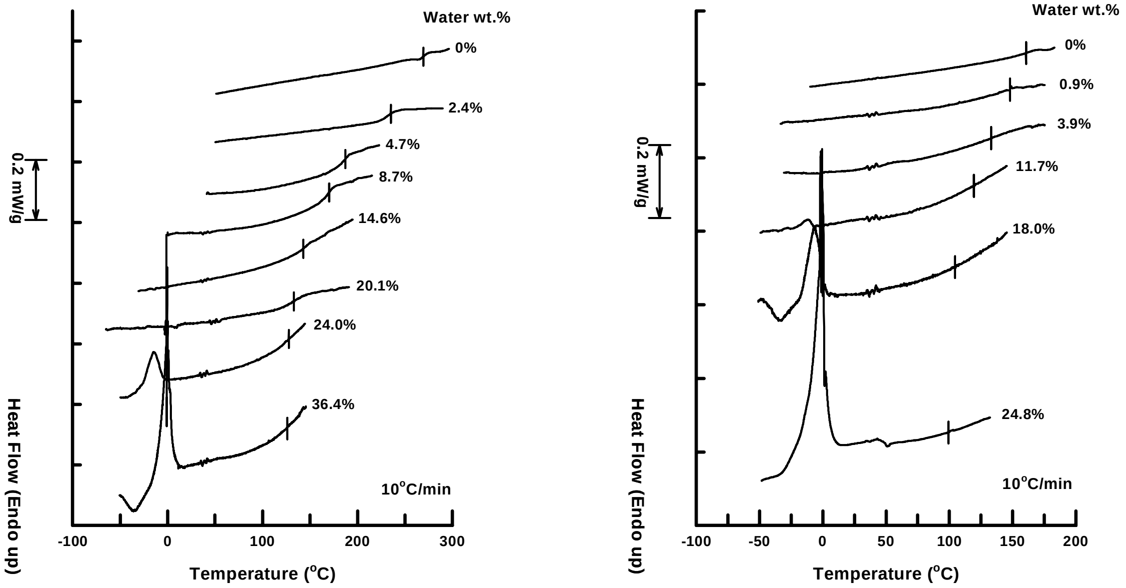

BPSH-40 **Nafion-1135**

Figure 10. DSC Thermograms of BPSH-40 and Nafion as a Function of Water Content

On a quantitative basis, it appears that the Nafion contains more free water than does the BPSH-40. Consequently, one may apply well known polymer science copolymer equations to the depression of Tg as a function of "comonomer" content, which in this case would be, in fact, the soluble water plasticization. Plots such as Figure 11 follow well known copolymer equations up to a certain concentration of water. Beyond that point, they no longer correspond to the equations, which we interpret as reflecting the behavior of the free water. The comparison with Nafion is very interesting. The Nafion material quickly departs from the copolymer equation, which is consistent with the fact that it has a much higher concentration of free water. This may be related to its higher electro osmotic drag and methanol permeabilities. Another important practical advantage of these ideas is shown Table 1, where we illustrate the depression of Tg in the fully hydrated copolymers. The tentative conclusion thus far is that the fully hydrated Nafion really has a Tg no higher than about 99-100ºC, whereas the copolymer systems investigated here are significantly higher. This would likely explain some earlier results reported wherein the BPSH-35 appeared to be more durable at elevated temperatures, especially in terms of its mechanical ability. Further confirmation of this has been obtained using dry samples of BPSH at 3 different compositions measuring dynamical mechanical behavior (Figure 13).

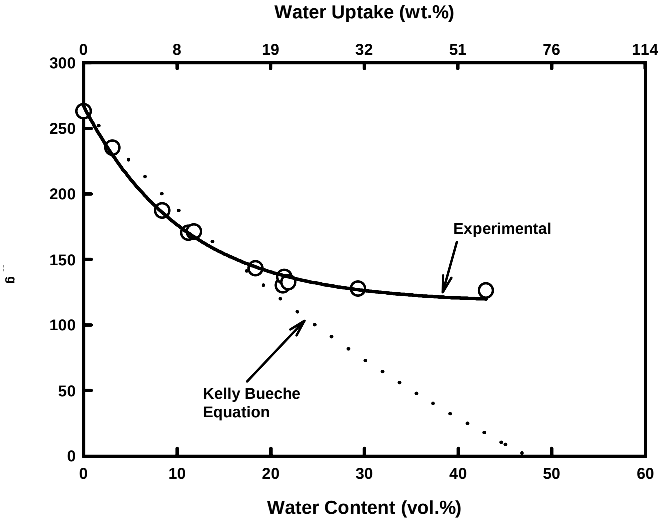

- Kelly Bueche equation

A: free volume fraction at T_g :4.8 10^{-4}
c: volume fraction of polymer
α_S: thermal expansion coefficient of the solvent

Ref. F. Kelly and F. Bueche, *J. Polym. Sci.* 549-556, 1961.

Figure 11. Influence of Water Incorporation on *Tg* Depression of BPSH-40

Table 1. *Tg* Depression of Fully Hydrated Copolymers

Copolymer	Water uptake (%)	T_g of dried sample (^{o}C)	T_g of fully hydrated sample (^{o}C)
BPSH-30	27	257	136
BPSH-40	50	267	126
BPSH-50	109	272	98
Nafion-1135	33	160	99

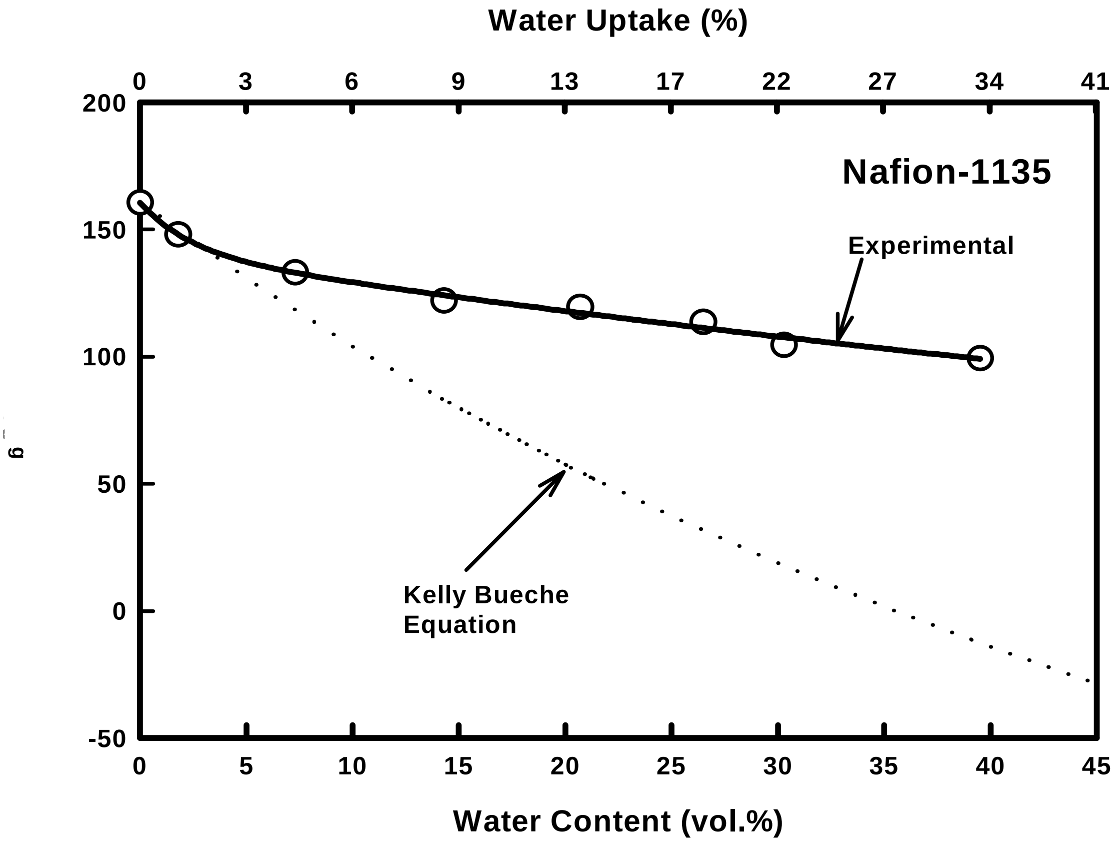

Figure 12. Influence of Water Incorporation on *Tg* Depression of Nafion-1135

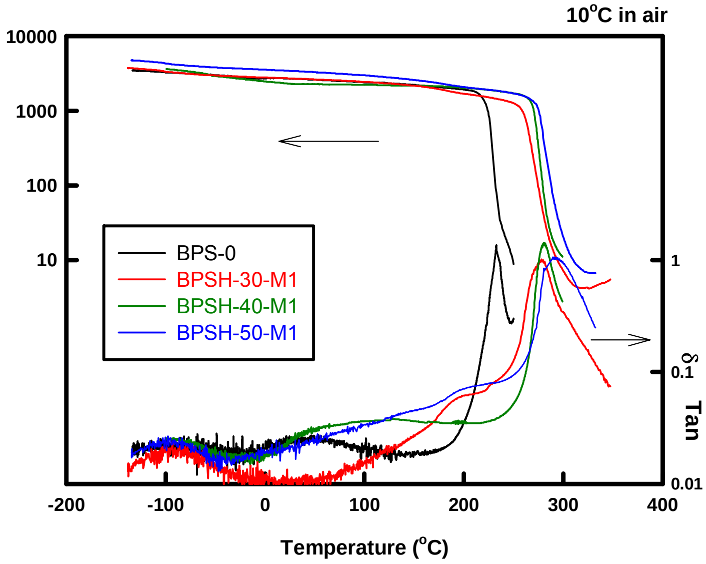

Copolymer	T_g	
	M1	*M2*
BPS-0	223	
BPSH-30	259	270
BPSH-40	268	272
BPSH-50	272	283

Figure 13. Effect of Degree of Sulfonation on Dynamic Mechanical Properties of BPSH

This demonstrates that the dry BPSH copolymers from the control, 30, 40 and 50 percent comonomer concentration have excellent stability at elevated temperatures and are inherently stiffer and stronger than the state-of-the-art perfluorinated copolymers. Subtleties in the degree of aggregation of the ionic groups appear to be present and are particularly further observed by examining the heterophase damping behavior of the same copolymers in Figure 13.

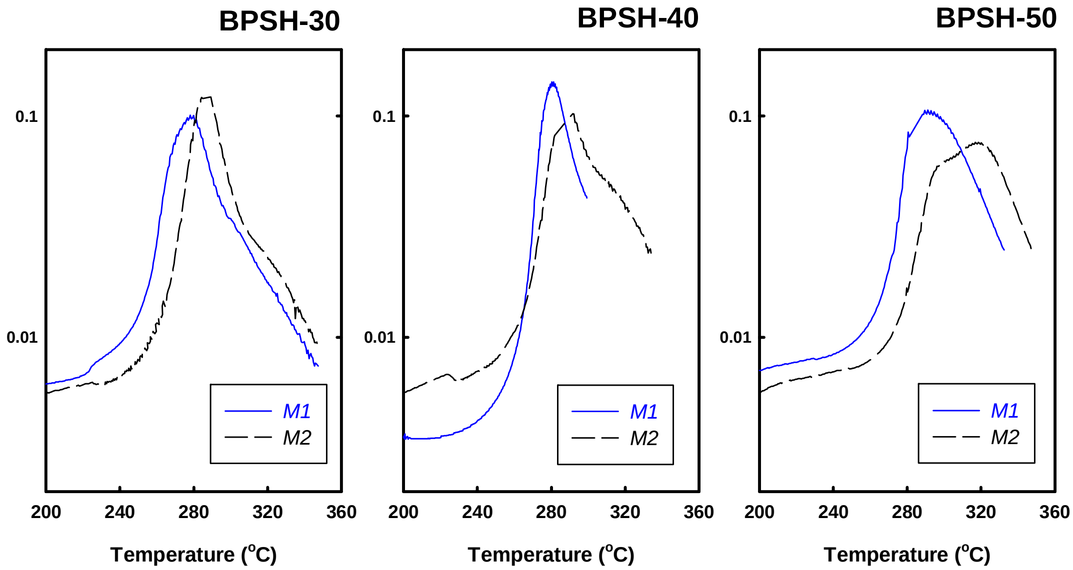

Figure 14. Comparison of *Tg* and Degree of Mixing

Summary

The use of thermal analysis, dynamic mechanical behavior and photoelectron spectroscopy complement the more traditional electrochemical characterization methods, including new impedance spectroscopy and classical conductivity. The results point the way toward more durable membranes and this work is ongoing.

Composite Membranes of BPSH and Phosphotungstic Acid

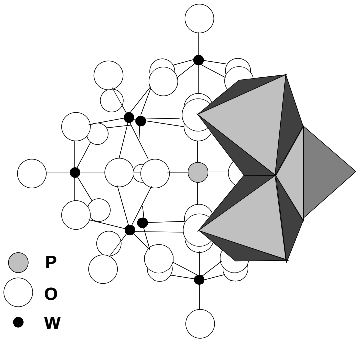

Structure of Keggin anion ($PW_{12}O_{40}^{3-}$)

- ✓ Conductive material (0.17 S/cm)
- ✓ Crystalline form ($H_3PW_{12}O_{40}\ 29H_2O$)
- ✓ Soluble in water or polar solvent
- ✓ Stable at temperatures higher than 100 °C

B.B. Bardin, S.V. et. al. *J. Phys. Chem. B*, 102, (1998) 10817.

Figure 15. Heteropolyacid ($H_3PW_{12}O_{40}$)

The FTIR spectra of the heteropolyacid (HPA) and HPA/BPSH composites, shown in Figure 16, demonstrate that both the terminal and bridging oxygen atoms of the HPA interact strongly with the polymer. This interaction most likely occurs at the sulfonic acid moieties. The proposed interaction is shown in Figure 17.

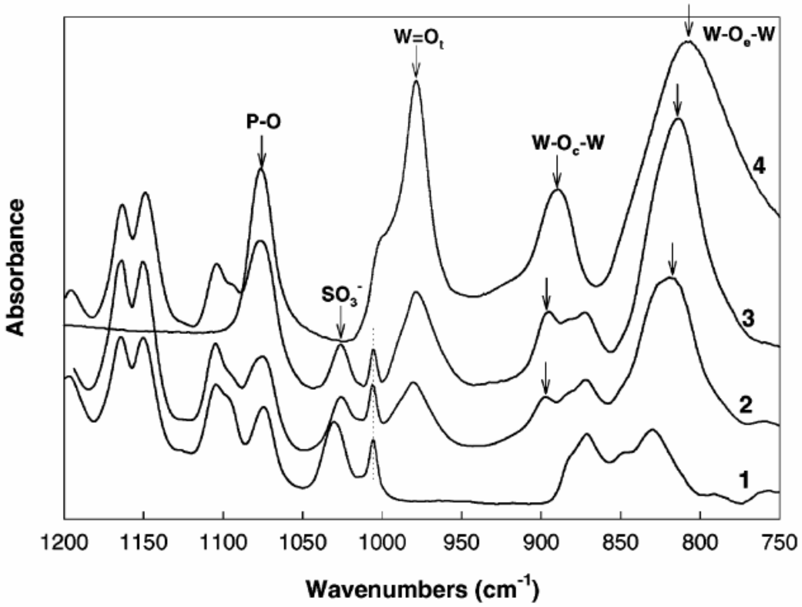

Figure 16: Effect of HPA concentration on the infrared spectra of HPA/BPSH-40 membrane at 140 ◦C. Line 1: BPSH-40; line 2: HPA/BPSH-40 (3:7); line 3: HPA/BPSH-40 (6:4); line 4: H3PW12O40·6H2O.

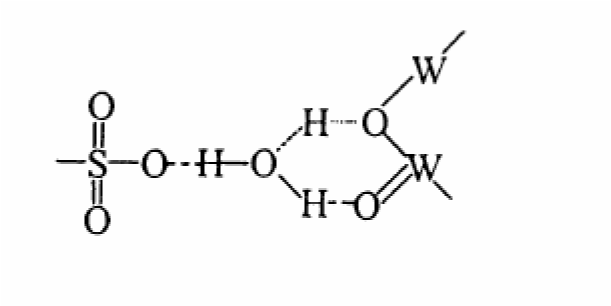

Figure 17. Proposed interaction of HPA and sulfonic acid groups of BPSH.

The extraction of HPA from the BPSH membranes after exposure to liquid water for 48 hours was determined to be dependent on the degree of disulfonation of the copolymer matrix (Table 3). Copolymers with higher levels of disulfonation had poorer retention of HPA than copolymers with lower sulfonation levels. The lower extraction from BPSH membranes than from Nafion membranes is evident in the AFM images also (Fig. 18).

Table 3. HPA extraction from Nafion 117 and BPSH Composite Membranes in Water.

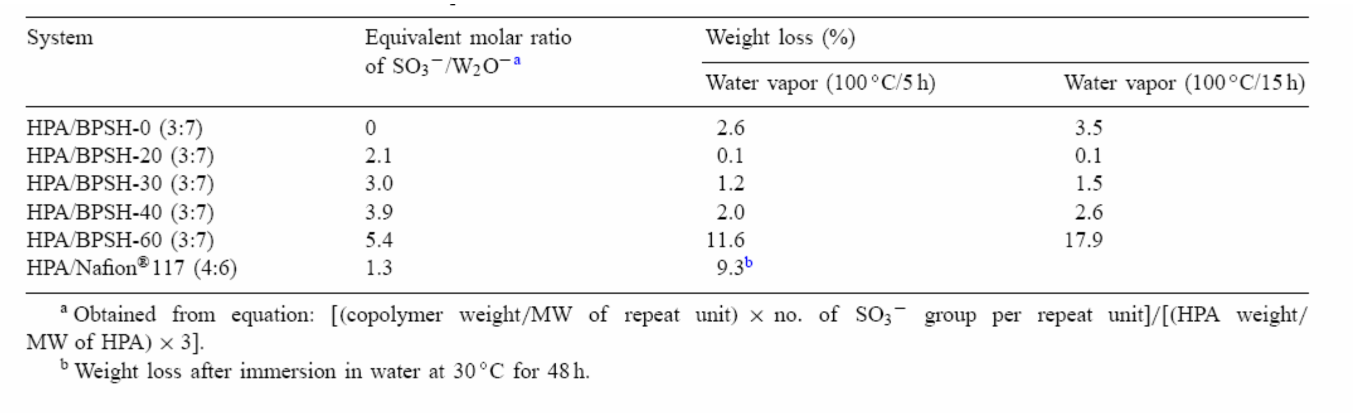

System	Equivalent molar ratio of SO_3^-/W_2O^-[a]	Weight loss (%)	
		Water vapor (100 °C/5 h)	Water vapor (100 °C/15 h)
HPA/BPSH-0 (3:7)	0	2.6	3.5
HPA/BPSH-20 (3:7)	2.1	0.1	0.1
HPA/BPSH-30 (3:7)	3.0	1.2	1.5
HPA/BPSH-40 (3:7)	3.9	2.0	2.6
HPA/BPSH-60 (3:7)	5.4	11.6	17.9
HPA/Nafion® 117 (4:6)	1.3	9.3[b]	

[a] Obtained from equation: [(copolymer weight/MW of repeat unit) × no. of SO_3^- group per repeat unit]/[(HPA weight/MW of HPA) × 3].

[b] Weight loss after immersion in water at 30 °C for 48 h.

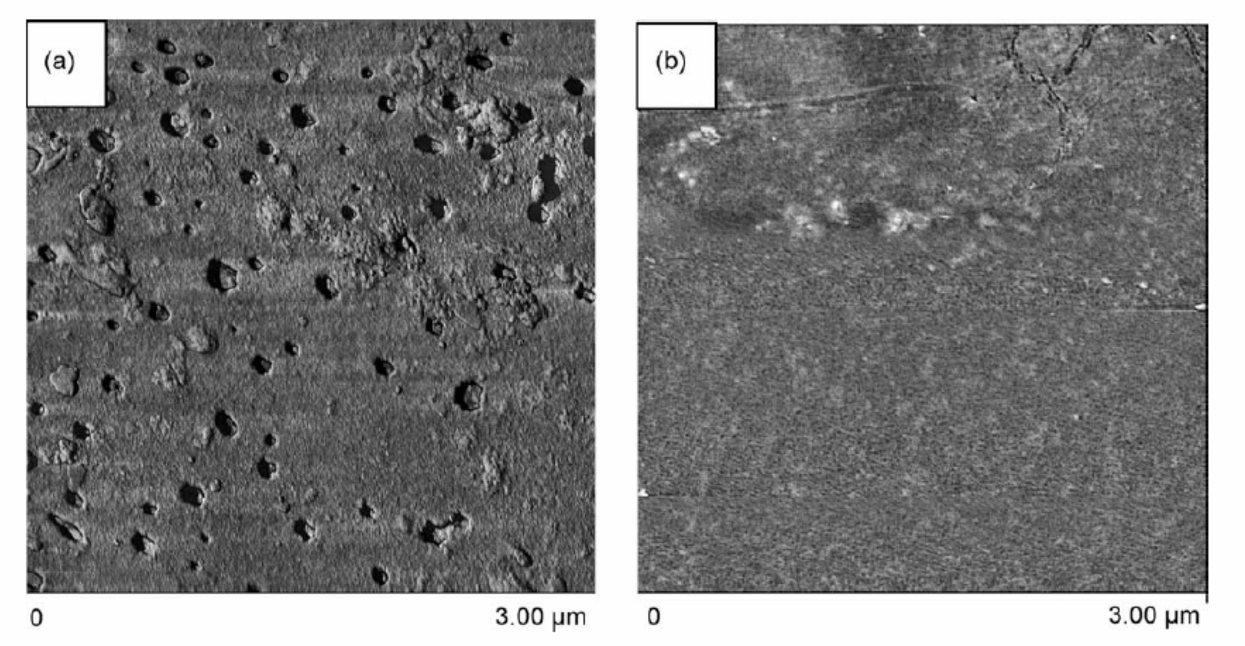

Figure 18. TM-AFM surface images after immersion in liquid water at 30 °C for 48 hours. (a) HPA/Nafion 117 (b) HPA/BPSH-40

The water uptake decreased as a function of HPA content (Fig. 19). This is most likely due to the sulfonic acid sites bonding with the HPA, leaving less sites for water to absorb. As expected, higher degrees of disulfonation resulted in higher water uptake.

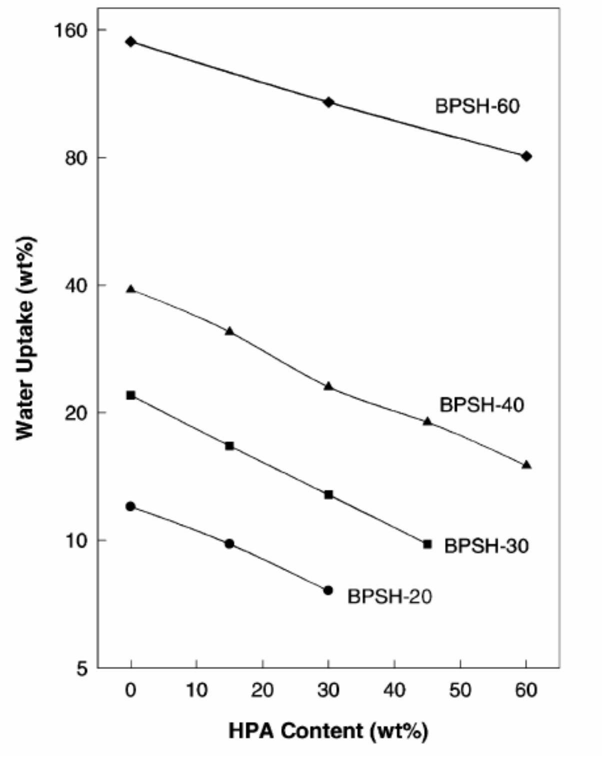

Figure 19. Influence of HPA content and percent disulfonation on water uptake of HPA/BPSH composite membranes.

Composite Membranes of BPSH and Zirconium Hydrogen Phosphate

We have successfully accomplished the synthesis of BPSH/Zirconium hydrogen phosphate (ZrP) composite membranes. These membranes have advantages in structural rigidity at elevated temperatures, as well as enhanced conductivities at elevated temperatures. The expected improvements in mechanical properties were confirmed by our testing. The morphology, the stress-strain properties, and dynamic mechanical behavior in air and water as shown in Figures 20-22.

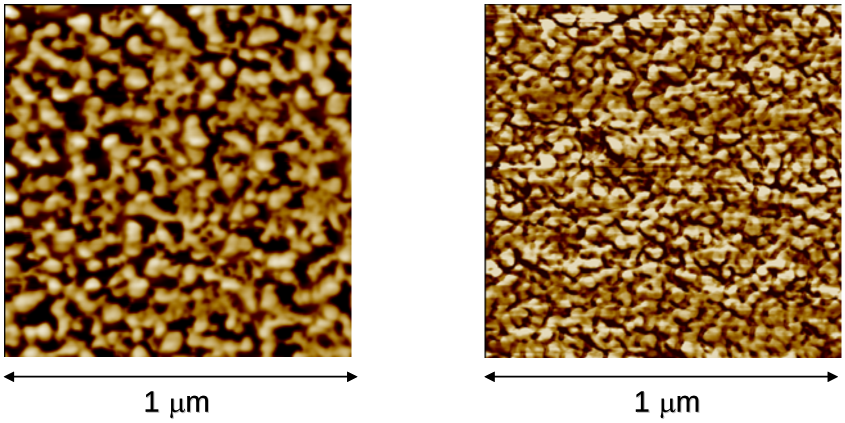

Phase Image of Phosphotungstic acid incorporated system

Phase Image of Zirconium hydrogen phosphate/ BPSH-40 composite

Figure 20. Phosphotungstic BPSH-HPA Composite Membranes

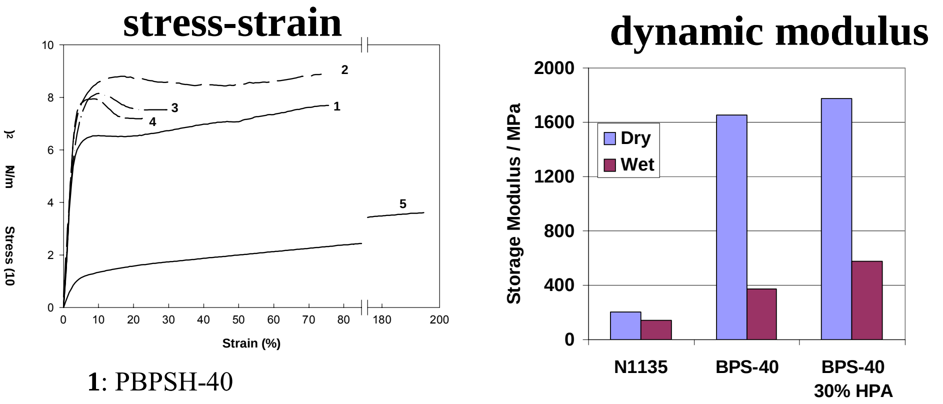

1: PBPSH-40
2: HPA 30 %
3: HPA 45 %
4: HPA 60 %
5: Nafion 117

dry: 25C ambient humidity
wet: 30C liquid water

Figure 21. Stress-Strain Properties and Modulus by In-Situ DMA

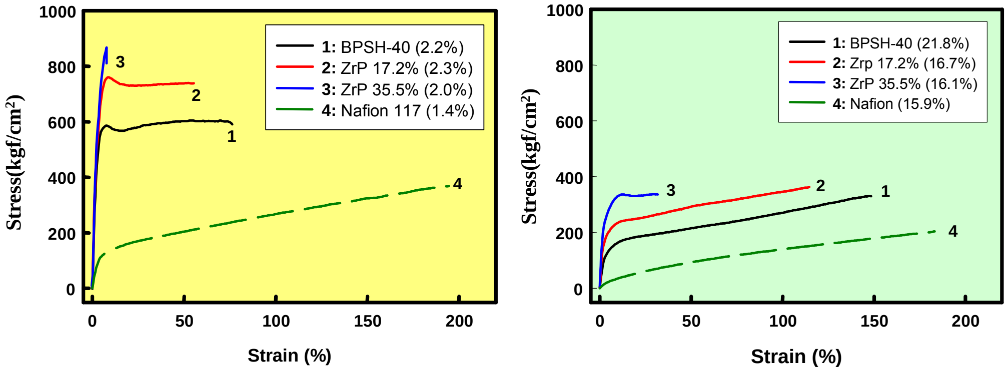

Dry Conditions **Wet Conditions**

Parenthesis: water content in weight percent

Test conditions: 25°C, 40% RH, Crosshead speed: 5mm/min, Number of specimen: 5

Figure 22. Stress-Strain Curves of ZrP/BPSH-40 Composite Membranes

The conclusion is that the host BPSH systems can well disperse the inorganic acid hydrate systems, which then allow one to obtain ductile tough films that are mechanically more stable at elevated temperatures.

High-Temperature Conductivity and Fuel Cell Performance

We have investigated the conductivity at elevated temperatures and high humidity by constructing a sealed-off cell, as shown in Figure 23.

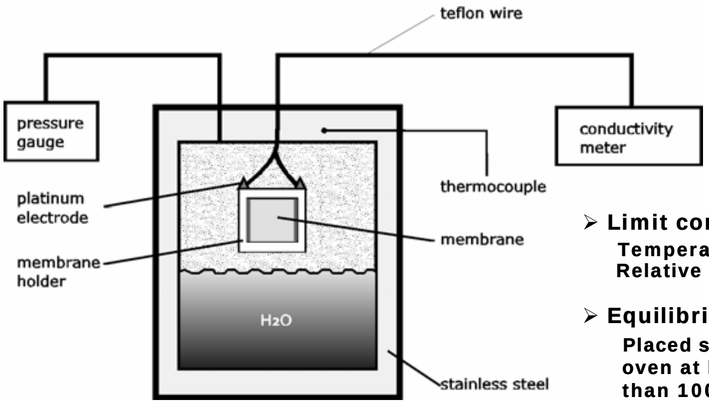

- **Limit conditions**
  Temperature: 140°C
  Relative Humidity:100%
- **Equilibrium conditions**:
  Placed sample in humidity oven at least 4 hrs at less than 100 °C and 2 hrs at above 100 °C at 100 % relative humidity.

  ***Total test hours*:~24 hrs.**

Figure 23. Schematic Setup of a Sealed-off Cell

This allows measurements to be taken to as high as 140°C under high (~100%) humidity conditions. Thus, we have investigated the influence of aging temperature on electrochemical stability at 30°C for BPSH-35, BPSH-40, and with a Nafion control, as illustrated in Figure 24.

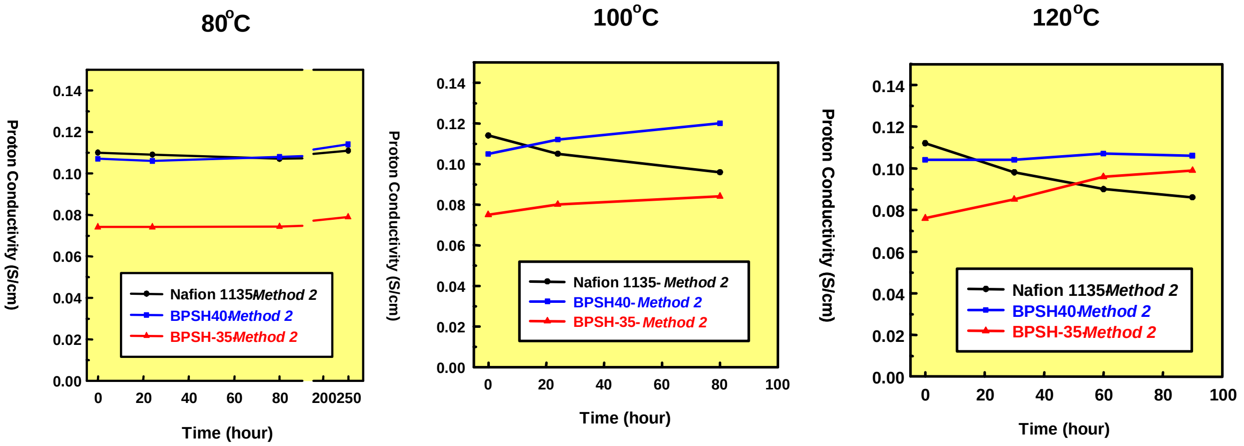

Aging procedure: Samples treated by *Method 2* (boiling in 0.5M H_2SO_4 following by deionized water) were placed in fully humidified condition at a given aging temperature. After a certain time, samples were taken and treated by *Method 1* (30°C H_2SO_4 following by deionized water) in order to remove any contaminants during aging procedure. Then proton conductivity was measured in liquid H_2O at 30°C.

Figure 24. Influence of Aging Temperature on Subsequent Electrochemical Stability at 30ºC

Interestingly, the new BPSH-35 copolymers appear to be mechanically more stable (less swelling) after the elevated temperature treatment than the current state of the art systems. The latter is not a chemical degradation, we suggest, but rather a mechanical morphology relationship, probably involving the relatively modest glass transition temperature of the Nafion, which has been reported by others to be about 126ºC. As a milestone, we have successfully generated membrane electrode assemblies (Figure 25) by creating dispersions from BPSH-30, -40, etc. Further details will be provided later, but essentially one can add an alcohol-water mixture to a solution of the copolymer to produce stable nanodispersions, which can then be combined with the platinum/carbon commercially available components to produce inks. These are then derived into anodes and cathodes and MEAs using procedures well established for Nafion. The membrane electrode assemblies that have been generated have been successfully converted into fuel cell components and tested by a VT Ph.D. candidate, Mr. Michael Hickner at Los Alamos National Labs. The performance curves (voltage vs. current) for hydrogen-air at 80ºC and 120ºC are shown in Figure 26.

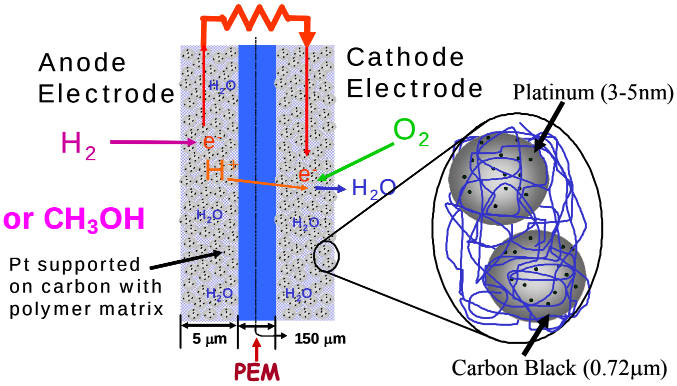

Electrochemistry

Anode: $2H_2 \rightarrow 4H^+ + 4e^-$

Cathode: $O_2 + 4H^+ + 4e^- \rightarrow 2H_2O$

Cell reaction $2H_2 + O_2 \rightarrow 2H_2O$

Energy Source

H_2 from hydrocarbon fuel

O_2 from air

* Product: H_2O

Pt Catalyst

$H_2 + 2Pt \rightarrow 2Pt\text{-}H$

$2Pt\text{-}H \rightarrow 2Pt + 2H^+ + e^-$

Anode Reaction

$CH_3OH + H_20 \Rightarrow CO_2 + 6H^+ + 6e^-$

Cathode Reaction

$3/2\ O_2 + 6H^+\ 4e^- \Rightarrow 3H_2O$

Overall Reaction

$CH_3OH + H_20 + 3/2\ O_2 \Rightarrow CO_2 + 3H_2O$

Figure 25

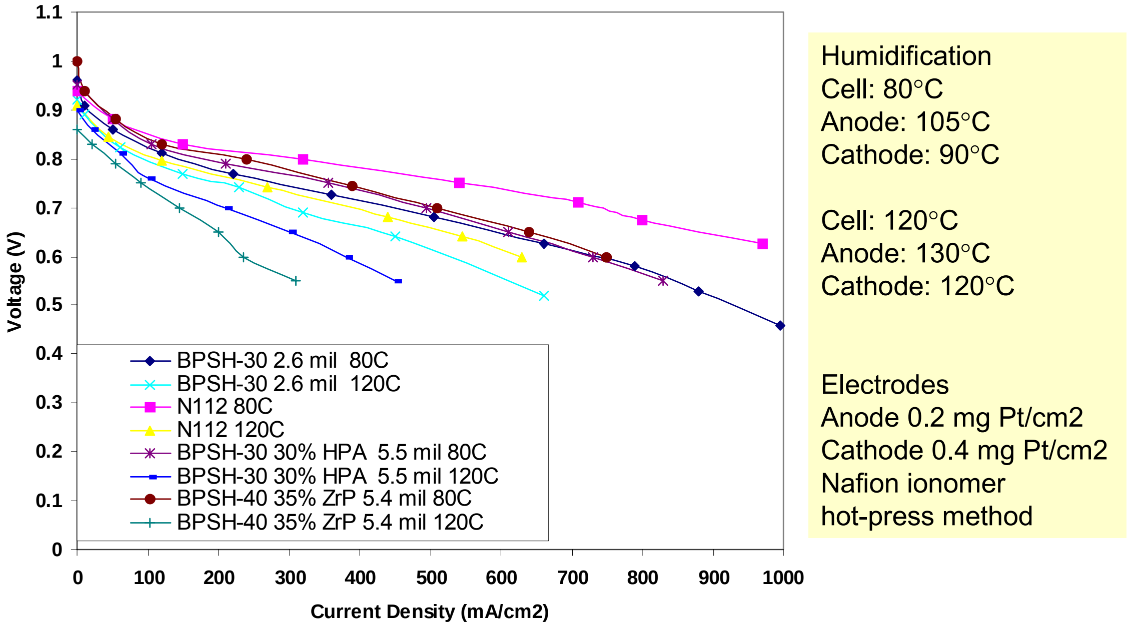

Figure 26: Voltage Current Performance Curves for MEAs at 80 or 120ºC (H2/Air)

The standard of comparison in this case is the 2 mil film Nafion known as 112, which stands for the equivalent weight of 1100, 2 ml. film thickness. The copolymer films were thicker, roughly 2.6 mils, but the performance curves are quite comparable. One can also see the possibility of generating fuel cells at temperatures as high as 120ºC under these partially humidified conditions. Here, we estimate the pressure is approximately 30 psig, which would be about 2 atmospheres. Although this may be higher than desired, it nevertheless is a major step forward to be able to demonstrate such results. Also included in the same curve (Fig. 26), are the initial results on the composite systems containing either the phosphotungstic acid (HPA) or the zirconium hydrogen phosphate (ZrP). One should note that the thicknesses of the composite films are, again, significantly higher – for example, 5-6 mils vs. 2; if one were to consider the interfacial losses because of the increased thickness, the results would be much closer to the Nafion values.

Lastly, we have begun to explore the stability of these materials on the fuel cell membranes shown in Figure 27. For 800 hours, which is a little more than a month, the membranes did not fail. The tests had to be discontinued for other reasons. The resistance was quite stable, as indicated, which implies that the membrane did not undergo any changes. For some purposes, e.g., portable power, this is already beginning to approach attractive stability. Of course, one hopes that another order of magnitude could be demonstrated. This will be attempted in the future.

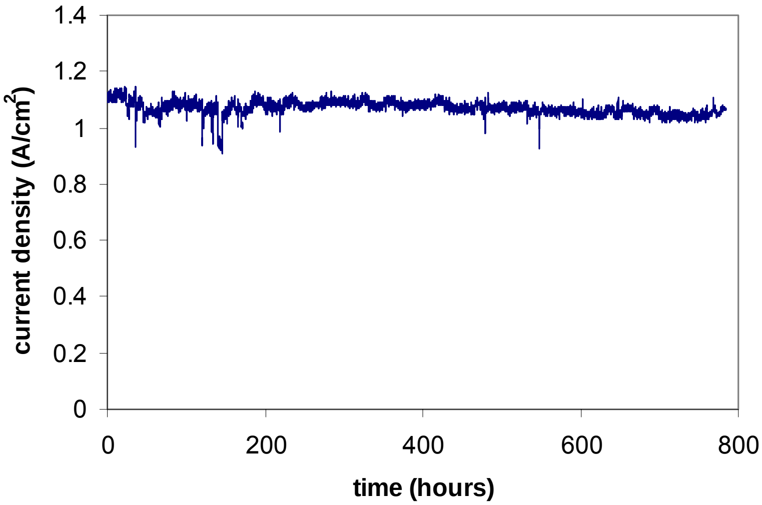

Conditions:
0.5 V cell voltage
80°C cell temp.
full humidification
Anode:
hydrogen 30 psig
0.2 mg Pt/cm^2
carbon supported catalyst
Cathode:
air 30 psig
0.4 mg Pt/cm^2
carbon supported catalyst

note: no change in cell resistance over the entire test indicates no change in membrane – minor performance drop most likely a result of electrode degradation

Figure 27. BPSH-30 H_2/Air Fuel Cell Life Test: ***Membrane is stable ≥ 800 hours***

Multiblock Copolymers from Sulfonated (2-aryl phenylene)-Poly(arylene ether sulfone)

We have succeeded in generating multi-block copolymers containing extremely stable poly(2-aryl *p*-phenylenes) and the BPSH unsulfonated block. The basic chemistry was demonstrated by our collaborator, Prof. Sheares, as illustrated in Scheme 3. Thus, hydroxyl-terminated poly(arylene ether sulfone)s were synthesized following procedures developed in our laboratory some time ago. In a novel way, activated fluorine endgroups were synthesized on the repeating unit of a substituted benzophenone polyphenylene.

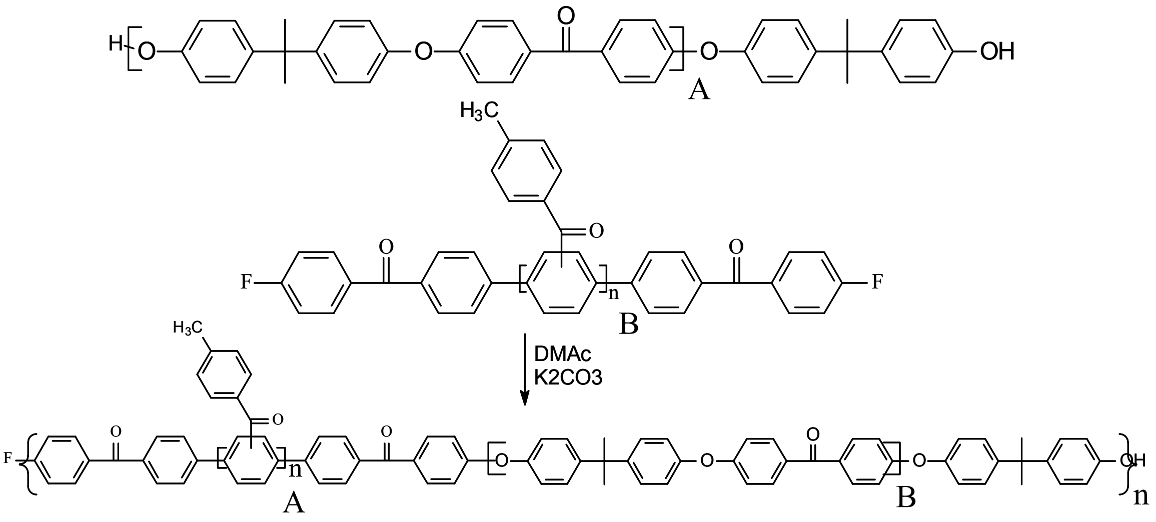

Valerie V. Sheares, et al, J. Polym Sci., Part A: Polymer Chemistry, 39, 3505-3512 (2001)

Scheme 3. Multiblock Copolymers from Poly(p-phenylene) Systems

The chemistry utilized the large reactivity differences between chloro and fluoro aryl ketones in nickel coupling chemistry. Essentially, the fluorinated group is inert under these conditions and provides an endblocking capability. In contrast, the subsequent nucleophilic aromatic substitution process proceeds nicely by displacement chemistry to produce a multiblock poly(arylene ether) substituted polyphenylene system, as shown in Scheme 3. With this background information, we have now prepared an oligomer following the chemistry outlined in Scheme 4, which produces a very well controlled reaction using the nickel coupling chemistry practiced by ourselves, Prof. Sheares, and others.

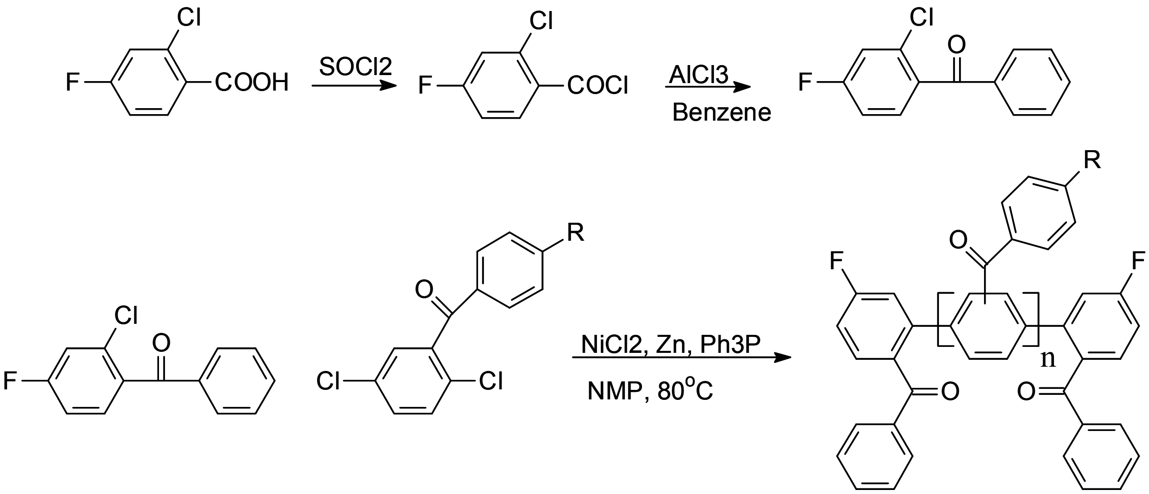

Scheme 4. Scheme Route to Functional Oligomers

The multiblock oligomer, sometimes called a macromonomer or a telechelic oligomer, was prepared in high yields as shown in Schemes 4 and 5. Carbon 13 NMR was used to characterize the molecular weight, because of the dissimilar resonance associated with the endgroup, as shown in Scheme 6. We prepared the hydroxyl terminated wholly aromatic “BPS” poly(arylene ether sulfone) by well known procedures, as shown in Scheme 7, and this was actually successfully conducted by a visiting professor from Hampton University, Prof. Grace Ndip, during the summer period that she spent with us. It was demonstrated that the reactive oligomer based on the biphenyl derivative could be selectively sulfonated to produce ion-conducting sites, as indicated in Scheme 8. The synthesis of the multiblock copolymer containing the sulfonated units has now been successfully conducted as shown in Scheme 9. Such a proton conductive structure is novel and an invention disclosure has been produced. Novel multiphase morphology is expected to show a number of interesting behaviors. Preliminary conductivities have been conducted and the block copolymers are observed to form creasible films, unlike most of the simple substituted polyphenylenes described in the literature.

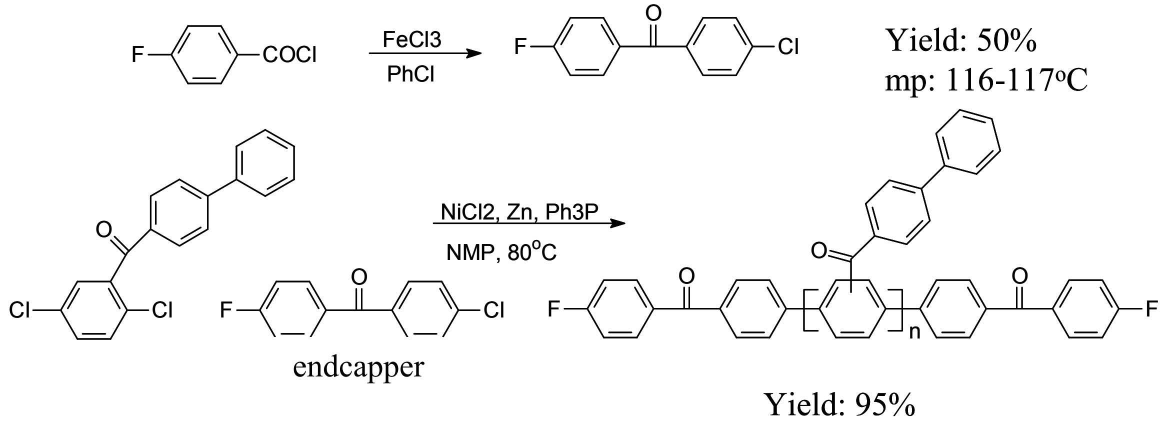

Scheme 5. Synthesis of Telechelic Substituted Poly(2-aryl phenylenes) Oligomers

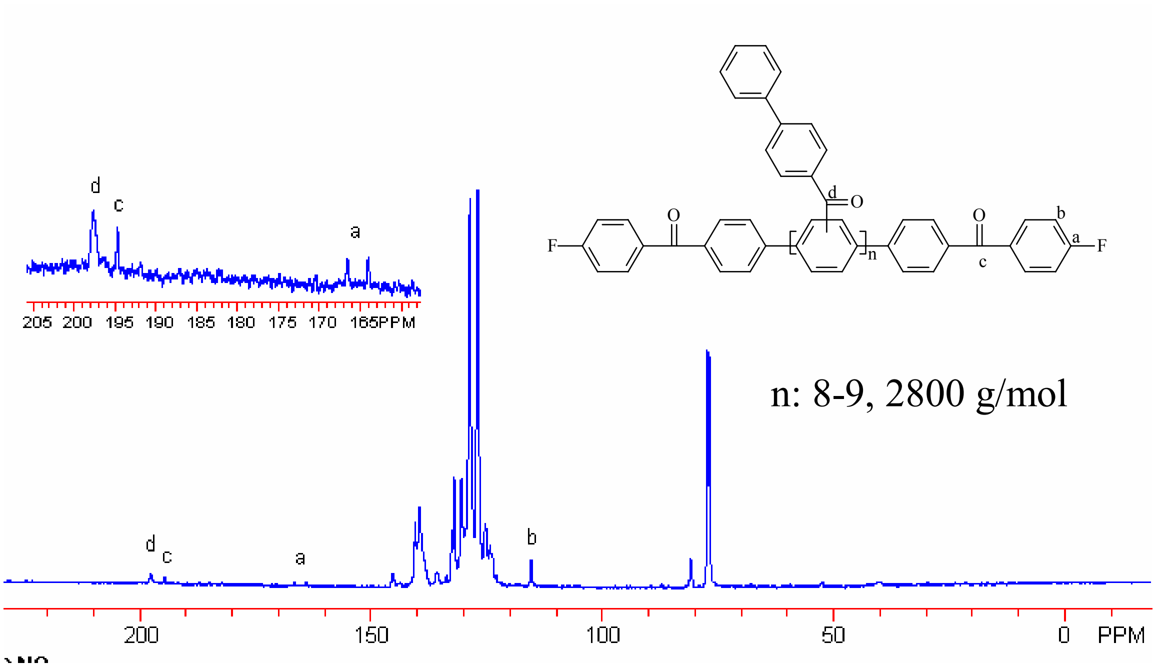

Scheme 6. 13C NMR of Endcapped Telechelic Oligomers

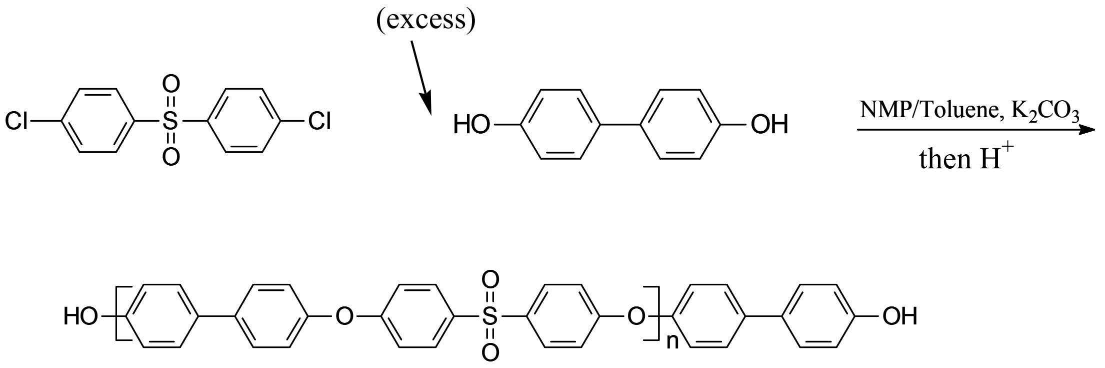

5K, determined by ^1H NMR

Scheme 7. Synthesis of Hydroxy-Terminated BPS Functional Oligomers
(prepared by Prof. Grace Ndip, Hampton University)

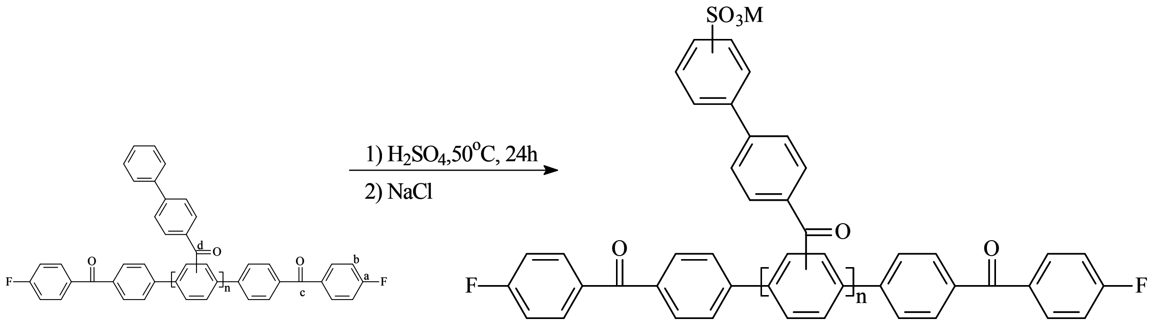

Scheme 8. Sulfonation of Activated Fluoro Endcapped Polyphenylene Oligomers

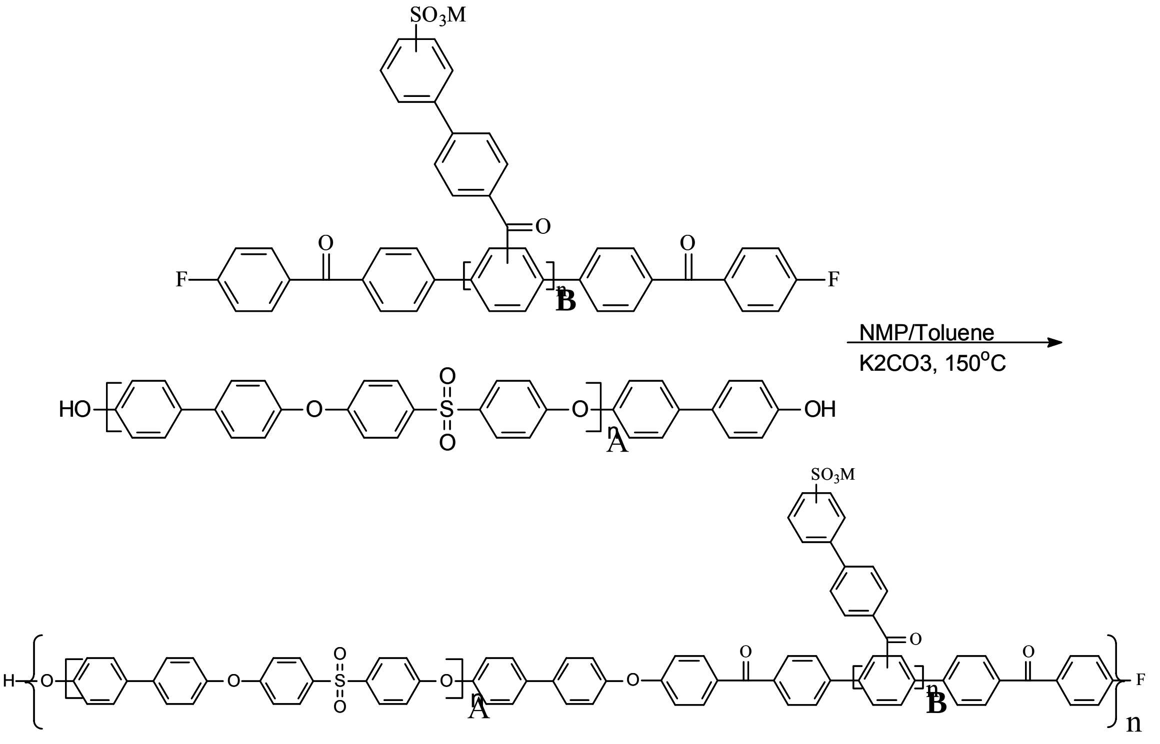

Scheme 9. Synthesis of Multiblock Sulfonated Poly (*p*-phenylene) Copolymers

Conversion of Pendent Sulfonic Acids into Sulfonimides

Conversion of sulfonic acids to sulfonamide groups was investigated. The driving force for conducting this research is related to the fact that the acidities of the sulfonimides are at least two orders of magnitude higher than the sulfonic acids. Our research, as well as others, would certainly suggest that this would lead to higher conductivities – perhaps even at a lower concentration of the ion-conducting sites, which would be desirable, both from an economic and a technical polymer science point of view. The literature shows, as indicated in Scheme 10, that it is possible to produce sulfonamides from poly (arylene ether ketone)s by first post-sulfonation and then by reaction with an amine.

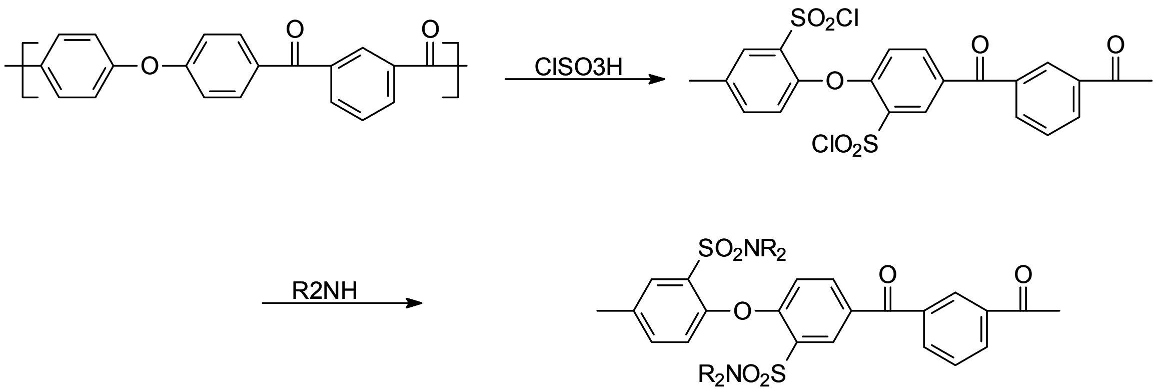

C.S. Marvel, et al., *J. Polym Sci*., Polymer Chemistry Edition 22, 295-301 (1984)

Scheme 10. Sulfonamidization of PEK

Recently, Allcock et al. have reported similar chemistry for substituted phosphazines (H.R. Allcock, et al. *Macromolecules*, 2002 35, 6390-6493). In our work, illustrated in Scheme 12, we have been able to derivatize the BPSH sulfonic acid systems by following one of two different reaction schemes, shown in Scheme 11 and 12. Thus, the sulfonic acid can be converted to a sulfonyl chloride, then neutralized with ammonium carbonate, followed by derivitization with trifluoro sulfonyl chloride to produce the sulfonimide. The initial conductivities were quite promising for this low level of ion conducting sites, and probably reflect the higher acidity, as postulated above. Scheme 12 outlines a separate route, which would convert BPSH first to the film forming chloride, following by reaction with the commercially available trifluoro sulfonyl amine to produce the sulfone amide. Thus far, both 30% and 40% copolymers have been prepared, which have significantly higher IECs as expected. The materials have been characterized by both infrared, as shown in Figure 28, and by NMR spectroscopy, as shown in Figure 29.

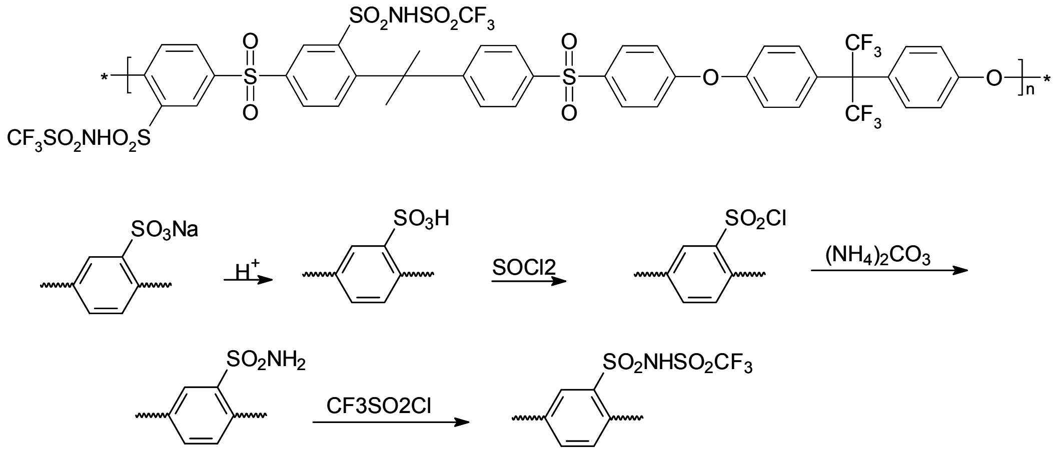

IEC (meq/g): 0.54 (calc. 0.63); Water uptake: 25%
Conductivity: 0.048 S.cm^{-1}

Scheme 11. Sulfonimidization of a Bisphenol AF Based Poly(arylene ether Sulfone) Sulfonated Copolymer

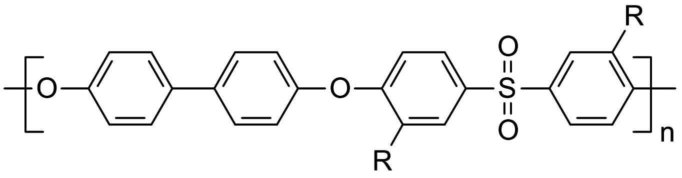

R= SO3H → SO2Cl → SO2NHSO2CF3

	Water uptake (%)	IEC (meq/g)
BPSNH-45	-	1.54 (calc. 1.52)
BPSNH-30	11 (24)	1.14 (1.2)(calc. 1.13)

Scheme 12. Conversion of BPSH to BPSNH

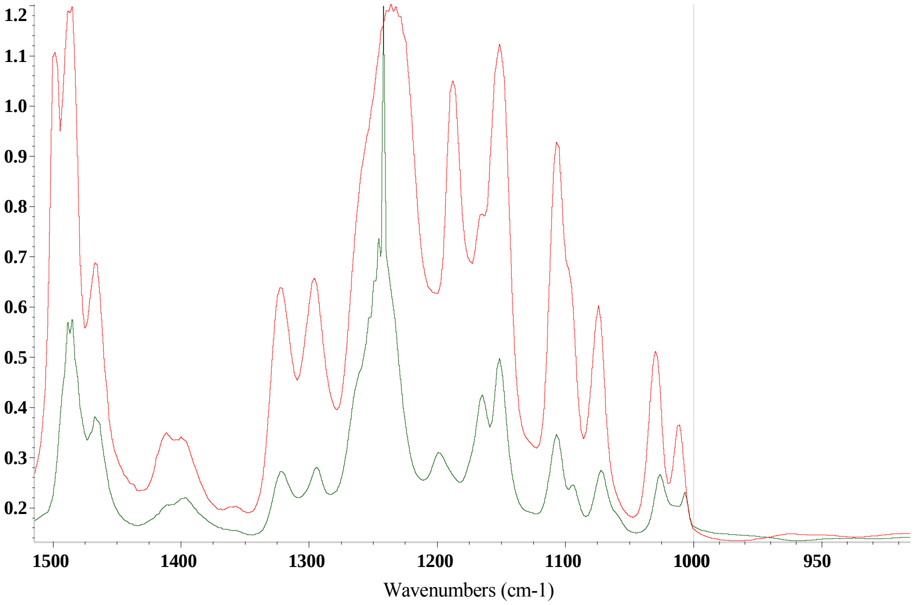

Figure 28. FTIR Spectra of BPSH-45 and BPSNH-30

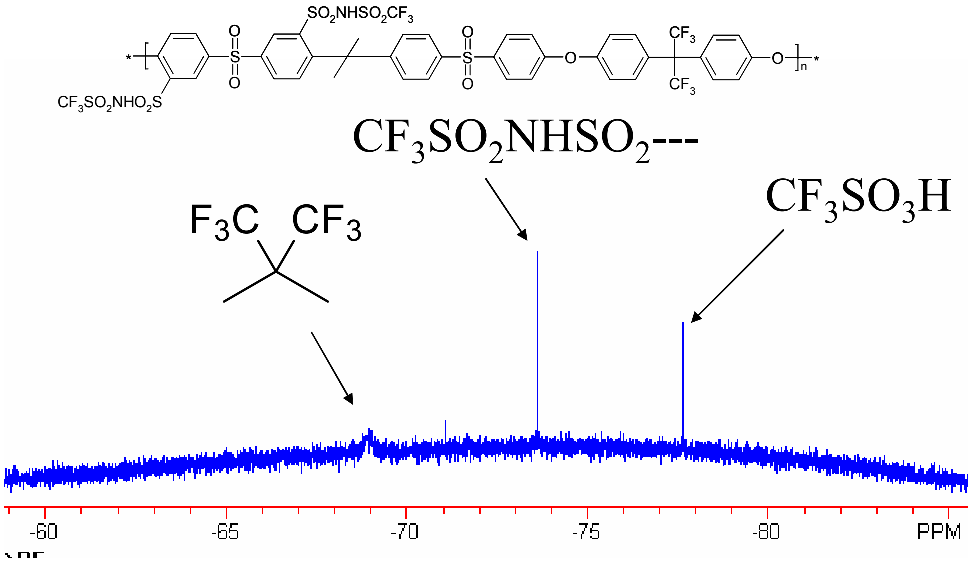

Figure 29. ^{19}F NMR Spectrum of 6F-PSNH-20

Comparison of Sulfonated Copolymers of Poly(arylene sulfide)s with Poly(arylene ether)s

Another area that has been of interest is to compare the behavior of poly(arylene sulfide)s with poly(arylene ether)s, with respect to their utilization in proton exchange membranes for fuel cells (Scheme 13).

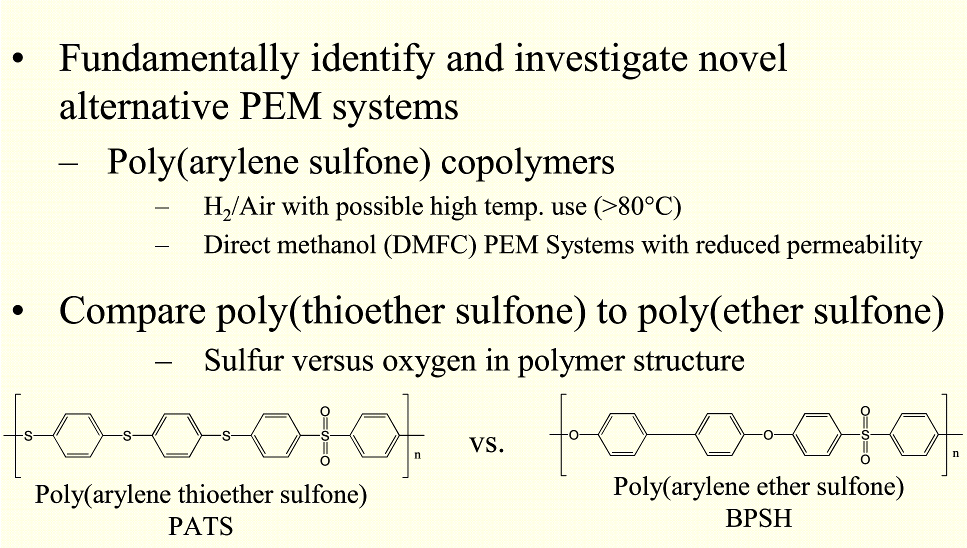

- Fundamentally identify and investigate novel alternative PEM systems
  - Poly(arylene sulfone) copolymers
    - H_2/Air with possible high temp. use (>80°C)
    - Direct methanol (DMFC) PEM Systems with reduced permeability
- Compare poly(thioether sulfone) to poly(ether sulfone)
    - Sulfur versus oxygen in polymer structure

Poly(arylene thioether sulfone)
PATS

vs.

Poly(arylene ether sulfone)
BPSH

Scheme 13

Our objectives here are to compare the polythioether sulfones with the polyether sulfones. Oxygen vs. sulfur is an important variable in the molecular design of these materials. The interest is in both higher temperature proton exchange membranes and also for DMFC fuel cell systems that would have reduced permeability to methanol. Poly(arylene thioether sulfone)s have been investigated previously in our laboratory (Scheme 13), however, the generation of proton exchange membranes has not been conducted before. The synthetic route for producing the new materials is shown in Scheme 14 and the polymerization procedures are quite analogous to the earlier studied BPSH systems. Either the fluorinated sulfone monomer or chlorinated sulfone monomer can be used; the latter is commercially more feasible but somewhat less reactive. Analysis of the copolymers is again possible by NMR spectroscopy, as shown in Figure 30, and high molecular weight film-forming copolymers could be produced as shown in Table 4. The influence of sulfonation on conductivity is analogous to the poly(arylene ether sulfone)s and is illustrated in Figure 31. Thus, a new family of sulfur containing proton exchange membranes has been generated. The materials are in many ways similar to the BPSH poly(arylene ether sulfone) series, but additional characterization is ongoing to discern potential differences in both conductivity and transport behavior.

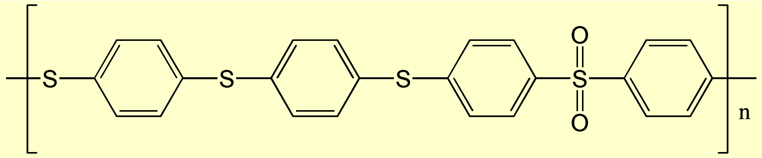

- •Good mechanical property
- •Excellent thermal Stability-possible use at 120°C
- •Good chemical stability-acids, bases and oxidants
- •Film forming high performance thermoplastics
- •Several monomers are commercially available
- •Direct polymerization of sulfonated monomer possible

Reference: Lui, Y.; Bhatnager, A.; Ji, Q.; Riffle, J. S.; Mcgrath, J. E.; Geibel, J. F. and Kashawagi, T. *Polymer,* **2000,** 41, 5137.

Scheme 14. Why Poly(arylene thioether sulfone)s? (PATS)

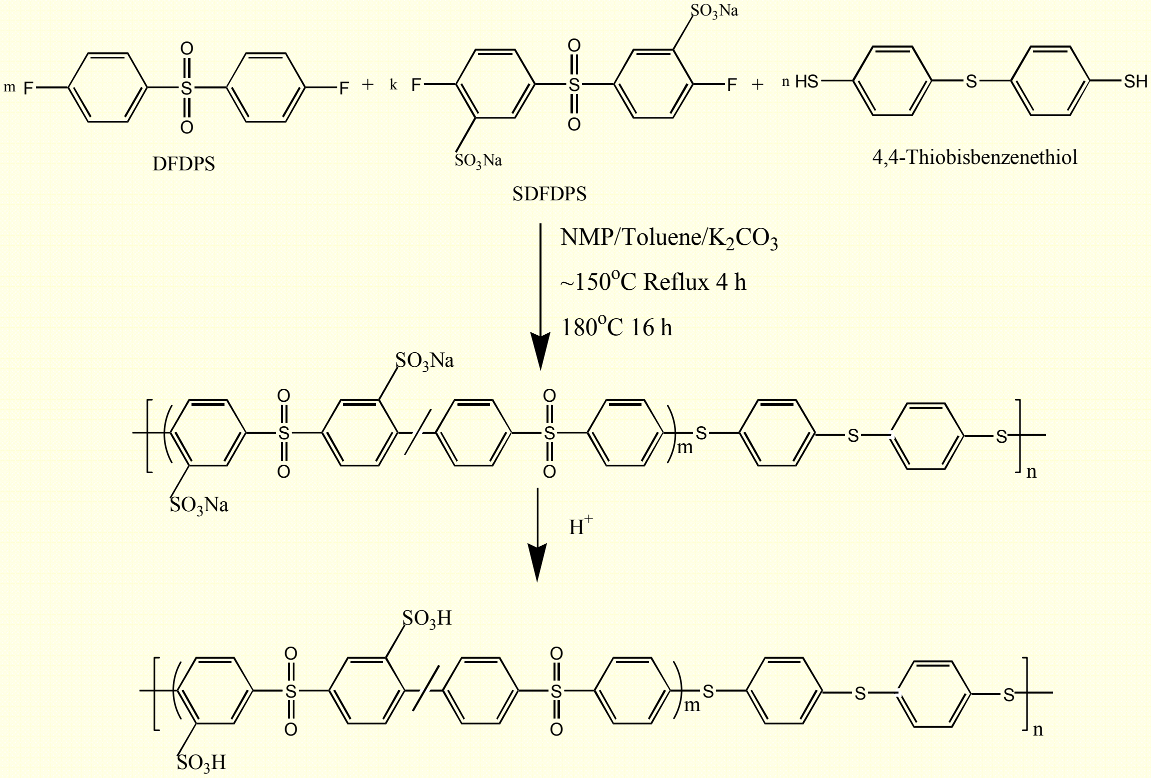

Scheme 15. Synthesis of Poly(arylene thioether sulfone) Copolymers

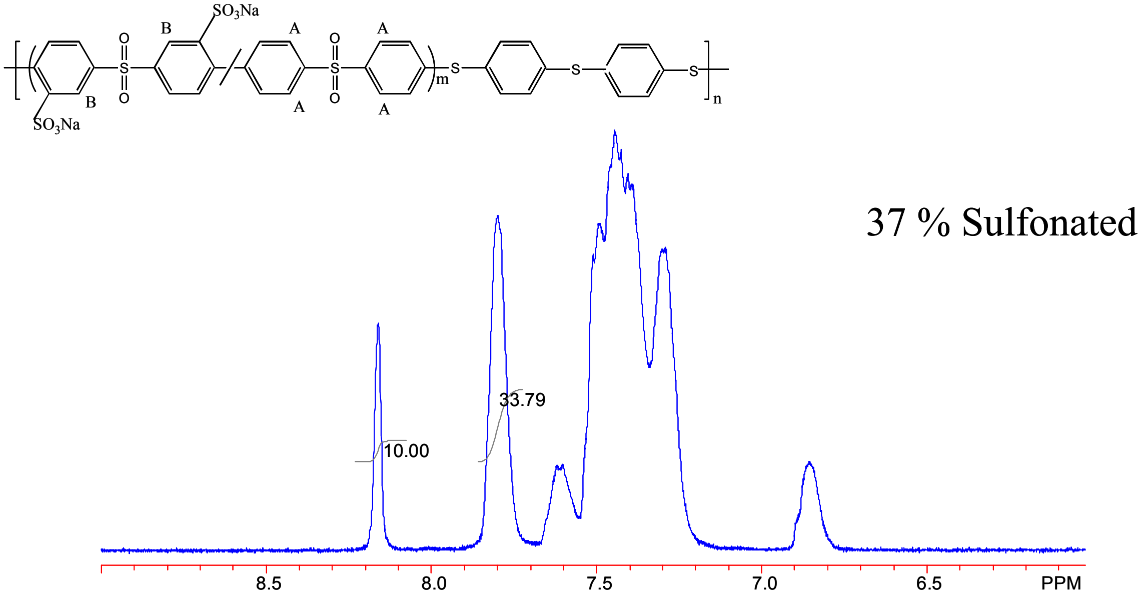

%Degree of sulfonation=(B/2)*100/(B/2 + A/4)

Figure 30. ^{1}H NMR of 40 mol% Sulfonated Copolymer

Table 4. Polymerization of DFDPS, SDFDPS and 4,4-Thiobisbenzenethiol (TBBT)

DFDPS **+** **TBBT** **+**	**Yield**	**I.V. dL/gm (NMP 25°C)**	**Obtained Sulfonation By ^{1}H NMR**	**Calc. Ion Exch. Capacity (IEC) (meq/gm)** **(Nafion^{TM} 1100 = 0.91)**
0% SDFDPS (Control)	90%	0.42	0%	0
20 mol % SDFDPS	91%	1.3	18%	0.81
30 mol % SDFDPS	92%	0.98	28%	1.17
40 mol % SDFDPS	90%	1.2	37%	1.51
50 mol % SDFDPS	92%	1.8	48%	1.83

- Polymerized in NMP at 180°C using K_2CO_3 for 16hrs.

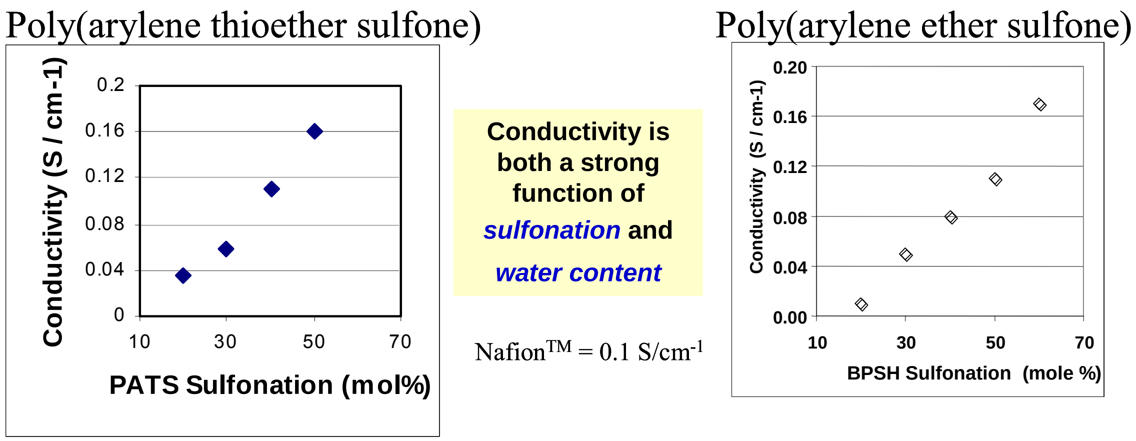
Poly(arylene thioether sulfone)

Poly(arylene ether sulfone)

Conductivity is both a strong function of *sulfonation* and *water content*

Nafion^{TM} = 0.1 S/cm^{-1}

30°C in liquid water

Acidification method: boiled in 0.5M H_2SO_4 for 2 hrs.,
boiled deionized H_2O for 2hrs.

Figure 31. Effect of Sulfonation on Conductivity for either poly(arylene thioether) or poly(arylene ether) Sulfonated Copolymers.

Morphology Control of Proton Exchange Membranes For Direct Methanol and Hydrogen-Air Fuel Cells

Morphology control is critical for both transport and selectivity. In the previous Third Quarter Report we demonstrated a number of differences between acidifying the membrane at room temperature vs. boiling the membrane at 100ºC. We refer to room temperature processes as Method 1 and the boiling procedure as Method 2. The atomic force microscopy (AFM) is very useful at characterizing these various structures, particularly in the tapping mode, and in Figure 32 we illustrate the surface morphology for the 40% copolymer after Method 1, Method 2, and exposure to high temperatures. For purposes of further discussion, we now refer to the transition regions as Regime 1, Regime 3, and Regime 3. One notes that the morphological structure is certainly more open in Regime 2, and in Regime 3 some irreversible deformations can take place, which influence both mechanical properties as well as conductivity. We interpret these transformations as resulting because the measurement temperature is actually higher than the hydrated Tg. Earlier we reported the influence of composition on the morphology of the copolymers, acidified with Method 1, and this is reproduced in Figure 33, below. Under these conditions the percolation limit for co-continuous morphology is around BPSH 50% copolymer, and the 50% system demonstrates the phase inversion. Importantly associated with that morphology change is a loss of strength and the development of hydrogel-like behavior for the 60% copolymer. Figure 34 relates the analogous behavior to the water sorption. Indeed, once can identify a shift from Region 1 to Region 2, which is furthermore influenced by the acidification temperature. These pseudo-phase diagrams are important for defining compositions that will desirably combine good mechanical behavior with satisfactory conductivities. During this period we have also begun to investigate the relaxation behavior of the proton exchange membrane BPSH Copolymers by NMR techniques. In Figure 35, we present information generated by NMR spin-spin relaxation times, often referred to as T2 in the NMR literature. This can begin to further clarify the rigid hard phase and soft phase behavior in these multiphase copolymers, which changes as a function of composition. It can also begin to predict where truly “free water” can occur. Three types of water were reported in the Third Quarterly Report by differential scanning calorimetry (DSC) measurements so that the NMR techniques spin-spin relaxation time is complementary, to those previously reported pressure DSC measurements.

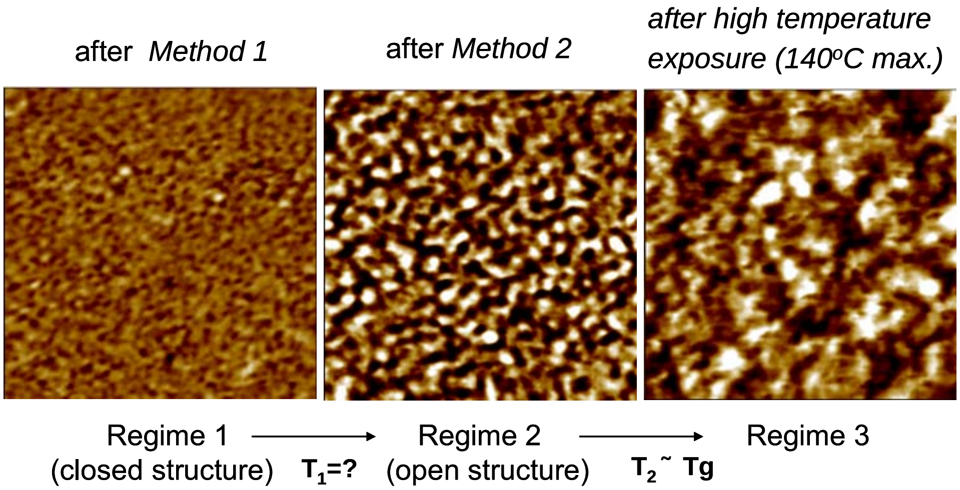

Figure 32. BPSH-40 Tapping Mode AFM Phase Images

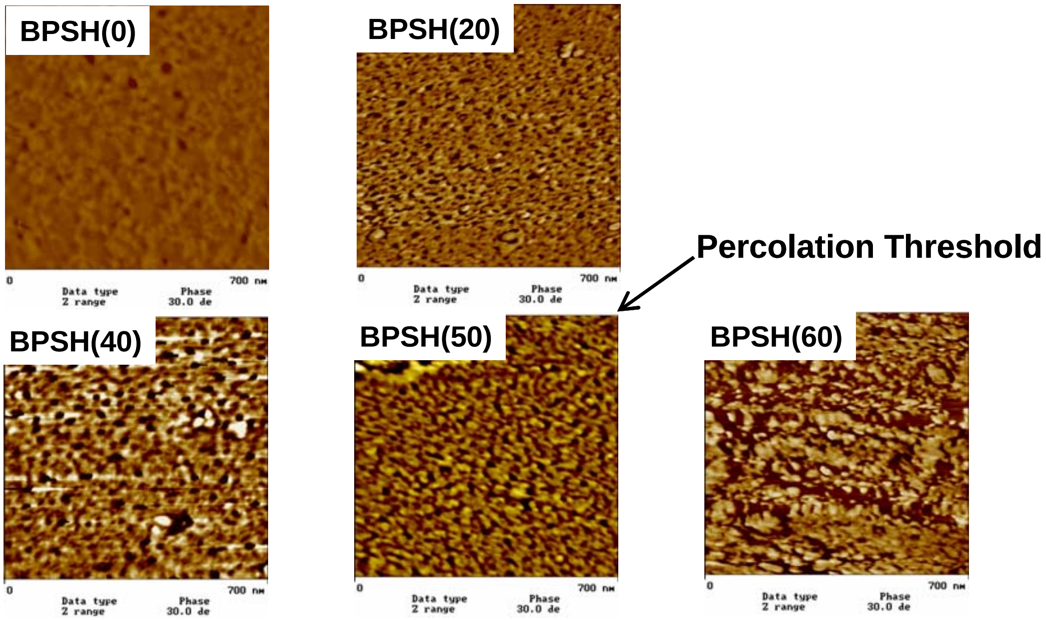

Scale: 700mn; Phase Angle: 30 degrees

Figure 33. Influence of Sulfonation Degree on Membrane Morphology Treated by Method 1 (AFM Tapping Mode Phase Image)

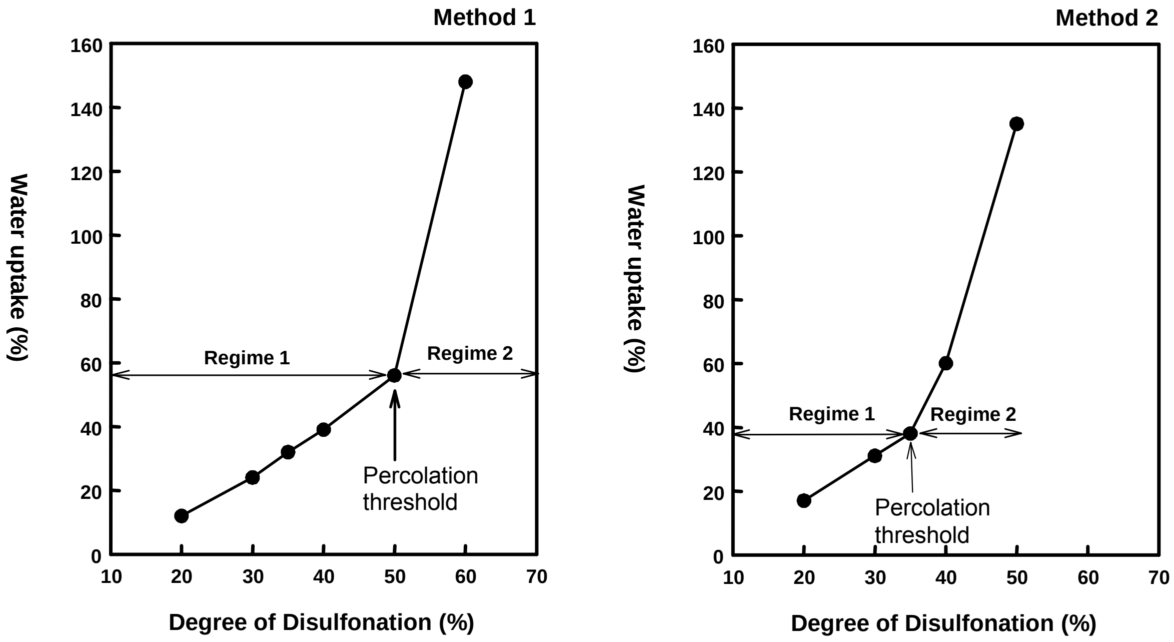

Figure 34. Effect of Acidification on Water Uptake and Percolation Threshold

Copolymer	Hard phase	Soft phase	Free water
BPS-0	100%	0%	0%
BPSH-10	90%	10%	0%
BPSH-20	54%	46%	0%
BPSH-30	34%	66%	0%
BPSH-40	28%	60%	12%
BPSH-60	0%	88%	12%

← Percolation Threshold

- *Accomplished by Dr. Limin Dong, 2002

✓ ^{1}H T_2 values are determine from the slope of the plot of ln M against time, where M is the amplitude of the spin-echo signal.

Figure 35. Water Composition in BPSH Treated by Method 2 Measured from Spin-Spin Relaxation Time (T_2)

During this period we constructed an experimental set-up for measuring methanol permeability. It is essentially outlined in Figure 36. The proton exchange membrane film is used to separate a methanol solution from the water solution, and as the methanol permeates through the film, it can be measured by noting the change in refractive index that is generated. The methanol permeability of PBSH can be plotted as shown in Figure 37, and consistent with the AFM pictures produced earlier the permeability can be defined into regimes, which are dependent upon percolation limits – and these are also functions of whether the films are acidified at room temperature or at 100ºC.

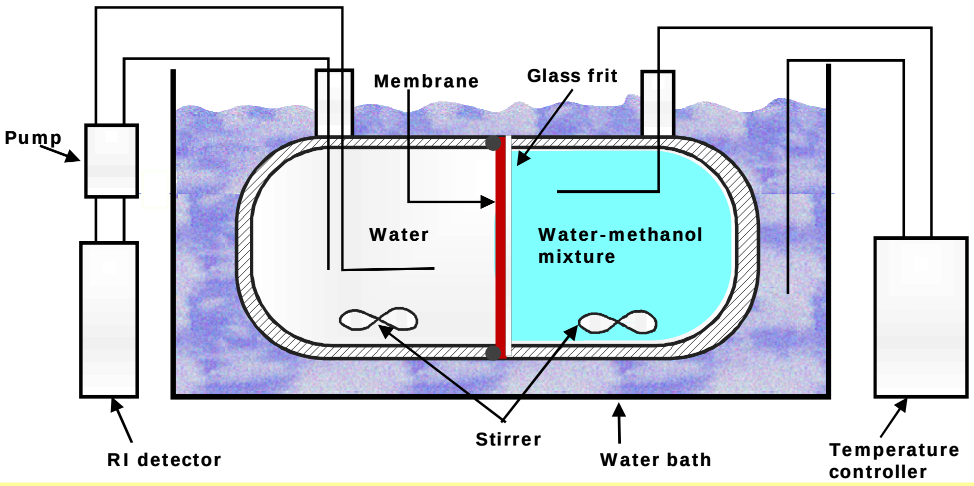

Test conditions

Flow rate for RI detector: 1 ml/min
Cell volume: left: 100ml; right: 98 ml
Initial methanol content: 2 mol
Total test time: 9 hr
Cross sectional area: 7.065 cm^2

Figure 36. Schematic Experimental Set-up Used to Measure Methanol Permeability

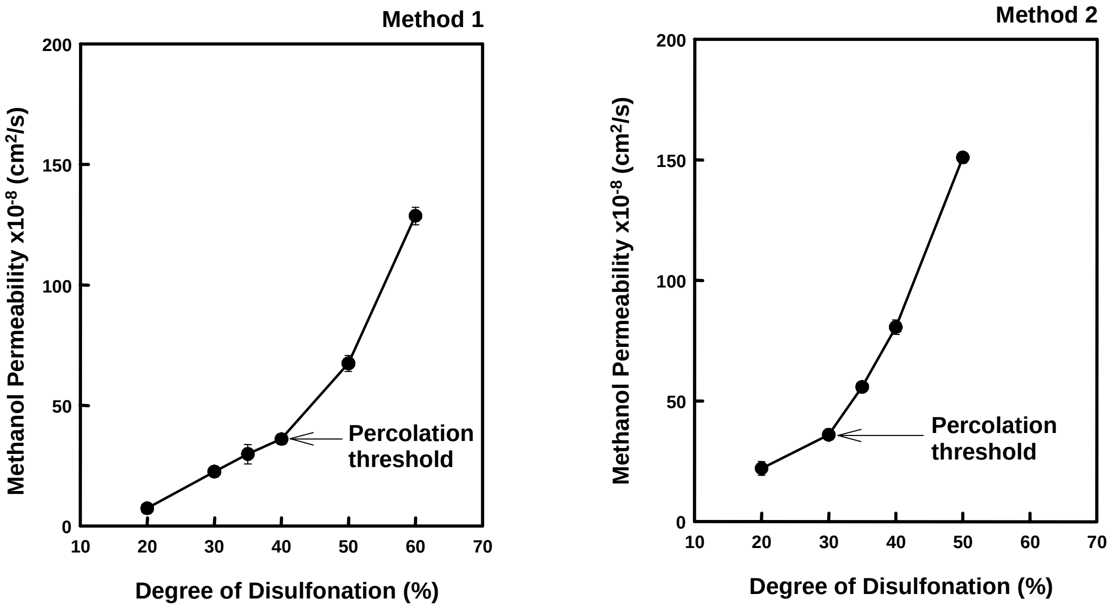

Figure 37. Effect of Composition and Acidification Method on Methanol Permeability of BPSH Copolymers
(*Methanol Concentration: 2 Molar*)

Transport of Water and Methanol through PEM Fuel Cells

The above methanol permeability technique was applied to several different BPSH copolymers, as well as a Nafion control. The data generated for methanol permeability are shown in Figure 38, along with electro osmotic drag coefficients conducted with collaborators at Los Alamos (Dr. B. Pivovar). The data show nicely the relationship between ion exchange capacity, water uptake, conductivity, methanol permeability and electro osmotic drag. The resulting systems can be used to correlate performance curves, such as the voltage current behavior shown above. BPSH systems clearly show superior behavior relative to Nafion 117 and can also be expected to show this improved behavior, largely on the basis of their lower permeability.

	ion exchange capacity (meq/g)	water uptake (wt %)	conductivity (S/cm)	methanol permeability (cm^2/s)	electro-osmotic drag coef. (N H_2O/H^+)
Nafion 117	0.91	19	0.11	$16.7*10^{-7}$	3.0
BPSH-40	1.71	58	0.10	$8.1*10^{-7}$	1.3
BPSH-35	1.51	38	0.08	$5.6*10^{-7}$	0.9
BPSH-30	1.32	31	0.06	$3.6*10^{-7}$	0.7

30°C in liquid water

Figure 38. General Membrane Properties

Scale-Up of BPSH Copolymers to Kilogram Quantities

In this section we discuss joint on-going interactions with the start-up company, Hydrosize, Inc. Hydrosize has reactor capability which is capable of synthesizing both the sulfonated monomer as well as the BPSH sulfonated copolymers in kilogram or perhaps larger concentrations. During this period, Hydrosize has demonstrated that following our procedures they can generate good yields of the sulfonated monomer. Analytical procedures have been developed at Virginia Tech, which allow the improved characterization of the crystallized monomer-grade material by HPLC chromatography and NMR spectroscopy. The combined techniques are continuing to yield information on how the sulfonation reaction can be further optimized. At the present time, good monomers can be made at temperatures of approximately 100°C, over a 4-6 hour period followed by salting out and then crystallization by alcohol-water mixtures. The optimum type of alcohol, e.g., methanol, ethanol, or isopropinol, has been investigated, as well as the ratio of the alcohol to the water for obtaining high purity and yet reasonable high yields of the sulfonated monomer. Further details will be reported in the next quarterly report. Suffice it to say that the monomer synthesized by Hydrosize has been effectively utilized to produce copolymers in the 30-40% ion conducting comonomer concentration, which has been achieved in appropriately high molecular weights (e.g., intrinsic viscosities of about 0.9 dl/g in NMP at 25ºC. The resulting materials make good films and improved film casting technique has been developed in our laboratories to provide samples to appropriate partners. Thus far, samples have been provided to General Motors, DuPont, Air Products, Motorola, and the catalyst manufacturer, OMG. Interactive discussions with the knowledge transfer partner are ongoing and preliminary results look quite promising, especially with respect to mechanical properties. We have held meetings in Blacksburg with the Hydrosize President, Dr. Heather Brink, and Vice President, Dr. Andrew Brink, and communication is continuing to optimize both the monomer and copolymer preparations.

Thus, it has been demonstrated that the overall process designed at Virginia Tech can be scaled in industrial scale pilot equipment to at least kilogram quantities.

Novel Proton Conducting Sulfonated Poly(arylene ether) Copolymers Containing Aromatic Nitriles

Abstract

High molecular weight nitrile-functional, (hexafluoroisopropylidene)diphenol based aromatic poly(arylene ether) copolymers with pendent sulfonic acid groups have been prepared by step copolymerization of 4,4'-(hexafluoroisopropylidene)diphenol, 2,6-dichlorobenzonitrile, and 3,3'-disulfonate-4,4'-dichlorodiphenylsulfone. Copolymers containing as much as 55 mole % disulfonated units were cast from dimethylformamide solutions to form tough ductile films. The films were converted from the salt to the acid forms with dilute sulfuric acid followed by deionized water. Dynamic TGA demonstrated that the well-dried, acidified, nitrile-containing copolymers had no weight loss up to 300 °C in air. A systematically varied compositional series showed increased glass transition temperatures, protonic conductivities, and hydrophilicities as a function of disulfonation. Films containing ≥20 mole % of the disulfonated repeat units had T_g's of 220 °C and higher. At approximately equivalent ion exchange capacities (IEC), e.g. 1 to 1.6 meq g^{-1}, the protonic conductivities of these films were comparable to other disulfonated poly(arylene ether sulfone) copolymers investigated. The benzonitrile-containing disulfonated copolymers also had reduced moisture absorption (10-15% by weight) compared to other disulfonated poly(arylene ether sulfone) copolymers with equivalent IEC's. The copolymer with 35 mole % of the disulfonated comonomer had a protonic conductivity >0.10 S cm^{-1} at 110 °C and 100% relative humidity. The protonic conductivities of the benzonitrile-containing copolymers decreased as expected as relative humidity was lowered. Atomic force microscopy in the tapping mode demonstrated that the acidified copolymer with 35 mole % disulfonated units was nanophase separated into an essentially co-continuous morphology of hydrophobic and hydrophilic domains. Further efforts are ongoing to translate these promising results into membrane electrode assemblies for proton exchange membrane fuel cell devices.

Introduction

The development of polymer electrolyte membrane fuel cells as alternative energy sources has been ongoing continuously since the 1960's [1]. Initially these devices were developed for specialized applications such as electrical power sources aboard spacecraft and submarines. However, the current vision is that polymeric electrolyte membrane (PEM) fuel cells can be implemented in many applications such as power sources for vehicles (i.e. cars, trucks, and locomotives), stationary power, and portable electronic devices. The conditions inside a fuel cell are harsh and include chemically active noble metal catalysts, highly acidic environments, fuels such as hydrogen, methanol and its partial oxidation products, oxidants such as oxygen, reactive radicals at electrodes, and process temperatures in excess of 100 °C [1]. Polymers containing perfluorosulfonic acid groups such as Nafion® have been used as separation membranes and these materials now represent the industrial standard. Such materials have demonstrated good performance at moderate temperatures (less than ~90 °C), relatively high humidities, and with pure hydrogen gas as the fuel [2].

There is significant interest in using fuels other than hydrogen such as methanol, methane, and gasoline. All of these fuels usually contain trace concentrations of gases such as carbon monoxide which poison and reduce efficiencies of fuel cell platinum catalysts [3]. At elevated temperatures (greater than 100 °C), carbon monoxide poisoning of platinum catalysts is less of a hindrance and cathode kinetics can be enhanced. However, limited operating temperatures and undesirably high methanol permeabilities of Nafion® membranes limit their scope of applicability.

The need for alternatives to copolymers containing perfluorosulfonic acid groups has led to development of a number of aromatic sulfonated polymers as membrane candidates. Poly(arylene ether sulfone)s are of considerable interest because these materials are well-known for their excellent thermal and mechanical properties as well as their resistance to oxidation and stability under acidic conditions [4-7].

Over the last 30 years, chemically modifying poly(arylene ether sulfone)s through sulfonation has been of great interest. Some of the early work in this area reported by Noshay and Robeson included electrophilic aromatic sulfonation of a commercial poly(arylene ether sulfone) under mild conditions [8]. Monosulfonation occurred at an activated ortho position relative to an ether oxygen on the bisphenol A rings with a 2:1 complex of SO_3 and triethylphosphate (Fig. 39) [9]. This procedure minimized undesirable side reactions such as branching and crosslinking. The sulfonated polymers were evaluated as materials for desalinization membranes for water purification [10,11]. However, these materials would have limited utility as fuel cell membranes because the sulfonation procedure only incorporated up to one sulfonic acid group on the polymer repeat unit. Location of the substituents on the bisphenol component of the repeat units, together with the limited number of sulfonic acid groups along the polymer chain, did not afford sufficient acidity for proton conducting fuel cell membranes. This approach was further explored in our laboratories and higher degrees of sulfonation resulted in excessive swelling in water [9].

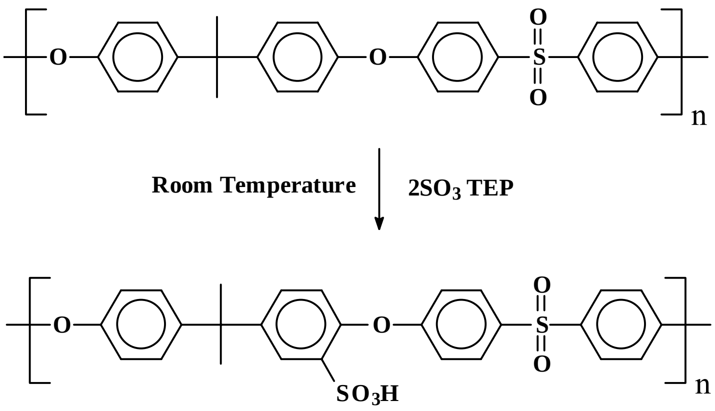

Figure 39. Post-sulfonation of a poly(arylene ether sulfone) [9]

We have recently investigated syntheses and characterization of wholly aromatic poly(arylene ether sulfone)s with two sulfonic acid groups on the rings adjacent (meta) to the sulfonyl groups [12-14]. The syntheses produced aromatic sulfone-activated aryl halide disulfonated monomers (in the salt form) which were copolymerized directly, as shown in figure 40 [12,13]. This approach was advantageous, since both the acidity and thermal stability of the copolymers were increased due to the electron withdrawing sulfonyl substituents being located on the same rings as the sulfonic acids. Moreover, these copolymers had two sulfonic acid groups per repeat unit, randomly distributed throughout the chains [15]. Direct copolymerization with the disulfonated comonomer also allowed precise control of the copolymer composition.

Robeson and Matzner [15], and Ueda et al. [16], earlier reported sulfonation of 4,4'-dichlorodiphenylsulfone with fuming sulfuric acid. The earlier procedure was modified to synthesize sulfonated 4,4'-dichlorodiphenylsulfone [12,13]. These directly copolymerized, disulfonated poly(arylene ether sulfone)s described in figure 2 had substantially lower methanol permeability, lower electro-osmotic drag, and comparable proton conductivities when compared to Nafion 117®.

This paper describes the synthesis and characterization of a series of high molecular weight, nitrile-functional, disulfonated poly(arylene ether sulfone)s by directly copolymerizing SDCDPS, 2,6-dichlorobenzonitrile, and hexafluoroisopropylidene diphenol (hexafluorobisphenol

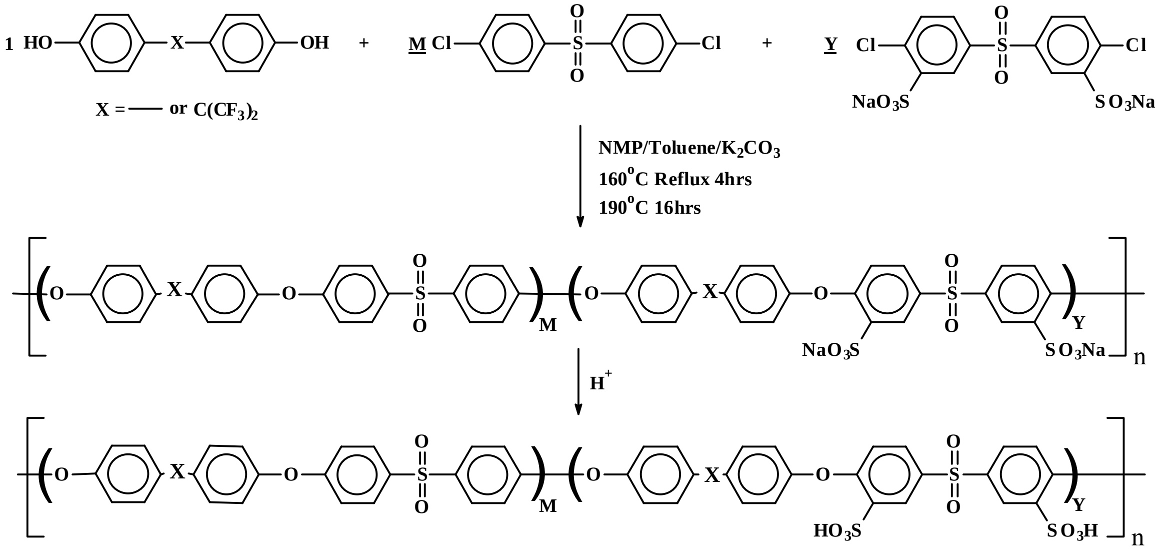

Figure 40. Synthesis of disulfonated poly(arylene ether sulfone) copolymers

A). Nitrile-activated aryl halide monomers are viable alternatives to sulfone and ketone electron withdrawing systems for polymerizations via nucleophilic aromatic substitution [5,7,17-20]. PEM membranes based on these materials are promising since good protonic conductivities at similar ion concentrations (i.e. ion exchange capacities) relative to earlier reported [12,13] disulfonated poly(arylene ether sulfone) copolymers have been demonstrated. The non-coplanar, fluorinated bisphenol monomer used in these copolymers also resulted in amorphous, soluble, film-forming materials with lower water absorptions relative to previously studied disulfonated poly(arylene ether sulfone).

Experimental

Materials

4,4’-Dichlorodiphenylsulfone (DCDPS) was generously provided by Solvay Advanced Polymers. The 4,4’-(hexafluoroisopropylidene)diphenol (hexafluorobisphenol A) was kindly provided by Ciba-Geigy, and used as received. DCDPS was recrystallized from methanol and dried under vacuum at 80 °C for 12 h. The 2,6-dichlorobenzonitrile (Aldrich) was recrystallized from methanol, then sublimed before use. Methanol, isopropanol, dimethylformamide, toluene, fuming sulfuric acid (30 wt % SO_3), potassium carbonate, and calcium hydride were purchased from Aldrich and used as received. N-Methylpyrrolidinone (NMP) (Aldrich) was purified by stirring overnight over calcium hydride, then distilled at ~80 °C under vacuum and collected over activated molecular sieves.

Synthesis

Synthesis of 3,3’-disulfonate-4,4’-dichlorodiphenylsulfone (SDCDPS)

4,4’-Dichlorodiphenylsulfone (12.5 g, 0.0437 mol) was dissolved in fuming sulfuric acid containing 30 wt % SO_3 (25 mL) and reacted for 6 h at 110 °C. The acidic solution was slowly added to ice water saturated with sodium chloride to precipitate the disulfonated monomer. The disulfonated monomer was recrystallized from a 15 wt % solution of 3:1 wt:wt isopropanol:water at 55 °C. It was then stirred overnight at room temperature in a fresh 15 wt % solution (3:1 wt:wt isopropanol:water) and collected via vacuum filtration. The monomer was dried overnight in a vacuum oven at 140 °C and stored at room temperature. The yield of the crude monomer was ~82%. However purification reduced the yield to 65%. Further studies directed toward on this process are in progress [21].

Synthesis of disulfonated poly(arylene ether) copolymers

An illustrative synthesis for a copolymer containing 30% of disulfonated repeat units and 70% of non-sulfonated, benzonitrile repeat units is provided. 4,4’-(Hexafluoroisopropylidene)diphenol and potassium carbonate were both dried in a vacuum oven overnight at ~60 °C just prior to weighing. 2,6-Dichlorobenzonitrile was dried under vacuum overnight at room temperature (instead of 60 °C) to avoid sublimation. 3,3’-Disulfonate-4,4’-dichlorodiphenylsulfone was not further dried. 4,4’-(Hexafluoroisopropylidene)diphenol (8.0000 g, 0.0238 mol), 2,6-dichlorobenzonitrile (2.8647 g, 0.0166 mol), 3,3’-disulfonate-4,4’-dichlorodiphenylsulfone (3.6209 g, 0.0071 mol) (Note: As determined by TGA, this monomer contained 3 wt % moisture which was accounted for in this calculation), and potassium carbonate (3.7812 g, 0.0274 mol) were charged to a 3-neck, round bottom flask equipped with a vacuum tight mechanical stirrer, Dean-Stark trap, and reflux condenser. Under constant stirring, ~20 mL of dry NMP and ~10 mL of toluene were added via syringe to form a pinkish-white hazy mixture. Under nitrogen purge, the reaction mixture was refluxed for 4 h using an oil bath heated to ~155 °C. After refluxing, the Dean-Stark trap was drained and the oil bath temperature was raised to ~200 °C. Over approximately 20 min, the toluene azeotrope was collected in the Dean-Stark trap, and the temperature was maintained at 200 °C for 20 h. Following the reaction, the highly concentrated (nearly 50% wt/vol solids), viscous mixture was diluted with ~20 mL of DMAc while still hot. The hot copolymer solution was precipitated by slow addition into ~500 mL of rapidly stirring isopropanol (in a blender). The product was vacuum filtered and dried at 60 °C in a vacuum oven for 12 h. A series of analogous copolymers were prepared with systematically varied fractions of disulfonated repeat units in a similar fashion by altering the relative concentrations of comonomers.

Membrane preparation

Approximately 1g of the copolymer in the sodium salt form was dissolved in ~7 mL of dimethylformamide and the solution was cast directly onto a glass plate positioned on a leveled hot plate. The glass plate was heated at 80 °C for ~12 h until most of the solvent was removed. The film was removed from the glass plate and immersed in a 0.5 M solution of aqueous sulfuric acid. The solution was heated to reflux and the film was acidified in the refluxing solution over ~2 h. The film was subsequently treated with refluxing deionized water for ~2 h. This acidification procedure has been referred to as “Method 2” in earlier papers [22]. The acidified films were dried in a vacuum oven overnight at 60 °C.

Characterization

Proton Nuclear Magnetic Resonance (^{1}H NMR)

^{1}H NMR spectra were collected at 80 °C on a Varian Unity 400 MHz instrument operating at a frequency of 399.954 MHz to analyze the SDCDPS monomer. A 22° pulse angle was used with an acquisition time of 3.7 s and a recycle delay of 1 s. *d_6*-Dimethylsulfoxide (*d_6*-DMSO) was used as the NMR solvent. In order to determine the copolymer compositions, the same instrument and solvent were used except the ^{1}H NMR data was collected at 25 °C.

Differential scanning calorimetry (DSC) and thermogravimetric analysis (TGA)

A TA Q1000 model DSC was used to determine the glass transition temperatures (T_g’s) of approximately 3 to 5 mg of the disulfonated polymer films. The films were further dried by heating over a temperature range of 100 to 300 °C at 5 °C min^{-1}, then quenched to 100 °C and heated a second time over the same temperature range at the same rate. The second heating cycle was used to determine the T_g of the copolymer. A TA Q0500 TGA was used to evaluate the thermo-oxidative stability of approximately 8 to 10 mg of the copolymers in air. The samples were heated to 150 °C and held at this temperature for 30 min to remove any residual water or solvent remaining in the copolymer films. The samples were cooled to room temperature and then heated to 900 °C at 10 °C min^{-1}. The temperature at which 5% weight loss occurred was recorded for each material.

Intrinsic viscosities

Approximately 20 mg of a copolymer was dissolved in 20 mL of NMP and filtered. Intrinsic viscosities of the samples were measured in NMP at 25 °C using an Ubbelohde viscometer.

Gel permeation chromatography (GPC)

GPC was performed using a Waters chromatograph equipped with a Waters 2414 refractive index detector calibrated with polystyrene standards and a Waters 1515 HPLC pump. The mobile phase was a 0.05 M solution of lithium bromide in NMP. The data was collected using Waters Styragel HT 4, 5, and 6 columns using a 1.0 mL min^{-1} flow rate at 60 °C.

Water absorption

After acidification, the membranes were vacuum dried overnight at 60 °C, weighed (dry weight), then immersed in deionized water for several days. During the first 24 hours of soaking, the weights of the films (wet weight) were measured several times. After the first 24 hours, the films were measured every 24 h. The weighing procedure involved removing the films from the deionized water, quickly patting them dry, and then re-measuring their weight. After weighing the films, they were re-submersed in deionized water. The water uptake of the films was recorded as a weight percent calculated from equation 1:

$$\text{Water uptake} = [(W_{wet}-W_{dry})/W_{dry}] \times 100 \qquad \text{Equation 1}$$

where W_{wet} and W_{dry} were the wet and dry weights, respectively [23].

Atomic force microscopy

The films were embedded in an epoxy (Epo-fix manufactured by Stuers, Inc.), cured for 12 h at room temperature, and a cross-section of each film was microtomed under liquid nitrogen. The microtomed samples were kept under vacuum at room temperature for ~6 h, then imaged immediately under a relative humidity of ~40%. The samples were imaged in the tapping mode using a Digital Instruments Dimension 3000 instrument equipped with a micro-fabricated cantilever with a force constant of 40 N m^{-1}.

Conductivity

A Hewlett-Packard 4129A LF impedance/gain phase analyzer was used to measure the resistance of each acidified film over a frequency range of 10 Hz to 1 MHz under fully hydrated conditions. The resistance of each film was measured at ~25 °C using the conductivity cell shown in Figure 41. The film geometry in the conductivity cell was such that the film resistance dominated the response of the system. The resistance of the film was recorded when the imaginary resistance was at a minimum. The detailed procedure has been reported previously [12].

Using the same analyzer, resistance of some films was measured as a function of relative humidity. (Note: The resistance of the film was recorded when the imaginary resistance reached a minimum.) The films were placed in a conductivity cell and the cell was stored in an ESPEC SH-240 temperature and humidity controlled oven. The resistance of the films was measured at 50, 75, 85, and 95% relative humidity at 80 °C. Upon changing the humidity level in the oven and before any resistance measurements were completed, the films were held for ~8 h to ensure that the moisture levels in the films were in equilibrium with the environment.

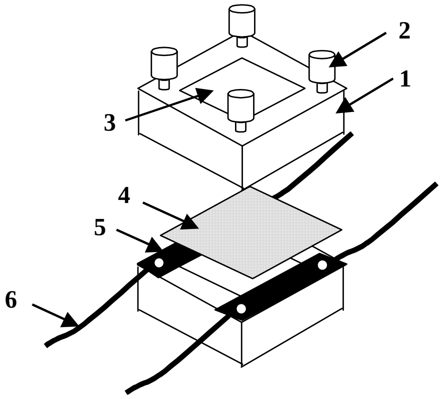

Legend
1. Teflon block
2. Thumbscrew
3. Open area to allow equilibration with environment
4. Membrane sample
5. Blackened Pt foil electrode
6. Pt lead

$$\partial = \frac{1}{R} \quad \frac{\ell}{A}.$$

Where ∂ = conductivity (S/cm)
R = resistance (ohms)
ℓ = length between electrodes (cm)
A = cross-sectional area of film (cm^2)

Figure 41. Conductivity cell

The protonic conductivities of the copolymer with 35% of the repeat units disulfonated were also measured as a function of temperature. The membrane was placed in the conductivity cell, then suspended above deionized water in a Parr pressure reactor (Fig. 42). The sample was heated to various temperatures ranging from 60 to 120 °C in the Parr reactor at 100% humidity under pressure. Upon reaching a particular temperature, the membrane was equilibrated for several hours with the environment, then the protonic conductivity was measured using the Hewlett-Packard impedance analyzer.

Methanol permeability

Methanol permeabilities of the acidified copolymer films were characterized by conducting diffusivity measurements in a membrane-separated diffusion cell [14]. A copolymer membrane was placed between two compartments: one filled with deionized water and the other filled with a 2M methanol/water solution. The temperature of the diffusion cell was maintained at 25 °C with a water bath and both compartments were stirred continuously during the experiments. Methanol permeabilities of the films were quantified using a differential refractometer and recirculating pump to measure the rates

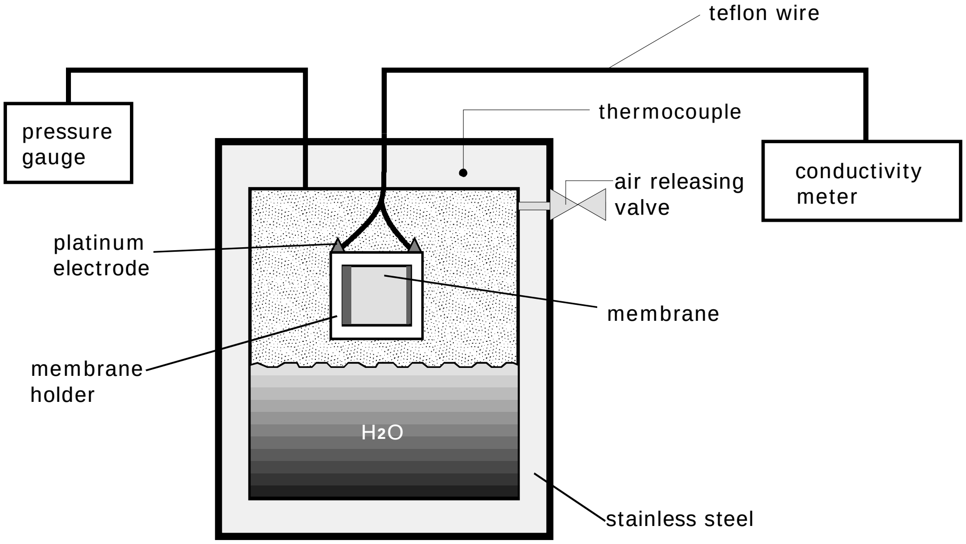

Figure 42. Parr reactor assembly for high temperature fuel cell measurements

of change of the methanol concentrations in the water-filled compartment. Diffusivities of the membranes were calculated from equation 2: where *D* was the diffusivity ($cm^2\ s^{-1}$), *H* was the partition coefficient, *l* the film thickness (cm), *A* was the cross-sectional area (cm^2), *t* was time (s), *V* was the cell volume (mL), *C* was the methanol concentration (wt %), subscript *a* noted the water cell, subscript *b* noted the cell containing the water/methanol mixture, and superscript *o* noted the initial conditions. Details concerning these calculations have been reported previously [24].

Results and Discussion

Synthesis of the disulfonated monomer, (3,3'-disulfonate-4,4'-dichlorodiphenylsulfone), and copolymers containing nitrile moieties.

3,3'-Disulfonate-4,4'-dichlorodiphenylsulfone was synthesized by electrophilic aromatic sulfonation of 4,4'-dichlorodiphenylsuflone in fuming sulfuric acid at 110 °C for 6 h. Due to the ortho-para directing effects of chlorine substituents and the meta directing effect of the sulfonyl group on the benzene rings of 4,4'-dichlorodiphenylsulfone, the 3 positions (ortho relative to chlorine) were sulfonated. ^{1}H NMR confirmed that substitution occurred in the 3 and 3' positions due to the chemical shift (8.4 ppm) of proton c (Fig. 43). The chemical shift of a proton on the aromatic carbon between the positions substituted with a chlorine and a sulfonate group was expected to be smaller due to more shielding relative to the expected shift for substitution in the 2 position (meta relative to chlorine).

The crude reaction product was isolated by adding the highly acidic reaction solution slowly into ice water saturated with sodium chloride. ^{1}H NMR suggested small amounts of the mono-sulfonated product remained at this stage (observed at 7.91, 7.86, and 7.68 ppm in Fig. 5). The crude monomer was purified by recrystallizing it from a 15% solids solution in 3:1 (wt:wt)

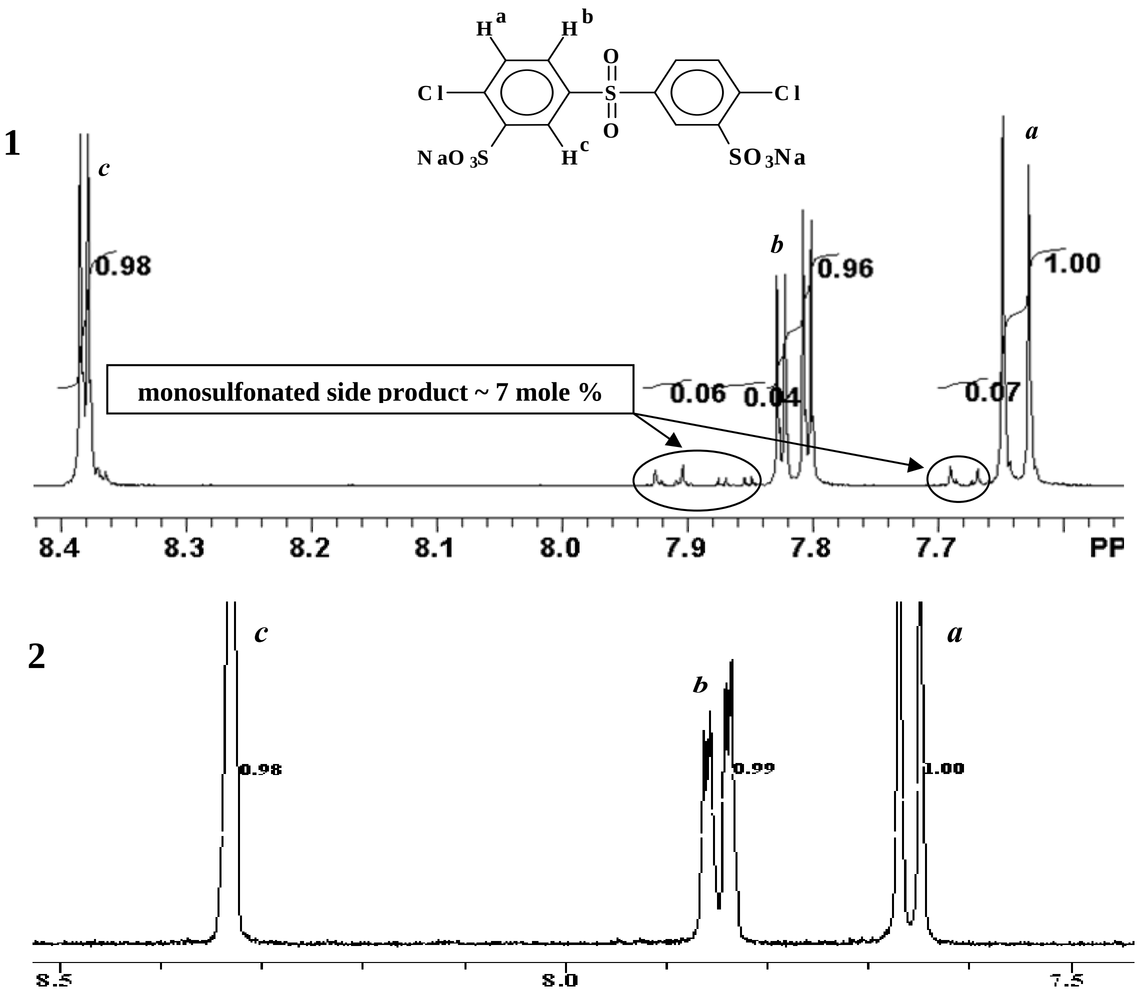

Figure 43. ^{1}H NMR at 80 °C of SDCDPS: 1) after recrystallization from an isopropanol:water (3:1 wt:wt) mixture 2) after recrystallization and extraction for 12 h at room temperature with an isopropanol:water (3:1 wt:wt) mixture

isopropanol:water. The crystallized monomer was subsequently extracted for approximately 12 hours at room temperature in a fresh isopropanol:water (3:1 wt:wt) mixture, then dried overnight under vacuum at 140 °C. After purification, the yield of the desired product was ~65%. After 12 hours of extraction, ^{1}H NMR showed that the mono-sulfonated side-product was removed (Fig. 43). The disulfonated monomer was dried under vacuum for ~12 hours at 140 °C, but TGA demonstrated that small amounts of moisture (~3-5 wt %) remained even after this drying process. Such behavior is consistent with a relatively stable, partially hydrated structure [16].

Syntheses of linear high molecular weight polymers via step growth polymerizations require highly accurate 1:1 functional group stoichiometries. Therefore, the residual moisture

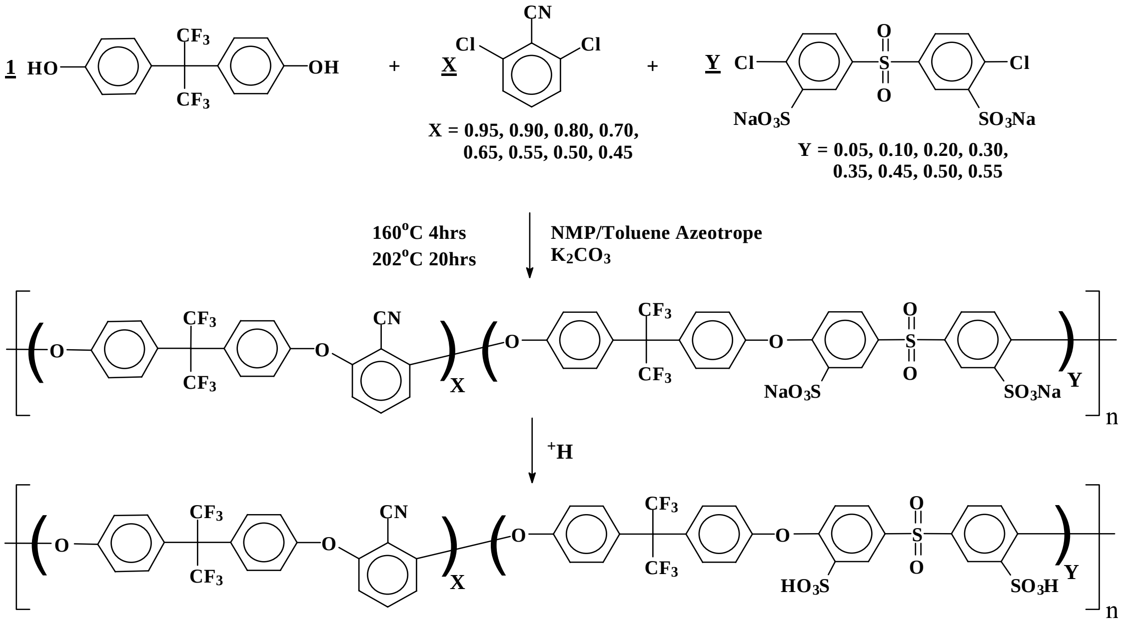

Figure 44. Synthesis of disulfonated poly(arylene ether benzonitrile) copolymers containing hexafluoroisopropylidene diphenol

concentration in the disulfonated monomer was determined via TGA so that it could be accurately included in the monomer charges.

A series of copolymers were prepared by nucleophilic aromatic substitution from 4, 4'-hexafluorobisphenol A as the diphenol and mixtures of 2,6-dichlorobenzonitrile and the disulfonated monomer, SDCDPS, as the activated dihalides (Fig. 44). The mole fractions of the disulfonated dihalide ranged from 0.05-0.55. All of the copolymers were prepared in NMP-toluene solvent mixtures utilizing potassium carbonate as a weak base to form the required phenolate nucleophile. The reactions were refluxed for four hours at 155 °C, then the toluene and any water were distilled from the mixtures at 200 °C with the aid of a Dean-Stark trap to desirably ensure anhydrous copolymerization processes [5,7]. The copolymerizations were maintained for 20 hours at 200 °C. The disulfonated monomer reacted slowly relative to its non-sulfonated counterpart, DCDPS, probably because of steric effects. Highly concentrated copolymerizations (~50 wt % reaction solutions) were utilized to achieve the high molecular weights needed for durable PEM systems.

Proton NMR confirmed that the copolymer compositions after purification were consistent with the charged monomer ratios (Fig. 45 and Table 5). Concentrations of disulfonated units were determined by ratioing the integrals corresponding to the aromatic protons meta to the nitrile groups to the aromatic protons ortho to the sulfone and sulfonate groups (proton a – meta to the nitrile group, proton i – ortho to the sulfone and sulfonate groups in Fig. 7). The ^{1}H NMR data indicated that SDCDPS was

Table 5: Theoretical versus experimental ^{1}H NMR integration ratios of protons "a" to "i" for disulfonated poly(arylene ether benzonitrile) copolymers containing hexafluoroisopropylidene diphenol with 5 to 50 mole % disulfonation

Copolymer	Theoretical ratio of proton a to i	Experimental ratio of proton a to i from ^{1}H NMR
95:5	0.95:0.05	0.95 ± 0.03 : 0.07 ± 0.03
90:10	0.90:0.10	0.90 ± 0.03 : 0.07± 0.03
80:20	0.80:0.20	0.80 ± 0.03 : 0.20 ± 0.03
70:30	0.70:0.30	0.70 ± 0.03 : 0.30 ± 0.03
65:35	0.65:0.35	0.65 ± 0.03 : 0.35 ± 0.03
55:45	0.55:0.45	0.55 ± 0.03 : 0.35 ± 0.03
50:50	0.50:0.50	0.50 ± 0.03 : 0.46 ± 0.03

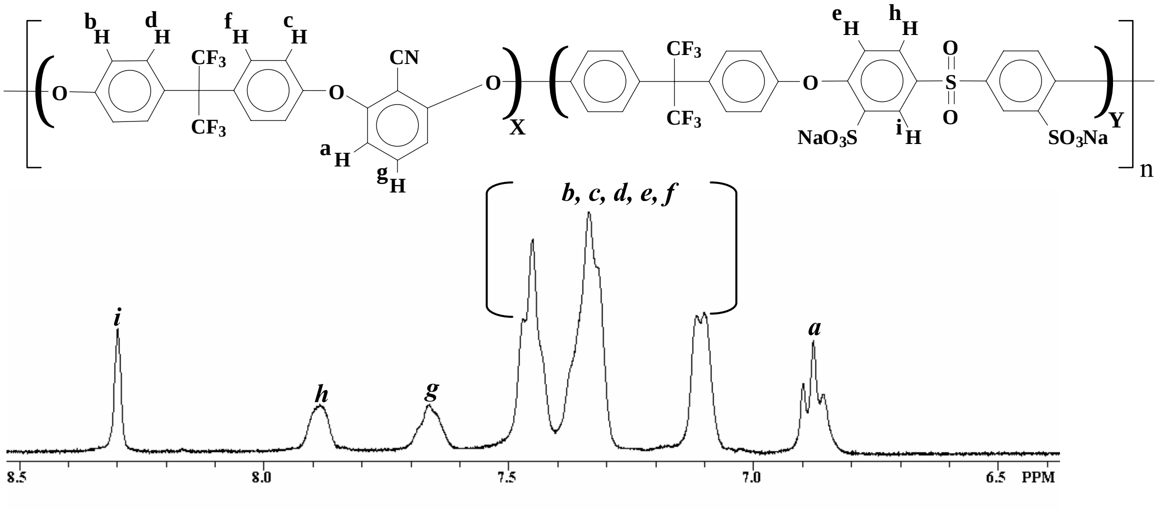

Figure 45. ^{1}H NMR of disulfonated poly(arylene ether benzonitrile) copolymers containing hexafluoroisopropylidene diphenol

quantitatively incorporated into the backbones of most of the copolymers in the series because the integral ratios were within experimental error of the charged compositions.

Relative molecular weights were analyzed with intrinsic viscosity measurements, and average molecular weights and polydispersities were measured using GPC with a 0.05 M lithium bromide-NMP solution as the mobile phase. One series of copolymers was synthesized with the moisture content in SDCDPS included in the charged monomer weights. By contrast, another series was prepared without considering the moisture weight in the monomer charges. Intrinsic viscosities were ~1.0 dL g^{-1} (NMP, 25 °C) or above for all of the materials wherein the moisture weight was accounted for, suggesting that high molecular weights were obtained in these cases (Table 6). The weight average molecular weights by GPC (calibrated against polystyrene standards) were substantially higher (~50,000 – 70,000 g mol^{-1}) for the series of copolymers where moisture in the SDCDPS was accounted for stoichiometrically during synthesis (Table 6). These high molecular weight copolymers formed tough, ductile, solvent cast films.

Table 6. **Intrinsic viscosities (NMP, 25 °C) and weight average molecular weights of disulfonated poly(arylene ether benzonitrile) copolymers containing hexafluoroisopropylidene diphenol with 20, 30, 35, and 50 mole % disulfonation**

Weight % of water in SDCDPS accounted for stoichiometrically	**Copolymer***	**Intrinsic Viscosity (dL $g^{-1)}$**	**M_W (g $mole^{-1}$)**	**Molecular Weight Distribution**
Yes	80:20	1.76	141,000	3.2
No	80:20	0.90	91,000	2.7
Yes	70:30	1.44	142,000	3.5
No	70:30	0.93	106,000	3.1
Yes	65:35	1.84	146,000	3.4
No	65:35	0.81	76,000	2.8
Yes	50:50	0.98	95,000	2.9
No	50:50	0.73	57,000	2.6

* mole % non-sulfonated:mole % disulfonated

Thermal properties of the disulfonated copolymers

Pendent sulfonate groups along a polymer chain elevate glass transition temperatures for at least two reasons. The sulfonate groups associate and increase intermolecular interactions, thereby reducing mobility. Secondly, these pendent groups are large and bulky. Both the ionomeric associative effect and the bulkiness of the sulfonate groups hinder rotation about the polymer chain. Glass transition temperatures of the copolymers were evaluated using DSC by heating the samples from 25 to 300 °C at 5 °C min^{-1}. The glass transition temperatures of the acidified copolymers increased substantially as the mole fraction of disulfonation was increased (Fig. 46).

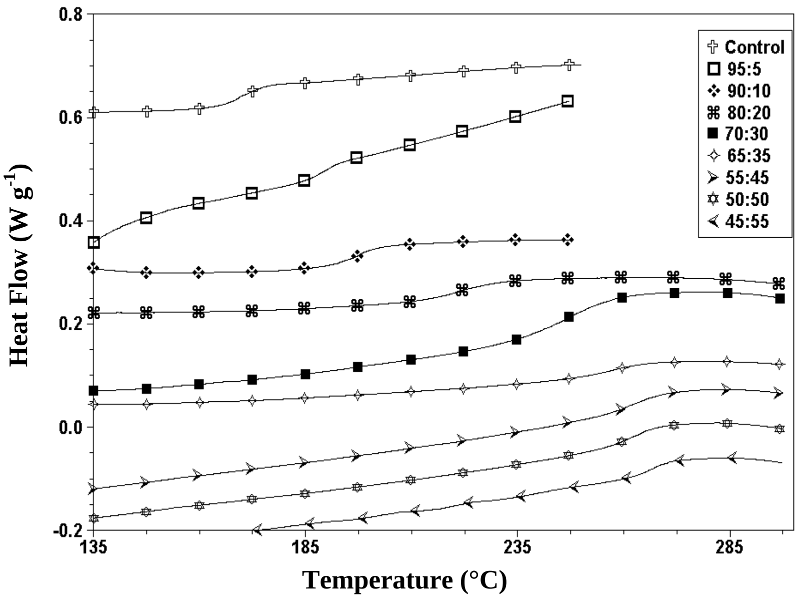

*** mole non-sulfonated: mole disulfonated**

Figure 46. Glass transition temperatures of disulfonated poly(arylene ether benzonitrile) copolymers containing hexafluoroisopropylidene diphenol (in the acidified form) containing 5 to 55 mole % disulfonation

The T_g's increased from 169 °C for the control (no sulfonation) to 258 °C for the copolymer containing 35 mole % disulfonated repeat units. Increasing the mole fraction of the disulfonated units beyond 0.35 caused little further increase in the glass transition temperatures. The acidified copolymers containing higher fractions of disulfonated units were heated to 400 °C to determine whether a second, high temperature transition due to a hydrophilic phase could be detected. A secondary transition was not detected up to 350 °C and heating beyond this temperature caused some degradation. This was consistent with thermal properties of previously reported sulfonated poly(arylene ether)s [9,12,13,25].

The mass losses with temperature of the acidified copolymer films were examined by TGA to determine the temperature range wherein the sulfonic acid groups cleaved from the copolymer chains. Copolymer films were heated to 150 °C and held at this temperature for 30 minutes to remove moisture. They were then cooled to room temperature and heated to 900 °C at 10 °C min^{-1}. The temperatures where 5% weight loss was observed and the percentages of char remaining were considered an evaluation of thermal stability. All of the disulfonated copolymers exhibited good thermal stability up to ~350 °C where weight loss was observed. The mass losses at this temperature increased as the level of disulfonation along the copolymer chain was increased (Fig. 47). This observation was consistent with previous measurements from our labs on other disulfonated poly(arylene ether)s [12]. The major weight losses were observed at ~500 °C and this was attributed to degradation of the copolymer backbones. All of the copolymers had char yields at 900 °C between ~15 and 35%, but these did not correlate with the concentrations of sulfonate groups.

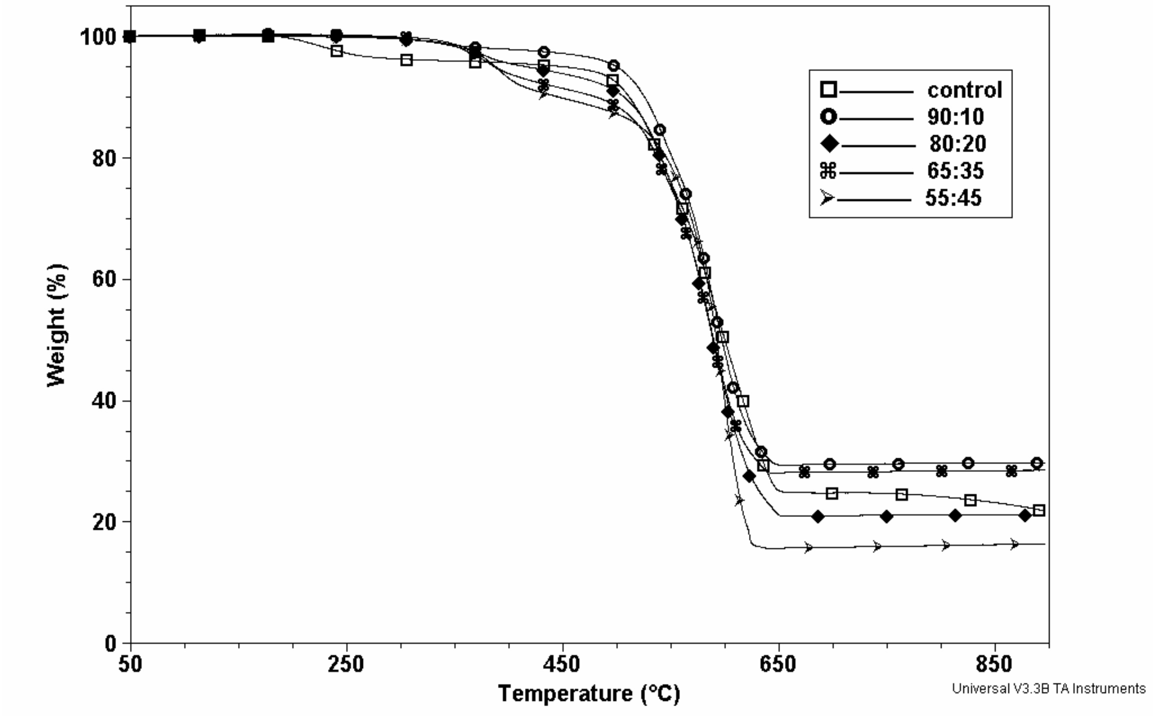

Figure 47. Weight loss profiles in air at 10 °C min^{-1} of disulfonated poly(arylene ether benzonitrile) copolymers containing hexafluoroisopropylidene diphenol with 0, 10, 20, 35, and 45 mole % disulfonation

Water uptake, methanol permeability, and morphology

Small-angle X-ray investigations of the morphology of Nafion®, a perfluorosulfonic acid copolymer, have demonstrated that this polymer is nanophase separated [26]. One phase consists of hydrophilic domains wherein polar sulfonic acid groups are aggregated. The other region is comprised of hydrophobic portions of the copolymer aggregated in clusters. In the currently studied disulfonated copolymers, the hydrophilic domains were primarily responsible for water absorption. Typically, the equilibrium water absorption of disulfonated poly(arylene ether sulfone)s, acidified using "Method 2" conditions, increases linearly up to about 0.40 mole fraction of disulfonated units. Beyond this level of sulfonation, water uptake increases drastically, signifying a change in phase morphology [12,14].

For comparisons, water absorptions of these benzonitrile-containing copolymers were measured (Fig. 48). Upon submersion in deionized water, the copolymer membranes with ≥0.1 mole fraction of disulfonated units reached an apparent equilibrium in water uptake within the first hour (Fig. 48). Water absorption increased linearly up to 0.35 mole fraction of the units disulfonated. Beyond this level of disulfonation, the water uptake increased drastically and the copolymer containing 0.55 mole fraction of disulfonated units absorbed ~300% water by weight. The ionic concentrations were expressed in terms of ion exchange capacities (IEC in meq g^{-1}) so that these copolymers could be compared to disulfonated copolymers previously studied (Table 7).

In comparison to disulfonated poly(arylene ether sulfone) copolymers prepared with biphenol or hexafluoroisopropylidene diphenol previously reported [12,13,27], as well as to Nafion 117®, the benzonitrile-containing copolymers with 20, 30, and 35 mole percents of the units disulfonated had lower water absorption (Table 7). Moreover, at equivalent IEC's, these copolymers absorbed considerably less moisture (Table 7). These aspects will require significant investigation to be better understood, but the effects may be related to the higher fluorine contents in the benzonitrile-containing materials. Such features may be important to form stable membrane electrode assemblies (MEA's) in fuel cells, which may require bonding to Nafion® perfluorinated electrodes.

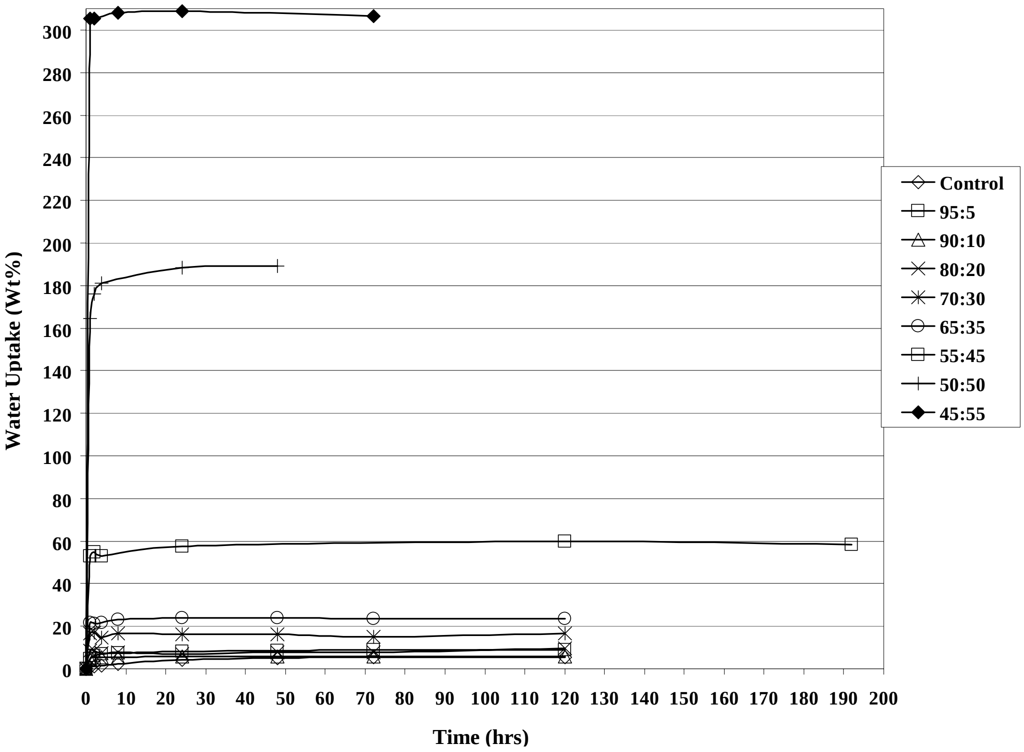

Figure 48. Water uptake (wt%) versus time for disulfonated poly(arylene ether benzonitrile) copolymers containing hexafluoroisopropylidene diphenol with 0 to 55 mole % disulfonation

Table 7: Water uptake (wt%) and calculated IEC values for Nafion 117® and three different disulfonated poly(arylene ether)s at 20, 30, and 35 mole % disulfonation

Mole % Disulfonation	Copolymer	Water Uptake (wt%)	IEC (meq•g^{-1})
20	*Disulfonated PAES	17	0.92
	**Disulfonated-6F-PAES	15	0.69
	***Disulfonated-6F-PAE-CN	7	0.82
30	*Disulfonated PAES	31	1.34
	**Disulfonated-6F-PAES	23	1.00
	***Disulfonated-6F-PAE-CN	16	1.16
35	*Disulfonated PAES	44	1.53
	**Disulfonated-6F-PAES	38	1.15
	***Disulfonated-6F-PAE-CN	24	1.32
-	Nafion 117®	19	0.91

*** Disulfonated poly(arylene ether sulfone) containing biphenol**

**** Disulfonated poly(arylene ether sulfone) containing hexafluoroisopropylidene diphenol**

***** Disulfonated poly(arylene ether benzonitrile) containing hexafluoroisopropylidene diphenol**

The phase morphology of the benzonitrile-containing poly(arylene ether) copolymer with 0.35 mole fraction of the repeat units disulfonated was investigated with AFM in the tapping mode. This copolymer exhibited a nanophase morphology as demonstrated by the dark and light regions (Fig. 49). The dark regions in the image depict softer hydrophilic regions containing water, while the light regions correspond to harder hydrophobic regions (Fig. 49). The dark regions were continuous and approximately 4-10 nm wide. The lighter regions were also continuous but ranged from about 25–40 nm. The benzonitrile-containing copolymer morphology ("B" in Fig. 49) was considerably different from a disulfonated poly(arylene ether sulfone) prepared from biphenol, DCDPS, and SDCDPS with 40% of the units disulfonated ("A" in Fig. 49). The disulfonated poly(arylene ether sulfone) copolymer ("A" in Fig. 49) had a more segregated morphology. Previous work has demonstrated that transforming morphologies of the hydrophilic domains from segregated to continuous in perfluorosulfonic acid copolymers [28] and in disulfonated poly(arylene ether sulfone)s [12,14] correlated with large increases in water uptake. The major increase in water uptake with ion content occurs at approximately 0.45 mole fraction of disulfonated units in the benzonitrile-containing copolymers (Fig. 50). Achieving low methanol permeation through a membrane is important for copolymer membrane performance in direct methanol fuel cells (DMFC). Recent research has demonstrated that disulfonated poly(arylene ether sulfone) copolymers have considerably lower methanol permeabilities and comparable proton conductivities when compared to Nafion 117® [14]. It has also been shown that methanol

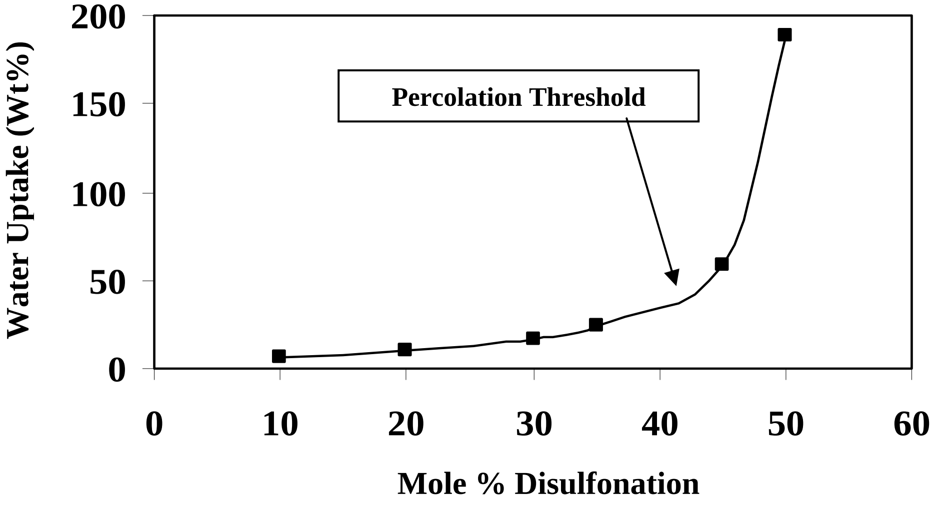

Figure 50. Water uptake (wt%) versus mole % disulfonation for disulfonated poly(arylene ether benzonitrile) copolymers containing hexafluoroisopropylidene diphenol

permeability and water uptake in disulfonated poly(arlyene ether sulfone)s are correlated [14]. As the fraction of disulfonated units is increased, both the water uptake and the methanol permeability increase.

Methanol permeabilities of disulfonated poly(arylene ether sulfone) copolymers with different chemical structures and Nafion 117® were compared at 25 °C (Table 8) [29-31]. The three disulfonated copolymers were selected because they had similar water absorption, IEC's, and protonic conductivities. Methanol permeabilities through the disulfonated copolymer containing the nitrile groups was higher than the other disulfonated poly(arylene ether sulfone)s, but still considerably lower than Nafion 117® (Table 8).

Conductivity

Protonic conductivities of the series of disulfonated copolymers containing nitrile groups were measured as a function of the mole fraction of disulfonated units, relative humidity, and temperature. The experiments were conducted in the conductivity cell submersed in deionized water (Fig. 51).

Table 8. Methanol permeabilities at 25 °C for Nafion 117® and three different disulfonated poly(arylene ether) copolymers

Copolymer-(mole % Disulfonation)	IEC (meq•g^{-1})	Methanol Permeability x 10^{-8} (cm^2•s^{-1})
*Disulfonated-PAES-(35 mole % Disulfonation)	1.53	55
**Disulfonated-6F-PAES-(40 mole % Disulfonation)	1.30	62
***Disulfonated-6F-PAE-CN-(35 mole % Disulfonation)	1.32	87
Nafion 117®	0.91	167

* Disulfonated poly(arylene ether sulfone) containing biphenol

** Disulfonated poly(arylene ether sulfone) containing hexafluoroisopropylidene diphenol

*** Disulfonated poly(arylene ether benzonitrile) containing hexafluoroisopropylidene diphenol

Protonic conductivities increased linearly from 0.0005 to ~ 0.10 S cm^{-1} as a function of the concentrations of disulfonated units at 25 °C (Fig. 51). Conductivity of the copolymer containing 0.45 mole fraction of disulfonated repeat units was 0.10 S cm^{-1}, comparable to Nafion 117®.

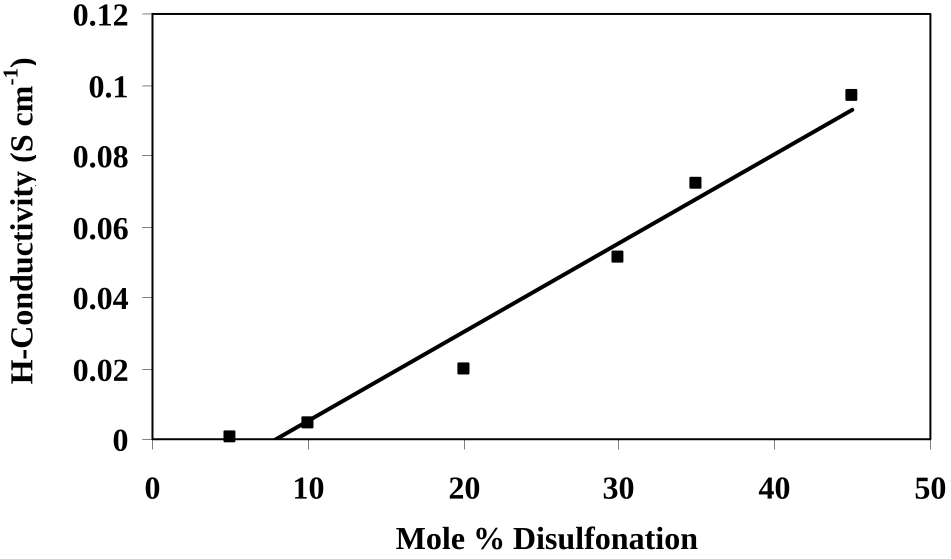

Figure 51. Protonic conductivity versus mole % disulfonation for disulfonated poly(arylene ether benzonitrile) copolymers containing hexafluoroisopropylidene diphenol

To compare acidities of the disulfonated benzonitrile-containing copolymers relative to two other disulfonated copolymers, protonic conductivities between 10 and 35 mole % disulfonation were analyzed as a function of IEC (Fig. 52). The two other polymers in the comparison were a biphenol-based disulfonated poly(arylene ether sulfone) and hexafluorobisphenol A-based disulfonated poly(arylene ether sulfone). Figure 52 shows that between IEC's of ~0.8 and 1.6 meq g^{-1}, the disulfonated benzonitrile-containing copolymers had comparable protonic conductivities relative to the other two copolymers. This is interesting since these materials have lower moisture sorption.

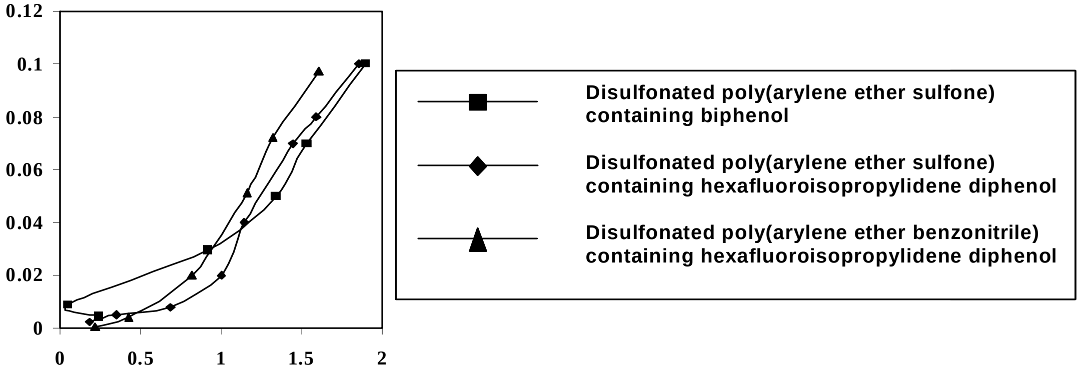

Figure 52. Protonic conductivity versus calculated IEC values for three different disulfonated poly(arylene ether) copolymers.

Protonic conductivities of the benzonitrile-containing copolymer containing 35 mole % disulfonated units were evaluated as a function of temperature, at 100% humidity in a Parr pressure reactor. As temperature was increased, protonic conductivities increased to 0.11 S cm^{-1} at ~110 °C. Further increases in temperature caused excessive swelling of the membranes and protonic conductivities could not be accurately measured (Fig. 53). This temperature versus conductivity behavior was similar to that of other disulfonated poly(arylene ether sulfone)s. The study demonstrated that protonic conductivities of the disulfonated benzonitrile-containing copolymer membranes could be increased to high levels at elevated temperatures.

It is of great interest for practical reasons to determine the performance of a PEM as relative humidity is reduced. Protonic conductivities of four disulfonated, benzonitrile-containing copolymers (20, 30, 35, and 45 mole % disulfonation) were studied as a function of humidity at 80 °C. As expected, protonic conductivities increased slightly as the relative humidity was increased from 50 to 85% in all four of the copolymers (Fig. 54). However, protonic conductivities of PEM's with 30, 35, and 45 mole % disulfonated units increased drastically when the relative humidity was elevated from 85 to 95%. The morphological structures of these copolymers as a function of relative humidities is currently under further investigation.

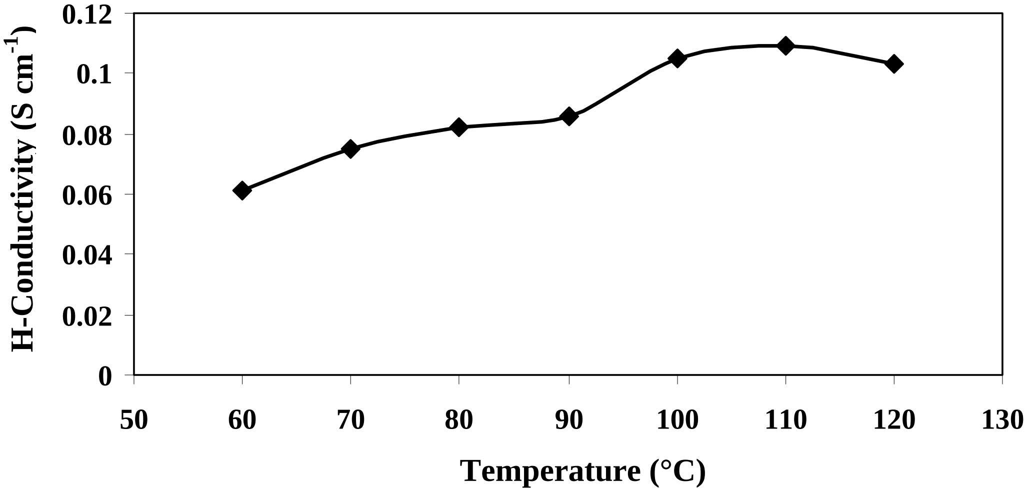

Figure 53. Protonic conductivity versus temperature for the 35 mole % - disulfonated poly(arylene ether benzonitrile) copolymer containing hexafluoroisopropylidene diphenol

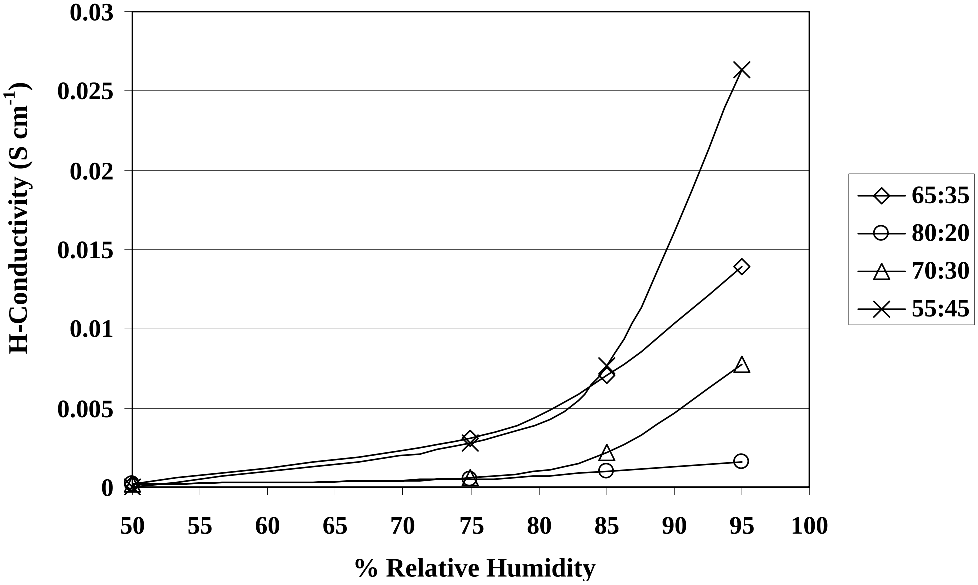

Figure 54. Protonic conductivity versus % relative humidity for the 20, 30, 35, and 45 mole % - disulfonated poly(arylene ether benzonitrile) copolymer containing hexafluoroisopropylidene diphenol

Conclusions

A series of high molecular weight, disulfonated, benzonitrile-containing, film-forming copolymers containing as much as 50 mole % disulfonation were synthesized and characterized by a variety of methodologies. For comparable IEC's from ~0.8 and 1.6 meq g^{-1}, these copolymers absorbed less water, but PEM's had comparable protonic conductivities relative to control disulfonated poly(arylene ether sulfone) copolymers. As expected, the protonic conductivities for the 35 mole % disulfonated copolymer were substantially improved with elevated temperatures, and reached values of 0.1 S cm^{-1} at 110 °C under full hydration. This was comparable to the Nafion 117® control. The lower water sorption may be a function of the higher fluorine content. This parameter may also lead to enhanced bonding to Nafion®-based electrodes, which is important for durable MEA's in PEM-based fuel cells.

References

[1] J.A. Kerres, Development of ionomer membranes for fuel cells, J. Membr. Sci., 185 (2001) 3-27.

[2] K.D. Kreuer, On the development of proton conducting polymer membranes for hydrogen and methanol fuel cells, J. Membr. Sci., 185 (2001) 29-39.

[3] R. Ianniello, V.M. Schmidt, U. Stimming, J. Stumper and A. Wallen, CO adsorption and oxidation on Pt-Ru alloys-dependence on substrate composition, Electrochim. Acta, 39 (1994) 1863.

[4] L.M. Robeson, A.G. Farnham and J.E. McGrath In *Dynamic mechanical characteristics of polysulfone and other polyarylethers*; D. J. Meier, Ed.; Gordon and Breach, 1978; Vol. 4, p 405.

[5] R.J. Cotter Engineering plastics: A handbook of polyarylethers; Gordon and Breach: London, 1995.

[6] J.J. Dumais, A.L. Cholli, L.W. Jelinski, J.L. Hedrick and J.E. McGrath, Molecular basis of the ß-transition in poly(arylene ether sulfone)s, Macromolecules, 19 (1986) 1884-1889.

[7] S. Wang and J.E. McGrath In *Synthetic Methods in Step-Growth Polymers*; M. Rogers, T. E. Long, Eds.; Wiley-Interscience: Hoboken, New Jersey, 2003; pp 327-364.

[8] A. Noshay and L.M. Robeson, Sulfonated polysulfone, J. Appl. Polym. Sci., 20 (1976) 1885.

[9] B.C. Johnson, I. Yilgor, C. Tran, M. Iqbal, J.P. Wightman, D.R. Lloyd and J.E. McGrath, Synthesis and characterization of sulfonated poly(arylene ether sulfone)s, J. Polym. Sci.: Part A: Polym. Chem., 22 (1984) 721-737.

[10] M.A. Dinno, Y. Kang, D.R. Lloyd, J.E. McGrath and J.P. Wightman In *Physiochemical Aspects of Polymer Surfaces*; K. L. Mittal, Ed.; Plenum Press: New York, 1983; Vol. 1, p 347.

[11] D.R. Lloyd, L.E. Gerlowski, C.D. Sutherland, J.P. Wightman, J.E. McGrath, M. Iqbal and Y. Kang, Poly(aryl ether) membranes for reverse osmosis, ACS Symp. Ser., 152 (1981) 327.

[12] F. Wang, M. Hickner, Y.S. Kim, T.A. Zawodzinski and J.E. McGrath, Direct polymerization of sulfonated poly(arylene ether sulfone) random (statistical) copolymers: candidates for new proton exchange membranes, J. Membr. Sci., 197 (2002) 231-242.

[13] F. Wang, M. Hickner, Q. Ji, W. Harrison, J. Mecham, T.A. Zawodzinski and J.E. McGrath, Synthesis of highly sulfonated poly(arylene ether sulfone) random (statistical) copolymers via direct polymerization, Macromol. Symp., 175 (2001) 387-395.

[14] Y.S. Kim, M. Hickner, L. Dong, B. Pivovar and J.E. McGrath, Methanol permeability of sulfonated poly(arylene ether sulfone) copolymers: effect of morphology, J. Membr. Sci., (2003) in press.

[15] L.M. Robeson and M. Matzner, Flame retardant polyarylate compositions, U.S. Patent 4,380,598 to Union Carbide, 1983.

[16] M. Ueda, H. Toyota, T. Ouchi, J. Sugiyama, K. Yonetake, T. Masuko and T. Teramoto, Synthesis and characterization of aromatic poly(ether suflone)s containing pendant sodium sulfonate groups, J. Polym. Sci.: Part A: Polym. Chem., 31 (1993) 853-858.
[17] J.L. Hedrick, D.K. Mohanty, B.C. Johnson, R. Viswanathan, J.A. Hinkley and J.E. McGrath, Radiation resistant amorphous-all aromatic poly(arylene ether sulone)s: synthesis, characterization, and mechanical properties, J. Polym. Sci.: Part A: Polym. Chem., 23 (1986) 287.
[18] R.N. Johnson, A.G. Farnham, R.A. Clendinning, W.F. Hale and C.N. Merriam, Poly(aryl ethers) by nucleophilic aromatic substitution I. Synthesis and properties, J. Polym. Sci.: Part A: Polym. Chem., 5 (1967) 2375.
[19] C. Genies, R. Mercier, B. Sillion, N. Cornet, G. Gebel and M. Pineri, Soluble sulfonated naphthalenic polyimides as materials for proton exchange membranes, Polymer, 42 (2001) 359-373.
[20] R. Viswanathan, B.C. Johnson and J.E. McGrath, Synthesis, kinetic observation, and characterizations of poly(arylene ether sulfone)s prepared by potassium carbonate DMAC process, Polymer, 25 (1984) 1827.
[21] M. Sankir, V.A. Bhanu, H. Ghassemi, K.B. Wiles, M.L. Hill, W. Harrison, M.J. Sumner, T.E. Glass, J.S. Riffle and J.E. McGrath, Systematic study of the synthesis and characterization of 3,3'-sulfonylbis(6-chlorobenzene sulfonic acid) disodium salt monomer for proton-conducting polymeric membranes in fuel cell applicaitions, Polymer Preprints, 44 (2003) 1079-1080.
[22] Y.S. Kim, L. Dong, M. Hickner, T.E. Glass, V. Webb and J.E. McGrath, State of water in disulfonated poly(arylene ether sulfone) copolymers and a perfluoro sulfonic acid copolymer (Nafion) and its effects on physico-electrochemical properties, accepted Macromolecules, (2003)
[23] T.A. Zawodzinski, T.E. Springer, J. Davey, R. Jestel, C. Lopez, J. Valerio and S. Gottesfeld, A cooperative study of water uptake by and transport through ionomeric fuel cell membranes, J. Electrochem. Soc., 140 (1993) 1981-1985.
[24] E.L. Cussler Diffusion mass transfers in fluid systems, 2nd Ed.; 2 ed.; Cambridge University: New York, 1997.
[25] J.F. O'Gara, D.J. Williams, W.J. Macknight and F.E. Karasz, Random homogeneous sodium sulfonate polysulfone ionomers: preparation, characterization, and blend studies, J. Polym. Sci.: Part B Polym. Phys., 25 (1987) 1519.
[26] T.D. Gieke, G.E. Munn and F.C. Wilson, The morphology in Nafion perfluorinated membrane products, as determined by wide-and small-angle X-ray studies, J. Polym. Sci.: Part B Polym. Phys., 19 (1981) 1687.
[27] W. Harrison, F. Wang, J. Mecham, V.A. Bhanu, M.L. Hill, Y.S. Kim and J.E. McGrath, Influence of the Bisphenol Structure on the Direct Synthesis of Sulfonated Poly(arylene ether) Copolymers. I, J. Polym. Sci.: Part A: Polym. Chem., 41 (2003) in press.
[28] G. Gebel and R.B. Moore, Small-angle scattering study of short pendant chain perfluorosulfonated ionomer membranes, Macromolecules, 33 (2000) 4850-4855.
[29] B.S. Pivovar, Y. Wang and E.L. Cussler, Pervaporation membranes in direct methanol fuel cells, J. Membr. Sci., 154 (1999) 155-162.
[30] X.M. Ren, Methanol cross-over in direct methanol fuel cells, Electrochem. Soc. Proc., PV95-23 (1995) 284-298.

[31] X.M. Ren, W. Henderson and S. Gottesfeld, Electro-osmotic drag of water in ionomeric membranes. New measurements employing a direct methanol fuel cell, J. Electrochem. Soc., 144 (1997) L267-L270.

Synthesis and Properties of New Sulfonated Poly(*p*-Phenylene) Derivatives for Proton Exchange Membranes

Background

Several high molecular weight poly(2,5-benzophenone) derivatives were synthesized by high yield nickel-catalyzed coupling polymerization of 4'-substituted 2,5-dichlorobenzophenones. The monomers were prepared by Friedel-Crafts catalyzed reaction of 2,5-dichlorobenzoyl chloride and several aromatic compounds. The resulting polymers are organo soluble in and show no evidence of crystallinity by differential scanning calorimetry (DSC). Thermo-oxidative stabilities of the polymers based on 5% weight loss via dynamic thermogravimetric analysis (TGA) were above 480^{o}C in air. Sulfonation of selected polymers utilizing concentrated or fuming sulfuric acid at room temperature introduced sulfonic acid moieties to the aromatic side group. Activated aryl fluorine was also used to generate pendent sulfonated functionalities. The sulfonated polymers were examined for ion exchange capacities, water absorption capacities and proton conductivities. The sulfonated polymers were not good film formers, but could be demonstrated to show high values of proton conductivity in the range of 0.06-0.11 S cm^{-1} when supported on glass fabrics or via polymer blending strategies.

Introduction

Poly(*p*-phenylene)s (PPPs) and especially their derivatives continue to receive much attention due to their excellent thermal, mechanical, and electrical properties.[1-4] One of main obstacles to the synthesis of high molecular weight poly(1,4-phenylene) itself is the low solubility of the growing rigid rod chains during polymerization. This problem has been overcome by introducing pendent groups to the phenyl rings which improve the solubility of PPP while retaining many of the most useful characteristics. Appropriately substituted materials are soluble and yet exhibit interesting thermal and mechanical properties.

One widely studied substituted PPP is poly(2,5-benzophenone) made, usually, from 2,5-dichlorobenzophenone (Figure 55). Poly(2,5-benzophenone) shows great promise as a high performance engineering thermoplastics with a glass transition temperature of 206^{o}C and 5% weight loss temperatures in nitrogen and air of 496 and 495^{o}C, respectively.[5] In addition, the tensile moduli of poly(2,5-benzophenone) far exceeds those of other high performance polymers, including poly(phenylene sulfide) and poly(ether ether ketone).[6] Commercial production of poly(2,5-benzophenone) derivatives, under the trade name Parmax is currently underway at Mississippi Polymer Technologies, Inc.[7]

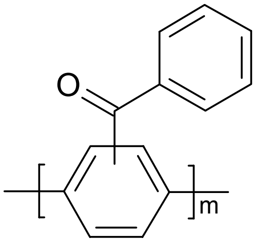

Figure 55. Structure of Poly(2,5-benzophenone)

While the pendent benzoyl group of poly(2,5-benzophenone) serves to solubilize the material, it also provide sites for further chemical modification. Unfortunately, the introduction of new functional groups along the backbone of poly(*p*-phenylene)s imposes some limitations. Typically, complications during polymerization due to the incompatibility of new functional groups with the catalyst system chosen for polymerization must be considered.

There are only a few methods for carbon-carbon coupling polymerization reactions. The palladium-mediated coupling of aromatic bromides with aromatic boronic acids (Suzuki coupling) has been reported as a successful way to make substituted poly(phenylene)s.[8-10] One of the most widely used synthetic procedures for the production of PPPs is the Ni(0) catalyzed coupling of dihalide) monomers.[11-14] The results, described by several research groups show that using the nickel coupling approach, a variety of homo- and copolymers can be prepared by properly choosing the starting materials.

Investigation of new proton exchange membranes (PEMs) for fuel cell applications has been recently a major point of attraction for several research groups.[15,16] Direct copolymerization of disulfonated 4,4'-dichlorodiphenylsulfone to high molecular weight copoly(arylene ether sulfone)s is a recent example of such efforts in order to make new PEMs with interesting behavior compared with state of the art Nafion® (a perfluorinated polymer commercially available from Dupont).[17]

Continuing our investigation on new PEMs, we herein report synthesis of several substituted poly(2,5-benzophenone)s and their copolymers. These polymers were chemically modified for the potential PEM applications.

Experimental

Materials. All reagents were purchased from Aldrich and used as received unless otherwise noted. Benzene and N-methylpyrrolidinone (NMP) were dried over calcium hydride and distilled before use. Triphenylphosphine was purified from n-hexane. Anhydrous nickel(II) chloride and zinc powder were stored under argon. 2,5-Dichlorobenzoyl chloride was prepared according to a procedure reported in the literature.[12]

Characterization. ^1H and ^{13}C NMR spectra were recorded on a Varian 400 spectrometer, using chloroform-d (CDCl3) and dimethylsulfoxide-d_6 (DMSO) as solvents. Glass transition temperatures (Tg) were determined by differential scanning calorimetry, using a Perkin-Elmer DSC 7 instrument at a heating rate of 20°C/min, under a stream of nitrogen. Thermogravimetric analyses (TGA) were performed on a Perkin-Elmer TGA 7 thermogravimetric analyzer at 10°C/min in air and nitrogen. Intrinsic viscosities were determined in NMP at 25°C using an Ubbelohde viscometer. Molecular weights were determined by gel permeation chromatography (GPC) (Waters, Breeze system) system consisting of three HT styrogel columns and a refractive index detector using NMP (containing 0.05 mol% LiBr) as the mobile phase at 60°C. Molecular weights were calculated from a calibration plot constructed with polystyrene standards.

Aqueous potentiometric titrations were conducted using an MCI Automatic Titrator Model GT-05. The membranes were soaked in deionized water containing sodium sulfate (1M solution) for 24 h at room temperature. The solutions were titrated by standard tetramethyl ammonium hydroxide. The data was used to quantitatively determine sulfonic acid concentration in the sulfonated polymers in terms of ion exchange capacity (IEC, meq/g).

Conductivity measurements were performed on the sulfonated polymeric membranes by placing the membranes between two platinum electrodes held by two Teflon-made frames. An impedance spectrum was recorded from 5 Hz to 13 MHz using a Hewlett Packard 4192 Impedance Analyzer. The resistance of the film was taken at the frequency that produced the minimum imaginary response. All impedance measurements were performed at 30°C in water.

Monomer synthesis. The monomers were prepared by Friedel-Crafts acylation of benzene, fluorobenzene, biphenyl and diphenylether according to a procedure described in the literature, with some modifications.[12] The reaction yields were in the range of 65-80%. All the monomers were purified by recrystallization and dried under vacuum at 50°C for 24 h.

2,5-Dichlorobenzophenone (**M1**): mp 88-89°C (lit.[5] mp 88.9°C) ^{1}H NMR δ 7.80 (m, 2H), 7.62 (ddd, 1H), 7.50 (dd, 2H), 7.38 (m, 3H); ^{13}C NMR δ 193.6 (C=O), 139.9 (C1), 135,8 (C1'), 134.1 (C4), 132.9 (C2), 131.3 and 131.1 (C3, C6), 130.1 (C2'), 129.6 (C5), 128.9 (C4'), 128.8 (C3').

4'-Fluoro-2,5-dichlorobenzophenone (**M2**): mp 87-88°C (lit.[18] mp 87.2°C) ^{1}H NMR δ 7.83 (ddd, 2H), 7.41 (m, 2H), 7.35 (dd, 1H), 7.15 (ddd, 2H); ^{13}C NMR δ 192.1 (C=O), 166.3 (d, C-F), 139.6, 133.0, 132.8 (d, C-F), 132.3 (d, C-F), 131.3, 131.2, 128.8, 116.0 (d, C-F), 19F NMR δ –73.9.

4'-Phenyl-2,5-dichlorobenzophenone (**M3**): mp 126-127°C, ^{1}H NMR δ 7.89 (d, 2H), 7.71 (d, 2H), 7.64 (d, 2H), 7.45 (m, 2H), 7.42 (m, 4H); ^{13}C NMR δ 193.2 (C=O), 146.8, 140.0, 139.6, 134.5, 132.9, 131.3, 131.1, 130.7, 129.5, 129.0, 128.9, 128.5, 127.4, 127.3.

4'-Oxyphenyl-2,5-dichlorobenzophenone (**M4**): mp 97°C, ^{1}H NMR δ 7.78 (dd, 2H), 7.41 (m, 4H), 7.35 (d, 1H), 7.23 (dd, 1H), 7.10 (dd, 2H), 7.00 (dd, 2H); ^{13}C NMR δ 192.2 (C=O), 163.0, 155.0, 140.1, 132.9, 132.5, 131.2, 130.9, 130.2, 130.1, 129.4, 128.7, 124.9, 120.5, 117.2.

2,5-Dichloro-4'-fluorodiphenyl sulfone was synthesized by reacting 2,5-dichlorobenzene-sulfonyl chloride with fluorobenzene in the presence of iron(III) chloride according to a procedure reported in the literature.[18] Mp: 147.5-148°C (lit. 145°C).

Polymer synthesis. A typical procedure will be described: To a previously flame-dried 100 mL two-neck flask, equipped with an overhead stirrer, were added zinc (3.56 g, 52.9 mmol), nickel (II) chloride (0.22 g, 1.71 mmol), triphenylphosphine (1.79 g, 6.83 mmol), 2,2'-dipyridyl (0.266 g, 1.71 mmol). Additions of the catalyst mixture to the reaction flask were made in a dry bag under an argon atmosphere. The flask was then sealed with a septum and 15 mL of anhydrous NMP was added via syringe. The mixture was heated in an oil bath to 80^{o}C under nitrogen with continuous stirring. The catalyst mixture undergoes a color change from yellowish brown to deep green and finally dark red. After the dark red appearance of the active catalyst, 17.1 mmol of monomer dissolved in 10 mL of anhydrous NMP syringed into the reaction flask. The reaction was allowed to proceed for 3-4h before precipitation into methanol containing 30% hydrochloric acid. After stirring for 12 h the yellow solid was filtered washed several times with water and methanol before drying in a vacuum oven to give product with 97-99% yield.

Poly[4-(4-sulfonatophenoxy)benzoyl-1,4-phenylene] (**SP2**). Poly(4'-fluoro-2,5-benzophenone) (**P2**) (1.0 g, 5 mmol), 4-hydroxybenzenesulfonic acid sodium salt dihydrate (5) (1.3 g, 6 mmol), anhydrous potassium carbonate (0.9 g, 6.6 mmol), NMP (30 mL) and toluene (10 mL) were added to a 100 mL 3-neck round-bottom flask, equipped with a magnetic stir bar, Dean-Stark trap, condenser and nitrogen inlet. The mixture was heated in an oil bath at 140^{o}C for 4 h. Then, the temperature was raised slowly and kept at 180^{o}C for 24 h. The reaction mixture was added to 500 mL methanol and stirred for 2 h. The precipitate was collected by suction filtration and vacuum dried for further investigation.

Sulfonated poly(phenylene)s (**SP1**): In a typical reaction, 0.5 g of pulverized poly(2,5-benzophenone) (**P1**) was dissolved in 10 mL of fuming sulfuric acid containing 30 wt% free SO_3. The solution was maintained at room temperature for the desired period of time before precipitating into a large amount of water. The sulfonated polymer was filtered and washed thoroughly with deionized water, and then dried for 24 hour at 80^{o}C before being used.

Film membrane preparation: Polymer films were difficult to cast, possibly due to chain rigidity, and were generally used in the form of glass fiber composites. Thus, a piece of glass cloth (thickness= 35 µm) was placed on a glass plate, then a filtered solution of resin was made by adding a solution of 0.5 g of polymer in 10 mL of NMP onto the glass cloth. The glass plate was covered with a dish and heated by an IR lamp at 60^{o}C under a flow of nitrogen for 24 hour. Composite membrane thickness was about 150 µm and the mass ratio of the glass fabric to the polymer was about 40 to 60.

Results and Discussion

Monomer Synthesis. 2,5-Dichlorobenzophenone (**M1**) and substituted 2,5-dichlorobenzophenones (**M2-4**) were synthesized by an aluminum chloride catalyzed Friedel-Crafts acylation of benzene and other aromatic compounds with 2,5-dichlorobenzoyl chloride as outlined in Scheme 16. 2,5-Dichlorobenzoyl chloride was prepared from 2,5-dichlorobenzoic acid and thionyl chloride and purified by vacuum distillation. In the case of acylation of biphenyl and diphenylether, addition of cyclohexane as solvent was necessary in order to dissolve the aromatic compound and form a suspension with aluminum chloride. Monomer purity was established by a sharp melting point and confirmed to be above 99% pure according to GC/MS. Monomer structures were confirmed by ^{1}H and ^{13}C NMR.

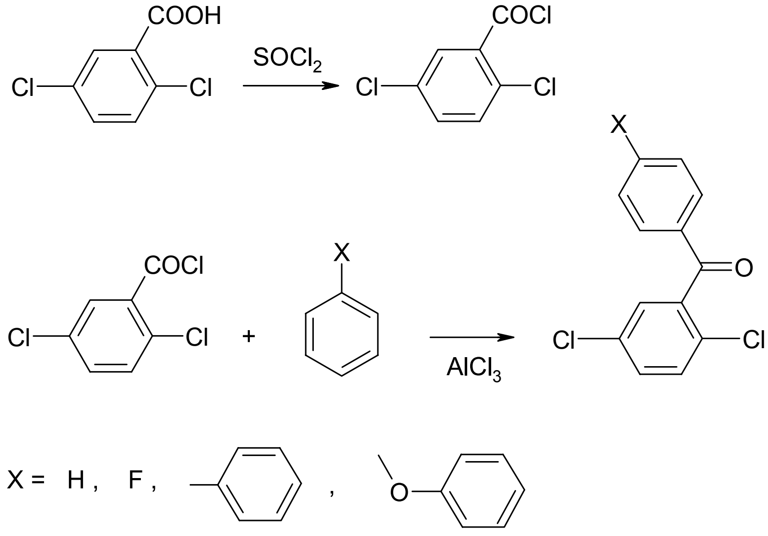

1 **2** **3** **4**

Scheme 16**. Synthesis of the monomers**

Polymer Synthesis and Characterization:

For the polymerization of 2,5-dichlorobenzo-phenone monomers, the procedures were based on our previous experience on synthesis of poly(arylene phosphine oxide) by nickel-catalyzed coupling polymerization.[19] It was apparent that the use of highly pure and dry reagents would be required for the successful preparation of high molecular weight polymers. The polymerization proceeded until the viscosity increased to a point where the reaction could no longer be stirred efficiently. Two copolymers **P1/P2** and **P1/P3** were also prepared from monomers **M1/M2** and **M1/M3**, respectively. The polymer structures are presented in Scheme 17 and 18. All the polymers were isolated in greater than 94% yield. The molecular weights measured by GPC and intrinsic viscosity values are summarized in Table 9 and 10. As shown in Table 9, the molecular weights of polymers **P1-P4**, determined by GPC relative to polystyrene standards, are in the same range (Mn = 2.0 x 10^4 g/mol). The high PD value for **P4** was due to a high molecular weight portion, which appeared as a tail in the GPC chromatogram.

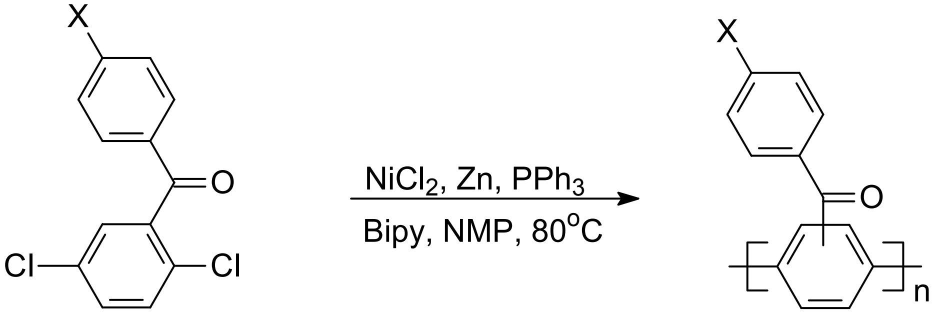

M1-4 P1-4

Scheme 17. Synthesis of the Polymers

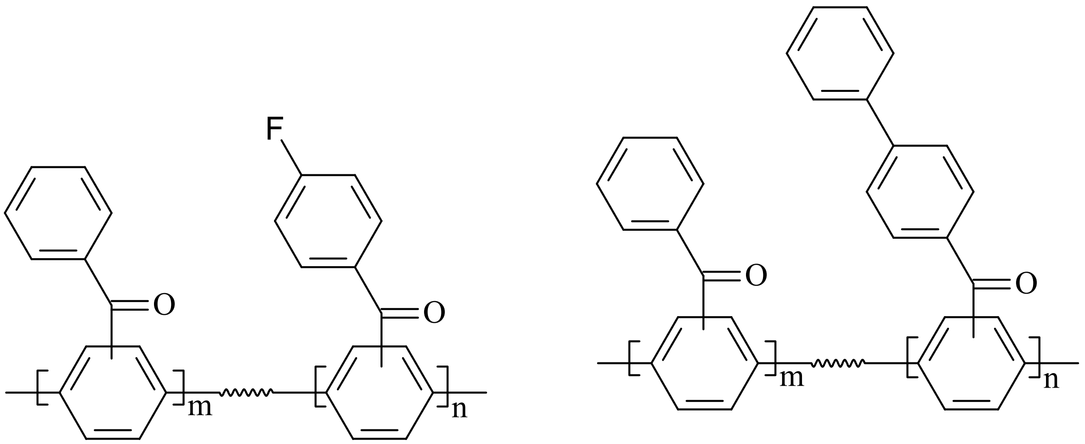

P1/P2 **P1/P3**

Scheme 18. Statistical (random) copolymers **P1/P2** and **P1/P3** (m:n = 1:1)

Table 9. GPC data on poly(2,5-benzophenone)s[a]

Sample	Mn ($x10^{-3}$ $gmol^{-1}$)	Mw ($x10^{-3}$ $gmol^{-1}$)	Mp ($x10^{-3}$ $gmol^{-1}$)	Mz ($x10^{-3}$ $gmol^{-1}$)	PD
P1	**20.0**	**58.6**	**43.6**	**131.9**	**2.9**
P2	**20.5**	**61.7**	**42.1**	**151.4**	**3.0**
P3	**20.1**	**95.2**	**39.8**	**433.0**	**4.7**
P4	**22.0**	**277.2**	**34.4**	**1426.2**	**12.5**
P1/P2	**14.1**	**38.8**	**27.8**	**91.4**	**2.7**
P1/P3	**19.9**	**64.6**	**48.3**	**156.2**	**3.2**
PS2	**2.8**	**3.3**	**2.5**	**4.0**	**1.1**
P1/PS2	**7.7**	**15.2**	**10.5**	**28.4**	**1.9**
SP1	**19.1**	**61.0**	**49.3**	**141.3**	**3.1**
SP2	**20.7**	**62.1**	**45.5**	**152.7**	**2.9**
SP3	**19.4**	**102.3**	**38.4**	**672.0**	**5.2**

(a) Based on polystyrene standards, NMP(containing 0.05 mol% LiBr) at 60°C.

Table 10. Characterization of poly(2,5-benzophenone)s

Polymer	η_{int} **(dL/g)**[a]	**TGA (5% weight loss)**[b] **N_2 (°C)**	**Air (°C)**
P1	0.96	526	520
P2	0.69	516	490
P3	0.67	524	521
P4	-	485	480
P1/PS2	0.17	-	-

(a) Data obtained in NMP at 25°C. (b) weight loss temperature obtained by TGA at 10°C/min.

Unfortunately, polymerization of 2,5-dichloro-4’-fluorodiphenyl sulfone (Scheme 19) via Ni(0) coupling reaction is known to form only low molecular weight oligomers.[18] The highest molecular weight oligomer (**PS2**) (Scheme 20) from 2,5-dichloro-4’-fluorodiphenyl sulfone in our experiment was 2.8 x 10^3 g/mol, as determined by GPC. Copolymerization of 2,5-dichlorobenzophenone and 2,5-dichloro-4’-fluorodiphenyl sulfone (80:20 mol ratio) also produced relatively low molecular weight product **P1/PS2** (7.7 x 10^3 g/mol, PD = 1.9). Both proton and carbon as well as ^{19}F NMR confirmed incorporation of diphenyl sulfone monomer in the final product. These data indicate that diphenyl sulfone monomer has good reactivity, compared to benzophenone monomers, under the Ni(0) coupling reaction and formation of low molecular weight polymer from 2,5-dichloro-4’-fluorodiphenyl sulfone is probably due to some for now, one or more undefined terminal side reactions.

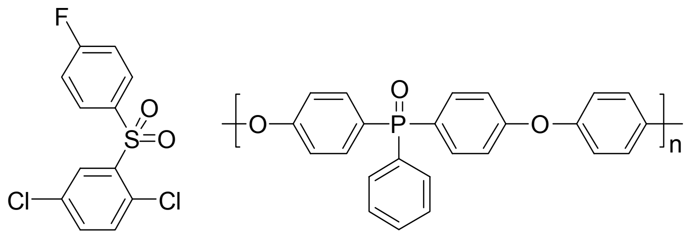

(A) (B)

Scheme 19. Structure of (A) 2,5-dichloro-4'-fluorodiphenyl sulfone and (B) PPO

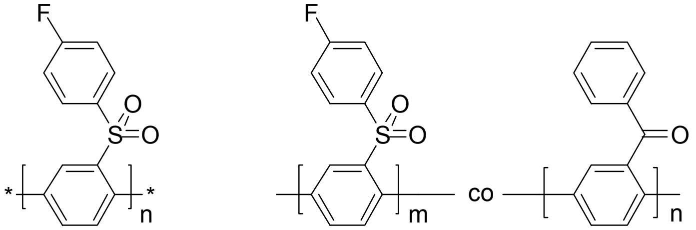

PS2 **P1/PS2**

Scheme 20. Structures of **PS2** and copolymer **P1/PS2**

Intrinsic viscosities of the ketone linked homopolymers were in the range of 0.69- 0.96 dL/g (NMP, 25^{o}C). These polymers are all amorphous materials and soluble in NMP and chloroform, except **P4** which was only partially soluble in chloroform. The films cast from NMP solution were transparent, yellow but somewhat brittle. Thermal behavior of polymers **P1-P4** is summarized in Table 10. The high thermal stabilities of these polymers were no doubt derived from their fully aromatic structure extending through the backbone and pendent groups. Polymer **P4** had lower 5% weight loss temperature in both nitrogen and air compared to others, which may have been due to the presence of relatively less thermally stable phenyl ether pendent group.

Introduction of the sulfonic acid group in polymer **P2** was possible by nucleophilic displacement of fluoro groups in **P2** by 4-hydroxybenzenesulfonic acid sodium salt to form sulfonated **P2** (**SP2**). The derivatization was similar to the polymerization of bisphenols and activated aromatic dihalides (Scheme 21). The ^{19}F and ^{13}C NMR spectra of **SP2** indicated that around 50% of fluorine groups in **P2** were displaced by oxybenzenesulfonic acid moieties (Figure 56). Model studies of 4-fluorobenzophenone under the same condition using 4-hydroxybenzenesulfonic acid sodium salt gave only 70% conversion of 4-fluorobenzophenone to substituted product. The deactivating effect of the sulfonate group on nucleophilicity of the phenoxide is believed to be a major reason for the incomplete conversion. Using a higher boiling point solvent and longer reaction times might improve the degree of conversion. Partial precipitation of sulfonated polymer during the reaction was probably another factor influencing conversion. Fluorine displacement reaction on **P2** shows no significant effect on the molecular weight of the polymer according to GPC results.

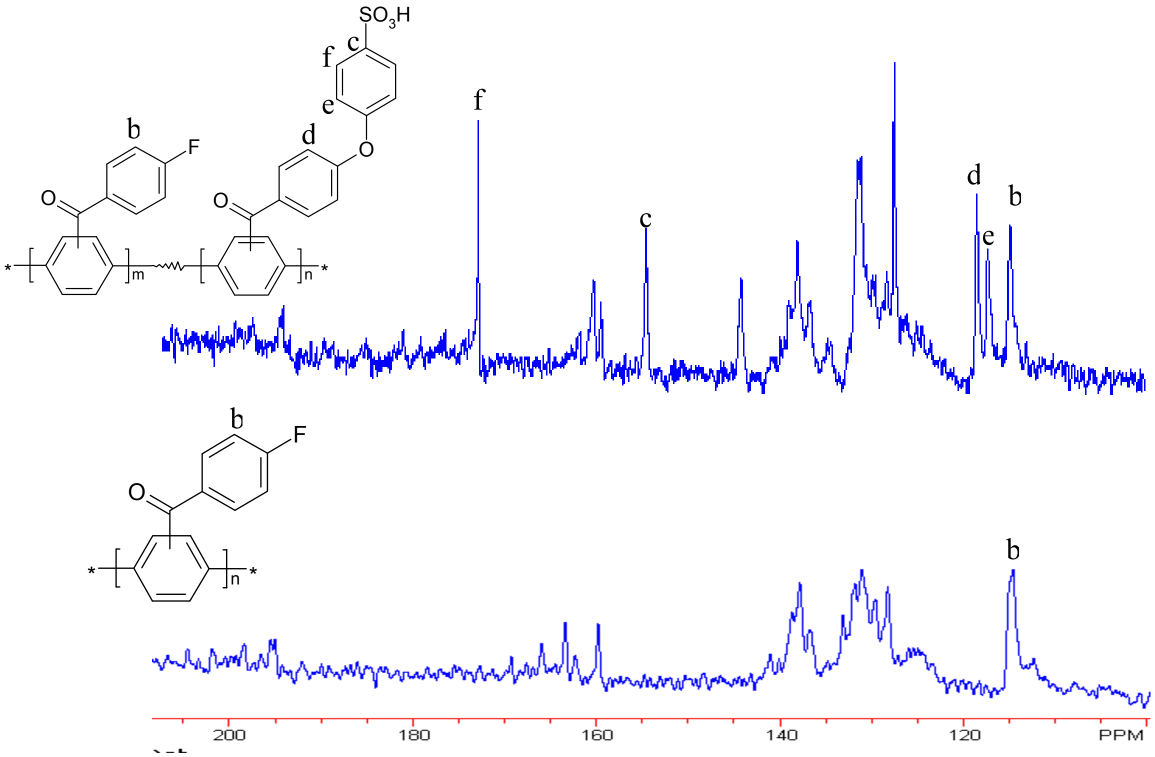

Figure 56. Comparative ^{13}C NMR spectra of **SP2** and **P2**

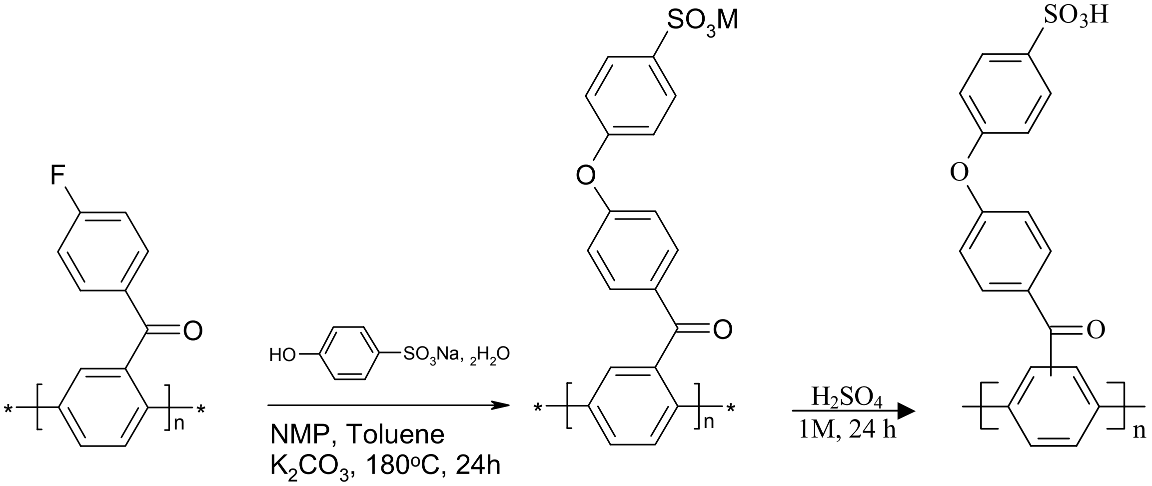

SP2

Scheme 21. Synthesis of polymer **SP2** via nucleophilic substitution

Sulfonation of polymers **P1**, **P3** and their copolymers by concentrated or fuming sulfuric acid for controlled periods of time resulted in derivatives with various levels of sulfonation. Sulfonation of **P1** and **P3** with fuming sulfuric acid proceeds very rapidly and it was somewhat difficult to control the degree of sulfonation. In contrast concentrated sulfuric acid showed no significant sulfonation of the deactivated pendent phenyl rings of **P1** under similar conditions and required much longer time and higher temperatures to effectively sulfonate. After treatment of polymer **P1** with fuming sulfuric acid for only 15 minutes at room temperature, it became partially soluble in boiling water. Extension of the reaction time to 60 minutes produced polymers, which were completely soluble in boiling water and products from longer reaction times were completely water soluble even at room temperature. Figure 57 shows ^{1}H NMR spectra of **P1** before and after treatment with fuming sulfuric acid for 30 and 90 minutes. GPC data of **SP1** and **SP3** show no major molecular weight change compared to their precursor **P1** and **P3**, respectively (Table 9). GPC results indicate that the polyphenylenes **P1** and **P3** are stable during the reaction with concentrated and fuming sulfuric acid and no noticeable decomposition reaction takes place. Sulfonation of 4-benzoylbiphenyl, as a model compound, by concentrated sulfuric acid at 80°C for several hours produces only a mono sulfonated product as determined by mass spectroscopy. Degrees of sulfonation were measured by titration and are reported as ion exchange capacities (IEC) (Table 11). IEC values for the products of reactions of **P1** with fuming sulfuric acid as a function of reaction time at room temperature are presented in Figure 4. Similar sulfonation experiments on **P3** and **P1/P3** (50/50) copolymers (Scheme 17) using concentrated sulfuric acid produced sulfonated polymers with IEC values in the range of 2-2.6 meq/g. The intrinsic viscosity values of these polymers after sulfonation increased about 20-30% compared to their values before sulfonation, which is probably due to the well known interactions between acid groups on the polymer chains. As an example, the intrinsic viscosity values for copolymer **P1/P3** before and after sulfonation showed an increase from 0.69 to 0.91 dL/g.

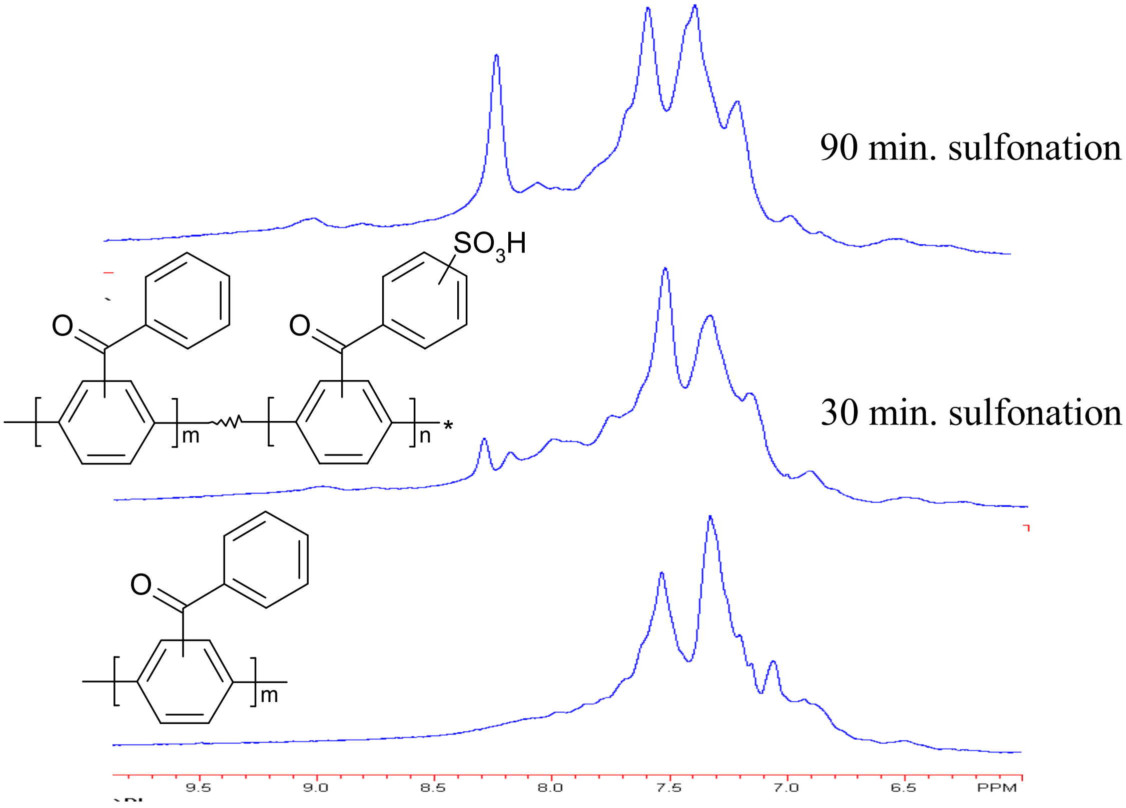

Figure 57. ^{1}H NMR spectra of P1 before and after sulfonation with fuming sulfuric acid

Table 11. Water uptake, IEC and conductivity of sulfonated **P1** (**SP1**) as a function of reaction time with fuming sulfuric acid

Sulfonation Time (min.)	Water Uptake (%)^a	IEC (meq/g)^b	Conductivity (mS.cm^{-1})^c
15	78	2.6	40
30	83	2.8	40
60	115	4.0	50
180	Soluble	6.5	-

(a) Polymers swellen in deionized water at r.t. for 24 hr. (b) Measured after soaking in saturated aqueous Na_2SO_4 solution for 24 hr, then titrated with tetramethyl ammonium hydroxide at r.t. (c) Measured on a polymer composite made from glass fabric and resin (40/60 w/w).

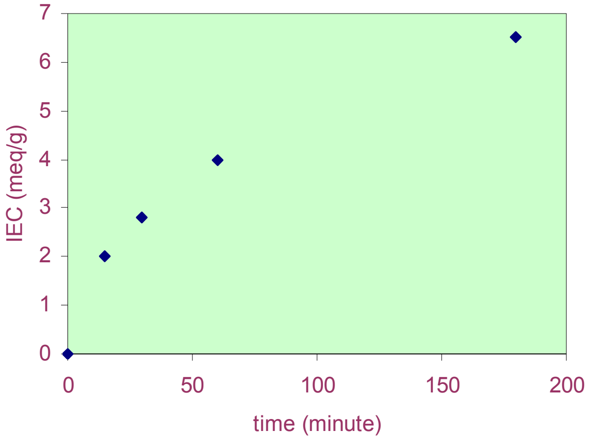

Figure 58. IEC values for sulfonated **P1** as a function of reaction time with fuming sulfuric acid at room temperature.

The poly(*p*-phenylene)s and their derivatives are known to form rather non-flexible films probably due to their rigid rod backbone. Even amorphous, high molecular weight polymers **P1-P4** formed brittle films. The inability of these polymers to form flexible and creaseable films was a barrier in their testing as a PEM. Polymer blends are a common and versatile way to develop new materials with desirable properties. However, the development of new useful blends is severely limited by the incompatibility of many polymer pairs of interest. After testing several polymers for compatibility, poly(arylene ether phosphine oxide) (PPO)[20] prepared in our laboratory was chosen to be the most compatible one with sulfonated poly(*p*-phenylene)s. It is known that the aryl phosphine oxide groups can form strong hydrogen bonding with acidic protons on the sulfonic acids groups. Several blends with varied ratios of sulfonated **P1** (**SP1**) copolymer (IEC= 2.8 meq/g) and a poly (arylene ether phenyl phosphine oxide) (PEPO) (Figure 5) (Mn= 61 Kg/mol, Mw= 145 Kg/mol, determined by GPC) were prepared. All the blends were opaque but formed better films. The blends containing less than 30 parts PEPO per 100 parts copolymer (p.h.v.) did not form suitable films. The 30 p.h.r. blend showed water uptake of around 68%. The IEC value for this sample was 2.0 meq/g and the conductivity in liquid water was measured to be 70 mS/cm. The second approach to produce membranes with sufficient mechanical strength was to utilize glass cloth as an inert, reinforcement and support agent. The weight percent of glass cloth in total composite was about 40.

The protonic conductivities of the membranes were measured at 30°C in liquid water. The proton conductivities of 90-110 mS/cm was found for **SP1** polymers in their acid form (products of **P1** after sulfonation with fuming sulfuric acid for 15-60 minutes, IEC 2.6-4.0 meq/g) (Table 11), while the conductivity of Nafion 1135 (IEC 0.91 meq/g) was 120 mS/cm under similar conditions. Conductivity values for sulfonated **P3** (**SP3**) were also in the range of 90-120 mS/cm. Greater ion exchange capacities are needed with sulfonated poly(*p*-phenylene)s to achieve similar conductivities to perfluorosulfonic acid Nafion polymers. This disparity may be attributed to the relative strengths of the acid groups in each system. The acidity of perfluorosulfonic acid is known to be much higher than the aryl sulfonic acid, therefore, it is reasonable that more acid moieties are needed in sulfonated poly(*p*-phenylene)s to achieve the desired conductivity.

Conclusions

The results further demonstrate the feasibility of synthesizing aryl-substituted poly(2,5-benzophenone)s via Ni(0)-catalyzed coupling polymerization. The versatility of Friedel-Crafts monomer synthesis provides an efficient way to afford the starting monomers. All the homopolymers and copolymers were soluble in common organic solvents allowing characterization and somewhat brittle film formation. Introduction of the sulfonic acid groups was also possible by substitution of activated fluoro group in **P2** or by sulfonation with sulfuric acid in other polymers and copolymers.

GPC results show number average molecular weight of approximately 20.0 x 10^3 g/mol for most polymers and copolymers. It has been also demonstrated that the molecular weight of the polymers is not seriously altered after sulfonation. Thermal stability of the unsulfonated polymers based on their 5% weight loss were determined by TGA under nitrogen and air to be around 480^{o}C.

Water uptake and ion exchange capacity values were reported for several of the sulfonated polymers. Both values increase as the degree of sulfonation increases as expected. Conductivity of the sulfonated polymers, in the form of composites or blends were determined to be in the range of 90-110 mS/cm in liquid water at 30^{o}C.

References

(1) Kovacic, P.; Jones, M. B. *Chem. Rev*., **1987**, 87, 357.
(2) Ueda, M.; Ichikawa, F. *Macromolecules*, **1990**, 23, 926.
(3) Percec, V.; Okito, S.; *J. Polym. Sci., part A: Polym. Chem*., **1993**, 31, 877.
(4) Yamamoto, T. *Prog. Polym. Sci*. **1992**, 17, 1153.
(5) Phillips, R. W.; Sheares, V. V.; Samulski, E. T.; DeSimone, J. M. *Macromolecules* **1994**, 27, 2354.
(6) Marrocco, M.; Trimmer, M.S.; Hsu, L.C. and Gagne, R.R. SAMPE Proceedings **1994**, 39, 1063.
(7) Mississippi Polymer Technologies, Incorporated; Maxdem, Inc. (www.maxdem.com).

(8) Rehahn, M.; Schluter, A. D.; Wegner, G. *Makromol. Chem*. **1990**, 191, 1991.
(9) Wallow, T. I.; Novak, B. M. *J. Amer. Chem. Soc*. **1991**, 113, 7411.
(10) Rehahn, M.; Schluter, A. D.; Wegner, G.; Feast, W. *J. Polymer* **1989**, 30, 1060.
(11) Colon, I.; Kwiatkowski, G. T. *J. Polym. Sci., part A: Polym. Chem*.,**1990**, 28, 367.
(12) Wang, Y.; Quirk, R. P. *Macromolecules* **1995**, 28, 3495.
(13) Pasquale, A. J.; Sheares, V. *J. Polym. Sci., part A: Polym. Chem*. **1998**, 36, 2611.
(14) Percec, V.; Zhao, M.; Bae, J. Y.; Hill, D. H. *Macromolecules* **1996**, 29, 3727.
(15) Kobayashi, T.; Rikukawa, M.; Sanui, K.; Ogata, N. *Solid State Ionics* **1998**, 106, 219.
(16) Kerres, J.; Ullrich, A.; Meier, F.; Haring, T. *Solid State Ionics* **1999**, 125, 243.
(17) Wang F.; Hickner, M.; Kim, Y. S.; Zawodzinski, T. A.; McGrath, J. E. *J. Membrane Science* **2002**, 197, 231. Harrison, W. L.; Wang, F.; Mecham, J. B.; Bhanu, V. A.; Hill, M.; Kim, Y.S.; McGrath, J. E. Journal of Polymer Science, Part A: Polymer Chemistry **2003**, 41(14), 2264-2276
(18) Bloom, P. D.; Sheares, V. V. *Macromolecules* **2001**, 34, 1627.
(19) Ghassemi, H.; McGrath, J. E. *Polymer*, **1997**, 38, 3139.
(20) Smith, C.D.; Grubbs, H.; Webster, H.F.; Gungor, A.; Wightman, J.P.; McGrath, J.E., High Performance Polymer, **1991**, 3(4), 211-229. Wang, S.; Zhuang, H.; Shobha, H.K.; Glass, T.E.; Sankarapandian, M.; Ji, Q.; Shultz, A.R.; McGrath, J.E. *Macromolecules*, **2001**, 34, 8051-8063.

New Multiblock Copolymers Of Sulfonated Poly(4'-Phenyl-2,5-Benzophenone) And Poly(Arylene Ether Sulfone) For Proton Exchange Membranes

Background

Rigid-rod poly(4'-phenyl-2,5-benzophenone) telechelic macromonomers were synthesized by Ni(0) catalytic coupling of 2,5-dichloro-4'-phenylbenzophenone and the end-capping agent 4-chloro-4'-fluorobenzophenone. The degree of polymerization was determined by ^{13}C NMR. The macromonomers produced were selectively sulfonated by concentrated sulfuric acid at 50^{o}C. The degree of sulfonation was controlled by varying the reaction time and was determined by titration. The nucleophilic step copolymerization of the fluoroketone activated sulfonated poly(4'-phenyl-2,5-benzophenone) oligomer (Mn = 3.05 x 10^3 g/mol) with hydroxyl terminated biphenol based polyarylethersulfone (Mn = 4.98 x 10^3 g/mol) afforded an alternating multiblock sulfonated copolymer that formed flexible transparent films, in contrast to the high molecular weight rigid rod homopolymers. They were tested for water absorption and proton conductivity by specific impedance. The synthesis and characterization of these multiblock copolymers are reported.

Introduction

Proton exchange or polymer electrolyte membrane (PEM) fuel cells have attracted much attention as alternative sources of electricity. The well known principle of fuel cells is based on electrical energy being generated via electrochemical formation of water from hydrogen and oxygen.[1] Hydrogen molecules are catalytically oxidized to protons at the anode, which migrate in solvated form through a PEM to the cathode where the reaction is completed with the oxygen reduction product.

For many years, polymer electrolytes bearing sulfonate groups have been investigated and utilized as cation exchange resins or membranes.[2-4] Considerable research effort has been recently made on the development of proton exchange membranes (PEM) fuel cells or direct methanol fuel cells (DMFC), in which the PEMs serve several functions, such as the barrier for the fuels, and the electrolyte for transporting protons from the anode to the cathode.[5] Currently, the sulfonated perfluorinated ionomer-based systems (Nafion®) produced by Dupont Co. are mostly used as the membranes. Nafion membranes show relatively high proton conductivity of 10^{-1} S cm^{-1} at room temperature when fully hydrated and display long term durability, but have technical limitations, such as low conductivity at low humidity or high temperatures (greater than 80°C), and high methanol permeability. However, there is an increasingly large amount of research activities to develop new membranes with improved performance. These membranes should exhibit low permeability to H_2 and O_2, high durability and good performance at higher operating temperatures (e.g., 120^{o}C), for H_2/Air FC and low methanol permeability in DMFC over a range of about 25-80^{o}C.

Poly(p-phenylene) (PPP) and especially its derivatives are a promising class of high-performance polymers because of their excellent thermal and mechanical properties.[6-11] One main limitation of the high molecular weight poly(1,4-phenylene) is the low solubility of the rigid rod chains during polymerization. Substituents can overcome this problem and afford high molecular weight substituted PPPs.[15] These include, poly(2,5-benzophenone)s, which are synthesized by nickel (0) catalytic coupling of bis(aryl halide)s or bis(aryl mesylate)s. They are well known for their high degrees of polymerization, good solubility in dipolar aprotic solvents, and several excellent thermal and mechanical properties.[12-13] In addition, several substituted poly(2,5-benzophenone)s were prepared by Ni(0) catalytic coupling of aromatic dichlorides. These materials provide a suitable route to introduce new functional groups to the side-chain through their substituents. For example, introduction of sulfonic acid and oxyphenyl sulfonic acid derivatives were reported previously.[2, 17]

The inability to form flexible films is a major drawback of most PPPs. Even amorphous, high molecular weight poly(2,5-benzophenone) suffers from this problem. The inability to form flexible, creaseable films from these stiff chains, remains a major barrier in the testing and development of PPP-based proton-exchange and gas-separation membranes and in other applications.

As an alternative to poly(2,5-benzophenone) homopolymers, one might use a rigid-rod telechelic or macromonomers (difunctional oligomers) units in multiblock copolymers.[11] The combination of poly(2,5-benzophenone) and other high-performance macromonomers should allow one to produce new materials that could represent a good balance of the homopolymers properties. Therefore, a more flexible, random coil film forming, thermally stable telechelic oligomer might be combined with a difunctional high-modulus rigid-rod PPP macromonomers to produce a hybrid material with many potential applications including membranes.

In the accompanying paper (Part I), we reported preliminary results on the synthesis of several substituted poly(2,5-benzophenone)s with different degrees of sulfonation.[14] These materials were tested as blends or composites and showed sufficiently high protonic conductivities to be further considered for PEM's in fuel cell applications. In this article, we utilize the end-capping of poly(4'-phenyl-2,5-benzophenone) with 4-chloro-4'fluorobenzophenone as previously reported [9] to produce rigid-rod difunctional activated aryl halide macromonomers. The resulting poly(4'-phenyl-2,5-benzophenone)s were subsequently sulfonated using concentrated sulfuric acid. The hydrophilic sulfonated poly(4'-phenyl-2,5-benzophenone) oligomer with labile fluorine end group were combined with hydrophobic hydroxy terminated biphenol poly(aryl ether sulfone) (PAES) to produce high molecular weight multiblock copolymer capable of forming more flexible films. Randomization by ether-ether interchange which well known to usually occur in pure poly(arylene ether)s obviously is avoided. [16]

Experimental

Materials: Most of the reagents were purchased from Aldrich and used as received unless otherwise noted. N-methyl-2-pyrrolidinone (NMP) and N,N-dimethylacetamide (DMAc) were dried over calcium hydride, distilled under vacuum and stored under nitrogen before use. Triphenylphosphine was purified by recrystallization from diethyl ether. 4'-Phenyl-2,5-

dichlorobenzophenone was recrystallized from ethanol. The end-capping agent 4-chloro-4'fluorobenzophenone was synthesized by an iron(III) chloride-catalyzed Friedel-Crafts acylation of chlorobenzene with 4-fluorobenzoyl chloride. The 4,4'-dichlorodiphenyl sulfone was kindly supplied by Solvay Advanced Polymers. The 4,4'-biphenol was donated by Hydrosize Inc.

Synthesis of a telechelic macromonomer (1):

To a previously flame-dried 100 mL two-neck flask, equipped with an overhead stirrer, were added zinc (3.56 g, 52.9 mmol), nickel (II) chloride (0.22 g, 1.71 mmol), triphenylphosphine (1.79 g, 6.83 mmol) and 2,2'-dipyridyl (0.266 g, 1.71 mmol). Additions of the catalyst mixture to the reaction flask were made in a dry bag under an argon atmosphere. The flask was then sealed with a septum and 15 mL of anhydrous NMP was added via syringe. The mixture was heated in an oil bath to 80°C under nitrogen with continuous stirring. The catalyst mixture undergoes a color change from yellowish brown to deep green and finally dark red. After the dark red appearance of catalyst a mixture of dry 2,5-dichloro-4'-phenylbenzophenone (17.1 mmol) and 4-chloro-4'fluorobenzophenone (1.9 mmol) dissolved in 10 mL of anhydrous NMP syringed into the reaction flask. The reaction was allowed to proceed for 3-4 h before precipitation into methanol containing 30% hydrochloric acid. After stirring for 12 h the yellow solid was filtered, washed several times with water and methanol before drying in a vacuum oven at 80°C to afford the product in 96% yield.

^{1}H NMR (400 MHz): 6.5-8.2 ppm. ^{13}C NMR (100.5 MHz): 198.2-197.0, 194.7, 165.0 (d, $^{1}J_{C\text{-}F}$ = 510 Hz), 144.2, 140.4, 139.4, 131,9, 130.5, 130.3, 129.1, 128.6, 128.0, 127.4, 126.9, 126.4, 115.4.

Sulfonation of substituted poly(phenylene)s (**2**): In a typical reaction 0.5 g of pulverized poly(2,5-dichloro-4'-phenylbenzophenone) (**1**) was dissolved in 10 mL of concentrated sulfuric acid (96-98%). The solution was maintained at 50°C for a controlled period of time before adding 50 g of crushed ice. A precipitate formed which was filtered and dried under vacuum at 120°C and subsequently used for multiblock copolymers preparation.

Biphenol based poly(arylene ether sulfone) functional oligomers (**3**): The desired hydroxyl-terminated poly(arylene ether sulfone) (PAES) was synthesized from 4,4'-dichlorodiphenylsulfone and 4,4'-biphenol as discussed in the literature.[18] Low molecular weight PAES was targeted by using an excess of biphenol as the end-capping group. Into a 100 mL three-necked flask equipped with a mechanical stirrer, nitrogen inlet and a Dean-Stark trap was added biphenol (3.35 g, 18.00 mmol) and 4,4'-dichlorodiphenylsulfone (4.77 g, 16.61 mmol). Potassium carbonate (7.2 g, 54 mmol) was added and sufficient NMP (40 mL) was introduced to make a 20% (w/v) solids concentration. Toluene (30 mL) was used as an azeotroping agent. The reaction mixture was heated under reflux at 150°C for four hours to dehydrate the system. The temperature was then slowly raised to 175°C to distill off the toluene. The reaction mixture was allowed to proceed at this temperature for another 16 hours and at 190°C for one hour, during which it became viscous. The reaction mixture was cooled to room temperature and filtered without dilution to remove the salts. The oligomer was isolated by precipitation in stirring methanol. The precipitate was filtered and washed several times with methanol, then carefully dried in a vacuum oven at 120°C for three days. It afforded a 94% yield and the proton NMR showed expected peaks between δ 6.8 and 8.0 ppm. The number of repeat units (n) was calculated using the peaks at δ 7.715 and 6.838 ppm to be about 12. Thus the number average molecular weight, Mn, was determined to be 5000 g/mol.

Multiblock PPP-PAES copolymer synthesis (**4**): The multiblock copolymer was synthesized from the fluorine-terminated activated aryl ketone polyphenylene **1** and the hydroxy-terminated poly(arylene ether) **3** oligomers. Into a 50 mL three-necked flask equipped with a mechanical stirrer, nitrogen inlet and a Dean-Stark trap was added macromonomer **1** (0.367 g, 0.15 mmol) and macromonomer **3** (0.75 g, 0.15 mmol). Potassium carbonate (0.05 g, 0.4 mmol) was added and sufficient DMAc (6 mL) was introduced to the mixture. Toluene (5 mL) was used as an azeotroping agent. The reaction mixture was heated under reflux at 150°C for four hours to dehydrate the system. The temperature was then slowly raised to 160°C to distill off the toluene. The reaction mixture was allowed to proceed at this temperature for another 16 hours. The reaction mixture was diluted by adding 6 mL of DMAc, allowed to cool to room temperature and the product was isolated by precipitation in stirring methanol. The precipitate was filtered and washed several times with methanol and water. It was then dried in a vacuum oven at 120°C for 24 hours. It afforded 1.06 g of product **4** (97% yield).

Sulfonated multiblock copolymers 5: The copolymers **5** were synthesized similarly to the procedure explained for copolymer **4**.

Results and Discussion

Synthesis of monomers and polymers. The 2,5-dichloro-4'-phenylbenzophenone was initially chosen as the monomer for its ability to form high molecular weight poly(4'-phenyl-2,5-benzophenone) via Ni(0) coupling reaction, and because the pendent phenyl rings of the repeat units can be selectively sulfonated by concentrated sulfuric acid.[17] The end-capping agent 4-chloro-4'-fluorobenzophenone was synthesized by Friedel-Crafts acylation of chlorobenzene with 4-fluorobenzoyl chloride. Sheares et al. prepared and used this end-capper in the synthesis of poly(4'-methyl-2,5-benzophenone) macromonomers.[9] The nickel-catalyzed polymerization was utilized to make fluorine terminated macromonomer **1** from 2,5-dichloro-4'-phenylbenzophenone and controlled amount of effectively monofunctional 4-chloro-4'-fluorobenzophenone in high yield (Scheme 22). Both monomer and the end-capping agent were dissolved in NMP and added to the polymerization flask containing a mixture of nickel chloride, 2,2'-bypyridyl and triphenylphosphine in NMP. The 4-chloro-4'-fluorobenzophenone was added at 0.25, 0.20, 0.125 mole fractions based on total monomer amount to produce a systematic series of fluorine-terminated poly(4'-phenyl-2,5-benzophenone)s **1a-c**. Carbon-13 NMR spectra was used to determine the degree of polymerization of macromonomer **1**, which was in good agreement with the targeted values. The peak assigned for the terminal carbonyl was compared with the peak corresponding to the carbonyl group on the benzophenone side groups for this calculation (Figure 59). The ^{19}F NMR spectrum of **1** shows two peaks at 106.7 and 106.9 ppm, which corresponds to terminal fluorine atoms (Figure 60). It is believed that these two resonances are due to the influence of regioirregularity of the PPP backbone. It is known that carbon-carbon coupling polymerization of 2-substituted 1,4-dichlorobenzene produce polymers with a mixture of head to head, head to tail and tail to tail linkages along the polymer chain. In the case of poly(4’-phenyl-2,5-benzophenone), benzoyl side groups attached to the benzene ring adjacent to the terminal groups provides a mixture of chemical environment for the terminal fluorine atoms. Fluorine NMR is known to be sensitive to substituents even on several chemical bonds away from the fluorine atom.

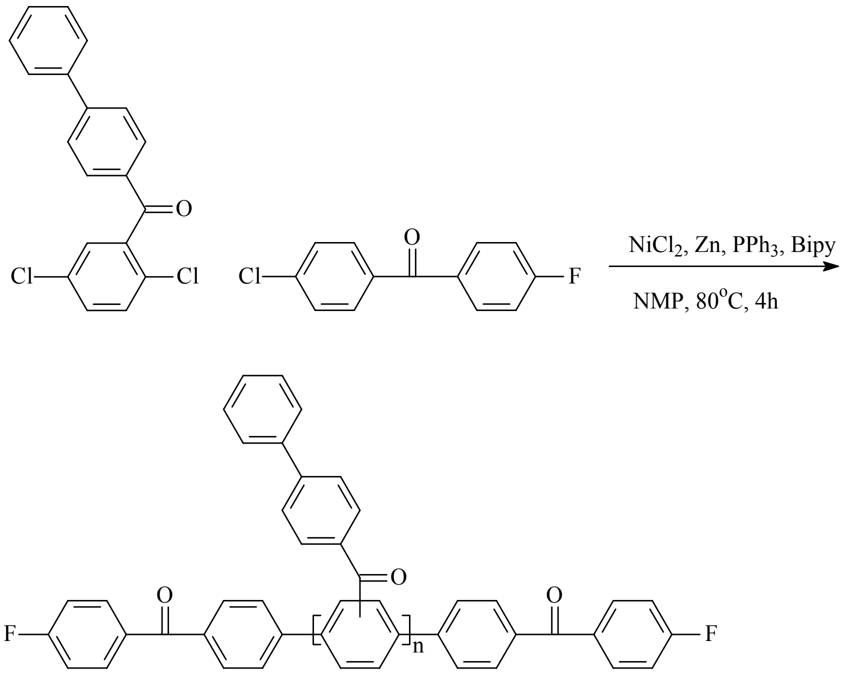

1

Scheme 22. Fluorine terminated poly(4’-phenyl-2,5-dichlorobenzophenone)

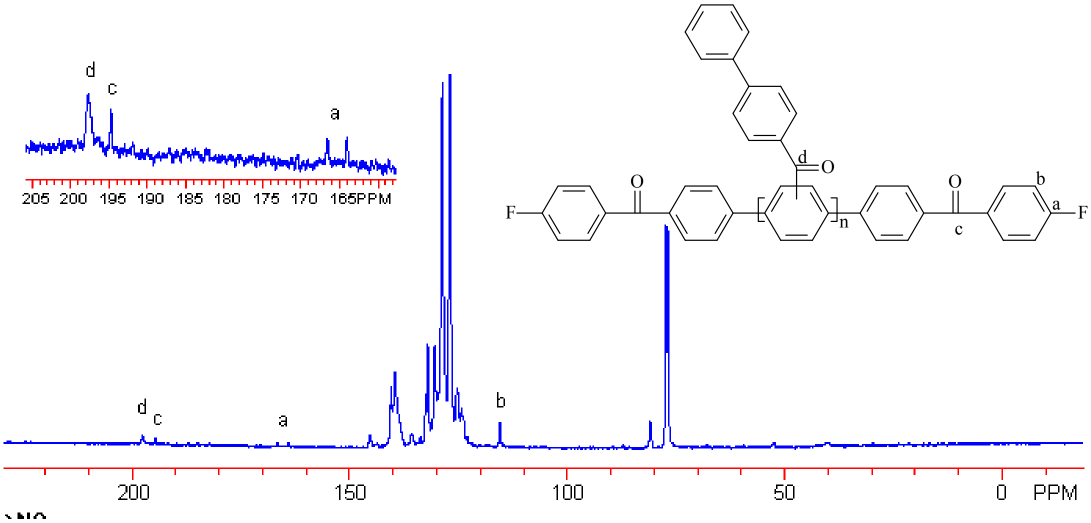

Figure 59. ^{13}C NMR spectrum of 1 in CDCl$_3$

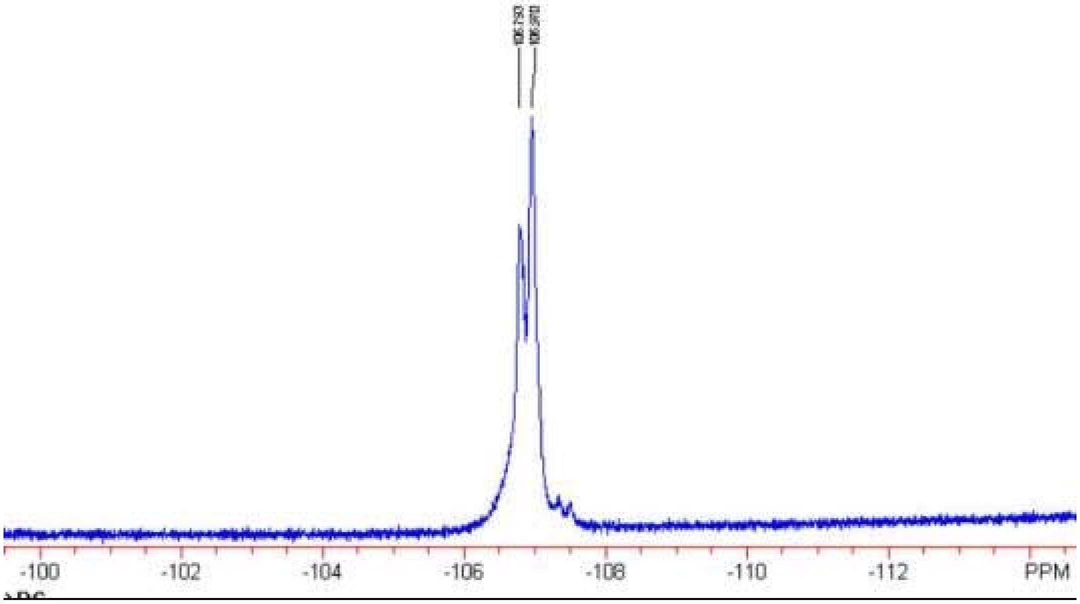

Figure 60. ^{19}F NMR spectrum of macromonomer **1**

Hydoxy terminated poly(arylene ether sulfone) oligomers **3** were synthesized and used as an approach to develop more flexible PPP film-forming materials. Biphenol monomer was used at 11.4, 10.8 and 9.1 mol% excess base on total amount of 4,4'-dichlorodiphenylsulfone to produce macromonomers **3a-c** with the target molecular weight of 5000, 3000 and 2400 g/mol, respectively (Scheme 23). As shown in Table 12, the molecular weights of macromonomers **3a-c** determined by GPC relative to polystyrene standards, decreased with the increasing amount of biphenol. GPC results show higher number average molecular weight of the macromonomers **3** compared to the target values and the polydispersities (PDs) approach 2 as the molecular weight increases. Also ^{1}H NMR was employed to determine absolute number-average molecular weight and degrees of polymerization. This was accomplished by integration of the aromatic protons of terminal group relative to the aromatic protons of phenylsulfone. Figure 61 presents the proton NMR spectrum of macromonomer **3** with degree of polymerization n=12 (5000 g/mol). As shown in Table 12 the molecular weights calculated from proton NMR spectra are very close to the target values where as the apparent Mn values obtained from GPC using polystyrene as the standard are almost double the target numbers.

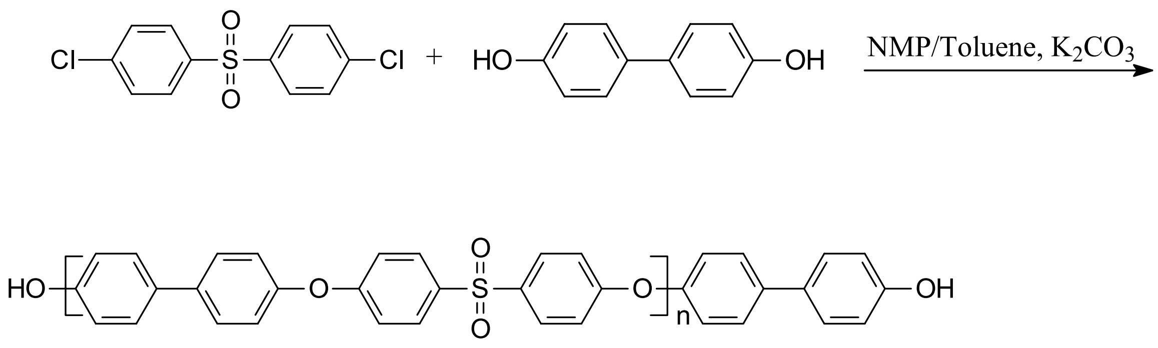

3

Scheme 23. Synthesis of hydroxy-terminated poly(arylene ether sulfone)

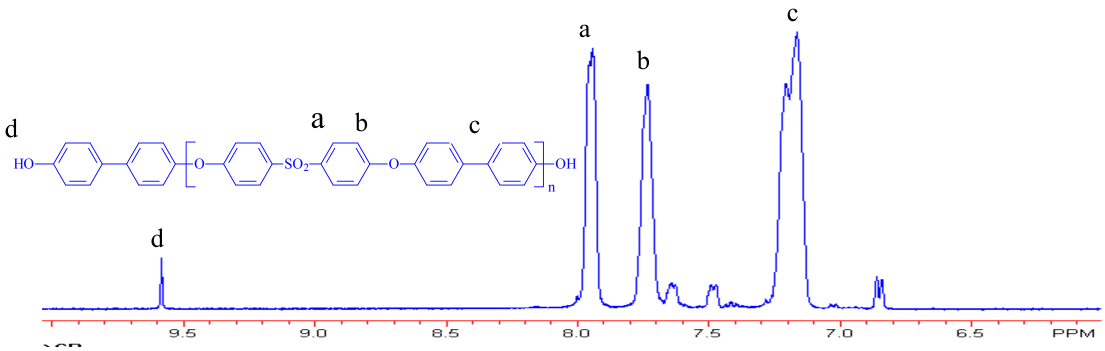

Figure 61. ^{1}H NMR of macromonomer **3**

Table 12. Physical characterization of macromonomers **3**

Sample	Molecular Weight(x10^{-3})^{1}	Molecular Weight(x10^{-3})^{2}	Intrinsic viscosity^{3}	Mn(x10^{-3})^{4}	Mw(x10^{-3})^{4}	PD
1	1.2	1.2	0.08	2.6	3.7	1.4
2	2.4	2.8	0.14	5.1	9.2	1.7
3	5.0	4.8	0.21	8.1	16.9	2.0

1) Target molecular weight. 2) Determined from ^{1}H NMR spectra. 3) NMP, 25^{o}C (dL/g).
4) Determined from GPC using polystyrene as standard, NMP(containing 0.05 mol% LiBr) at 60^{o}C.

The reaction of **1** with dihydroxy end-capped **3** afforded a transparent film-forming copolymer **4** (Scheme 24). Multiblock **4** showed only one glass transition at 225°C, detected by differential scanning calorimetry (DSC), which is close to that of the polyethersulfone block. The glass transition temperature reported for commercial polyethersulfone RADEL® is 220°C.[19] The intrinsic viscosity values for copolymer **4** was determined as 0.65 dL/g in NMP at 25°C. Number average molecular weight of this copolymer based on GPC analysis was 11.6 kg/mol with PD of 2.7, which should be considered only an approximation.

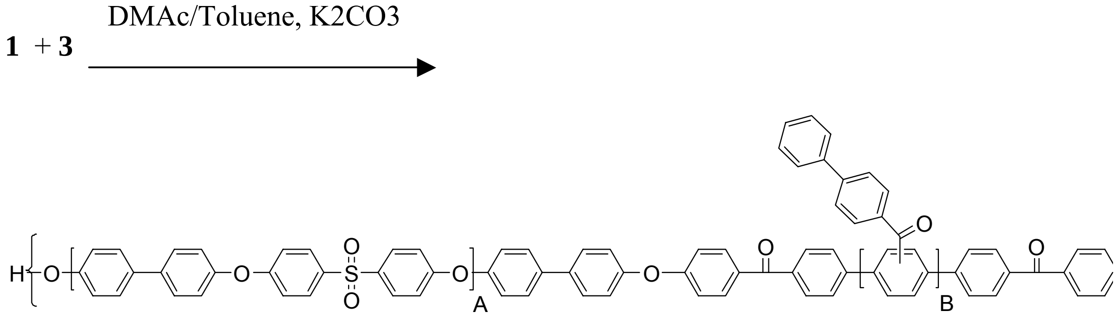

4

Scheme 24. Multiblock copolymer **4**

Introduction of sulfonic acid groups into the multiblock copolymers was possible by first reacting the macromonomer **1** with concentrated sulfuric acid at 50°C (Scheme 25). Terminating the reaction at different time periods controlled the degree of sulfonation. The result shows that the sulfonation reactions proceed very fast and approached the theoretical values within the first two hours and stays almost constant thereafter (Figure 62). All the sulfonated macromonomers **2** were soluble in hot water, except those with one-hour or less sulfonation reaction time. The degree of sulfonation, which is shown as ion exchange capacity (IEC) was measured by titrating the samples in aqueous solution containing sodium sulfate with standard sodium hydroxide solution (0.01 N). The IEC values were used to estimate the number of sulfonic acid groups and allowed an extrapolation of the molecular weight of macromonomer **2**. Figure 62 shows a plot of IEC value vs sulfonation reaction time for sulfonated macromonomer **2**.

1

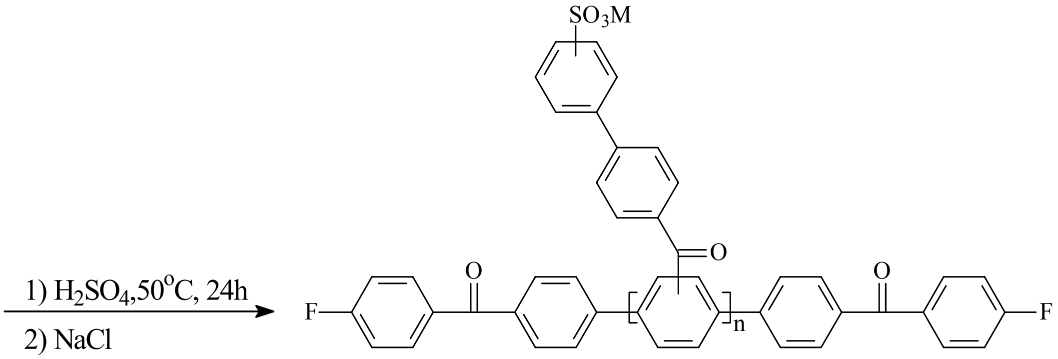

2

Scheme 25. Sulfonation of macromonomer **1**

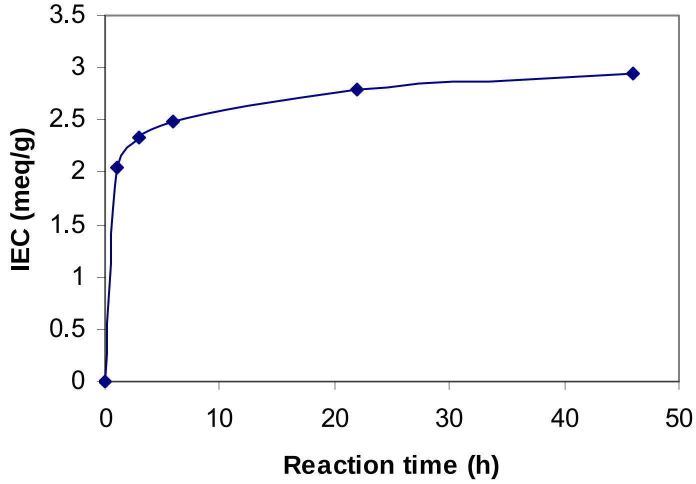

Figure 62. Ion exchange capacity vs reaction time at 50°C for sulfonated macromonomer **2**

Several multiblock copolymers **5** were synthesized from sulfonated macromonomer **2** and hydroxy-endcapped polyethersulfone **3** in a similar way as copolymer **4** (Scheme 26). All copolymers were recovered by filtration in yields greater than 91% after precipitation into methanol and drying at 100°C under vacuum. The most noticeable feature of the copolymers such as **5** was their ability to form more flexible ductile films compared to the sulfonated polyphenylenes homopolymers reported in Part I.[17]

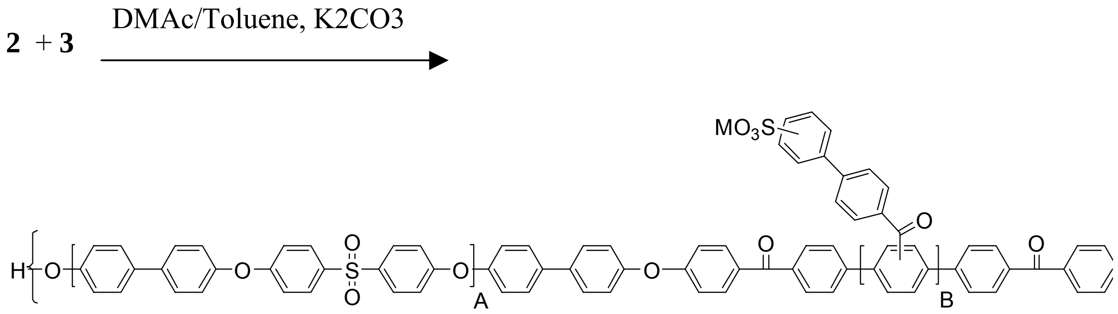

5

Scheme 26. Synthesis of multiblock copolymers **5**

Solution properties of copolymers. Intrinsic viscosities of the unsulfonated copolymer **4** was 0.65 dL/g and for the sulfonated copolymers **5** were around 0.35 dL/g. The molecular weights of the copolymers determined by GPC (polystyrene standard) showed Mn of 12 Kg/mol for unsulfonated copolymer **4** and between 13 to 17 kg/mol for sulfonated copolymers **5** (Table 13). Lower intrinsic viscosity values for sulfonated copolymers compared to **4** are attributed to lower molecular weight of these copolymers. In general, it was difficult to achieve equivalent stoichiometry during the polycondensation of the macromonomers. The problem becomes even more obvious in the case of sulfonated macromonomers **2**, due to the ambiguities related to the exact number of sulfonate groups in the oligomer. The DSC thermograms shown in Figure 63 suggest only one transition, which is surprising but may reflect the relatively short block lengths.

Table 13. GPC results for copolymers 4 and 5

Sample	**IV (dL/g)^{1}**	**Mn(x10^{-3})^{2}**	**Mw(x10^{-3})^{2}**	**PD**
4	0.65	11.6	32.3	2.7
5-a	0.35	17.3	38.5	2.2
5-b	0.35	13.2	29.1	2.1
5-c	0.34	14.8	33.5	2.2

1) NMP, 25oC (dL/g).

2) Determined from GPC using polystyrene as standard, NMP(containing 0.05 mol% LiBr) at 60^{o}C.

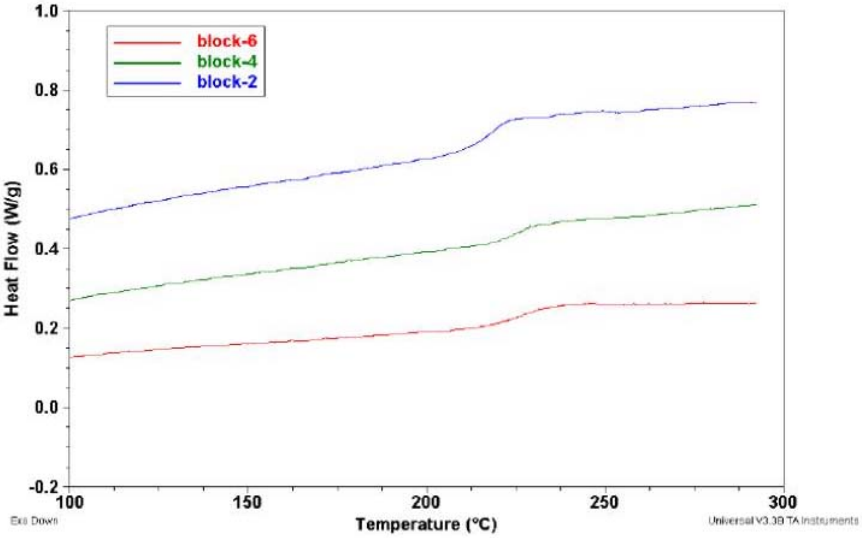

Figure 63. DSC thermogram of copolymer 4 (a) and two sulfonated copolymers (b and c)

Ion exchange capacity, water uptake and conductivity. Conversion of copolymers **5** from the sulfonate salt to the acid form **6** was accomplished by treating copolymers **5** in boiling sulfuric acid solution (0.5M) for 2 hours and then washing with deionized water and finally boiling in deionized water for 2 hours.[5] The IEC values of the copolymers **6** were measured in a similar way as described for macromonomer **2**. In all cases the experimental IEC values were lower than the theoretical values calculated for an ideal alternating multiblock, indicating that there was somewhat less than quantitative incorporation of sulfonated macromonomers.

Water uptake (expressed in weight percent) was measured by weighing the polymer films in their acid forms under dry and wet conditions. The amount of water uptake was closely related to the amount of sulfonic acid groups in the copolymers, as expected. As shown in Table 14, water uptake in samples **6d-f** having the same size of sulfonated phenylene block increased as the size of hydrophobic poly(arylene ether sulfone) block decreased. This was also observed in sample **6b** with higher degree of sulfonation compared with **6a**. Sample **6c**, which contains the highest concentration of sulfonic acid groups in the series, became a highly hydrated hydrogel and the film was mechanically weak. This behavior probably reflects a composition where the hydrophilic domains are continuous.[5]

The proton conductivities of the membranes were measured at 25^{o}C in liquid water as discussed earlier.[5] The acid form membranes (Figure 64) had proton conductivities of 0.024, 0.026, 0.034 and 0.036 S.cm^{-1} for the **6a** (IEC 0.70 meq/g), **6b** (IEC 0.75 meq/g), **6d** (IEC 0.94 meq/g) and **6f** (IEC 1.20 meq/g), respectively. It is known that the higher proton conductivity can be achieved by increasing the number of acid groups (higher IEC) in the membrane. While these values are lower than the control commercial membrane Nafion® 1135 (IEC 0.91 meq/g) (which was 0.12 S.cm^{-1}) or previously reported systems,[5] they are considered promising and further compositions are being investigated, along with more detailed thermal and mechanical behavior.

Table 14. Selected properties of copolymers **6**

Sample	**m:n**	**degree of $SO3H^1$**	***Water up take*** **(%)**	**IEC (meq/g)**	**Conductivity $(S.cm^{-1})^2$**
6-a	12:8	75%	22	0.70	0.024
6-b	12:8	95%	28	0.75	0.026
6-c	12:16	~100%	-	-	-
6-d	12:10	~100%	31	0.94	0.034
6-e	6:10	~100%	55	1.35	-
6-f	7:10	~100%	50	1.20	0.036

1) Calculated after titration of sulfonated phenylene macromonomer. 2) 30°C, liquid water.

Conclusions

Multiblock copolymers derived from fluoroketone terminated sulfonated benzoyl substituted polyphenylenes, as the hydrophilic block, and hydroxyl functional poly(arylene ether sulfone) as hydrophobic block were successfully prepared by nucleophilic step copolymerization. Initial T_g values for both unsulfonated control and sulfonated multiblock shows only one transition at 225°C close to the poly(arylene ether sulfone) segments via DSC. The segments may not be of sufficient length to develop two T_g values. The sulfonated copolymers such as **6** formed good ductile films and showed proton conductivity up to 0.036 $S.cm^{-1}$. Both the proton conductivity and water swelling of the membranes were influenced by the amount of sulfonic acid groups.

References

(1) http://www.lanl.gov/worldview/science/features/fuelcell.html

(2) Kobayashi, T.; Rikukawa, M.; Sanui, K.; Ogata, N. *Solid State Ionics* **1998**, 106, 219-225.

(3) Bae, J. M.; Honma, I.; Murata, M.; Yamamoto, T.; Rikukawa, M.; Ogata, N. *Solid State Ionics* **2002**.

(4) Kerres, J.; Ullrich, A.; Meier, F.; Haring, T. *Solid State Ionics* **1999**, 125, 243-249.

(5) Wang, F.; Hickner, M.; Kim, Y. S.; Zawodzinski, T. A.; McGrath, J. E. *J. Membrane Science* **2002**, 197, 231-242. Harrison, W. L.; Wang, F.; Mecham, J. B.; Bhanu, V. A.; Hill, M.; Kim, Y. S.; McGrath, J. E., Journal of Polymer Science, Part A: Polymer Chemistry (2003), 41(14), 2264-2276.

(6) Bloom, P. D.; Sheares, V. V. *Macromolecules*, **2001**, 34, 1627-1633.

(7) Wang, W.; Quirk, R. P. *Macromolecules*, **1995**, 28, 3495-3501.

(8) Sheares, V. V.; Pasquale, A. J., *J. Polym. Sci. Part A; Polym* **1998**, 36(14), 2611-2618.

(9) Bloom, P. D.; Sheares, V.V. *J. Polym. Sci. Part A; Polym. Chem*. **2001**, 39, 3505-3512.

(10) Percec, V.; Bae, J.Y.; Zhao, M.; Hill, D.H. *J. Org. Chem*. **1995**, 60, 1066-1069.

(11) Noshay A.; McGrath J.E. Block Copolymers: Overview and Critical Survey, Academic Press, **1977**.

(12) Percec, V.; Bae, J.Y.; Zhao, M.; Hill, D.H. *Macromolecules*, **1996**, 29, 3727-3735.

(13) Pasquale, A. J.; Sheares, V. V. *J. Polym. Sci. Part A; Polym. Chem*. **1998**, 36, 2611-2618.

(14) Ghassemi, H.; McGrath, J. E. *Polym. Prepr*. **2002**, 43(2).

(15) Ghassemi, H.; McGrath, J. E. *Polymer* **1997**, 38(12), 3139-3143.

(16) Attwood, T. E.; Newton, A. B.; Rose, J. B. *British Polymer Journal* **1972**, 4(5), 391-9; Wang, S. and McGrath, J.E., "Synthesis of Poly(arylene ether)s," in Synthetic Methods in Step-Growth Polymers, T.E. Long and M. Rogers (Eds), pp. 327-374, John Wiley and Sons, NY, (2003).

(17) Ghassemi, H.; McGrath, J.E.; B.M. Culbertson, Editor, *J. Polym. Sci. Part A; Polym. Chem*. **2003**, (this issue).

(18) Webster, D. C.; McGrath, J. E, Contemporary Topics in Polymer Science, Plenum Press, **1984**, 4 959-75.

(19) www.solvaymembranes.com

New Multiblock Copolymers Containing Hydrophilic-Hydrophobic Segments for Proton Exchange Membranes

Introduction

The introduction of ionic groups into high-performance polymers has attracted much interest because of their potential usefulness as high-temperature-operating ion-exchange resins and polymer electrolyte membranes (PEMs) for fuel cells. The principle of fuel cells is based on electrical energy being generated via electrochemical formation of water from hydrogen and oxygen. Hydrogen molecules are oxidized to protons at the anode, which migrate in the form of hydronium ions (H_3O^+) through a proton-conducting electrolyte to the cathode.

For many years, polymer electrolyte bearing sulfonate groups have been investigated and utilized as cation exchange resins or membranes.[1-3] Considerable research effort has recently made on the development of PEM fuel cells or direct methanol fuel cells (DMFC), in which the PEMs serve as the barrier for fuels, and the electrolyte for transporting protons from the anode to the cathode.[4] Currently, the sulfonated perfluorinated ionomer-based systems (Nafion) produced by Dupont Co. are used as proton exchange membranes. Despite of their technical limitations, such as low conductivity at low humidity or high temperatures (greater than 80ºC), and high methanol permeability, Nafion membranes show relatively high proton conductivity of 10^{-1} S cm^{-1} at room temperature and satisfactory durability. There is an increasingly large amount of research activities to develop new membranes with better performance compared to Nafion. These membranes should exhibit high durability and good performance at high operating temperatures (120-150°C), (H_2/Air) or lower methanol permeability (DMFC).

Sulfonation of poly(phenylene oxide)[5], poly(phenylene sulfide)[6], polysulfone[7] and poly(p-phenylene)s[8] in order to produce new proton- exchange membranes have been studied by several research groups. In these post-sulfonated polymers, the sulfonic acid group is usually restricted to the activated sites on the aromatic ring. However, precise control over the location and degree of sulfonation can be difficult. Direct copolymerization of 3,3'-disulfonate-4,4'-dihalodiphenylsulfone monomer with several bisphenolates, has been reported[9] as a successful alternative to over come some of the problems associated with post-sulfonation approach.

Previously, we reported synthesis of multiblock copolymers by reacting hydrophilic fluorine-terminated sulfonated poly(2,5-benzophenone) oligomers with hydrophobic hydroxyl-terminated biphenol poly(arylene ether sulfone).[10] These multiblock polymers have great potential as proton-exchange membranes.

Herein, we report new multiblock copolymers containing perfluorinated poly(arylene ether) as hydrophobic segment and disulfonated poly(arylene ether sulfone) as the hydrophilic segment. A major objective of this work is to produce thermally and hydrolytically stable, flexible membrane films with low methanol permeability and high proton conductivity.

Experimental

Materials: All reagents were purchased from Aldrich and used as received unless otherwise noted. N-methyl-2-pyrrolidone (NMP), dimethylsulfoxide (DMSO) and N,N-dimethylacetamide (DMAc) were dried over calcium hydride, distilled under vacuum and stored under nitrogen before use. THF was dried and distilled over sodium. 4,4'-Biphenol obtained from Eastman Chemical. The specialty monomer 4,4'-difluorodiphenylsulfone (DFDPS) was purchased from Aldrich and recrystallized from toluene. The sulfonated comonomer, 3,3'-disulfonated-4,4'-difluorodiphenylsulfone (SDFDPS) was synthesized in-house from 4,4'-dichlorodiphenylsulfone (DFDPS) according to a method which is reported elsewhere.[9] Decafluorobiphenyl was purchased from Aldrich Chemical Co. and dried under vacuum at 60^{o}C for 24 hours before use. 4,4-Hexafluoroisopropylidenediphenol (bisphenol AF or 6F-BPA), received from Ciba, was purified by sublimation and dried *in vacuo*.

Characterization: ^{1}H, ^{19}F and ^{13}C NMR analyses were conducted on a Varian Unity 400 spectrometer. Conductivity measurements were performed on the acid form of the membranes using a Solatron 1260 Impedance analyzer.

Synthesis of telechelic macromonomer (1): A typical polymerization procedure was as follows; decafluorobiphenyl (3.007 g, 9.0 mmol) and 6F-BPA (2.689 g, 8.0 mmol) were dissolved in DMAc (40 mL) (to make a 14% (w/v) solid concentration) and benzene (4 mL) in a reaction flask equipped with a nitrogen inlet and magnetic stirrer. The reaction mixture was stirred until completely soluble and then an excess of K2CO3 (3.31 g, 24 mmol) was added. The reaction bath was heated to 120°C during 2 h and kept at this temperature for 4 h. The mixture was precipitated into 200 mL of acidic water/methanol (1:1 in volume fraction). The precipitated polymer was filtered and successively washed with deionized water. Drying of the product at 80°C under vacuum gave essentially quantitative yield of white polymer **1.** ^{1}H-NMR (CDCl3): □ 7.10(d, 2H), 7.45(d, 2H). ^{19}F-NMR (CDCl3): -64.0 (CF3), -137.5, -152.4 (Ar-F), -137.2, -149.8, -160.2 (Ar-F). ^{13}C-NMR (CDCl3): 115.4, 128.8, 132.0, 157.1 (6F-BPA), 118.4, 122.1, 125.8, 129.7 (-CF3), 103.1, 134.7, 140.1, 143.3, 146.4 (fluorobiphenyl). Molecular weight: Mn= 8.0K, Mw=15.9K with a polydispersity of 1.97.

Biphenol based poly(arylene ether sulfone) (**2**): The desired hydroxyl-terminated sulfonated poly(arylene ether sulfone) (BPS) was synthesized from 3,3'-disulfonated-4,4'-difluorodiphenylsulfone (SDFDPS) and biphenol. Low molecular weight BPS polymers were targeted using an excess biphenol as the end-capping group. Into a 100 mL three-necked flask equipped with a mechanical stirrer, nitrogen inlet and a Dean-Stark trap was added biphenol (0.3724 g, 2.0 mmol) and 4,4'-difluorodiphenylsulfone (0.7688 g, 1.66 mmol). Potassium carbonate (0.828 g, 6 mmol) was added and sufficient DMSO (7 mL) was introduced to make a 14% (w/v) solid concentration. Toluene (5 mL) was used as an azeotroping agent. The reaction mixture was heated under reflux at 150^{o}C for four hours to dehydrate the system. The temperature was then slowly raised to 160^{o}C to distill off the toluene. The reaction mixture was allowed to proceed at this temperature for another. The reaction mixture was cooled to 90^{o}C before addition of fluorine terminated oligomer **1**.

Multiblock copolymer synthesis (**3**): The mutiblock copolymer was synthesized from the fluorine-terminated polymer **1** and the dihydroxyl-terminated telechelic macromonomer **2**. To a preformed solution of polymer **2** was added a solution of macromonomer **1** (1.90 g, 0.355 mmol) in DMSO (10 mL) followed by 5 mL of benzene. The addition of macromonomer **1** solution was done in several portions during one hour. The reaction mixture was stirred at 90°C for 2 h and at 110°C for 8 h. The viscosity of the mixture increased dramatically during the course of the reaction to the point that more DMSO (40 mL) needs to be added to improve efficiency of stirring. The reaction product was precipitated into 600 mL of water/methanol (1:1 in volume fraction). The precipitated polymer was filtered and first treated in boiling deionized water for 24 h and then treated in boiling THF for 4 h before being dried at 80°C for 48 h in a conventional oven. The reaction yield was 75-80%.

Results and Discussion

As depicted in the following Schemes 27, 28, and 29, a series of multiblock copolymers were prepared by the reaction of the dialkali metal salt of bisphenol-terminated disulfonated poly(arylene ether sulfone)s with decafluorobiphenyl-terminated poly(arylene ether)s in a polar aprotic solvent. The reaction was rapid and yielded copolymers with light yellow color. The dialkali metal salts of bisphenol-terminated disulfonated poly(arylene ether sulfone) were generated using 3,3'-disulfonated-4,4'-difluorodiphenylsulfone and excess amount of biphenol in the presence of potassium carbonate at 160°C (Scheme 28). By controlling the amount of biphenol monomer two samples with target molecular weight of 5K and 15K was prepared. The sulfonated copolymers were used in next step without isolation. Similarly, decafluorobiphenyl-terminated poly(arylene ether)s were synthesized using 6F-BPA and excess amount of decafluorobiphenyl in DMAc-benzene mixed solvent (Scheme 27).

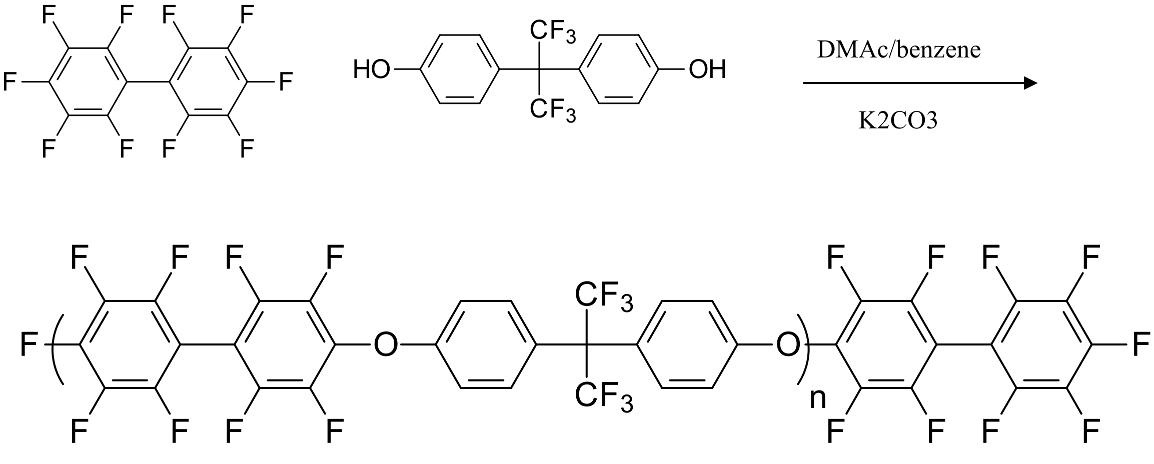

1

Scheme 27. Decafluorobiphenyl-terminated poly (arylene ether)s

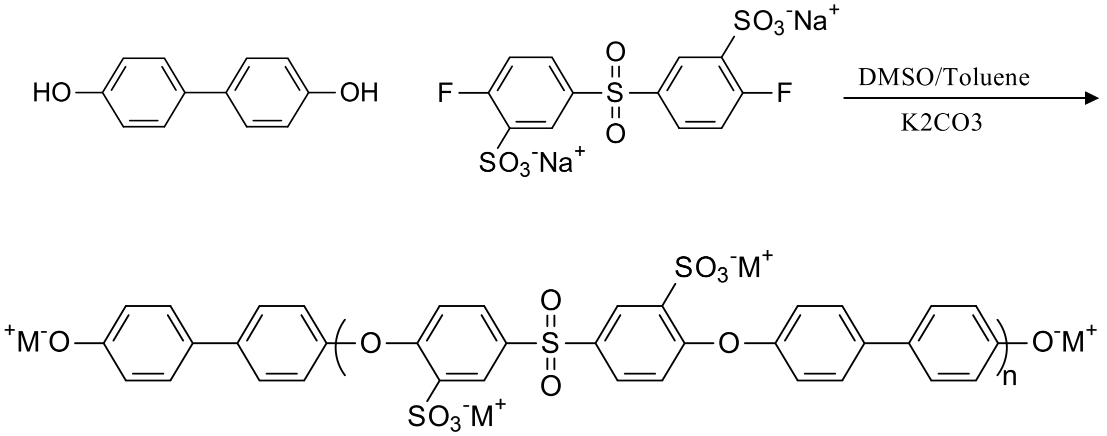

2

Scheme 28. Synthesis of diphenolate-terminated sulfonated poly(arylene ether sulfone)

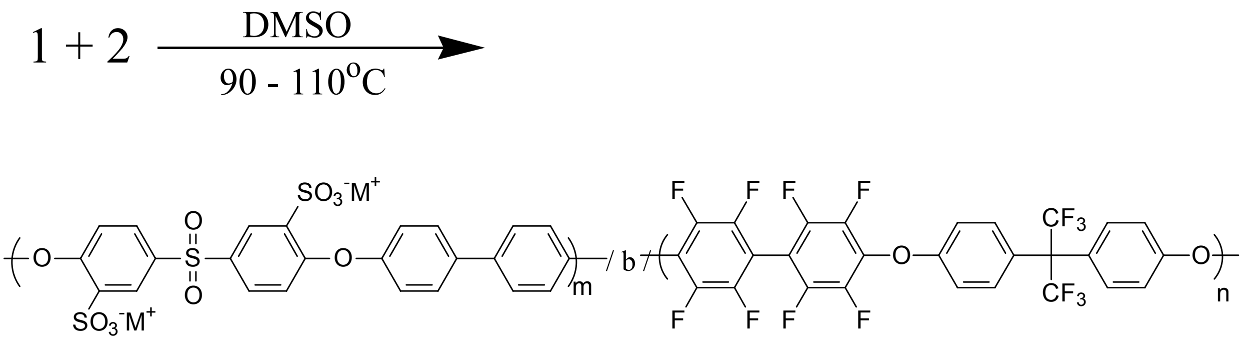

3

Scheme 29. Multiblock Copolymer 3.

It is well known that perfluoroaromatic monomers are highly reactive toward the nucleophilic aromatic substitution reaction and high molecular weight polymers form at relatively low temperature and short periods of time.[11-13] Four fluorinated samples were synthesized with molecular weights ranging from 2.8K to 60K. Low molecular weight samples formed white powder-like product after isolation, whereas the high molecular weight sample formed white fibrous material. The molecular structure of polymer **1** was confirmed by ^{19}F NMR in CDCl3, and compared with 6F-BPA and decafluorobiphenyl. Figure 64 shows the aromatic region of ^{19}F NMR spectrum for polymer **1** with target molecular weight of 5K. This spectrum shows two major peaks at -137.5 and -152.4 ppm, which were assigned to the aromatic fluorine atoms of decafluorobiphenyl units. The enlarged spectrum of the aromatic region reveals three small peaks at -137.2, -149.8 and -160.2 ppm. Comparison of these peaks with those in the ^{19}F NMR spectrum of decafluorobiphenyl suggest that these small peaks can be assigned to the pentafluorophenyl end group of the polymer. Relative integral intensity of the small peaks to the major peaks was used to estimate degree of polymerization.

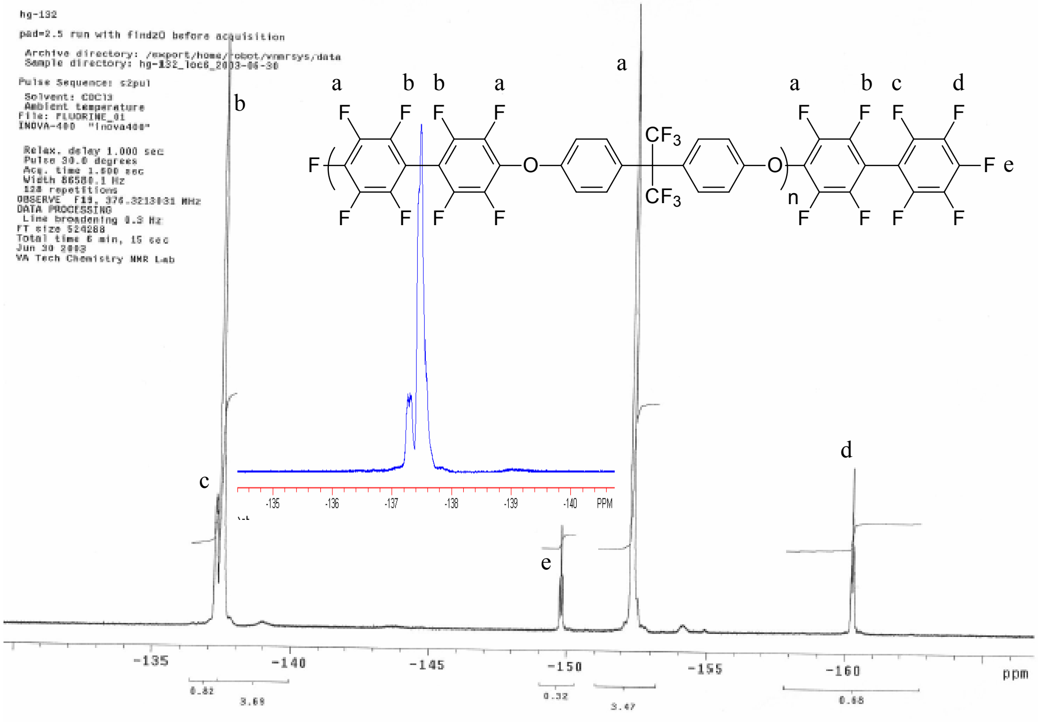

Figure 64. ^{19}F NMR spectra of decafluorobiphenyl-terminated poly(arylene ethers)

Reaction of the fluorinated oligomer **1** with preformed sulfonated **2** proceeded rapidly as evidenced by a sharp increase in viscosity of reaction solution mixture in the first 1-2 h. Dilution of reaction mixture with DMSO had little effect on lowering the viscosity of the solution. Products after isolation were treated in boiling water and boiling THF separately, in order to purify the product from any unreacted starting oligomers. After testing the samples it was found that about 20-25% of the products are soluble in THF. Further investigation revealed the nature of THF soluble part to be oligomer **1**. This result may explain the low yield obtained for these reactions.

In spite of incomplete reaction of reactants, multiblock copolymers **3** formed flexible films when cast from solution. These films were tested for ion exchange capacity by titrating with sodium hydroxide standard solution (Table 15). The multiblock copolymers had high water uptake both in salt and acid form. **Conductivity of these materials in their fully hydrated form in liquid water showed values between 0.12-0.32 S/cm (Table 15). As expected, the behavior is quite different than for random copolymers.**

Table 15. Characterization of the Block Copolymers made in DMSO

Sample	Block size (Kg/mol)[1]		IEC (meq/g)[2]		Water Uptake (%)	Conductivity (S.cm-1)[3]
	S	F	Calc.	Exp.		
3a	5	2.8	2.05	2.29	470	0.32
3b	15	15	1.30	1.46	260	0.16
3c	5	5	1.6	1.5	130	0.12

(1) (S) represents the sulfonated block and (F) represents the fluorinated block. (2) Samples were acidified in 0.5 M boiling sulfuric acid for 2 h and boiling deionized water for 2 h. (3) measured at room temperature in liquid water.

References

(1) Kobayashi, T.; Rikukawa, M.; Sanui, K.; Ogata, N. *Solid State Ionics* **1998**, 106, 219-225.
(2) Bae, J. M.; Honma, I.; Murata, M.; Yamamoto, T.; Rikukawa, M.; Ogata, N. *Solid State Ionics* **2002**.
(3) Kerres, J.; Ullrich, A.; Meier, F.; Haring, T. *Solid State Ionics* **1999**, 125, 243-249
(4) Wang, F.; Hickner, M.; Kim, Y. S.; Zawodzinski, T. A.; McGrath, J. E. *J. Membrane Science* **2002**, 197, 231-242.
(5) Cooper, J.E. *J. Polym. Sci. Part A; Polym. Chem*. **1971**, 9, 2361.
(6) (a) Hruszka, P.; Jurga, J.; Brycki, B. *Polymer* **1992**, 33, 248; (b) Miyatake, K.; Shouji, E.; Yamamoto, K.; Tsuchida, E. *Macromolecules* **1997**, 30, 2941.
(7) Iqbal, M.; Wightman, J. P.; Lloyd, D. R.; McGrath, J. E., *J Polym Sci Polym Chem Ed* **1984**, 22, 721.
(8) Ghassemi, H.; McGrath, J. E. *J. Polymer*, accepted, **2004.**
(9) Harrison, W. L.; Wang, F.; Mecham, J. B.; Bhanu, V. A.; Hill, M.; Kim, Y. S.; McGrath, J. E. *J. Polym. Sci. Part A; Polym. Chem*. **2003**, 41, 2264-2276.
(10) Ghassemi, H.; Grace, N.; McGrath, J. E. *Polymer, accepted* **2004**.
(11) Liu, F.; Ding, J.; Li, M.; Day, M.; Robertson, G.; Zhou, M.;Macromol,Rapid Commun. **2002**, 23, 844-848.
(12) Kim, J. P.; Kang, J. W.; Kim, J.J.; Lee, J.S.; Polymer, 2003, 44, 4189-4195.
(13) Kameneva, T. M.; Malichenko, B. F.; Shelud'ko, E. V.; Pogorelyi, V. K.; Sherstyuk, A. I.; Rozhenko, A. B. Zhurnal Organicheskoi Khimii **1989**, 25(3), 576-82.

VISCOMETRIC BEHAVIOR AND MOLECULAR WEIGHT CHARACTERIZATION OF SULFONATED POLY(ARYLENE ETHER SULFONE) COPOLYMERS

Introduction

Proton exchange membrane (PEM), the key component of fuel cell, is responsible for the proton transport from the anode to the cathode, therefore directly determining the performance of the fuel cell. PEMs must have good mechanical, thermal and chemical stabilities and still have high proton conductivity. Many families of polymers with differing chemical structures and various strategies for incorporation of sulfonic acid groups have been explored as PEM materials. Sulfonated poly(arylene ether sulfone)s are promising candidates due to their good acid and thermal oxidative stabilities, high glass transition temperatures and excellent mechanical strengths. Our group has reported synthesis of poly(arylene ether sulfone) copolymers by directly copolymerizing sulfonated monomers (1). This procedure is more preferable relative to post modification method since it is easy to control the degree of sulfonation and avoid the side reactions. However, this new synthetic route brought a whole new challenge in determining the molecular weight of the final polymer product. Molecular weight is a critical parameter defining PEM durability and this has not been properly characterized for any PEM membranes including Nafion, which is probably the most glaring omission in new ion conducting polymer research (2). In the post modification method, sulfonic acid groups are formed by chemical modification of polymeric precursors and MW characterization of precursors is usually performed. The aim of this work was to study dilute solution behavior and develop techniques for the proper MW characterization of the ion-containing PEMs.

Experimental

Materials. *Tert*-butylphenyl terminated sulfonated poly(arylene ether sulfone) copolymers with different molecular weight (20 kg/mol ~ 50 kg/mol) were prepared by direct polymerization of the activated halides, biphenol and a t-butylphenyl endcapping reagent as shown in Scheme 30 (3). For all copolymers, the mole ratio of 4,4'-dichlorodiphenylsulfone(DCDPS) to 3,3'-disulfonated 4,4'-dichlorodiphenylsulfone (SDCDPS) was fixed to 6.5/3.5. The molecular weight determined from 1H NMR spectra was consistent with the theoretical values. BPS35-control copolymer, with SDCDPS/DCDPS of 3.5/6.5 was also prepared from biphenol, DCDPS and SDCDPS under the similar polymerization condition without endcapping agent, in which the stoichiometry between dihalide monomers and biphenol was maintained at 1:1. GPC and intrinsic viscosity measurement show that it has higher molecular weight than all the other endcapped BPS35 as expected.

Intrinsic Viscosity Measurement. Viscosity measurements were carried out with a Cannon Ubbelholde viscometer with a flow time of about 98s for pure NMP at 25 °C. The temperature was regulated at 25 ± 0.1 °C. Each solution for viscometry was freshly prepared and was kept at 25.0 ± 0.1 °C for 10 min prior to the measurement. All the solutions were filtered in order to remove undissolved particles before introduction into the viscosimeter. The polymer concentration were suitably chosen to obtain relative viscosities in the appropriate range. After each determination, the viscometer was flushed at least 3 times with distilled water before rinsing with acetone prior to drying in the oven. This procedure was important because acetone is a precipitant for the copolymer. For the same reason, acetone vapor must be thoroughly removed before the introduction of the next solution.

GPC Measurement. GPC experiments were performed on a liquid chromatograph equipped with a Waters 1515 isocratic HPLC pump, Waters Autosampler, Waters 2414 refractive index detector and Viscotek 270 dual detector. LiBr/NMP was used as the mobile phase. The column temperature is maintained at 60 °C because of the viscous nature of NMP. Both the mobile phase solvent and sample solution were filtered before introduction to the GPC system.

Results and Discussion

Figure 65 presents the evolution of the reduced viscosity and inherent viscosity versus concentration of BPS35-control sample in salt-free NMP and in 0.05M LiBr/NMP respectively. The solution properties of BPS35 in the polar medium NMP with and without added salt are radically different. A polyelectrolyte effect is clearly observed. As one dilutes a charged macromolecule, they experience molecular coil expansion, exhibiting higher reduced viscosity as the concentration is reduced due to the charge repulsion along the polymer backbone (4). The presence of small electrolyte LiBr, whichdetermines the solution ionic strength, screens out charges and the repulsive interactions, affords a linear plot and enables us to obtain conventional extrapolations to dilute solution viscosity. Thus the key for the dilute solution viscosity measurements for ion-containing PEM is the introduction of a low molar mass salt, which is often quite appropriately able to screen the charges. However, based upon the consideration that the optimum salt concentration might depend upon the chemical structure, molar mass range, charged density etc., dilution viscosity measurements of different MW BPS35 samples in NMP containing various concentrations of LiBr from 0.01M to 0.1M were also performed. Linear plots were obtained for all the samples in all these salt concentrations. Intrinsic viscosity data obtained for different concentrations of salt were presented in table 16. One trend can be observed from the tabulated data. Increasing of the salt level decreases the intrinsic viscosity. It is clearly shown that the intrinsic viscosity drops significantly from the salt level of 0.01M to 0.05M for all the samples. Obviously 0.01M LiBr is not enough to screen the charges of BPS35. Furthermore, for the samples with the MW lower than 50K there shows only small decrease of intrinsic viscosity, probably within the experimental error, from the salt level of 0.05M to 0.1M. For the samples with MW equal or higher than 50K, there shows still further decrease of intrinsic viscosity from the salt level of 0.05 to 0.1M.

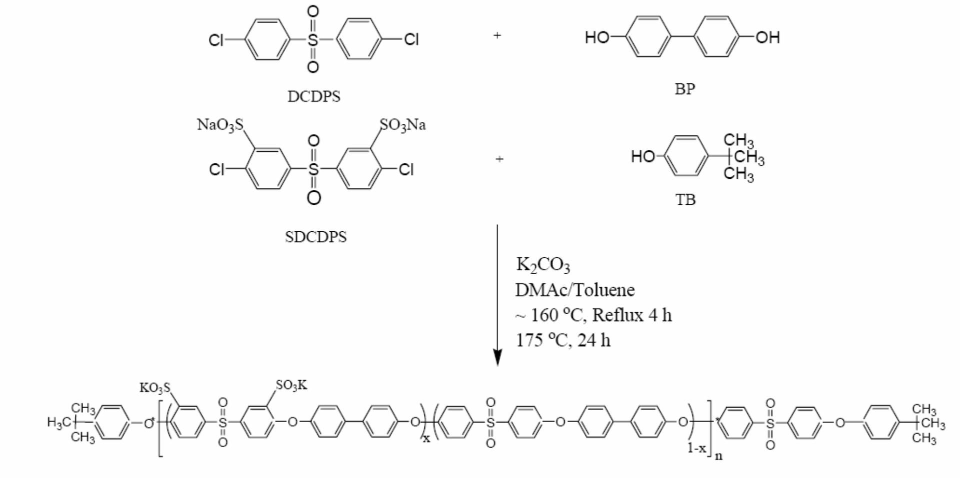

x=0.35 BPS35_20K, BPS35_40K, BPS35_50K

Scheme 30. Synthesis of tert-butylphenol terminated poly(arylene ether sulfone)s containing sulfonate groups.

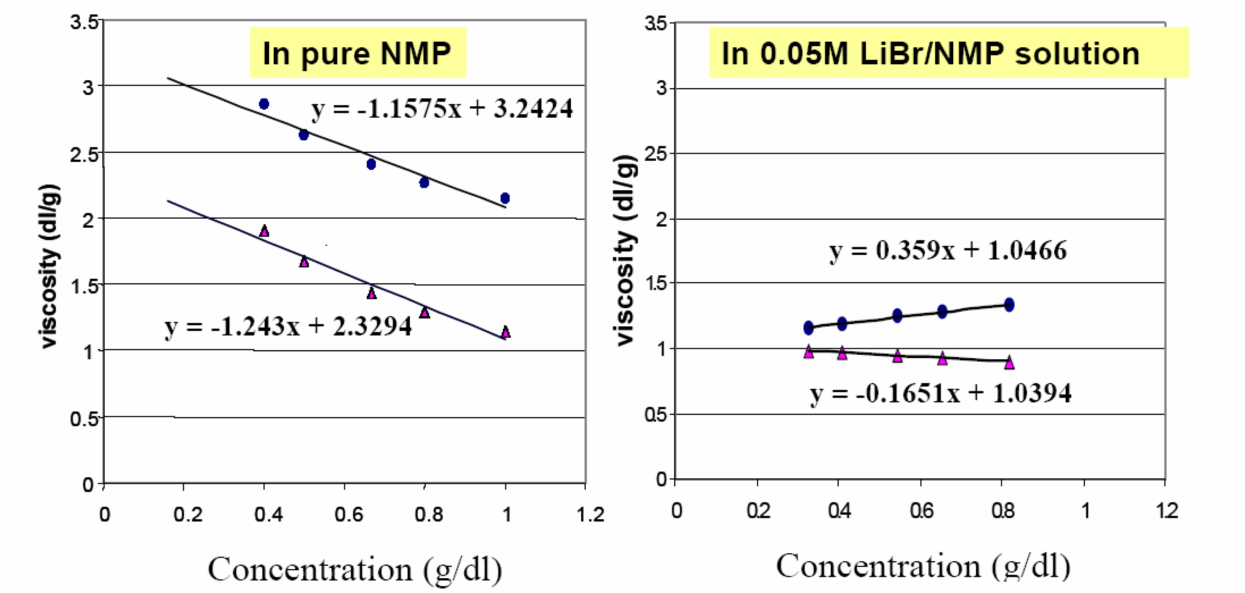

Figure 65. Evolution of the reduced viscosity and inherent viscosity versus concentration of BPS35-control sample in salt-free NMP and in 0.05M LiBr/NMP respectively.

Table 16. Summary of Intrinsic Viscosity Result of BPS35 at Different Salt Levels.

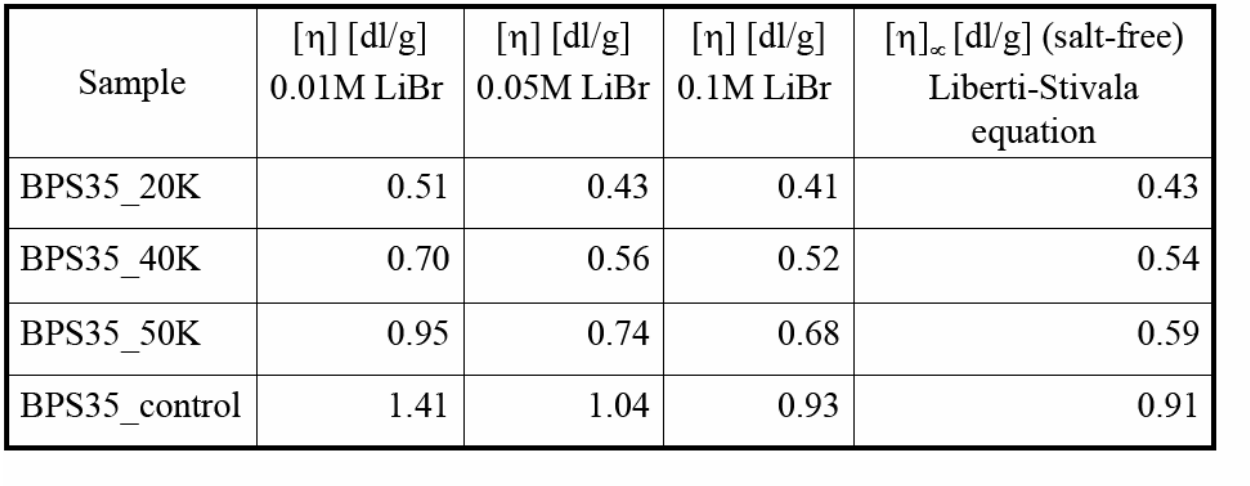

Sample	[η] [dl/g] 0.01M LiBr	[η] [dl/g] 0.05M LiBr	[η] [dl/g] 0.1M LiBr	[η]∞ [dl/g] (salt-free) Liberti-Stivala equation
BPS35_20K	0.51	0.43	0.41	0.43
BPS35_40K	0.70	0.56	0.52	0.54
BPS35_50K	0.95	0.74	0.68	0.59
BPS35_control	1.41	1.04	0.93	0.91

For salt-free polyelectrolyte solutions, an empirical analysis could also be performed to extract the intrinsic viscosity by extrapolation to infinite concentration using the Liberti-Stivala equation (5,6).

$$\eta_{red} = [\eta]_\infty + k \frac{[\eta]_\infty}{\sqrt{c}}$$

Where $[\eta]_\infty$ represents the intrinsic viscosity when the charges are shielded to the extent that the macromolecule behaves as a noncharged chain and is determined from the extrapolation to infinite concentration. Figure 66 shows the evolution of reduced viscosities for BPS35 with different molecular weights in salt-free NMP. The plot of η_{red} versus c-1/2 is presented in Figure 67. The viscosity of BPS35 solutions is well represented by the Liberti-Stivala equation since a linear behavior is obtained. [η]∞ values of BPS35 samples with different molecular weights obtained by linear extrapolation were listed in Table 16.

The GPC measurement of BPS35 was also performed using NMP/LiBr as the mobile phase. The existence of charged groups in the copolymer coil may causes some specific problems in interpreting the results of GPC because, in addition to size exclusion, some additional mechanism might be involved (7). Our result shows that GPC coupled with the light scattering detection seems to be a very promising way to characterize the MW of ion-containing PEMs.

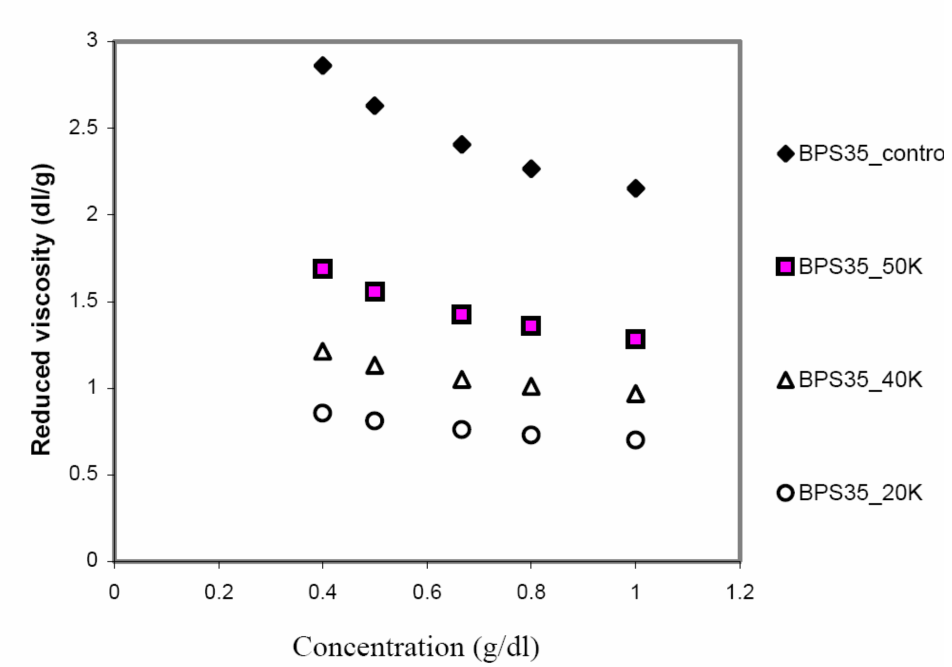

Figure 66. Concentration dependence of reduced viscosity of BPS35 in salt-free NMP

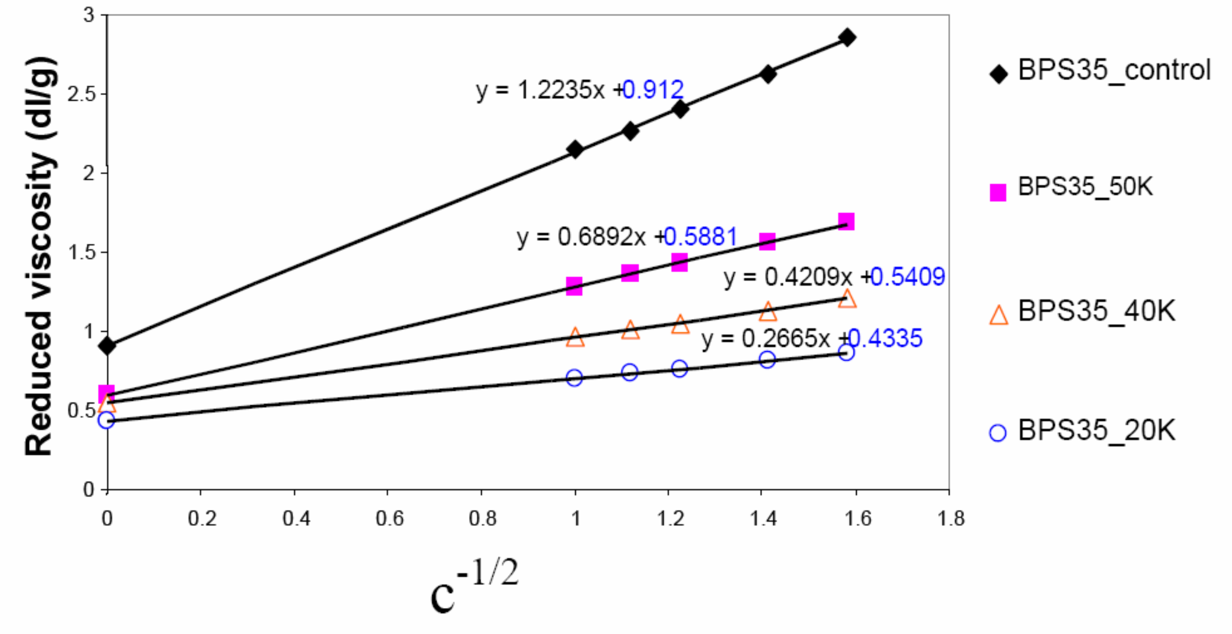

Figure 67. η_{red} versus c$^{-1/2}$ of BPS35 solutions in salt-free NMP

Conclusions

Intrinsic viscosity measurements of BPS35 with different molecular weights were conducted in NMP with different concentration levels of LiBr. The salt (LiBr) was used to shield the polyions from intramolecular expansion and afforded linear plots. For salt-free BPS35 solutions, the viscometric behavior is shown to fit well with the Liberti-Stivala equation.

References

(1) Wang, F.; Hickner, M.; Kim, Y.S.; Zawodzinski, T.; McGrath, J.E.; *J. of Membr. Sci*, **2002**, 197,231-242

(2) Hickner, M. A.; Ghassemi, H.; Kim, Y. S.; Einsla, B. A.; McGrath, J.E.; Alternative polymer systems for proton exchange membranes (PEMs), *Chem. Rev.*, **2004**, 104, 4587

(3) Wang, F.; Glass, T., Li, X.; Hickner, M.; Kim Y.S.; J.E. McGrath, *Polymer Preprint*, **2002**, 43(1), 492-493

(4) Cohen, J.; Priel, Z.; Rabin, Y.; *J. Chem. Phys*. **1988**, 88, 7111

(5) Yan, L.; Dougherty, T. J.; Stivala, S. S.; *J. Polym. Sci. Part A2*, **1972**, 10, 171

(6) Aldebert, P.; Gebel, G.; Loppinet, B.; Nakamura, N.; *Polymer*, **1995**, 36, 431-434

(7) Blagodatskikh, I. V.; Sutkevich, M. V.; Sitnikova, N. L.; Khokhlov. A. R.; *J. Chromatography A*, **2002**, 976, 155-164

DEVELOPMENT OF FUEL CELL BIPOLAR PLATES FROM GRAPHITE FILLED WET-LAY THERMOPLASTIC COMPOSITE MATERIALS

(Donald Baird and Jianhua Huang)

Introduction

The significant and growing interest in fuel cells for stationary power and transportation has been demonstrated by the attention these technologies are receiving from both government and industries, especially the automotive sector. As one of the key components of polymer electrolyte membrane (PEM) fuel cells, bipolar plates must have high electrical conductivity, sufficient mechanical integrity, corrosion resistance, low gas permeability, and low-cost as a result of both material selection and processing methodology if they are to be widely used in the automotive industry ([1]).

Historically graphite bipolar plates have been used in PEM fuel cells for space, military and other special applications. Graphite plates have good electrical conductivity, excellent corrosion resistance and a density lower than that of metal plates. The problems with graphite plates are their brittleness and porous structure, and the cost associated with machining the gas flow channels into the plates. In addition, post-processing (such as resin impregnation) is needed to make the plate impermeable to the fuel and oxygen ([2]). Because the material and manufacturing costs of the graphite plates are prohibitive for at least automotive applications, extensive efforts have been made to develop alternative materials and bipolar plates, including metallic and graphite-based composite bipolar plates. Materials for metallic plates include stainless steel, titanium, and aluminum with stainless steel being considered most promising for commercialization ([3]). Metallic bipolar plates usually have high bulk electrical and thermal conductivities, good mechanical properties and negligible gas permeability. New techniques such as continuous rolling or batch stamping have also been developed to facilitate the mass production of metallic bipolar plates. However, because metals have low corrosion resistance, a conductive and low-cost coating must be applied to the surfaces of the plates to form a protective layer, which has been found to be very difficult to accomplish ([3]). In addition, the weight of metal plates is a disadvantage, especially in transportation applications.

Graphite-based composite bipolar plates are made from a combination of graphite or carbon powder filler and a polymer resin with conventional polymer processing methods like compression molding or injection molding. They offer the advantages of lower cost, higher flexibility and greater ease of manufacturing than graphite plates. They are also light in weight compared to metallic and graphite plates. The gas flow channels can be molded directly into the plate, eliminating the need for the costly machining step. Both thermoplastic and thermosetting resins have been used to fabricate the plate ([4], [5]).

Ideally the composite plates should meet the following requirements:

- high electrical conductivity (DOE target ([5]): > 100 S/cm)
- good mechanical properties (PlugPower's targets ([7]): tensile strength > 41 MPa, flexural strength > 59 MPa, impact strength > 40.5 J/m (0.75 ft-lb/in); DOE target ([5]): crush strength > 4200 kPa)
- thermal stability at fuel cell operating temperature (-40 to 120°C for fuel cell driven vehicles)

- chemical stability in the presence of fuel, oxidant and product water, which may be slightly acidic (down to PH 4) (DOE target ([5]): corrosion $< 16\ \mu A/cm^2$)
- low permeability to fuel and oxidant (DOE target ([5]): H_2 permeability $< 2\times10^{-6}\ cm^3/cm^2$-sec)
- low thermal expansion
- high thermal conductivity (PlugPower's target ([7]): >10 W/m-K)
- rapid processability

Thermoplastic resins such as polyvinylidene fluoride (PVDF), liquid crystalline polymer (LCP), poly(phylene sulfide) (PPS), and thermosetting resins such as phenolics, epoxies and vinyl esters have been used in fabricating composite bipolar plates ([5]). In all cases, excessive carbon or graphite fillers (> 60 wt%) have to be incorporated into the composite to meet the minimum requirement on electrical conductivities. Some typical conductivity values reported for polymer/graphite materials are 100 S/cm in the in-plane direction and 20 S/cm in the through-plane direction. Various mechanical properties (flexural, tensile and impact strength, et al.) have been reported for composites which depend on the type of polymer resins and reinforcing fibers used, but all composites fail to meet the industrial target values as mentioned above. In fact, the mechanical strength of the bipolar plate is more important than originally believed. If the material is tough enough, a thinner plate and higher stack compaction pressure can be used to reduce the bipolar plate resistance and interfacial resistance within the stack, and, thus, improve the performance of the fuel cells. The weight and volume of the fuel cells (very important for use in vehicles) would also be reduced accordingly. The problem is, it is difficult to increase the electrical conductivity and mechanical properties further for polymer composite plates.

Recently researchers at Oak Ridge National Laboratory (ORNL) developed carbon/carbon composite bipolar plates and claimed that the plates had high electrical conductivity and excellent physical properties ([8]). The manufacturing process consists of multiple steps, including the production of carbon fiber/phenolic resin preforms (by slurry-molding process) followed by compression molding, and the pyrolysis and densification by a chemical vapor infiltration (CVI) process. The technology was reportedly under scale up by Porvair Fuel Cell Technology. However, the process is likely too complicated and costly to be applied in civil applications such as automotive.

In 1997, a new technology for making conductive materials was reported by Tucker et al ([9]). They made wet-lay sheet materials (mats consisting of graphite particles, thermoplastic fibers and glass or carbon fibers) using a slurry-making process and then compression molded them to form conductive composite plaques. The composites containing 50 wt % graphite, 10 wt % glass, and 40 wt % PET were reported to have a volume electrical conductivity of 100 S/cm and tensile strength of 51 MPa. The objective of this work is to determine whether the wet-lay sheets can be used to form bipolar plates with well-defined gas flow channels by mean of compression molding and whether the plates will exhibit high through-plane electrical conductivity and mechanical toughness required for bipolar plates.

Experimental

Production of wet-lay composite sheet materials

Wet-lay sheets containing graphite particles, thermoplastic (PPS or PET) fibers, and carbon or glass fibers were generated with a slurry making process on a Herty papermaking machine donated by DuPont. First the cut thermoplastic fibers were mixed with water, and the suspension was agitated in a pulper for 10 minutes. The cut carbon fibers and graphite particles were added next and mixed for about 3-6 minutes. The slurry was then diluted with re-circulating water and fed to the forming box of the machine at a constant rate. The collected sheet material was then conveyed through an oven set at the melting point of the thermoplastic fibers to evaporate the water and partially melt the thermoplastic fibers. The porous sheet materials were then rolled for later use.

Compression molding of wet-lay composite plates

Direct molding. The sheets were cut according to the mold size and stacked in the mold. The assembly was then placed in a hydraulic press and pressed at 270 ~ 285°C for PET based composites and 305~310°C for PPS based materials for about 10 minutes. The typical pressure used was 6.89 MPa (1000 psi). The platen heaters were then turned off and the mold was allowed to cool. The pressure was maintained until the mold temperature reached 30°C and then the platens were released. The assembly was then removed from the press and the flat plaque or bipolar plate was removed from the mold. It should be noted that this is not the process envisioned for commercialization. Heating by the means of induction will be used for this purpose.

Wet/Dry lay. The approach is similar to direct molding except that additional graphite particles (TIMREX provided by Timcal America Inc) were added and sandwiched between porous sheet materials before they were stacked in the mold. As a result, the compression-molded plates had a graphite loading higher than the wet-lay sheet materials.

Skin-core laminate. This method was the same as the direct molding or wet/dry lay process mentioned above, except that the wet-lay sheet stacks were covered with a mixture of poly(vinylidene fluoride) (Kynar 761 provided by Atofina Chemicals) and graphite particles before the mold was closed. The molded plates, thus, had a skin layer formed by poly(vinylidene fluoride)/graphite mixture and a core layer the same as that made from wet-lay sheets through direct or wet/dry lay molding.

Measurement of in-plane electrical conductivity

The in-plane bulk conductivities were measured according to ASTM Standard F76-86. The test method A (for Van der Pauw specimens) or B (for parallelepiped specimens) of the standard was used in accordance with the sample shapes. In case that the samples were circular or square plaques (Van der Pauw specimens), the sheet resistance, R_S, was obtained from the two measured characteristic resistances R_A and R_B by numerically solving the Van der Pauw equation:

$$\exp(-\pi R_A/R_S) + \exp(-\pi R_B/R_S) = 1 \qquad (1)$$

The resistivity, ρ, is given by $\rho = R_S d$, where d is the thickness of the specimen. The volume conductivity σ, is $1/\rho$. For samples cut from a compression-molded plaque with size of 76.2 mm by 76.2 mm by 2 mm, test method B was used. The measurement was made for each specimen in the following way. The current contacts covering the entire end of the specimen were connected to a DC source to allow a constant current to pass through the specimen. The voltage drop was measured across the specimen with a Keithley 2000 digital multi-meter. The conductivity values for eight specimens were then averaged to give the final conductivity value of the sample. All specimens were tested at ambient conditions.

Measurement of through-plane electrical conductivity

The through-plane conductivities were measured based on the method proposed by L. Landis and J. L. Tucker with some modifications ([10]). A 25.4 mm by 25.4 mm composite sample was cut and placed between two gold-plated copper test electrodes. Between the electrode and sample a graphite diffusion layer (GDL) paper was added to improve electrical contact of the sample with the electrode. The test cell was placed under pressure to simulate conditions more similar to those in a fuel cell. The system was initially preconditioned at a pressure of 10.3 MPa (1500 psi) for three cycles, then the resistance of the test cell was measured five times at 6.89 MPa (1000 psi) and the average value calculated. The sample was removed, and the resistance of the test cell (including GDL papers) was measured again under the same condition to obtain the “base” resistance. Subtracting the base resistance from the total gave the sample resistance. The resistivity or conductivity of the sample was determined by the following equation:

$$\rho = R_S A/L = (R_T - R_B)A/L \qquad (2)$$

$$\sigma = 1/\rho \qquad (3)$$

where ρ is resistivity, A is the cross-sectional area of the sample, L is the thickness of the same, R_T, R_B and R_S are total resistance, baseline resistance and sample resistance, respectively.

Measurement of mechanical properties

The tensile and flexural (three-point bending) tests were performed on an Instron 4204 Tester at room temperature (23°C) in accordance with ASTM D638 and D790 standards, respectively. The specimen sizes were 76.2×7.7×2.0 mm (L×W×T) for the tensile test, and 76.2×12.7×3.2 mm for the flexural test. The thickness of the samples was about 2 mm. The Izod impact test (unnotched) was performed on a Tinius Olsen 92T Impact Tester based on ASTM D-256. The sample had a size of 64.0×12.7×3.3 mm. Dynamic mechanical properties of the wet-lay composite as a function of temperature were measured on a Rheometrics RMS-800 at frequency of 10 rad/s and shear strain of 0.1%. The temperature scan was performed from ambient temperature to 250 °C with a heating rate of 2°C/min. The expansion of the sample during the test was recorded to evaluate the thermal expansion coefficient of the sample.

Measurement of half-cell resistance of the bipolar plates

To measure the half-cell resistance, an experimental apparatus similar to that used in the through-plane conductivity test was established. A single-sided bipolar plate with size of 12.1 cm × 14.0 cm × 0.32 cm and active area of 100 cm^2 was placed between two pieces of carbon paper (TORAY TGP-H-120), each of which was in contact with a gold-plated copper plate (current collector) on the opposite side. The size of carbon papers is 10 cm × 10 cm on the channel side and 12.1 cm × 14.0 cm on the flat side of the plate(this is actually a mono-polar plate). While a constant current (typically 250 mA) was passed through the current collectors, the potential drop between the collectors was measured. The half-cell resistance was then calculated based on Ohm’s law. The measurements were made with a one-ton load or 1.0 MPa (145 psi) on the channel side, a typical clamp pressure used in the actual PEM fuel cell stacks. The baseline of resistance, that is, the resistance of the testing circuit excluding the bipolar plate but including carbon papers and everything else, was measured every time after the testing of the plate. This was done to ensure the stability of the baseline of the instrument and to evaluate the contribution of the bipolar plate to the whole half-cell resistance.

Production of wet-lay composite materials and bipolar plates

The scheme for production of the wet-lay composite materials and bipolar plates is shown in Fig.68. The composition of the wet-lay composite sheet materials produced and used in this work is listed in Table 17. Note there are two kinds of PET based wet-lay

Table 17 Compositions of wet-lay composite materials.

Name	Polymer		Graphite			Reinforcement
	Wet-lay	Dry-lay	Wet-lay	Dry-lay	Total	
WDL-65	PET,40%		TC300, 50%	KS150	65%	Glass Fiber
WDL-65/F2G8	PET,40%	PVDF,20%	TC300, 50%	KS150	66.5%	Glass Fiber
WDL-75/F1G9	PET,40%	PVDF,10%	TC300, 50%	KS150	78%	Glass Fiber
PPS-TC70	PPS, 23%		TC300, 70%		70%	Carbon Fiber
PPS-KS70	PPS, 23%		KS150, 70%		70%	Carbon Fiber
PET-TC70	PET, 23%		TC300, 70%		70%	Carbon Fiber
PET-KS70	PET, 23%		KS150, 70%		70%	Carbon Fiber

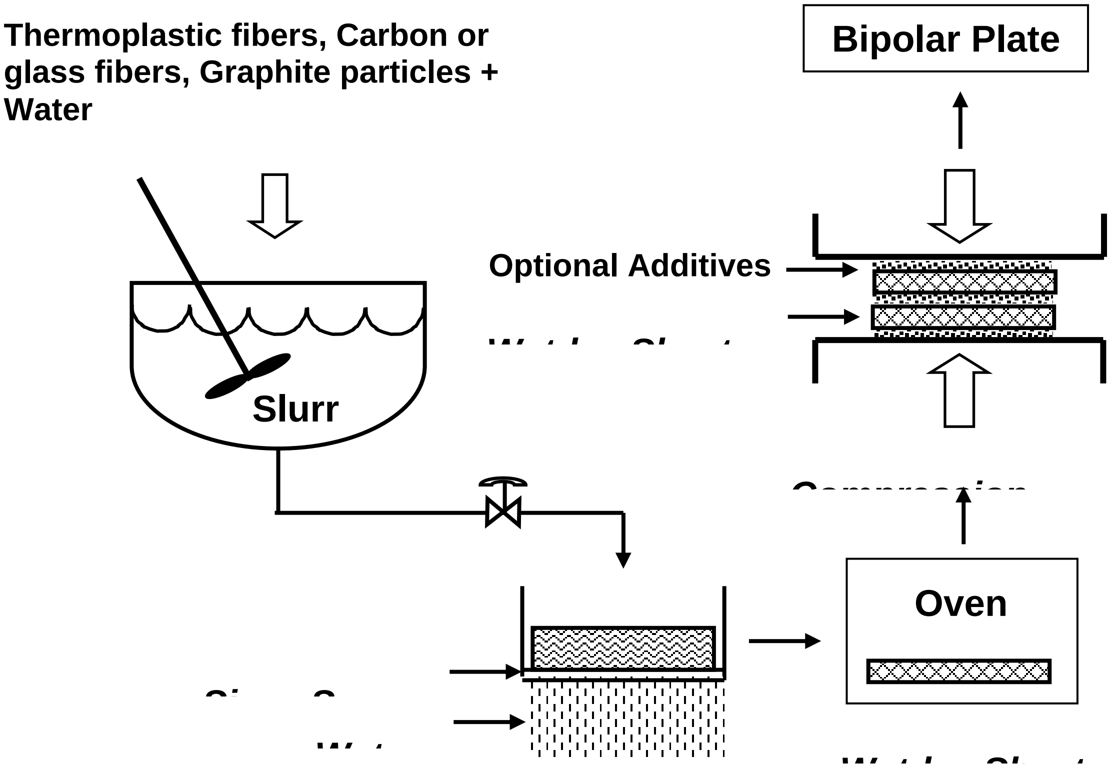

Figure 68 Schematic diagram of manufacture of wet-lay composite sheets and bipolar plates.

sheets used in this work. One is SC500 with fixed composition of 50 wt% graphite particles, 40 wt% polyester fibers and 10 wt% glass fibers which was a development grade material provided by DuPont. The other one as well as the all the PPS based wet-lay sheets were fabricated at Virginia Tech with a Herty papermaking machine donated by DuPont (see Fig.69). In the initial stage of this study, the SC500 wet-lay sheets were the only conductive wet-lay composites available to us and were, therefore, used to test the feasibility of using wet-lay sheets as bipolar plate materials. Because the SC500 sheets contain 50% graphite only, a dry-lay method was used to add more graphite to the porous sheets before the compression-molding process to increase the conductivity of the plate. The product was, therefore, called wet-dry lay composite or bipolar plate. While PET may not be an ideal matrix for bipolar plate applications in the fuel cell environment, our preliminary result showed that the wet-lay composites could be very promising materials for producing bipolar plates. We then turned our attention to the modification of the PET based material to address the hydrolysis issue of polyesters, and the production of a new wet-lay composite with more stable polymers.

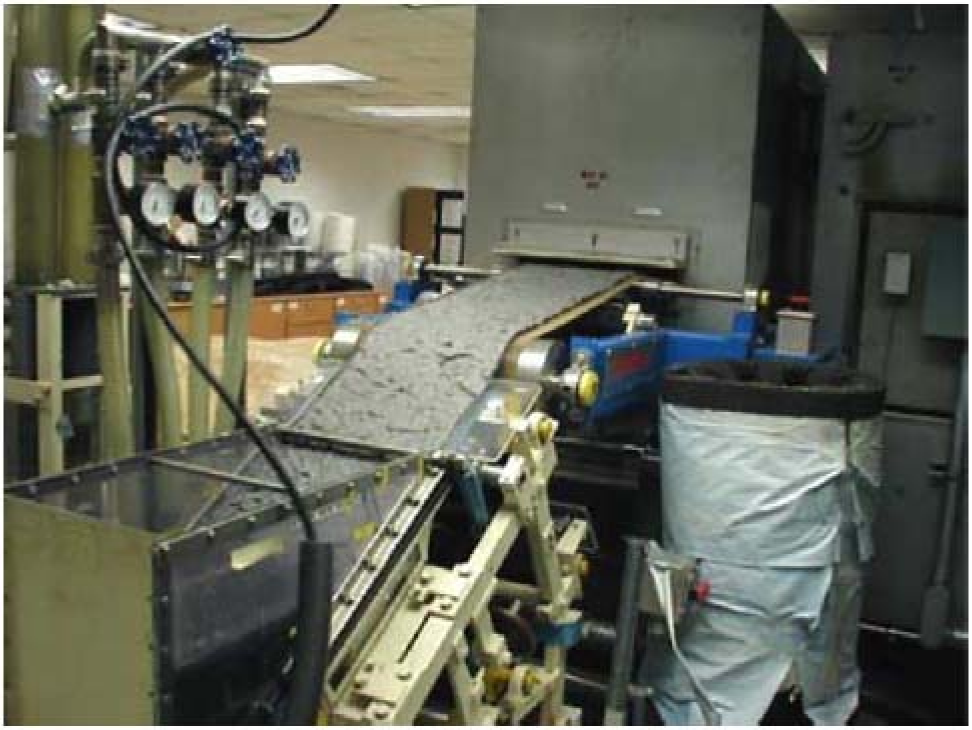

Figure 69 Picture showing the manufacture of wet-lay sheets on a Herty papermaking machine.

The effort to address the hydrolysis of the PET composite lead to the finding that a mixture of chemical resistant polymers and graphite particles could be used to form a protective layer for the PET based composite plate. The polymer to be used in the skin layer should meet a number of requirements, including excellent chemical resistance, moldable at a temperature matching that of PET (note: the PET-based wet-lay material is used in the core), excellent electrical conductivity after doped with graphite fillers, and formation of a composite with good adhesion at the interfaces. Considering that poly(vinylidene fluoride) (PVDF) has these properties([11]), as well as a broad processing temperature range (from 175°C to above 300°C ([12])) that overlaps with the molding temperature of PET, we chose Kynar 761, a powder form of PVDF produced by Atofina Chemicals for the skin layers. The processing and compression molding conditions for laminate bipolar plates are basically the same as the wet/dry lay composite plates as was described above.

An alternate thermoplastic used in making the wet-lay composite sheets is polyphynelesulfide, PPS, fibers. PPS is a semi-crystalline polymer with a melting point of 280°C and a high degree of chemical resistance. It is generally regarded as second only to polytetrafluoroethylene (PTFE) in overall chemical resistance ([13]). The superior chemical resistance of PPS, coupled with excellent mechanical properties, dimensional stability, and high temperature resistance, makes it one of the ideal matrices for the composite bipolar plates.

To make composite bipolar plates with gas flow channels molded into the plate, the composite material must have good formability. This is because the flow channels in bipolar plates are usually densely spaced, and are narrow and relatively deep (say 0.8 mm or 1/32 inch in width and depth). For the wet-lay composite sheets, we needed to know whether they were deformable enough in the compression molding process to form the channels and other features of the bipolar plates. If not, the flow channels would have to be machined instead of molded. To evaluate the formability of the wet/dry lay composite, we designed and fabricated a standard (7-channel) bipolar plate mold and used it in the compression molding process. In Fig.70 are presented the compression-molded bipolar plates produced with this mold and wet-lay composite materials(We note that these are really mono-polar plates as the channels have been molded into one side of the plate initially). It can be seen that the composites could be molded to form well-defined gas flow channels. The formability of the wet-lay composites is good enough to produce bipolar plates with good shape and definition. In addition, these materials have the potential to be rapidly heated and molded by means of the compression molding process. The detail of the fabrication scheme will be described in a later paper.

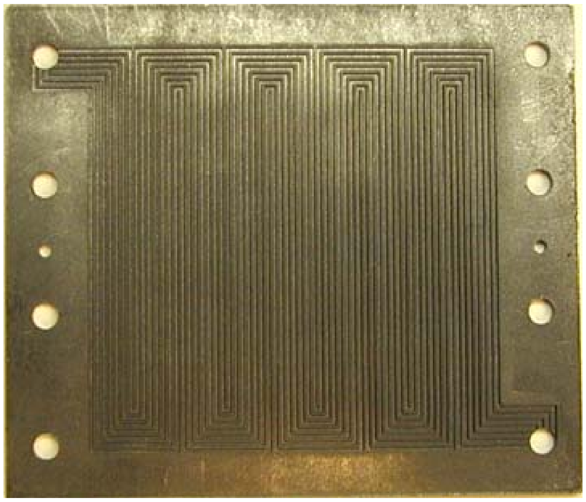

(A)

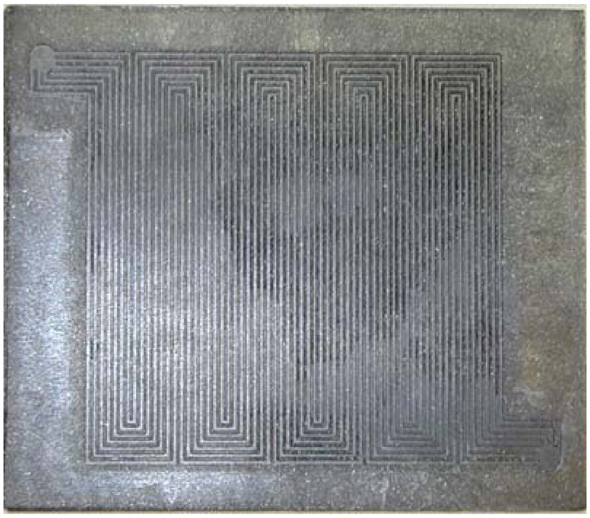

(B)

Figure 70 Pictures of compression-molded composite bipolar plates (single-sided) from PET (A) and PPS (B) based wet-lay composite sheets.

Electrical conductivity of wet-lay composite materials

Electrical conductivity is one of the most important properties of bipolar plates. Moreover, it is important to realize that the graphite filled polymer plates may have different properties and performance in different directions. More specifically, if the length direction of the plate is designated as X, the width direction as Y, and the thickness direction as Z, then the properties in the X-Y plane and along the Z direction (the same as the compaction direction of the compression molding in general) may be quite different. A measurement made in and through the X-Y plane is, therefore, needed to evaluate the properties of the plate comprehensively. Technically, the measurement of through-plane conductivity is difficult to obtain compared to the in-plane conductivity measurement. This is probably why the earlier literature reported the in-plane conductivity of the bipolar plates only. In fact, because the electrons need to pass through the bipolar plate, the through-plane conductivity is obviously more important than the in-plane conductivity for a bipolar plate.

In Fig.71 are presented the bulk conductivities (in-plane and through-plane) of wet-lay composite materials. Most of the plates have in-plane conductivities higher than 200 S/cm, well exceeding the DOE target value (100 S/cm) for composite bipolar plates ([5]). The values are also higher than those of the other polymer composite bipolar plates with similar graphite loadings (see Table 18). It is noted that the carbon/carbon composite bipolar plates developed by the Oak Ridge National Laboratory have an electrical conductivity of 200~300 S/cm ([8]). However, because they must use pyrolysis and CVI (Chemical Vapor Infiltration) processes (which represent over 70 percent of total cost of C/C plates ([8])) in making the bipolar plates, one should be able to manufacture the wet-lay bipolar plates at much less cost compared to the carbon/carbon bipolar plates.

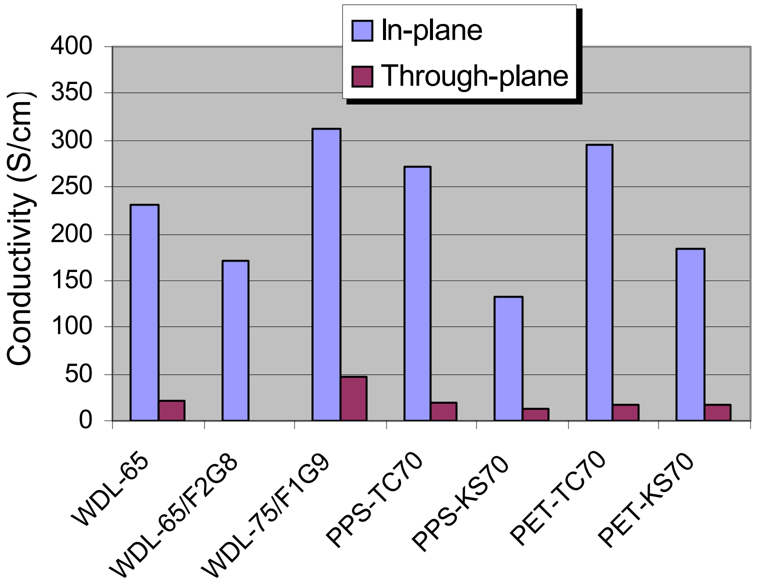

Figure 71 Electrical conductivity of wet-lay composite materials.

Table 18 Properties of polymer composite bipolar plates.

Manufacturer	Polymer	% Graphite + Fibers	Conductivity (S/cm)		Mechanical Strength	
			In-plane	Through-plane	Tensile (MPa)	Flexural (MPa)
GE[11]	PVDF	74	119			36.2
GE[14]	PVDF	64 + 16 CF	109			42.7
LANL[15]	Vinyl Ester	68	60		23.4	29.6
Premix[15]	Vinyl Ester	68	85		24.1	28.2
BMC[15]	Vinyl Ester	69	30		26.2	37.9
Commercial[15]			105		19.3	20.7
BMC 940[16]	Vinyl Ester		100	50	30.3	40.0
Plug Power[7]	Vinyl Ester	68	55	20	26.2	40.0
DuPont[17]				25-33	25.1	53.1
SGL[18]			100	20		40.0
H_2Economy[19]			67			29.4
Virginia Tech[20]	PET	65 + 7 GF	230	18-25	36.5	53.0
Virginia Tech	PPS	70 + 6 CF	271	19	57.5	95.8

Also included in Fig. 71 are the through-plane conductivities of the wet-lay composites. It is apparent that the through-plane conductivities for all wet-lay composites are significantly lower than the in-plane conductivities. This difference was also observed for other compression molded bipolar plates (see Table 18). The degree of the anisotropy is, however, not as high as what we saw for the wet-lay composites. This might be attributed to the following possible factors. First, the graphite particles may orient in a plane perpendicular to the direction of the compaction force during molding. This possibility exists in all polymer/graphite systems as long as the aspect ratios of the graphite particles are not unity. Second, when forming the wet-lay sheet materials, the thermoplastic fibers and reinforcing fibers will orient in the sheet plane direction (perpendicular to the thickness direction) and might induce the graphite particles to orient in the same way. Third, the graphite particles used in the wet-lay may have a higher aspect ratio than that used in other composite plates. It is believed that for compression-molded composite bipolar plates, the higher the aspect ratio of the graphite used, the greater the ratio of in-plane to through-plane conductivities. This might also explain the fact that PPS-70TC, the wet-lay composites with TC300 graphite (with greater aspect ratio), have a higher ratio of in-plane to through-plane conductivities compared to PPS-70KS, the one with KS150 graphite (with smaller aspect ratio) (see Fig.71). Fig.71 also shows that the PPS-70TC and PPS-70KS wet-lay composites have similar through-plane conductivities. This suggests that although the use of more spherically shaped graphite could reduce the in-plane to through-plane conductivity ratio, it might not necessarily help in improving the through-plane conductivities of the composites. This matter is, however, subject to further investigation.

Mechanical properties of wet-lay composite materials

In addition to the electrical conductivity, the bipolar plates should also have adequate mechanical properties to be used in the fuel cell stacks. For example, the target values for flexural, tensile and impact strengths are 59 MPa, 41 MPa and 40.5 J/m, respectively ([7]).

However, for polymer composites doped with conductive particles or fibers, it is difficult to get high conductivity and sufficient mechanical properties at the same time. As a result, the mechanical properties (such as flexural, tensile and impact strengths) of composite bipolar plates available today are still significantly lower than the target values (see Table 18).

In Fig.72 are presented the tensile and flexural strength of wet-lay composite plates. The flexural and tensile strengths of all wet-lay composites are higher than those of other polymer composite plates with the same or similar graphite loadings. Among these wet-lay composites, the PPS based composites have the best mechanical properties, with both flexural and tensile strengths being significantly higher than PlugPower's target values. If a comparison is made between PPS based wet-lay composites with different graphite particles, one can find that the one with KS150 graphite has higher strength and modulus. This may be attributed to the fact that the dispersion of KS150 graphite in the composite is better than that of TC300 graphite. For the skin-core laminate composite materials, because the skin layers consisting of PVDF and graphite are not as strong as the PET based wet/dry lay materials (core material), lower mechanical properties are expected for the laminate composite compared to the wet/dry lay composite. From Fig.72 one can see that the skin-core composites do lose some tensile strength. For flexural properties, however, no degradation in flexural strength is observed after the skin layer was added. This result suggests that a skin layer of 10 to 20% of the plate thickness has only minor, if any, influence on the mechanical properties of the composite materials.

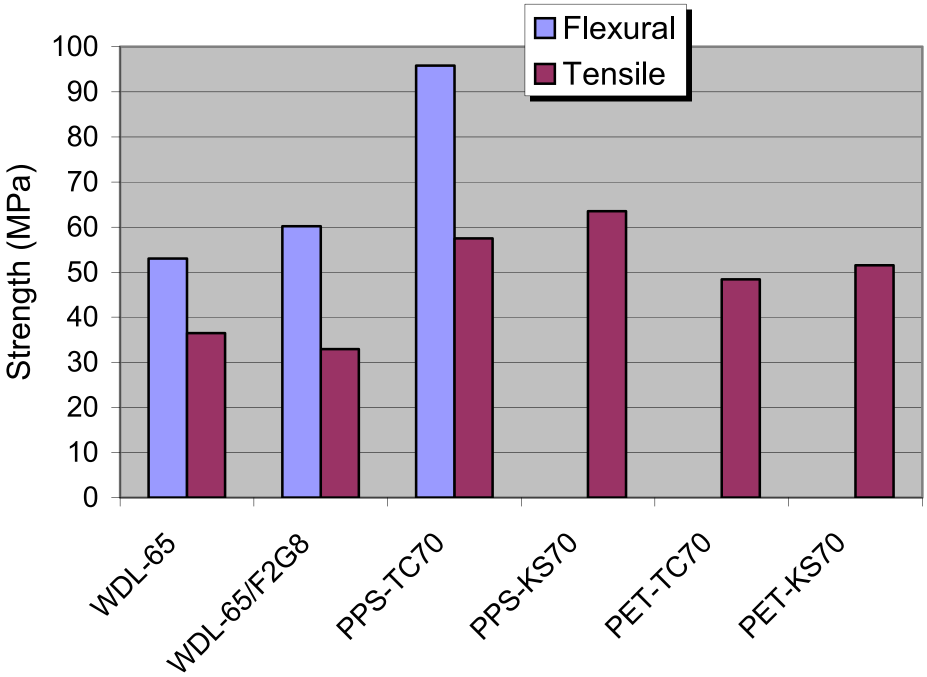

Figure 72 Tensile and flexural strength of wet-lay composite materials.

The skin-core wet-lay composite plate has advantages over the composite plate consisting of PVDF (Kynar) and graphite (the same components used in the skin layers) only ([11]). As can be seen from Table 19, the Kynar/graphite composite (26/74) developed by GE has an electrical conductivity of 119 S/cm and flexural strength of 37.2 MPa. After carbon fiber was used (Kynar/graphite/carbon fiber = 20/64/16), the flexural strength rose to 42.7 MPa while the electrical conductivity decreased to 109 S/cm ([14]). In comparison, our skin-core composite plate has higher electrical conductivity and mechanical properties. In addition, the laminate composites should have a lower raw material cost, as the price of PET is much lower than that of PVDF.

Table 19 Property comparisons for composite bipolar plates.

Binders	Fillers, Wt%	In-plane Conductivity (S/cm)	Flexural Strength (MPa)	Source
KYNAR	74% Graphite	119	37.2	US 4,214,969
KYNAR	74% (Graphite+CF)	109	42.7	US 4,339,322
KYNAR+PET	66.5% Graphite Skin/Core=10/90 Kynar/Graphite=20/80	171	60.2	Present work
KYNAR+PET	68% Graphite Skin/Core=20/80 Kynar/Graphite=20/80	163	54.4	Present work

It is noted that Besmann et al. ([8]) reported a flexural strength of 175 MPa for their carbon/carbon plates. However, because the property was obtained by means of a biaxial flexure test, not the standard three-point flexure as defined by ASTM D790, it is difficult to compare their results with other reported strength data.

The wet-lay composite bipolar plates have also excellent impact strength. In Fig.73 is presented the Izod impact strength (unnotched) of the PPS-TC70 composite plate. The value is two times higher than the target value, five times higher than that of Plug Power's plates ([7]) and over ten times higher than that of the DuPont's plates ([17]). These are the only companies who reported impact strength data for their plates.

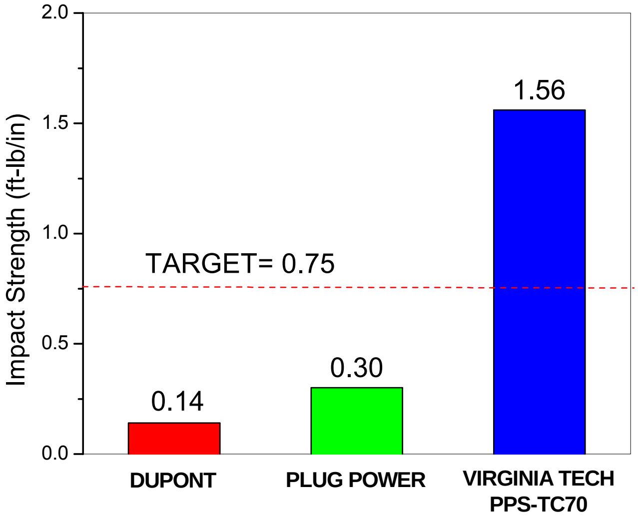

Figure 73 Impact strength (unnotched) of composite bipolar plates.

It is not clear why the wet-lay composite plates have such excellent mechanical properties. One possible answer could be the unique structure of the wet-lay sheet materials. Traditionally, for making polymer composite bipolar plates, the thermoplastics in powder form were used to allow for more uniform blending with the graphite particles or other fillers and then used in compression molding. Although these polymer particles might bind the whole composite together after being heated and compression-molded, there are actually weld lines everywhere inside the composite. The situation is worse considering that a relatively low molding temperature has to be used to get as high electrical conductivity as possible. This is why most of the graphite composite bipolar plates, including those containing carbon fibers ([14]) or glass and graphite fibers ([1]), have inadequate mechanical properties. In contrast, the wet-lay composite materials have a much different structure. The base materials for compression molding are porous sheets consisting of fine thermoplastic fibers and reinforcing fibers. The web-like structure makes the molded composites much stronger than that made from the mixture of the graphite and thermoplastic powders. In addition, the reinforcing fibers (carbon or glass fibers) with length of 2.54 cm can be used in the wet-lay process without any difficulties. The use of carbon fiber reinforced PPS makes the composite even stronger.

Thermo-mechanical properties

In Fig.74 is presented the dynamic mechanical properties of the wet-lay composite materials as a function of temperature, from which the thermo-mechanical properties of the material can be estimated. At 80°C (a typical running temperature for PEM fuel cells), the PPS-TC70 the wet-lay composite has a value of G' of 6.43 GPa, which is about 97% of that at ambient conditions (6.63 GPa). Even at 150°C, the composite still retains 57% of G' at room temperature. PlugPower has reported a storage modulus (flexural or three-point bending) of 5.51 GPa at 150°C for their bipolar plate, whereas their target is 8.27 GPa. Because the magnitude of the flexural modulus is typically three times as large as that of the shear modulus, our bipolar plate at 150°C should have a flexural modulus of over 11 GPa, which is significantly higher than PlugPower's target values.

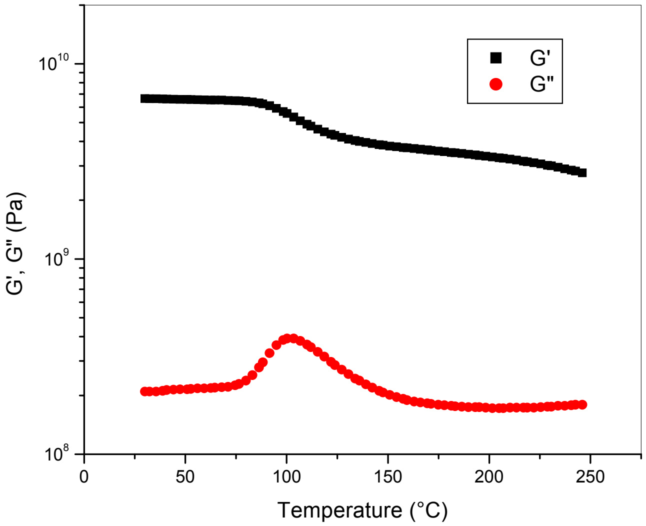

Figure 74 Dynamic mechanical properties of PPS based wet-lay composite materials as a function of temperature at frequency of 10 rad/s.

From DMTA (dynamic mechanical temperature analysis) testing, the thermal expansion (ΔL/L) of the sample as a function of temperature can be obtained at the same time. The thermal expansion coefficient can be determined from the ΔL/L–T plot. The result indicates that the composite has a low thermal expansion coefficient (5.23×10^{-5} cm/cm·°C at 80°C), as does the pure PPS polymers ($4.9 \sim 5.9 \times 10^{-5}$ cm/cm·°C at 20°C). This is also an advantage of the PPS based composite bipolar plates, as a low thermal expansion coefficient is desired for bipolar plates ([3]).

Half-cell resistance of wet-lay composite bipolar plates

While electrical conductivities (in and through-plane) are important in characterizing the materials used in the manufacture of bipolar plates, the performance of the bipolar plate itself is needed. Due to the differences in the molds and the polymer flow patterns, the compression molded bipolar plates may have properties quite different from those of the flat plate test specimens. In addition, the contact resistance between bipolar plates and gas diffusion layers (GDL) also contribute to the total resistance. To evaluate these important properties of the bipolar plates, a test termed the half-cell resistance test was found to be useful. In Fig. 75 is presented the configuration we used in the test. The method is similar to that reported by others, except that the baseline resistance (i.e. the resistance of testing circuit excluding the bipolar plate but including carbon papers and anything else) test is performed following half-cell testing. The test of baseline resistance was found important because the contact resistances between current collector (such as gold plated copper plates) and carbon papers (usually inserted between the collector and bipolar plate) could differ dramatically depending on the specific collectors used.

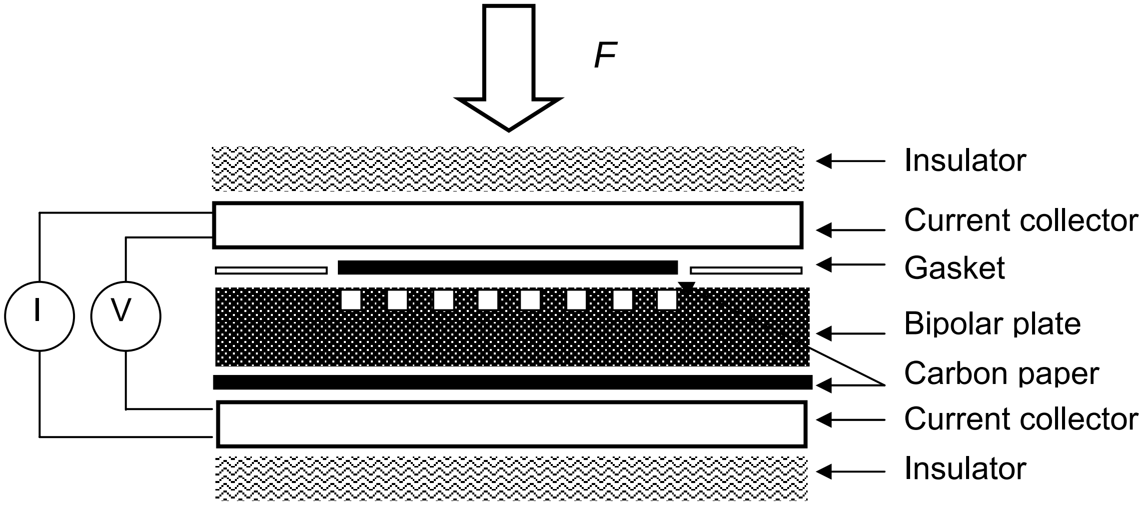

Figure 25 Schematic diagram of testing cell used in the half-cell resistance measurement.

In Fig.76 are presented the half-cell resistances of the wet-lay composite bipolar plates and the corresponding baseline resistances. The data for the POCO AXF-5Q graphite plate (with the same design and geometric size) are also included for comparison. It can be seen that, while the baseline resistances in all cases are almost the same (about 0.01 Ω-cm^2), the bipolar plates made from different materials have much different half-cell resistances. The PPS based wet-lay composite plate (PPS-TC70) and PET based one (WDL-65) have similar half-cell resistances (~ 0.039 Ω-cm^2). The resistance of the plates is, thus, close to 0.029 Ω-cm^2). Comparatively, the POCO graphite plate has a much lower half-cell resistance (about 1/3 of the wet-lay composites). Considering the baseline resistance, the resistance of the graphite plate is more than 10 times smaller than that of the composite plates. This is reasonable considering the large difference in the through-plane conductivities of the materials (about 680 S/cm for graphite vs. 20 S/cm for wet-lay composites). Obviously, the electrical conductivity of the composite bipolar plates is not as good as the graphite plate. Improvement of the through-plane conductivity of the wet-lay composites is needed.

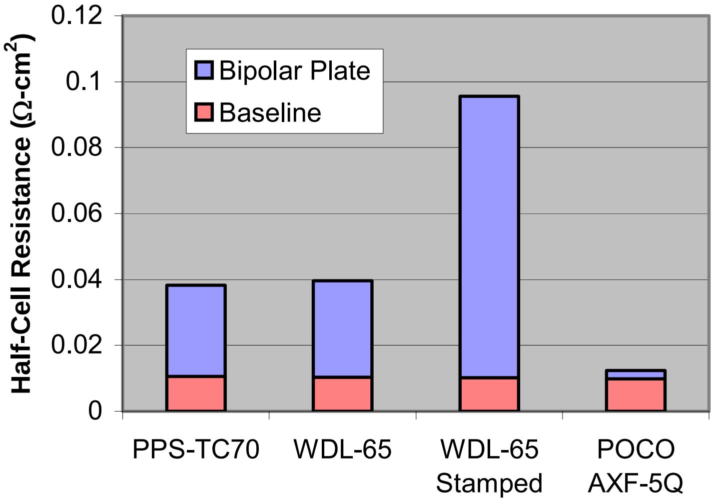

Figure 76 Half-cell resistance of bipolar plates at room temperature (23°C).

Fig.76 also shows the half-cell resistance of the compression molded wet-lay composite plate labeled as WDL-65S. The plate was made in two steps. First, a flat panel was compression-molded from a stack of porous wet-lay sheets. The flat panel was then used in compression molding (stamping with the bipolar plate mold) to form a single sided bipolar plate. It was found that the plate had also a good shape and high definition gas flow channels and looked as good as the directly molded WDL-65 plates (refer to Fig.3). However, this result showed that the molded and then stamped plate had a higher resistance compared to the conventional plates. This may be attributed to the fact that in the stamping process, the flowability of the graphite particles is lower than that of molten polymers in the composite, resulting in the formation of resin-rich zones or layers in the rib area of the bipolar plate. This may be an issue which will have to be addressed when one tries to develop a commercial fabrication process for the bipolar plates.

There are reports showing that the half-cell resistance or the fuel cell *I-V* (current-voltage) performance of the composite plates could be very close to that of the graphite bipolar plates even though the composite has a through-plane conductivity significantly lower than that of the pure graphite (see for example ref. [22] & [23]). This fact seems to suggest that the composite plates actually have performances close to the graphite plate. This may not be true, however. For example, Cho et al. ([22]) found that, under a pressure of 180 N/cm^2, their pure graphite, composite A and composite B, plates have half-cell resistances of 30.2, 31.7 and 33.4 mΩ-cm^2, respectively, while the bulk conductivities of the plates are 593.5, 76.3 and 66.0 S/cm. They attributed these results to the fact that by compressing the carbon composites, carbon powders formed a compact network of carbon powders. However, we believe that the results are related to the high baseline resistance. Theoretically, the graphite plate and composite plate (with bulk resistance much higher than that of graphite) could have similar half-cell resistance when the baseline resistances are different, or the baseline resistances are much higher than the bulk resistance of the composite plate. In the latter situation, the baseline resistance is so large that the difference between bulk resistances of graphite and composite plates is nearly negligible.

Therefore, the similarity in half-cell resistances does not necessarily mean the performance (in conducting electricity) of the bipolar plates is similar. It can, thus, be concluded that it makes little sense to compare half-cell resistances of bipolar plates without the baseline information. Even if the baselines are the same, the magnitude of baselines is also needed to make a proper judgment. The same issue should also exist in the fuel cell test, especially the single cell test in which the ratio of baseline and half-cell resistances is probably greater than that of the stacks. Effort should be made to measure the baseline or contact resistance between the current collector and GDL papers.

Conclusions

This work shows that graphite filled wet-lay composite sheets may be used to produce bipolar plates with high electrical conductivity, high corrosion resistance, excellent mechanical properties, and potentially rapid manufacturability. The sheets consisting of graphite particles, thermoplastic fibers and reinforcing fibers are generated by means of a wet-lay process and are highly formable. The porous sheets together with optional additives are then stacked and compression molded to form bipolar plates with gas flow channels. The use of the wet-lay composite in the formation of bipolar plates has multiple advantageous. First, it increases in-plane conductivities of the composite plate significantly while maintaining the through-plane conductivity. Second, it dramatically increases the mechanical properties of the composites. The PPS based composite bipolar plate is the first polymer composite bipolar plate that meets industrial requirements (targets) for tensile, flexural and impact strengths. Third, one can use different components including polymers, graphite particles and reinforcement for the core and outer layers of the plate, respectively, and optimize the properties and/or reduce the cost of the plate. Moisture sensitive polymers like PET can be used for bipolar plates as long as a chemically stable polymer is used to form a protective layer. The half-cell resistances of the wet-lay composite plates were also determined to evaluate the performance of the plates. It is pointed out that the measurement of the baseline resistance is important in interpreting the half-cell resistances of bipolar plates. The through-plane conductivity (around 20 S/cm) and half-cell resistance of the bipolar plate indicate that the through-plane conductivity of the material needs some improvement.

References

[1] D. Busick, M. Wilson, in: D. H. Doughty , L. F. Nazar, M. Arakawa, H. Brack, K. Naoi (Eds.), New Materials for Batteries and Fuel Cells, Materials Research Society Symposium Proceedings Vol. 575, Materials Research Society, Pennsylvania, 2000, pp. 247-251.

[2] G. Hoogers, in: G. Hoogers (Ed.), Fuel Cell Technology Handbook, CRC Press, Boca Raton, Fla. 2003, pp.(4-21)-(4-23).

[3] J. Wind, A LaCroix, S. Braeuninger, P. Hedrich, C. Heller, M. Schudy, in: W. Vielstich, H. A. Gasteiger, A. Lamm (Eds.), Handbook of Fuel Cells – Fundamentals, Technology and Applications Vol. 3: Fuel Cell Technology and Applications, Wiley & Sons, New York, 2003, pp.294-307.

[4] G. O. Mepsted, J. M. Moore, in: W. Vielstich, H. A. Gasteiger, A. Lamm (Eds.), Handbook of Fuel Cells – Fundamentals, Technology and Applications Vol. 3: Fuel Cell Technology and Applications, Wiley & Sons, New York, 2003, pp.286-293.

[5] K. Robberg, V. Trapp, in: W. Vielstich, H. A. Gasteiger, A. Lamm (Eds.), Handbook of Fuel Cells – Fundamentals, Technology and Applications Vol. 3: Fuel Cell Technology and Applications, Wiley & Sons, New York, 2003, pp.308-314.

[6] D. Haack, R. Torre, K. Butcher, in: "Fuel Cell Technology: Opportunities and Challenges", Topical Conference Proceedings, 2002 AIChE Spring National Meeting, New Orleans, LA, March 10-14, 2002, pp.454-459.

[7] J. G. Clulow, F. E. Zappitelli, C. M. Carlstrom, J. I.L. Zemsky, D. N. Busick, M. S. Wilson, in: "Fuel Cell Technology: Opportunities and Challenges", Topical Conference Proceedings, 2002 AIChE Spring National Meeting, New Orleans, LA, March 10-14, 2002, pp.417-425.

[8] T. M. Besmann, J. W. Klett, J. J. Henry, Jr., E. Lara-Curzio, J. Electrochem. Soc., 147 (2000) 4083-4086.

[9] K. W. Tucker, G. P. Weeks, US 5,614,312 (1997).

[10] L. Landis, J. L. Tucker, R&D Magazine, October 2002, pp 36-38.

[11] R. J. Lawrance, US 4,214,969 (1980).

[12] Kynar® and Kynar Flex® PVDF Technical Brochure, Elf Atochem North America, Inc.

[13] J. W. Gardner, P. J. Boeke, in: Rubin I I (Ed.), Handbook of Plastic Materials and Technology, Wiley, New York, 1990, p. 423.

[14] E. N. Balko, R. J. Lawrance, US 4,339,322 (1982).

[15] M. S. Wilson, D. N. Busick, US 6,248,467 (2001).

[16] http://www.fuelcell-info.com.

[17] http://www.dupont.com/fuelcells/pdf/plates.pdf.

[18] http://www.sglcarbon.com/sgl_t/fuelcell/products/bma5.html.

[19] http://www.h2economy.com/bp1.htm.

[20] J. Huang, D. G. Baird, Proceedings of ANTEC 2003, Nashville, TN, May 4-8, 2003, pp. 2151-2155.

[21] J. Huang, D. G. Baird, Proceedings of ANTEC 2004, Chicago, IL, May 16-20, 2004, pp.1405-1409.

[22] E. A. Cho, U. S. Jeon, H. Y. Ha, S. A. Hong, I. H. Oh, J. Power Sources, 125 (2004) 178-182.

[23] H. Kuan, C. M. Ma, K. H. Chen, S. Chen, J. Power Sources, 134 (2004) 7-17.

A Single Domain PEMFC Model Based on an Agglomerate Catalyst Geometry (Nathan Siegel, Michael Ellis, Doug Nelson, and Michael von Spakovsky)

Introduction

A steady two-dimensional computational model for a proton exchange membrane fuel cell (PEMFC) is presented. The model accounts for species transport, electrochemical kinetics, energy transport, current distribution, and water uptake and release in the catalyst layer. The governing differential equations are solved over a single computational domain, which consists of a gas channel, gas diffusion layer, and catalyst layer for both the anode and cathode sides of the cell as well as the solid polymer membrane. The model for the catalyst regions is based on an agglomerate geometry, which requires water species to exist in both dissolved and gaseous forms simultaneously within the catalyst layers. Data related to catalyst structure, which was required by the model, was obtained via a microscopic analysis of a commercially available MEA. The coupled set of differential equations is solved with a commercial computational fluid dynamics solver and is readily adaptable with respect to geometry and material property definitions.

Model Development – Catalyst Structure

A 5cm^2 MEA was purchased from ElectroChem from which cross-sections were prepared and analyzed with a scanning electron microscope (SEM), and a tunneling electron microscope (TEM)(1). The cross-sections for SEM analysis were prepared by three methods in order to evaluate which worked best. The first method involved freezing the sample in liquid nitrogen and fracturing it. This technique provided a clean section for viewing, but also caused the gas diffusion layer to de-laminate from the assembly. The second method was to simply cut the MEA at room temperature with a razor. The blade was pushed directly down on top of the MEA as opposed to cutting across it. This resulted in a clean section also, but there was some dragging of the polymer through the sample, as it is fairly malleable at room temperature. For the third method, the sample was frozen in liquid nitrogen and then cut as per the second method. This provided the best results of all.

The structure of the catalyst layer is shown in Figures 77 and 78. Figure 77 shows the presence of pores on the order of 1 micron in size throughout the catalyst layer. Figure 78 is a higher magnification image of the same region and shows the carbon support structure onto which the platinum catalyst particles are deposited. The individual carbon support particles, which are nominally 40-50 microns in length, are bound to neighboring particles with ion conducting polymer, in this case Nafion™. A group of bound support particles is referred to as an agglomerate and can be thought of as a large sphere containing many smaller spheres (the catalyzed support particles). The electrochemical reaction progresses as gaseous reactants dissolve in and diffuse through the agglomerate to the Pt catalyst sites contained within. By assuming that the agglomerates have a spherical structure, it is possible to use SEM images, including Figure 77, to estimate the average agglomerate size. Figure 77 is also used to estimate the void fraction or porosity of the catalyst layer which influences how readily gas is transported to the agglomerates. Both the size of the agglomerates and the porosity have a significant impact on catalyst performance.

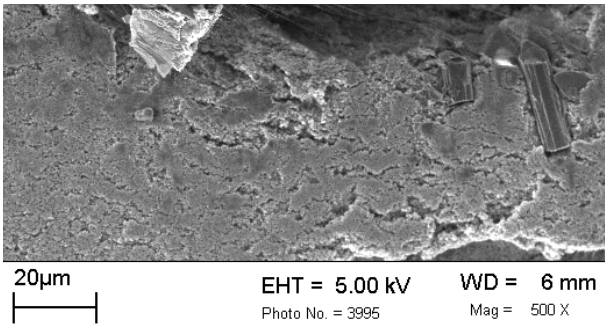

Figure 77. Catalyst layer showing the presence of macro-pores 1-5 microns in size. The pores facilitate gas transport

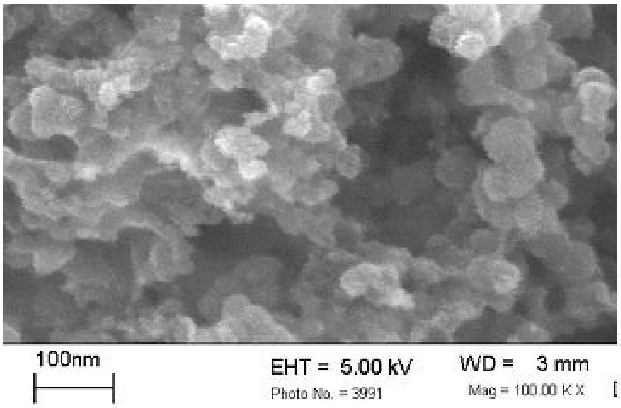

Figure 78. SEM image of catalyst showing individual support particles.

A TEM analysis was performed to investigate catalyst structure on an even smaller scale. Figure 79 clearly shows the individual carbon support structures as well as the platinum catalyst particles. There is no evidence of nano-scale pores shown in Figure 79. This indicates that in order for reactants to reach the catalyst site, they must first dissolve into the polymer and then diffuse through it. The result is an additional transport resistance that is included in the model in the form of a transport efficiency term called the effectiveness.

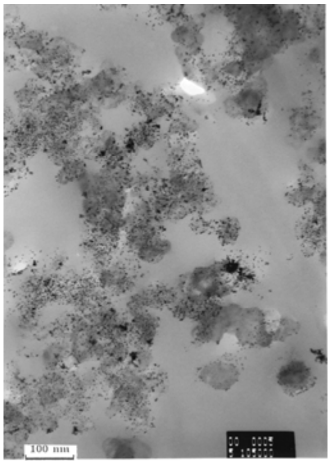

Figure 79. TEM image showing support particles and

Model Development - Numerical Considerations

The solution domain for the model is shown in Figure 80. The outer surfaces of the gas channels are bounded by the collector plates (not shown) and are impermeable to gases. As part of the single domain formulation, each governing equation is solved throughout the entire domain, even if the equation is not physically valid in every region. This is accomplished using a variety of numerical techniques [2,3]. The mesh is divided into 25 elements along the flow direction and 91 elements perpendicular to it.

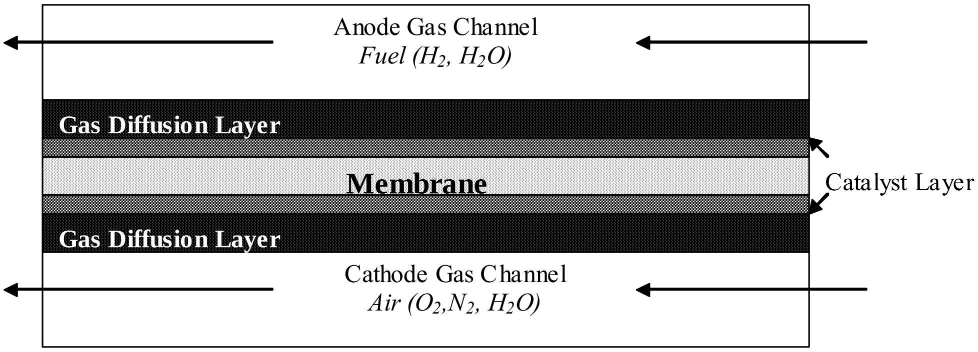

Figure 80. Solution domain for the numerical model

The solver used in the analysis is a commercially available CFD package called CFDesign v5.1 which was modified to include functionality specific to the fuel cell model (4). A total of eleven partial differential equations are solved accounting for the flow field (momentum and continuity), transport of reactants in the gas phase, transport of water dissolved in the polymer, protonic and electric potential, and energy. The base case parameters are shown in Table 20.

Table 20. Physical parameters used in the model

Parameter	Value
Inlet relative humidity, anode	90%
Inlet relative humidity, cathode	70%
Inlet velocity, anode	700 mm/s
Inlet velocity, cathode	2400 mm/s
Hydrogen concentration	2.70x10^{-8} mol/mm^{3}
Oxygen concentration	6.34x10^{-9} mol/mm^{3}
Inlet pressure	1.2 atm
Reactant inlet temperature	353 K
Ambient temperature	300 K
Length	60 mm
Width, gas channel	0.5 mm
Width, gas diffusion layer	0.1 mm
Width, membrane	0.1 mm
Width, catalyst	0.01 mm
Mesh size, LxW	25 x 91

Modeling Results

A polarization curve is shown in Figure 81. The curve illustrates the three regions of fuel cell operation; low load which is dominated by activation losses, intermediate load where ohmic losses start to become large, and high load where concentration losses limit the amount of current that the fuel cell can supply. The use of an agglomerate catalyst structure is crucial to accurately predicting performance in the high load region as it

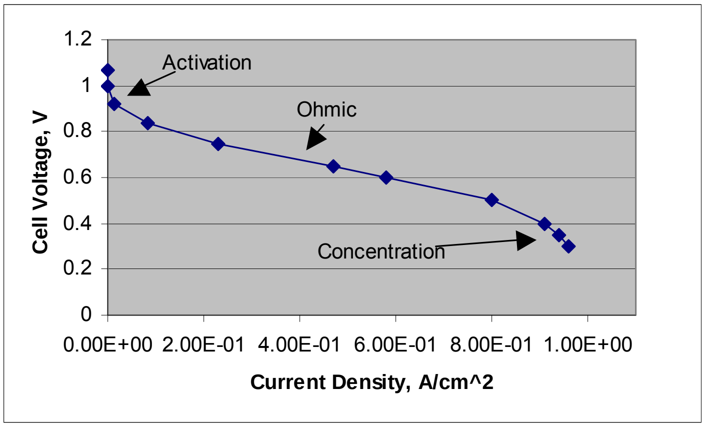

Figure 81. Cell polarization curve showing three operating regions

includes effects accounting for reactant transport limitation at high current density.

The effectiveness is an indicator of the mass transfer limitation resulting from gas species diffusing through polymer-coated agglomerates in order to reach the Pt reaction sites. It is principally dependent on the size and shape of the agglomerates and on the reaction rate. Figure 6 shows how the effectiveness changes in the anode catalyst layer for three different current densities. A low value of effectiveness indicates a large transport resistance, which contributes to concentration over-potential. Another way of looking at this is to view the effectiveness as a measure of catalyst utilization. A value of 1.0 means that all of the Pt sites in an agglomerate are being used, a value less than 1.0 indicates that reactant is not diffusing through the entire spherical agglomerate and therefore not reaching some of the Pt catalyst sites. Increasing either the current density or the path length (agglomerate size) that the reactant must travel to reach the reaction site will lower the effectiveness and increase over-potential.

In past agglomerate catalyst models, the gaseous reactant concentration through the catalyst layer was considered to be constant(5). In this current model, reactant concentration can vary in two dimensions. Figure 83 shows the concentration profile for oxygen gas along the cathode flow channel near the inlet. As the reactants (oxygen at the cathode and hydrogen at the anode) are consumed, the concentration drops. This leads to less reactant available for the electrochemical reaction at the catalyst sites and results in additional concentration over-potential.

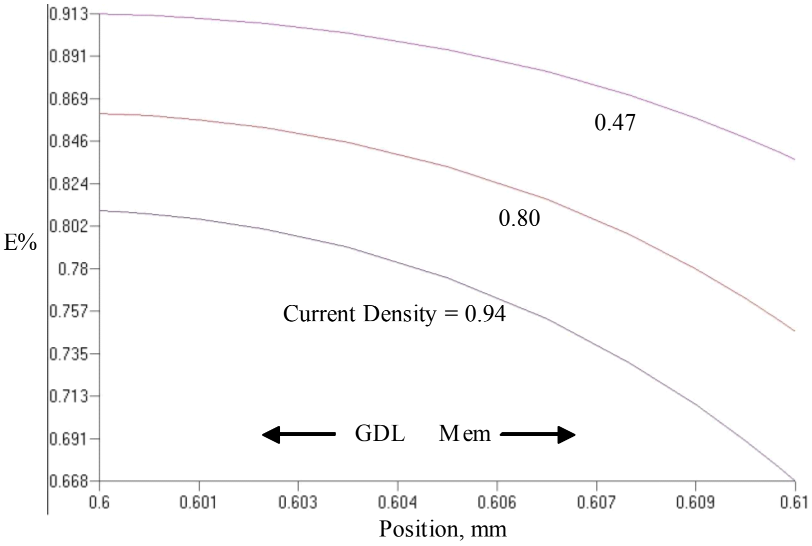

Figure 82. Effectiveness across anode catalyst

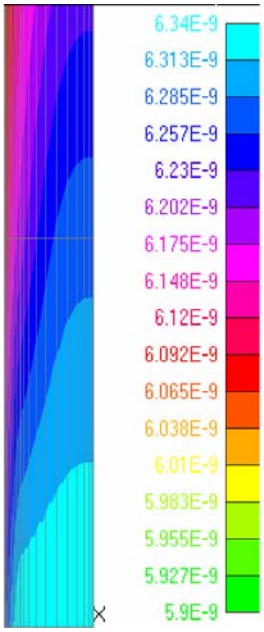

Figure 83. Oxygen concentration profile near cathode inlet

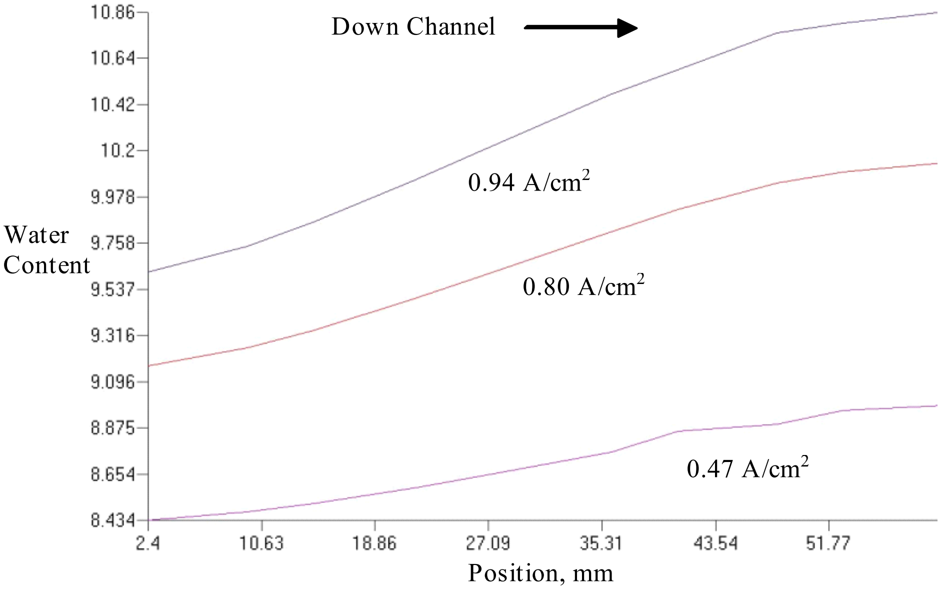

Figure 84. Membrane water content down the channel

The level of hydration or water content of the polymer membrane strongly influences the performance of the cell in the ohmic region shown in Figure 81. As water content increases, so does protonic conductivity which leads to a reduction in ohmic losses. Figure 84 shows the water content of the polymer membrane as it changes down the channel for three different values of current density. The water content is lowest at the inlet and increases down the channel due to water production via reaction at the cathode. The model allows for water to be transported by diffusion and electro-osmotic drag between the anode and cathode sides of the fuel cell.

References

1. ElectroChem, Inc. www.fuelcell.com
2. Suhas V. Patankar, Computation of Conduction and Duct Flow Heat Transfer, Innovative Research, Maple Grove, 1991.
3. S. Um, C.Y. Wang, K.S Chen, "Computational Fluid Dynamics Modeling of Proton Exchange Membrane Fuel Cells," J.Electrochem.Soc, Vol. 147, No. 12, pp. 4485-4493, 2000.
4. CFDesign v5.1, Blue Ridge Numerics, Charlottesville, VA
5. K. Broka, P. Ekdunge, "Modeling the PEM fuel cell cathode," J. Applied Electrochemistry, Vol. 27, pp. 281-289, 1997.

Single Domain PEMFC Model Based on Agglomerate Catalyst Geometry

Introduction

In recent years, the proton exchange membrane (PEM) fuel cell has received a great deal of attention, from the automotive industry in particular, as a candidate for near future power generation applications. PEM fuel cells are particularly suited to automotive applications primarily because of their relatively low operating temperature, efficiency, and high power density that is comparable to existing internal combustion technology. However, like many emerging technologies, PEM fuel cells must overcome certain engineering and economic obstacles if they are ever to become commercially viable. In short, PEM fuel cells must become more efficient and lower in cost. Improvements in cell design and materials development can help to achieve these goals. There are two approaches to improving cell design and materials development. The first is to design and build test cells and evaluate their performance. This method can yield useful information, but it is also costly and time consuming. In addition, although it is relatively easy to evaluate a cell's total current and voltage and from these generate a polarization curve, it is much more difficult to evaluate operating parameters in situ, which is vital to understanding how a design performs over a range of operating conditions. In order to obtain data such as reactant concentration profiles, membrane hydration, and temperature distributions inside the cell, it is more convenient to simulate the fuel cell with a mathematical model.

In the past, most mathematical models focused on the cathode side of the fuel cell only; the reason being that the cathode activation overpotential is the single largest source of inefficiency in the fuel cell. These models also typically include the membrane, as it contributes to ohmic overpotential, and the gas diffusers. The catalyst layer itself has generally been modeled as an interface and denoted the point at which source terms for species consumption or production were applied. The work by Springer et al. [1] laid the foundation for many future numerical models. In their paper, they present a one-dimensional model, the principal focus of which is water transport through the membrane. Their model shows that the net water transport per proton is much less than the measured electro-osmotic drag coefficient for a fully hydrated membrane, which indicates the presence of other important water transport mechanisms. Bernardi and Verbrugge [2] present a model with the focus on species transport, electrochemistry, and catalyst utilization in which they conclude, among other things, that the transport of gases dissolved in the polymer phase of the electrodes affects catalyst utilization and limits cell performance. This model is based on a pseudo-homogeneous catalyst layer structure in which the layer has no pores through which gas can be transported to the reaction sites. Rather, the reactants must dissolve into the polymer phase and diffuse through the nonporous catalyst layer to reach the reaction sites. This approach can be computationally advantageous as the equations describing transport in the catalyst layer are relatively simple. The disadvantage is that the pseudo-homogenous catalyst layer structure does not allow for transport of reactants in the gas phase within this layer. Research has shown that the catalyst layer is porous and that reactants can be transported throughout in the gas phase [3,4]. The model of Broka and Ekdunge [4] represents one of the first applications of an agglomerate catalyst layer structure to a PEM model. In this model, Broka and Ekdunge show, through microscopic analysis, that the catalyst layer is made up of clumps of carbonsupported Pt catalyst surrounded by a thin layer of Nafion and separated by pores. These clumps are referred to as agglomerates. The principal difference between this type of model and the pseudo-homogenous model is that in the agglomerate model, reactants can move in the gas phase rather than solely has a dissolved species through the catalyst layer. Broka and Ekdunge also show that the agglomerate model is better suited to modeling fuel cell behavior at high current densities, where concentration overpotential becomes dominant. In their model, they assume that the gaseous reactant concentration is constant across the catalyst layer. In the model presented in this paper, the reactant concentration is treated as variable.

In recent years, modeling efforts, both our own [5–7] and that of others (e.g. [8–12]), have increased in complexity. Most current models are multi-dimensional, include mass transport of multiple species, and include the entire fuel cell geometry from one gas channel to the other. Some models also account for two-phase flow, which is necessary when modeling the effects of liquid water production and flooding. Zhou and Liu [8] developed a three-dimensional fuel cell model based on the earlier work of Gurau et al. [9]. As part of the work they show how the model solution is affected when transitioning from a two-dimensional to a three dimensional geometry. Their model focuses on species transport as well as current and temperature distribution. To solve the model, they partitioned the solution domain into three coupled regions, which is a more involved process for the user than is the single domain approach used in this work. In addition, water uptake and release within the polymer portion of the catalyst layers is neglected. Um et al. [10] present a transient, three-dimensional model and show that an interdigitated flow field can help to reduce mass transfer limitations. They use a single domain solution approach and neglect water uptake and release in the catalyst layer. Shimpalee et al. [11] also present a three-dimensional model but do not include transport through the catalyst layer as it is modeled as an interface. They show that the direction of water transport through the membrane can affect current density distribution patterns. A model including two-phase flow is presented by Natarajan et al. [12]. They show that liquid water buildup in the cathode has a substantial influence on cell performance. Their model is two-dimensional and focuses on liquid water transport in the porous media of the gas diffuser. The catalyst layer is an interface and only the cathode side of the cell is included. It should be noted that with the exception of Broka and Ekdunge, all of the models mentioned above either treat the catalyst layer as a pseudo-homogeneous film or simply as an interface.

This paper describes a mathematical model that simulates the transport of gaseous species, energy, protonic current, and water dissolved in the polymer phase of the catalyst layers and membrane. The catalyst layer is modeled as having an agglomerate structure, and the effect of catalyst layer structure on cell performance is also examined. The model is based on the finite element method and is formulated as a single solution domain problem. Consequently, interface conditions between the individual fuel cell elements need not be specified, and the only boundary conditions required are at the outer surfaces of the model.

Model development

Fig. 85 shows the solution domain of the model. In the anode and cathode gas channels, fuel and oxidant flow along the surface of the membrane electrode assembly. In these regions, the flow is considered to be laminar. Reactants move from the gas channels into the gas diffusion layers (GDL) which consist of a thin sheet of carbon paper, the purpose of

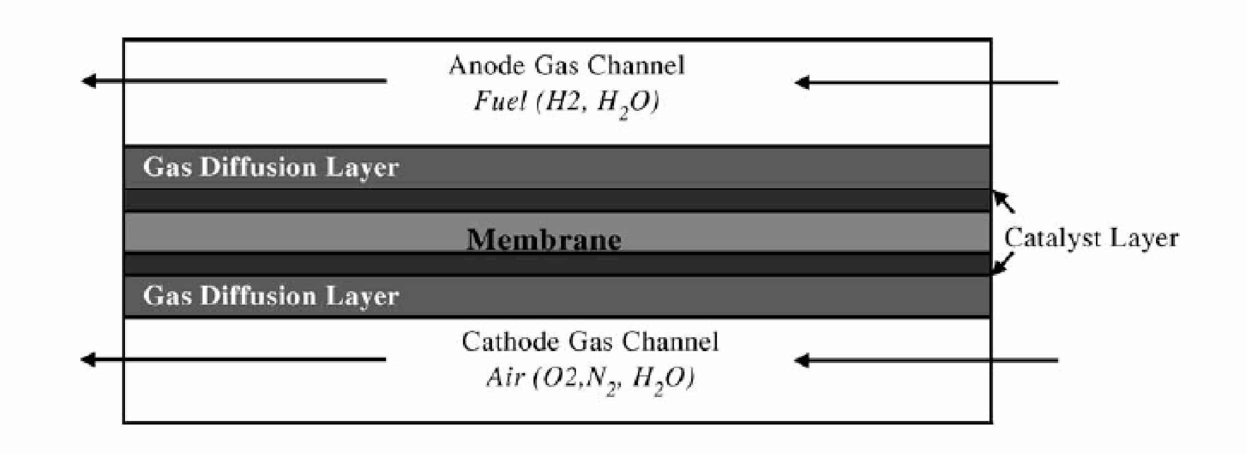

Figure 85: Solution Domain

which is to evenly distribute the reactants across the catalyst layers and provide an electrical connection with the collector plate (not shown). The catalyst layers are among the more important parts of the fuel cell as it is within these regions where all of the electrochemical reactions take place. A large portion of the work presented in this model involves the characterization and modeling of the catalyst layers. The polymer membrane, which is assumed to be impermeable to reactant gases, transports only protons and dissolved water. Both ionic conductivity and ionomer content in the MEA have a significant of impact on cell performance.

Catalyst layer structure To develop an accurate description of the catalyst layer, a 5 cm^2 MEA was purchased from ElectroChem Inc. Cross sections of the MEA were prepared and analyzed with a scanning electron microscope (SEM) and a transmission electron microscope (TEM). The cross sections for SEM analysis were prepared by three methods in order to evaluate which worked best. The first method involved freezing the sample in liquid nitrogen and fracturing it. This technique provided a clean section for viewing but also caused the gas diffusion layer to delaminate from the assembly. The second method was to simply cut the MEA at room temperature with a razor. The blade was pushed directly down on top of the MEA as opposed to cutting across it. This also resulted in a clean section, but there was some dragging of the polymer through the sample as it is fairly malleable at room temperature. For the third method, the sample was frozen in liquid nitrogen and then cut as per the second method. This provided the best results of all. Preparation of the cross sections for TEM analysis involved encasing the sample in epoxy and then using a diamond knife, or microtome, to slice off very thin sections (70 nm) for viewing. The samples were cut at room temperature. The structure of the fuel cell MEA is shown in Fig. 86. The region labeled A in this image is the gas diffusion layer. Region B is the catalyst layer. In this region there is no carbon paper, only polymer encapsulated catalyst sites called agglomerates. Region C is the polymer membrane. Fig. 87 shows a higher magnification view of the catalyst layer labeled B in Fig. 86. Fig. 87 along with Fig. 86 can be used to estimate the mean agglomerate size, the thickness of the active layer, and the void fraction of the active layer. The agglomerate size and void fraction were evaluated through the use of image analysis and enhancement software. By enhancing the SEM and TEM images, it is possible to highlight certain catalyst characteristics of interest and perform quantitative analyses. Geometric information about the catalyst structure can be used in conjunction with manufacturer’s data for catalyst loading to estimate the specific catalyst area. Pores can be seen in the catalyst layer on the order of 1–10 mm in size. These are referred to as macropores.

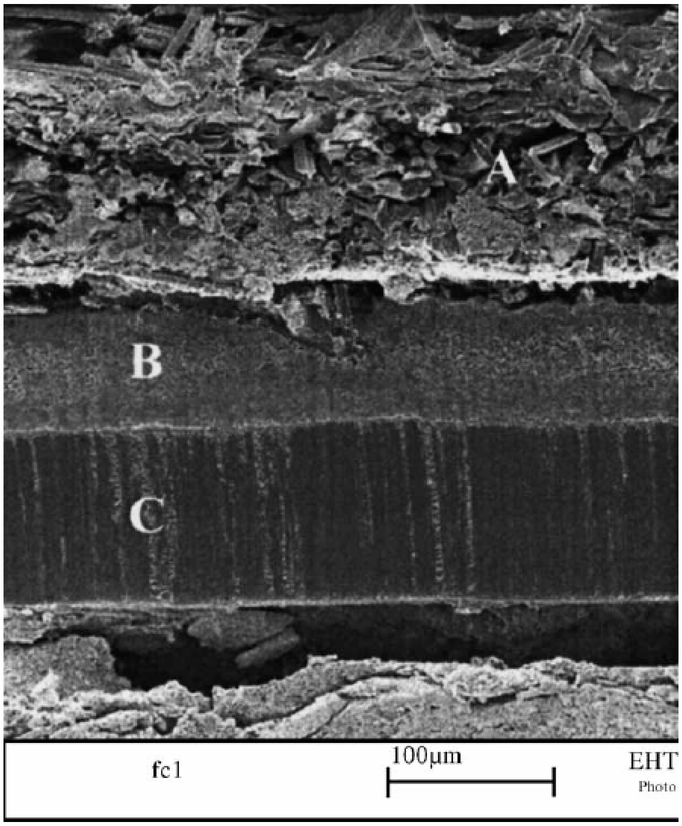

Figure 86: Freeze cut cross section of ElectroChem MEA. Image magnification is 200x.

Fig. 88 shows a schematic of the agglomerate catalyst layer geometry used in this model. Reactant gas flows through the catalyst macro-pores and then dissolves into and diffuses through the agglomerate to the carbon-supported platinum reaction sites.

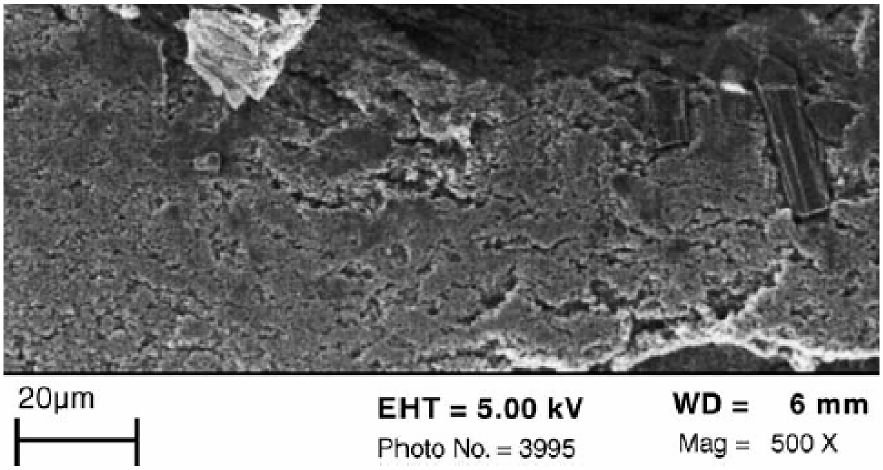

Figure 87: Room temperature cut section of MEA showing the catalyst layer.
Image magnification is 500x.

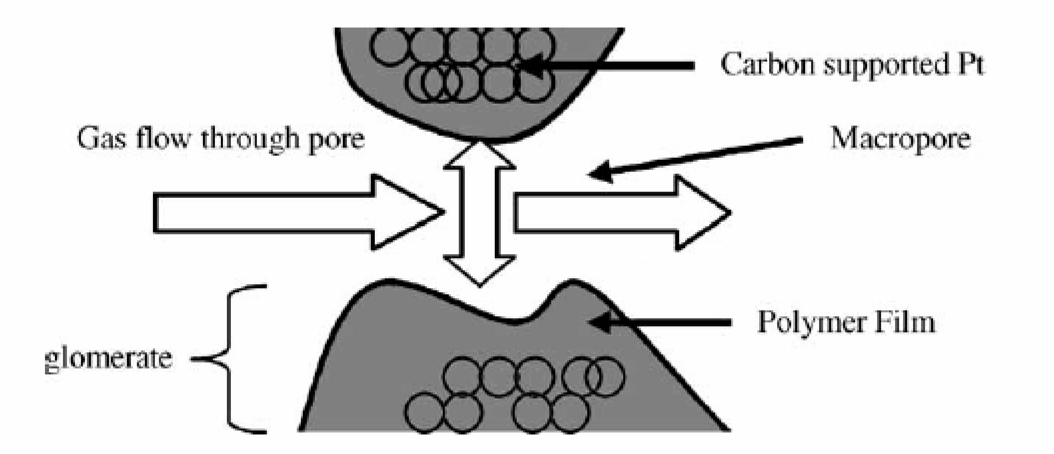

Figure 88: Agglomerate catalyst geometry.

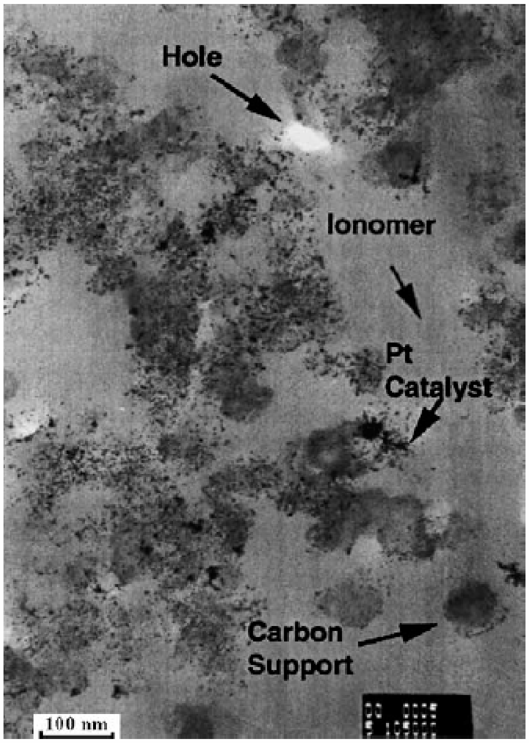

Figure 89: TEM image of an agglomerate. Magnification is 18,400x.

Figs. 89 and 90 show TEM images of an agglomerate. In these images, it is possible to see the individual Pt catalyst particles as well as the carbon support. As indicated in Fig. 89, the light gray area between the carbon and Pt particles is ionomer. The white areas are holes, not to be confused with pores. These holes result from the pullout of carbon-supported catalyst during sample preparation. Indeed, nanoscale pores are absent from the TEM images. This is an important observation as it indicates that gas transfer in the porous catalyst is facilitated primarily by macro-pores on the order of 1–10 mm in size. Fig. 90 is a higher magnification image in which the Pt catalyst particles are well defined. These Pt particles are nominally 3 nm in diameter. However, as a consequence of the technique used to deposit the catalyst, the individual particles have a tendency to clump together. When the catalyst particles form clumps, there is a reduction in the amount of surface area available for reaction, which can be viewed as a decrease in catalyst utilization.

Table 21: Governing equations.

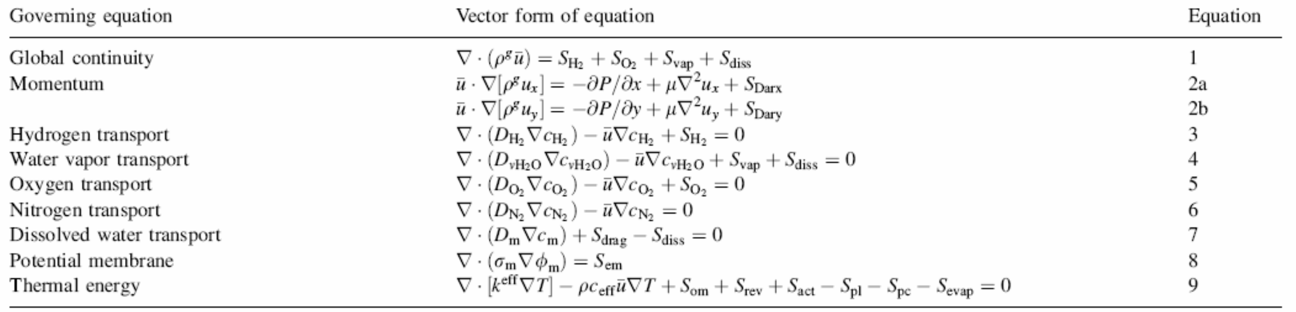

Governing equation	Vector form of equation	Equation
Global continuity	$\nabla \cdot (\rho^g \bar{u}) = S_{H_2} + S_{O_2} + S_{vap} + S_{diss}$	1
Momentum	$\bar{u} \cdot \nabla[\rho^g u_x] = -\partial P/\partial x + \mu \nabla^2 u_x + S_{Darx}$	2a
	$\bar{u} \cdot \nabla[\rho^g u_y] = -\partial P/\partial y + \mu \nabla^2 u_y + S_{Dary}$	2b
Hydrogen transport	$\nabla \cdot (D_{H_2} \nabla c_{H_2}) - \bar{u} \nabla c_{H_2} + S_{H_2} = 0$	3
Water vapor transport	$\nabla \cdot (D_{vH_2O} \nabla c_{vH_2O}) - \bar{u} \nabla c_{vH_2O} + S_{vap} + S_{diss} = 0$	4
Oxygen transport	$\nabla \cdot (D_{O_2} \nabla c_{O_2}) - \bar{u} \nabla c_{O_2} + S_{O_2} = 0$	5
Nitrogen transport	$\nabla \cdot (D_{N_2} \nabla c_{N_2}) - \bar{u} \nabla c_{N_2} = 0$	6
Dissolved water transport	$\nabla \cdot (D_m \nabla c_m) + S_{drag} - S_{diss} = 0$	7
Potential membrane	$\nabla \cdot (\sigma_m \nabla \phi_m) = S_{em}$	8
Thermal energy	$\nabla \cdot [k^{eff} \nabla T] - \rho c_{eff} \bar{u} \nabla T + S_{om} + S_{rev} + S_{act} - S_{pl} - S_{pc} - S_{evap} = 0$	9

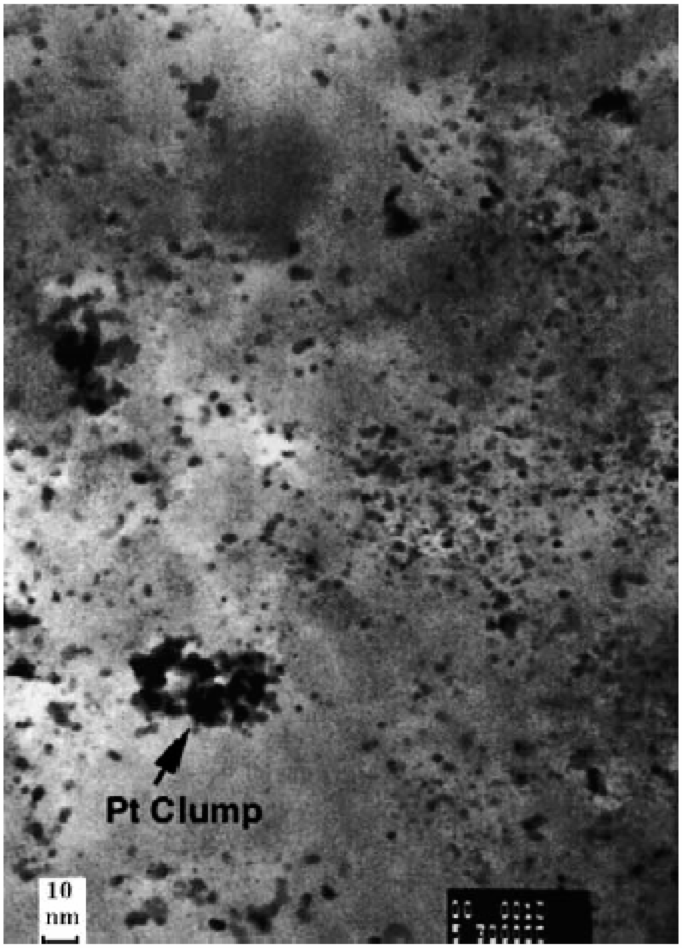

Fig. 6. TEM image of an agglomerate showing Pt catalyst particles and clumping. Image magnification is 485,500×.

The physical parameters used in the model can be found in Table 21. These parameters, some of which were determined by the microscopic analyses discussed earlier, must be used in conjunction with the appropriate mathematical relations to accurately model fuel cell performance.

Governing equations and closure relations

Eq. (1) in Table 21 reflects conservation of mass for all gas species. A source term reflects changes in the overall gasphase mass due to consumption or production of gas species via reaction and mass transfer between the water in the gas phase and that dissolved in the polymer. The total density of the gas mixture is expressed as the sum of the individual species concentrations multiplied by their respective molar masses. The momentum equations, Eqs. (2a) and (2b), are expressed as the Navier–Stokes equations in vector form, modified with a source term to account for Darcy flow in the porous regions of the model. The Darcy source is active in the GDL and catalyst layers only; the inertial and viscous terms are neglected in these regions.

Table 22: Source terms.

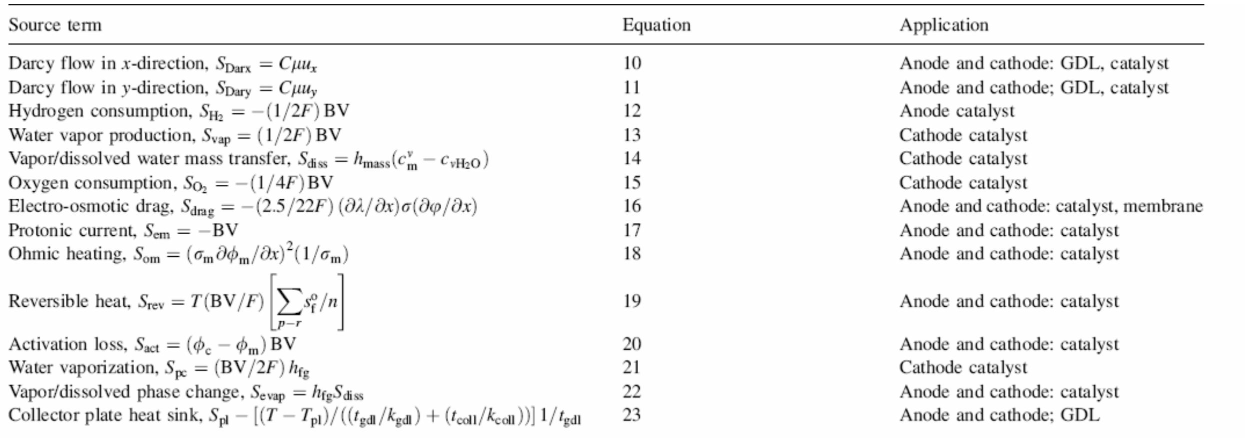

Source term	Equation	Application
Darcy flow in x-direction, $S_{\mathrm{Darx}} = C\mu u_x$	10	Anode and cathode: GDL, catalyst
Darcy flow in y-direction, $S_{\mathrm{Dary}} = C\mu u_y$	11	Anode and cathode; GDL, catalyst
Hydrogen consumption, $S_{\mathrm{H_2}} = -(1/2F)\,\mathrm{BV}$	12	Anode catalyst
Water vapor production, $S_{\mathrm{vap}} = (1/2F)\,\mathrm{BV}$	13	Cathode catalyst
Vapor/dissolved water mass transfer, $S_{\mathrm{diss}} = h_{\mathrm{mass}}(c_{\mathrm{m}}^{\mathrm{v}} - c_{v\mathrm{H_2O}})$	14	Cathode catalyst
Oxygen consumption, $S_{\mathrm{O_2}} = -(1/4F)\,\mathrm{BV}$	15	Cathode catalyst
Electro-osmotic drag, $S_{\mathrm{drag}} = -(2.5/22F)\,(\partial\lambda/\partial x)\sigma(\partial\varphi/\partial x)$	16	Anode and cathode: catalyst, membrane
Protonic current, $S_{\mathrm{em}} = -\mathrm{BV}$	17	Anode and cathode: catalyst
Ohmic heating, $S_{\mathrm{om}} = (\sigma_{\mathrm{m}}\partial\phi_{\mathrm{m}}/\partial x)^2(1/\sigma_{\mathrm{m}})$	18	Anode and cathode: catalyst
Reversible heat, $S_{\mathrm{rev}} = T(\mathrm{BV}/F)\left[\sum_{p-r} s_{\mathrm{f}}^{\mathrm{o}}/n\right]$	19	Anode and cathode: catalyst
Activation loss, $S_{\mathrm{act}} = (\phi_{\mathrm{c}} - \phi_{\mathrm{m}})\,\mathrm{BV}$	20	Anode and cathode: catalyst
Water vaporization, $S_{\mathrm{pc}} = (\mathrm{BV}/2F)\,h_{\mathrm{fg}}$	21	Cathode catalyst
Vapor/dissolved phase change, $S_{\mathrm{evap}} = h_{\mathrm{fg}}S_{\mathrm{diss}}$	22	Anode and cathode: catalyst
Collector plate heat sink, $S_{\mathrm{pl}} - [(T - T_{\mathrm{pl}})/((t_{\mathrm{gdl}}/k_{\mathrm{gdl}}) + (t_{\mathrm{coll}}/k_{\mathrm{coll}}))]\,1/t_{\mathrm{gdl}}$	23	Anode and cathode; GDL

The gas species equations are given in Eqs. (3)–(6). The diffusion coefficients are based on a simplification of the Stefan–Maxwell equations and are modified by a porosity factor [9]. Each of these equations has an advective term equal to the product of velocity and concentration gradient. The general form of these equations would also include the complement to this term, the product of concentration and velocity gradient. In preliminary simulations, the velocity gradient was found to be negligible for most of the solution domain, with the exception of the inlet and exit, and for this reason the product of concentration and velocity gradient is omitted from the gas species equations. The source terms for hydrogen and oxygen species, Eqs. (12) and (15) in Table 22, account for consumption via reaction. The source term for water vapor accounts for production of water at the cathode, Eq. (13).

Water exists in dissolved form within the polymer membrane

and a portion of the polymer phase of the catalyst layer. Dissolved water is transported through the polymer by diffusion and electro-osmotic drag only. A convective term would have to be added if the gas pressures in the anode and cathode were different; for this work the anode and cathode pressures are within 3% of each other and so the convective transport of water through the MEA is neglected. A source term is needed to account for mass transfer between the dissolved and vapor phases within the catalyst layer. This term, Eq. (14), is applied to both the dissolved water species equation and to the water vapor equation. Eq. (7) is the transport equation for dissolved water.

The transport of protons in the polymer portions of the fuel cell is described by Eq. (8). The source term, Eq. (17), represents the production/consumption of protons via the electrochemical reactions in the catalyst layers. The rate of the electrochemical reaction is described by the Butler–Volmer relation, Eq. (24). The electrical potential is assumed to be constant over each electrode. It is set to zero on the anode side and to the difference between the cell voltage and the open circuit voltage on the cathode side.

The energy equation is expressed by Eq. (9) and contains sources for ohmic heating due to ionic resistance Eq. (18), reversible heat Eq. (19), heat produced via activation losses Eq. (20), and heat exchange involved in the phase change of water. There are two terms related to phase change energy transfer. The first accounts for the energy needed to vaporize the water produced via reaction Eq. (21). One of the assumptions of thismodel is that water is produced in the liquid phase and instantly vaporized, provided that the cathode stream is not saturated. The energy required for the vaporization must then be included. The other term accounts for water moving between the dissolved and vapor phases Eq. (22). The enthalpy of the water dissolved in the polymer is assumed to be the same as the enthalpy of liquid water.

In this model, the collector plates are not included in the solution domain. In an actual fuel cell, the shoulder of the plates would be in contact with the MEA and provide a low resistance pathway for heat. The source term Spl Eq. (23) approximates the amount of heat that would move through the collector plates had they been part of the solution domain.

Table 23 contains the closure relations needed to complete the mathematical model. Eq. (24) is the Butler–Volmer equation as expressed for an agglomerate catalyst geometry [4]. The first term in the denominator effectively sets the maximum flux of reactant that can pass through the polymer layer surrounding an agglomerate. This term is based on a dissolved gas concentration at the gas/polymer interface given by a Henry's law relation, Eq. (26). The reactant flux limit establishes the limiting current of the cell. The second term in the denominator includes the reaction rate, Eq. (25), and is similar to that used by Broka and Ekdunge. with the exception that in this model the concentration of reactant (either oxygen or hydrogen) is assumed to vary across the width of the catalyst layer. Hence the term c_, which is the dissolved reactant concentration, is not constant The effectiveness, given as Eq. (27), is a measure of how readily reactants diffuse through the agglomerates [4]. An effectiveness of 1.0 would indicate that reactants diffusing through the agglomerates encounter no resistance. Eq. (29) is an effective diffusion coefficient which allows for an approximate solution to the multi-component species equations without having to solve the full set of Stefan–Maxwell equations [9]. Eqs. (31) and (32) are the diffusion coefficients for water in Nafion and the ionic conductivity of Nafion, respectively [1]. Eq. (34) relates membrane water content to the dissolved water concentration while accounting for the swelling of the membrane with water sorption.

Table 23: Closure relations.

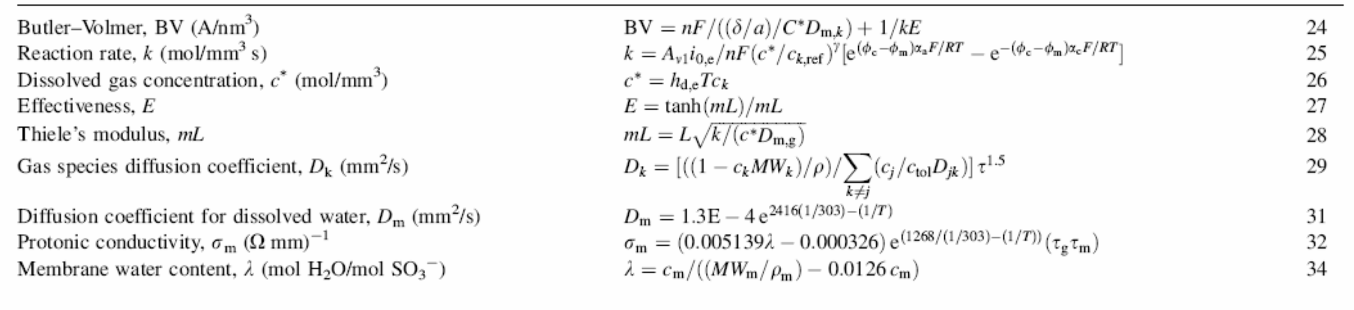

Butler–Volmer, BV (A/nm^3)	$\mathrm{BV} = nF/((\delta/a)/C^*D_{\mathrm{m},k}) + 1/kE$	24
Reaction rate, k (mol/mm^3 s)	$k = A_{\mathrm{v}1}i_{0,\mathrm{e}}/nF(c^*/c_{k,\mathrm{ref}})^{\gamma}[\mathrm{e}^{(\phi_\mathrm{c}-\phi_\mathrm{m})\alpha_\mathrm{a}F/RT} - \mathrm{e}^{-(\phi_\mathrm{c}-\phi_\mathrm{m})\alpha_\mathrm{c}F/RT}]$	25
Dissolved gas concentration, c^* (mol/mm^3)	$c^* = h_{\mathrm{d,e}}Tc_k$	26
Effectiveness, E	$E = \tanh(mL)/mL$	27
Thiele's modulus, mL	$mL = L\sqrt{k/(c^*D_{\mathrm{m,g}})}$	28
Gas species diffusion coefficient, D_k (mm^2/s)	$D_k = [((1 - c_kMW_k)/\rho)/\sum_{k \neq j}(c_j/c_{\mathrm{tol}}D_{jk})]\,\tau^{1.5}$	29
Diffusion coefficient for dissolved water, D_m (mm^2/s)	$D_\mathrm{m} = 1.3\mathrm{E} - 4\,\mathrm{e}^{2416(1/303)-(1/T)}$	31
Protonic conductivity, σ_m $(\Omega\ \mathrm{mm})^{-1}$	$\sigma_\mathrm{m} = (0.005139\lambda - 0.000326)\,\mathrm{e}^{(1268/(1/303)-(1/T))}\,(\tau_\mathrm{g}\tau_\mathrm{m})$	32
Membrane water content, λ (mol H_2O/mol $SO_3{}^-$)	$\lambda = c_\mathrm{m}/((MW_\mathrm{m}/\rho_\mathrm{m}) - 0.0126\,c_\mathrm{m})$	34

Table 24 contains a listing of the boundary conditions required by the model. Boundary conditions are specified at the inlets and outlets to both gas channels while the remaining external surfaces of the solution domain are assumed to have zero flux conditions. Although the model presented does not include transient effects, initial conditions (ICs) are specified for the species equations as well as the dissolved water equation. Specifying ICs helps to stabilize the numerical solution and also decreases the amount of time needed to reach a converged solution. The ICs for the species equation are the same as the inlet boundary conditions. The dissolved water equation IC is set in a manner to be consistent with the water vapor equation to which it is coupled by Eq. (14). In addition to the governing equations and closure relations, certain values for material properties and other physical parameters are needed to complete the model. The numerical values for the physical parameters used in the model are given in Table 25.

Numerical considerations

The outer surfaces of the gas channels shown in Fig. 85 are bounded by the collector plates (not shown) and are impermeable to gases. As part of the single domain formulation, each governing equation is solved throughout the entire domain, even if the equation is not physically valid in every region. This is accomplished using a variety of

Table 24: Boundary conditions for base case.

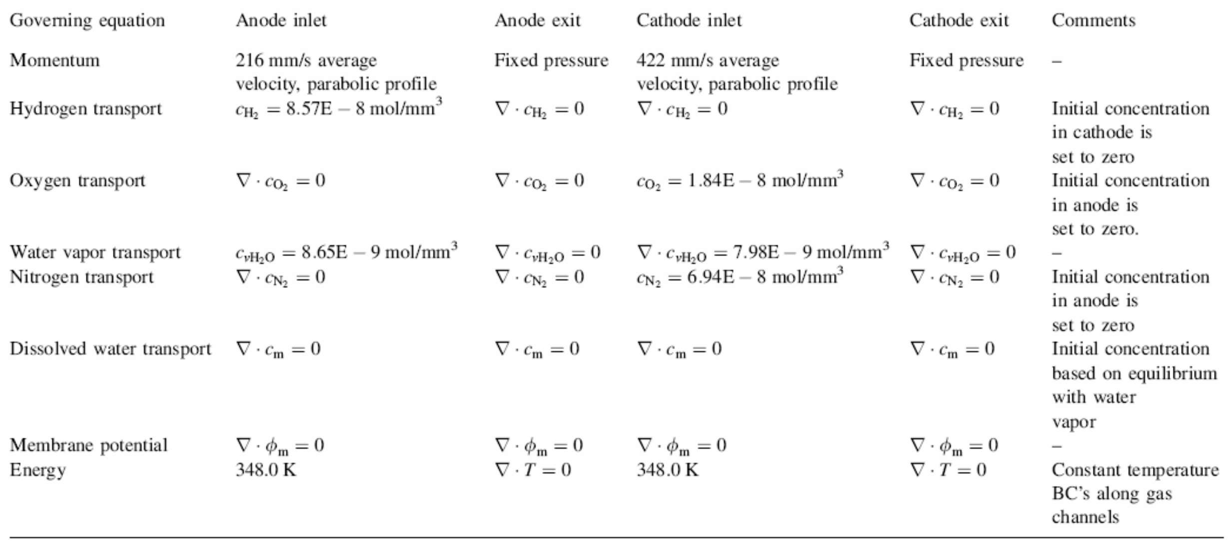

Governing equation	Anode inlet	Anode exit	Cathode inlet	Cathode exit	Comments
Momentum	216 mm/s average velocity, parabolic profile	Fixed pressure	422 mm/s average velocity, parabolic profile	Fixed pressure	–
Hydrogen transport	$c_{H_2} = 8.57\mathrm{E} - 8$ mol/mm^3	$\nabla \cdot c_{H_2} = 0$	$\nabla \cdot c_{H_2} = 0$	$\nabla \cdot c_{H_2} = 0$	Initial concentration in cathode is set to zero
Oxygen transport	$\nabla \cdot c_{O_2} = 0$	$\nabla \cdot c_{O_2} = 0$	$c_{O_2} = 1.84\mathrm{E} - 8$ mol/mm^3	$\nabla \cdot c_{O_2} = 0$	Initial concentration in anode is set to zero.
Water vapor transport	$c_{vH_2O} = 8.65\mathrm{E} - 9$ mol/mm^3	$\nabla \cdot c_{vH_2O} = 0$	$\nabla \cdot c_{vH_2O} = 7.98\mathrm{E} - 9$ mol/mm^3	$\nabla \cdot c_{vH_2O} = 0$	–
Nitrogen transport	$\nabla \cdot c_{N_2} = 0$	$\nabla \cdot c_{N_2} = 0$	$c_{N_2} = 6.94\mathrm{E} - 8$ mol/mm^3	$\nabla \cdot c_{N_2} = 0$	Initial concentration in anode is set to zero
Dissolved water transport	$\nabla \cdot c_\mathrm{m} = 0$	$\nabla \cdot c_\mathrm{m} = 0$	$\nabla \cdot c_\mathrm{m} = 0$	$\nabla \cdot c_\mathrm{m} = 0$	Initial concentration based on equilibrium with water vapor
Membrane potential	$\nabla \cdot \phi_\mathrm{m} = 0$	$\nabla \cdot \phi_\mathrm{m} = 0$	$\nabla \cdot \phi_\mathrm{m} = 0$	$\nabla \cdot \phi_\mathrm{m} = 0$	–
Energy	348.0 K	$\nabla \cdot T = 0$	348.0 K	$\nabla \cdot T = 0$	Constant temperature BC's along gas channels

Table 25: Physical parameters.

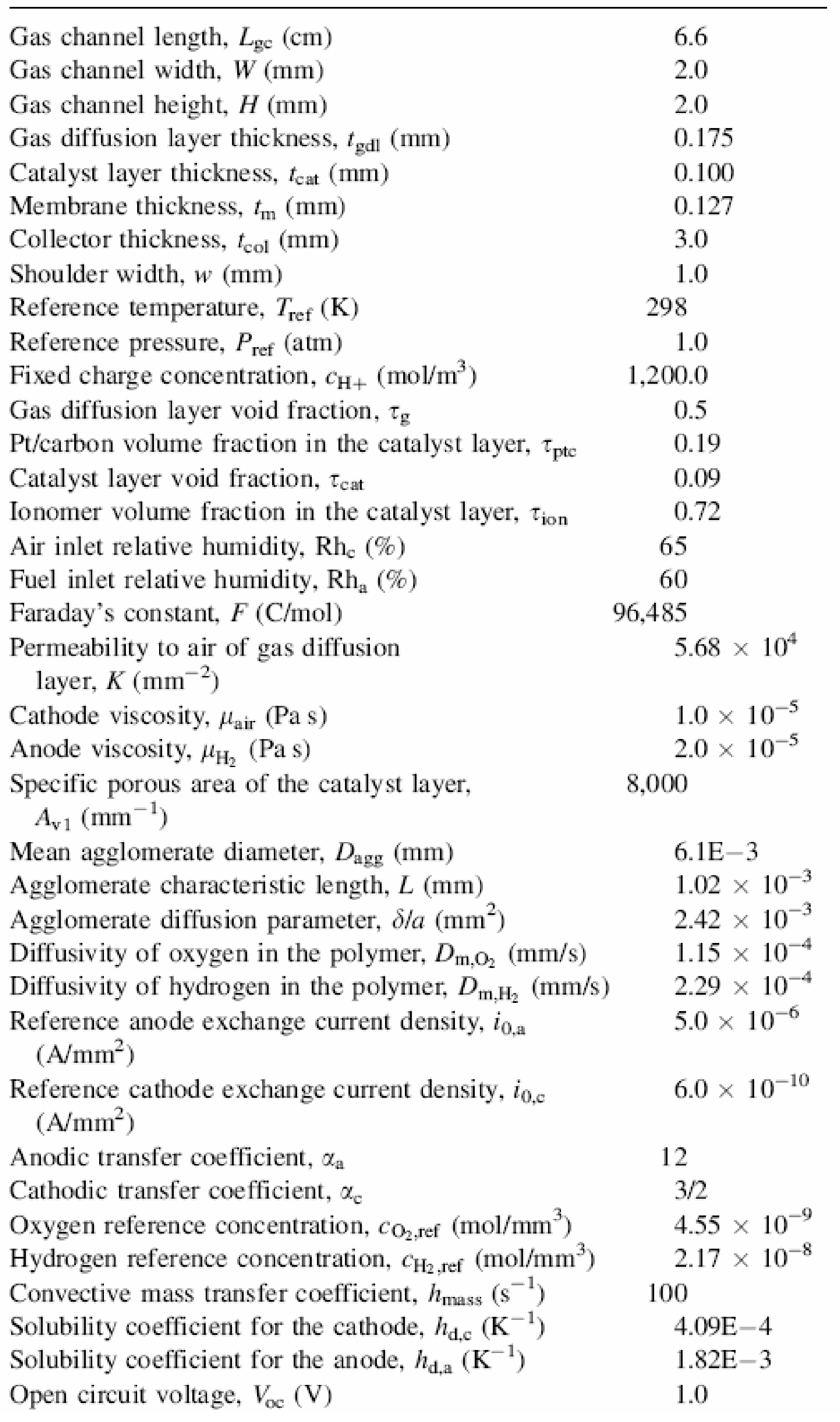

Gas channel length, L_{gc} (cm)	6.6
Gas channel width, W (mm)	2.0
Gas channel height, H (mm)	2.0
Gas diffusion layer thickness, t_{gdl} (mm)	0.175
Catalyst layer thickness, t_{cat} (mm)	0.100
Membrane thickness, t_m (mm)	0.127
Collector thickness, t_{col} (mm)	3.0
Shoulder width, w (mm)	1.0
Reference temperature, T_{ref} (K)	298
Reference pressure, P_{ref} (atm)	1.0
Fixed charge concentration, c_{H+} (mol/m^3)	1,200.0
Gas diffusion layer void fraction, τ_g	0.5
Pt/carbon volume fraction in the catalyst layer, τ_{ptc}	0.19
Catalyst layer void fraction, τ_{cat}	0.09
Ionomer volume fraction in the catalyst layer, τ_{ion}	0.72
Air inlet relative humidity, Rh$_c$ (%)	65
Fuel inlet relative humidity, Rh$_a$ (%)	60
Faraday's constant, F (C/mol)	96,485
Permeability to air of gas diffusion layer, K (mm^{-2})	5.68×10^4
Cathode viscosity, μ_{air} (Pa s)	1.0×10^{-5}
Anode viscosity, μ_{H_2} (Pa s)	2.0×10^{-5}
Specific porous area of the catalyst layer, A_{v1} (mm^{-1})	8,000
Mean agglomerate diameter, D_{agg} (mm)	6.1E−3
Agglomerate characteristic length, L (mm)	1.02×10^{-3}
Agglomerate diffusion parameter, δ/a (mm^2)	2.42×10^{-3}
Diffusivity of oxygen in the polymer, D_{m,O_2} (mm/s)	1.15×10^{-4}
Diffusivity of hydrogen in the polymer, D_{m,H_2} (mm/s)	2.29×10^{-4}
Reference anode exchange current density, $i_{0,a}$ (A/mm^2)	5.0×10^{-6}
Reference cathode exchange current density, $i_{0,c}$ (A/mm^2)	6.0×10^{-10}
Anodic transfer coefficient, α_a	12
Cathodic transfer coefficient, α_c	3/2
Oxygen reference concentration, $c_{O_2,ref}$ (mol/mm^3)	4.55×10^{-9}
Hydrogen reference concentration, $c_{H_2,ref}$ (mol/mm^3)	2.17×10^{-8}
Convective mass transfer coefficient, h_{mass} (s^{-1})	100
Solubility coefficient for the cathode, $h_{d,c}$ (K^{-1})	4.09E−4
Solubility coefficient for the anode, $h_{d,a}$ (K^{-1})	1.82E−3
Open circuit voltage, V_{oc} (V)	1.0

numerical techniques [9,13]. The domain is divided into 35 x 147 elements. Mapped meshing was used to maintain a sufficient mesh density throughout the model domain. A sensitivity analysis was conducted by doubling the number of elements in the mesh. The solution changed on average by less than 0.33% and so was assumed to be mesh independent.

Results and discussion

Fig. 91 shows an experimental polarization data set for a 50 cm^2 ElectroChem cell operating at the conditions given in Table 26. Also plotted in Fig. 91 is a curve showing the cell polarization predicted using the model operating under the same conditions. The numerical results are consistent with the data set over the entire operating range. In this model, the transport of reactants through the catalyst layer occurs along two parallel pathways. The first is gas transport by diffusion and advection through the macro-pores within the catalyst layer (shown in Fig. 86). As the reactants pass through the pores, they dissolve into the catalyst agglomerates and diffuse inward through the surrounding polymer to the carbon-supported platinum reaction sites. For a fixed volume of carbon-supported catalyst particles, a change in the catalyst layer void fraction requires a corresponding change in the fraction of ionomer in the catalyst layer. Fig. 92 shows cell performance as void fraction is changed at a cell voltage of 0.5 V. The optimal catalyst layer void fraction for the test MEA at this voltage is 0.04 or 4%. The

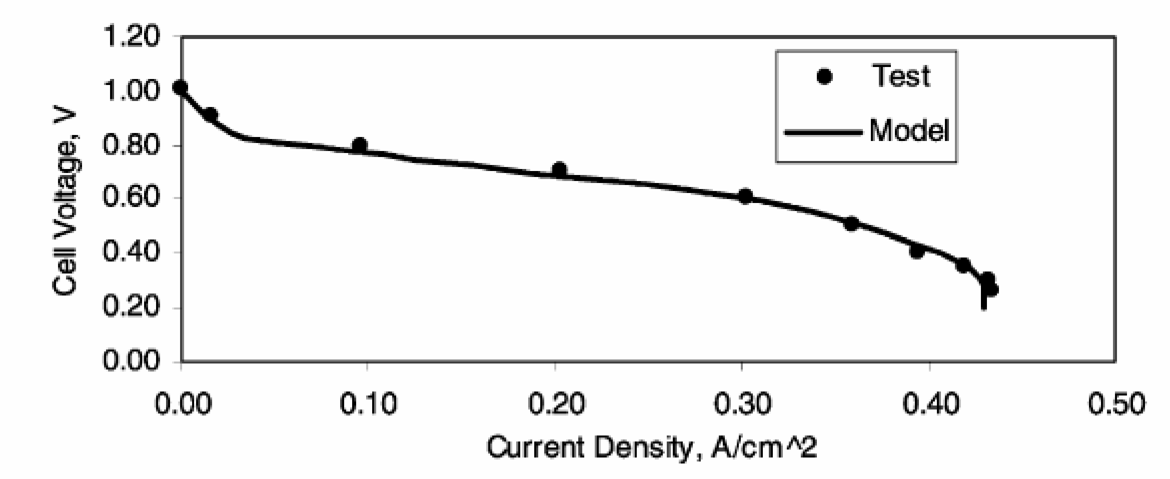

Figure 91: Numerical and experimental performance curves for test cell.

Table 26: Physical conditions for fuel cell test.

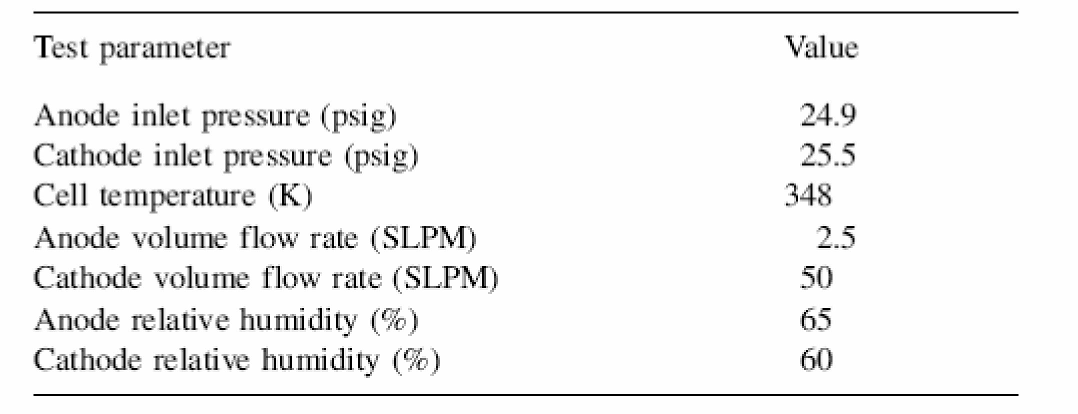

Test parameter	Value
Anode inlet pressure (psig)	24.9
Cathode inlet pressure (psig)	25.5
Cell temperature (K)	348
Anode volume flow rate (SLPM)	2.5
Cathode volume flow rate (SLPM)	50
Anode relative humidity (%)	65
Cathode relative humidity (%)	60

results in Fig. 92 show that for void fractions less than 0.04 the cell performance drops rapidly. This is due to rapidly increasing concentration overpotential. As the void fraction and permeability decrease, reactant transport by diffusion and advection within the catalyst layer drops sharply. The effect is exacerbated by the fact that the catalyst layers on the test MEA are relatively

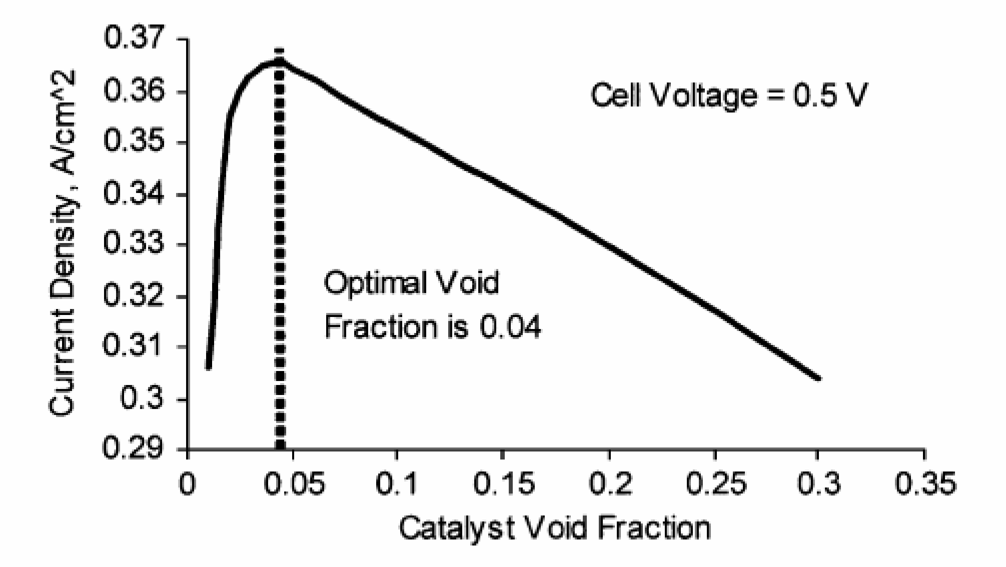

Figure 92: Cell performance variation with catalyst layer void fraction.

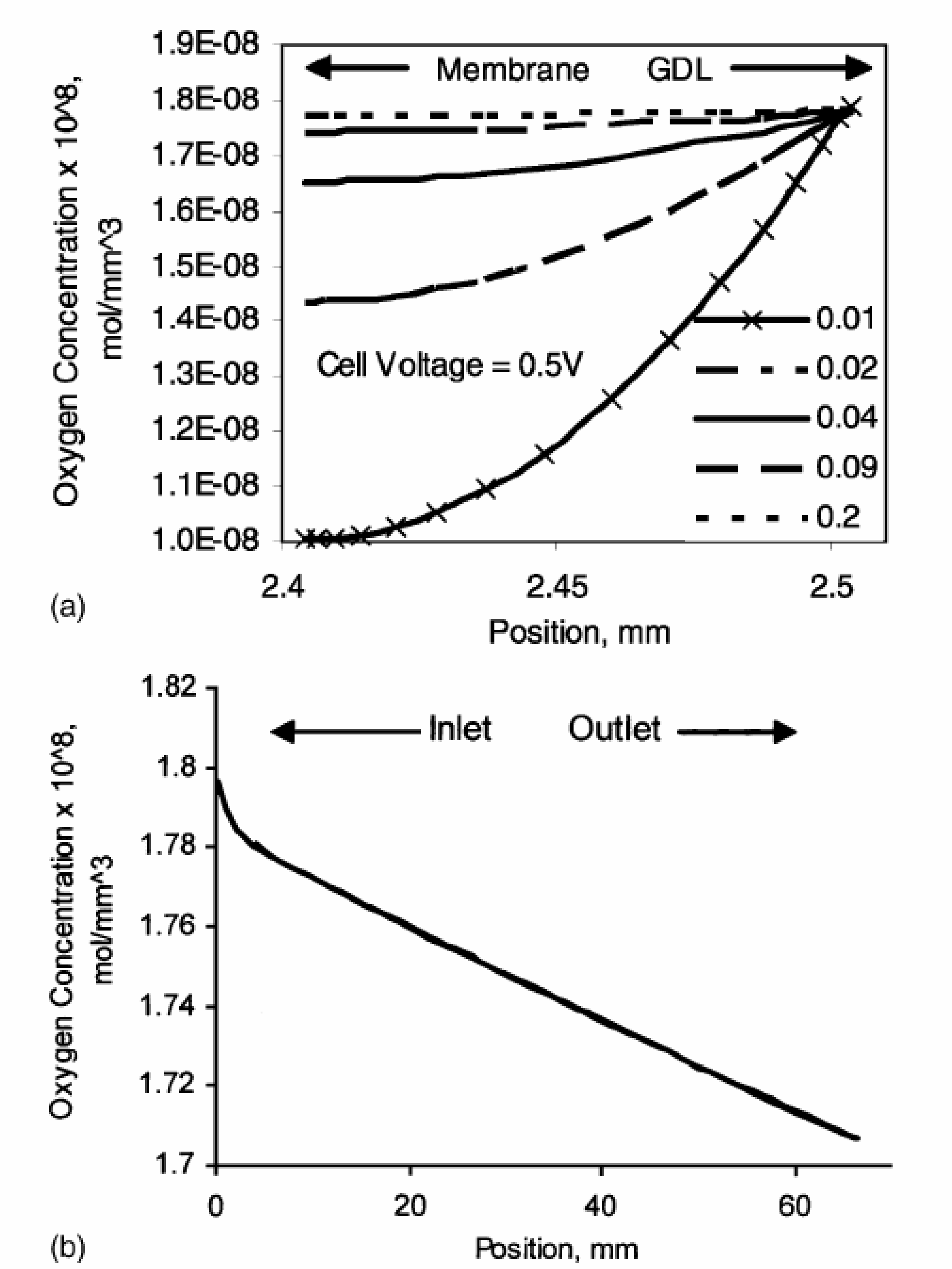

Figure 93: (a) Oxygen concentration change across the cathode catalyst layer. (b) Oxygen concentration change down the cathode flow channel, 9% void fraction. Inlet conditions as per Table 24.

thick, 100 mm. Catalyst layer thickness also plays a role in the performance drop off for void fractions greater than 0.04. As the void fraction increases, the ionomer fraction must decrease. Thus, while an increase in porosity improves mass flow and reduces concentration overpotential, it also increases the ohmic overpotential. Since the catalyst layers are so thick (relatively long ionic conduction pathway), the test cell is particularly sensitive to changes in ionic conductivity.

Fig. 93a shows the variation of oxygen concentration through the fuel cell (perpendicular to the flow direction) as the void fraction is varied. Fig. 93b shows the oxygen variation down the channel at the catalyst layer/membrane interface.

Fig. 93a shows that the overall decrease in concentration of oxygen through the catalyst is not a linear function of void fraction. As the void fraction changes from 0.04 to 0.02, the concentration drop increases by roughly 15%. As the void fraction changes from 0.02 to 0.01 the concentration drop increases by approximately 44%. This can be attributed to the effect of permeability on reactant transport. Fig. 93b shows that at the base case conditions, the oxygen concentration drops by 5% down the channel. The non-linear portion of the curve can be attributed to developing flow effects and higher local reaction rates.

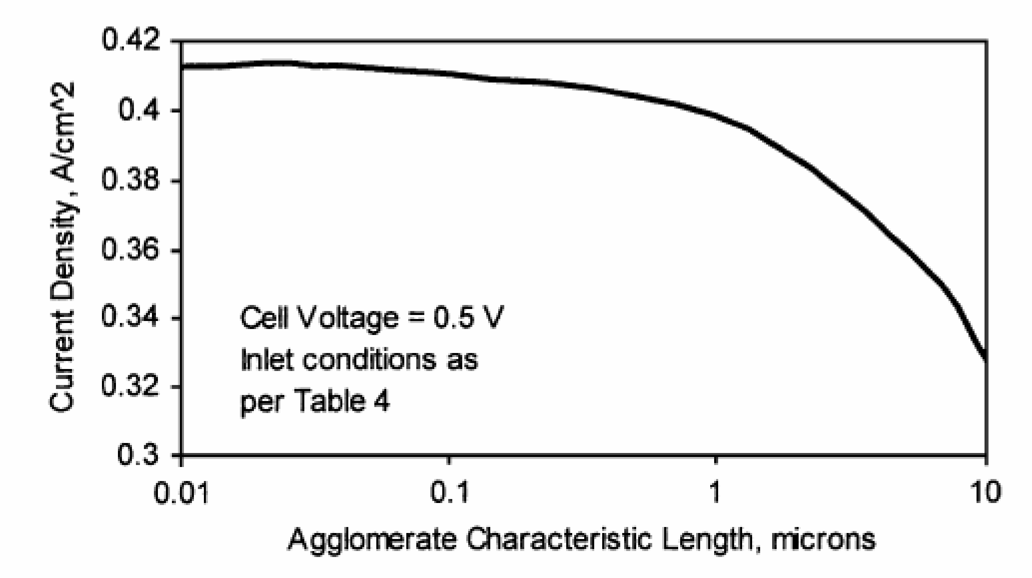

Figure 94: Cell performance variation with characteristic length of the catalyst agglomerates.

Fig. 94 shows the effect of the characteristic length of the catalyst agglomerates on fuel cell performance.

The results in this figure indicate that the size of the catalyst agglomerates can significantly affect cell performance. As agglomerate size increases, the reactants must diffuse through a greater distance to reach the catalyst sites, thus causing an increase in concentration overpotential. The smallest possible characteristic length is about 0.01 mm, which is the ratio of the volume to surface area for a single catalyzed carbon support particle with an assumed spherical geometry (50 nm diameter). One way to reduce the characteristic length is to create a catalyst layer with smaller agglomerates. Another way is to control the shape of the agglomerates, i.e. use a structure with a low volume to surface area ratio, such as a ribbon. For the test cell used in validating the model, the average characteristic agglomerate length was determined from the SEM analysis to be about 1 μm.

Conclusions

A steady state, two-dimensional model of a proton exchange membrane fuel cell has been developed for the purpose of predicting fuel cell behavior over a range of operating conditions and for use as a design tool. Work currently underway will expand this model to three-dimensional and incorporate liquid water transport. Results from our two-dimensional model were presented and validated with experimental data. Electron microscopy was found to be an effective method for determining certain physical parameters used in the model such as catalyst void fraction, agglomerate size, and catalyst layer thickness. The void fraction of the catalyst layer was found to significantly influence cell performance. Model results show that a void fraction of 0.04 in the catalyst layer is optimal for the ElectroChem MEA on which the model is based. In addition increasing the agglomerate characteristic length leads to a decrease in cell performance primarily due to increased diffusive resistance to reactant flow. Control of catalyst layer structure at the microscopic level, particularly void fraction and characteristic agglomerate length, could lead to better cell performance in the high current density region where concentration overpotential is most significant.

References

[1] T.E. Springer, T.A. Zawodzinski, S. Gottesfeld, Polymer electrolyte fuel cell model, J. Electrochem. Soc. 138 (8) 2334–2341.
[2] D.M. Bernardi, M.W. Verbrugge, A mathematical model of the solidpolymer-electrolyte fuel cell, J. Electrochem. Soc. 139 (9) 2477–2490.
[3] K.A. Starz, J. Koehler, K. Ruth, M. Vogt, Advanced MEA Technology of Mobile PEMFC Applications, Fuel Cell Power for Transportation, SP-1691, 2002.
[4] K. Broka, P. Ekdunge, Modelling the PEM fuel cell cathode, J. Appl. Electrochem. 27 (1997) 281–289.
[5] B Olsommer, Mathematical Model for a PEM Fuel Cell, Internal Report, Energy Management Institute, Mechanical Engineering, Virginia Polytechnic and State University, Blacksburg, VA, 2000.
[6] B. Eaton, M.R. von Spakovsky, M.W. Ellis, D.J. Nelson, B. Olsommer, N. Siegel. One-dimensional, transient model of heat, mass, and charge transfer in a proton exchange membrane, in: Proceedings of International Mechanical Engineering Congress and Exposition, IMECE'2001, ASME, AES, vol. 40, New York, NY, November 2001.
[7] D. Genevey, M.R. von Spakovsky, M.W. Ellis, D.J. Nelson, B. Olsommer, F. Topin, N. Siegel, N. Montel, Transient Model of the Heat, Mass and Charge Transfer as well as Electrochemistry in the Catalyst Layer of a PEMFC, in: Proceedings of International Mechanical Engineering Congress and Exposition, IMECE'2002, ASME IMECE Paper No. 33322, New York, NY, November 2002.
[8] T. Zhou, H. Liu, 3-D model of proton exchange membrane fuel cells, in: Proceeding of the ASME Heat Transfer Division, HTD, vol. 366–361, 2000.
[9] V. Gurau, H. Liu, S. Kakac, Two-dimensional model for proton exchange membrane fuel cells, J. AIChE 44, 2410–2422.
[10] S. Um, C.Y. Wang, K.S. Chen, Computational fluid dynamics modeling of proton exchange membrane fuel cells, J. Electrochem. Soc. 147 (12) (2000) 4485–4493.

[11] S. Shimpalee, S. Dutta, J.W. Van Zee, Numerical prediction of local temperature and current density in a PEM fuel cell, in: Proceedings of the ASME Heat Transfer Division, HTD, vol. 366–361, 2000.
[12] D. Natarajan, T.V. Nguyen, A two-dimensional, two-phase, multicomponent, transient model for the cathode of a proton exchange membrane fuel cell using conventional gas distributors, J. Electrochem. Soc. 148 (12) 1324–1335.
[13] S. Patankar, Numerical Heat Transfer and Fluid Flow, Hemisphere, Washington, DC, 1980.

A Two-Dimensional Computational Model of a PEMFC with Liquid Water Transport

Introduction

The development of economical, commercially available proton exchange membrane (PEM) fuel cells is essential to the development of a hydrogen based energy infrastructure. The PEM fuel cell is particularly important to the development of hydrogen fueled vehicles as demonstrated by the fact that all of the major automobile manufacturers are currently involved in some level of PEM fuel cell research with the goal of widespread commercialization within 10–15 years. To realize this and other development goals, fuel cell technology must continue to improve with respect to cost and performance. Computational models of fuel cells can contribute to this effort by providing researchers with the ability to create and optimize fuel cell designs rapidly and inexpensively before actually building a prototype.

Overview of fuel cell models

The need for computational tools to support the design process has led to the development of a number of fuel cell models. These models can generally be characterized by the scope of the model. In many cases, modeling efforts focus on a specific part or parts of the fuel cell, like the cathode catalyst layer [1–4], the cathode electrode (gas diffusion layer plus catalyst layer) [5], or the membrane electrode assembly (MEA) [6,7]. These models are very useful in that they may include a large portion of the relevant fuel cell physics while at the same time having relatively short solution times. However, these narrowly focused models neglect important parts of the fuel cell making it impossible to get a complete picture of the phenomena governing fuel cell behavior. Models that include all parts of a fuel cell are typically two- or three-dimensional and reflect many of the physical processes occurring within the fuel cell [8–12]. Comprehensive models rely on the determination of a large number of properties and operating parameters and can be much more computationally intensive, leading to longer solution times. However, these disadvantages are typically outweighed by the benefit of being able to assess the influence of a greater number of design parameters and their associated physical processes. The model presented in this work is a comprehensive two-dimensional model that includes multicomponent and multiphase transport both along the flow direction (down the gas channel) and through the MEA.

Models of liquid water transport

A comprehensive computational model should include the equations and other numerical relations needed to fully define fuel cell behavior over the range of interest. Early multidimensional models described gas transport in the flow channels, gas diffusion layers (GDLs), and the membrane [11,10]. More recent models include a detailed description of the catalyst layers that reflects the agglomerate nature of these regions [12]. Recently, there has been an interest in describing operating regimes that are dominated by mass transport limitations resulting, in part, from the formation and transport of liquid water within the fuel cell. To model fuel cell performance in these regimes, it is necessary to include equations that describe not only the motion of water within the liquid phase, but also mass transfer between phases. He et al. [15] present a model for liquid water transport in the cathode gas diffusion layer of a fuel cell with an interdigitated flowfield. As part of their work they formulate a switching function that is used to toggle source terms on and off depending on whether water is condensing into the liquid phase or evaporating into the vapor phase. They also introduce a term to account for water transport by advection, or transport due to the motion of the bulk flow, which is an important transport mechanism for interdigitated flowfields. In a continuation of this work, Natarajan and Nguyen [16] develop a diffusive expression to account for water transport via capillary pressure in the porous electrode. They neglect water transport by advection since their model uses a conventional flowfield.Wang andWang [17] have also developed a model for two phase flow in an interdigitated cathode. They assume transport by capillary pressure only and do not include mass transport between phases. All three of these models treat the catalyst layer as an interface and so do not consider effects due to water buildup within the catalyst layer. The model of Baschuk and Li [18] is one-dimensional and includes liquid water effects in both the gas diffusion layer and the catalyst layer. In the Baschuk and Li model, phase change is neglected and the volume fraction of liquid water in the porous regions must be specified as opposed to being calculated.

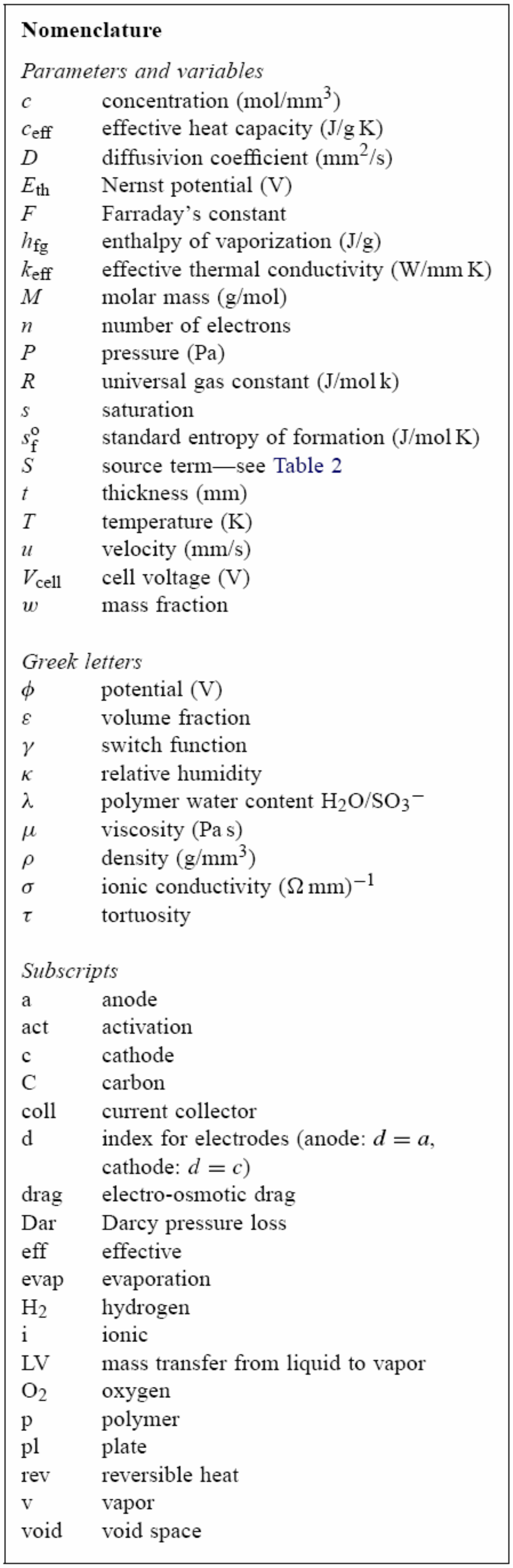

Nomenclature

Parameters and variables

c	concentration (mol/mm^3)
c_{eff}	effective heat capacity (J/g K)
D	diffusivion coefficient (mm^2/s)
E_{th}	Nernst potential (V)
F	Farraday's constant
h_{fg}	enthalpy of vaporization (J/g)
k_{eff}	effective thermal conductivity (W/mm K)
M	molar mass (g/mol)
n	number of electrons
P	pressure (Pa)
R	universal gas constant (J/mol k)
s	saturation
$s_{\mathrm{f}}^{\mathrm{o}}$	standard entropy of formation (J/mol K)
S	source term—see Table 2
t	thickness (mm)
T	temperature (K)
u	velocity (mm/s)
V_{cell}	cell voltage (V)
w	mass fraction

Greek letters

ϕ	potential (V)
ε	volume fraction
γ	switch function
κ	relative humidity
λ	polymer water content $H_2O/SO_3{}^-$
μ	viscosity (Pa s)
ρ	density (g/mm^3)
σ	ionic conductivity (Ω mm)$^{-1}$
τ	tortuosity

Subscripts

a	anode
act	activation
c	cathode
C	carbon
coll	current collector
d	index for electrodes (anode: $d = a$, cathode: $d = c$)
drag	electro-osmotic drag
Dar	Darcy pressure loss
eff	effective
evap	evaporation
H_2	hydrogen
i	ionic
LV	mass transfer from liquid to vapor
O_2	oxygen
p	polymer
pl	plate
rev	reversible heat
v	vapor
void	void space

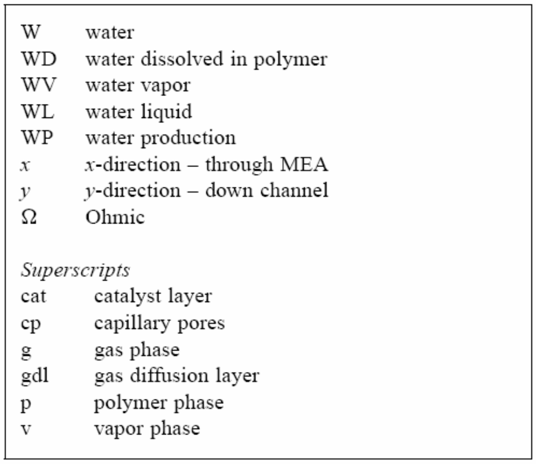

W	water
WD	water dissolved in polymer
WV	water vapor
WL	water liquid
WP	water production
x	x-direction – through MEA
y	y-direction – down channel
Ω	Ohmic

Superscripts

cat	catalyst layer
cp	capillary pores
g	gas phase
gdl	gas diffusion layer
p	polymer phase
v	vapor phase

Determination of physical properties

Another important part of developing a useful computational fuel cell model is the accurate determination of the physical properties on which the model is based. These properties may include: porosity of the gas diffusion layer and catalyst layer; the ionic conductivity of the polymer membrane; mass transfer coefficients; kinetic parameters such as the exchange current density and reaction surface area; and structural properties such as the thicknesses of the catalyst layers, membrane, and gas diffusion layers. Many of these properties can be experimentally determined with considerable accuracy. Others, like interphase mass transfer coefficients, are more difficult to determine and must be estimated. In either case, it is important to take great care with the values used as they may significantly affect the results [1]. Prior research has determined many of the physical properties needed for modeling. The work by Parthasarathy et al. [13] and Zhang et al. [19] contains experimentally determined values for many of the kinetic parameters involved with the oxygen reduction reaction occurring at the cathode as well as data regarding the solubility and diffusivity of oxygen in Nafion®. Ihonen et al. [14] present data for the pore size distribution and porosity of the catalyst layer. In their work, they compare the pore size distribution as determined by both gas and mercury porosimetry and show that the two methods provide nearly identical results for the catalyst layers that they tested. Many of the required properties for Nafion® 1100, including ionic conductivity and the electro-osmotic drag coefficient, can be found in the work by Springer et al. [6]. Marr and Li [2] present data for catalyst surface area as it relates to the type of catalyst used in the MEA. This data is for a perfectly uniform catalyst deposition. However, transmission electron microscope (TEM) images such as those shown by Siegel et al. [12] reveal that the catalyst deposition is not uniform and property data must be modified to account for the effect of catalyst non-uniformities. In the current work, we experimentally determine the catalyst layer porosity and thickness using a scanning electron microscope (SEM) and the reaction surface area using cyclic voltammetry.

Characteristics of present model

The present work presents a comprehensive model of a PEM fuel cell that incorporates the significant physical processes and the key parameters affecting fuel cell performance. The model is two-dimensional and includes the transport of gaseous species, protons, energy, and water dissolved in the ion conducting polymer. The model also addresses the transport of liquid water within the fuel cell with liquid water assumed to be transported by capillary pressure within the gas diffusion layers and catalyst layers and by advection within the gas channels. Water is assumed to be exchanged among three phases—liquid, vapor, and dissolved1—and equilibrium among these phases is assumed. Electrochemical kinetics are modeled with standard rate equations adapted to an agglomerate catalyst structure. The model reflects the influence of numerous parameters on fuel cell performance including geometry, porosity of the cell materials, catalyst area, polymer properties, catalyst layer composition, and others. This paper describes the development of the model, the determination of properties for use in the model, the validation of the model using experimental data, and the application of the model to explain observed experimental phenomena.

Model development

Fig. 95 shows the solution domain of the model. In the anode and cathode gas channels, fuel and oxidant flow along the surface of the membrane electrode assembly. In these regions, the flow is considered to be laminar. Reactants move from the gas channels into the gas diffusion layers (GDL) which serve to more uniformly distribute the reactants across the surface of the catalyst layer. In the catalyst layers, the reactants are transported by diffusion and advection while participating in electrochemical reactions. The polymer membrane is assumed to transport only protons and dissolved water. The current collector plates are not explicitly included in the computational model. Their influence with respect to energy transport is included and discussed in the next section.

Governing equations

The governing equations include conservation of mass, momentum, ionic charge, and energy as well as individual species conservation equations. The governing equations are presented in Table 27. Related terms that describe the rate at which the conserved quantity is added or removed from the solution domain are referred to as "source" terms and are presented in Table 28. Constitutive relations describing reaction rates, polymer properties, gas properties, and liquid properties are provided in Table 29. Each of the governing equations is developed for the entire solution domain of the model with source and transport terms modified in each region to reflect the appropriate physical phenomena. Eq. (1) describes conservation of mass for the entire gas phase. Source terms reflect changes in the overall gas phase mass flow due to consumption or production of gas species via reaction and due to mass transfer between water in the vapor phase and water that is in the liquid phase or dissolved in the polymer. The system of equations that model the interphase mass transfer is described in more detail in the following section. The gas phase mixture density is determined from the temperature, pressure, and mixture molar mass using the ideal gas equation, Eq. (33). Conservation of momentum is expressed by the Navier–Stokes equations in vector form, Eqs. (2a) and (2b), which are modified by source terms described by Eqs. (9) and (10) to account for Darcy flow in the porous regions of the model. The Darcy terms are active in the GDLs and catalyst layers only; the inertial and bulk viscous terms are neglected in these regions. The species equations for oxygen and water vapor are given by Eqs. (3) and (4), respectively. For both the anode and cathode sides of the cell, the number of species equations is one less than the number of species. At the anode, the species equation for water vapor is solved. The hydrogen mass fraction is calculated from the solution to the water vapor equation and the overall gas phase conservation equation. At the cathode, both water vapor and oxygen species equations are solved. The nitrogen mass fraction is determined from the solutions to these species equations and the overall gas phase conservation equation. The diffusion of each species within the bulk flow is given by the first term on the right side. The diffusion coefficients for multi-component flow, which are determined by Eqs. (34a)–(34c), are based on a simplification of the Stefan-Maxwell equations and in porous regions are modified by porosity and tortuosity factors [9,22]. The advective term for each of the species equations is separated into two parts. The first is equal to the product of velocity, mixture density, and mass fraction gradient. The second term is the product of mass fraction and the divergence of total mass flux. For the oxygen species equation, Eq. (3), the consumption of oxygen via reaction is reflected in the source term given by Eq. (12). The water vapor transport equation, Eq. (4), reflects the movement of water vapor by diffusion and bulk motion; the exchange of water between the vapor phase and the liquid phase is given by Eq. (14); the exchange of water between the vapor phase and the dissolved phase by Eq. (15); and the production of water by Eq. (13).

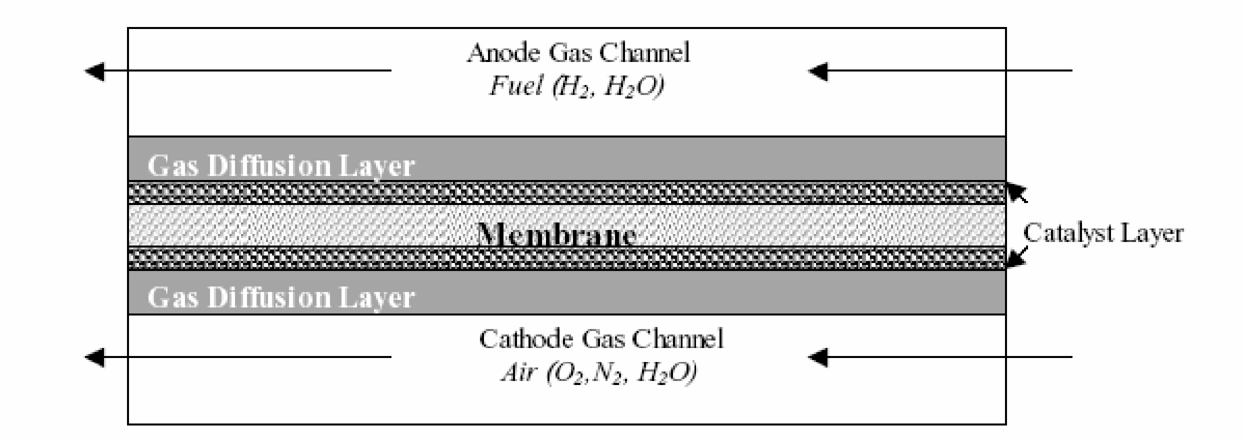

Figure 95: Solution domain.

Table 27: Governing equations.

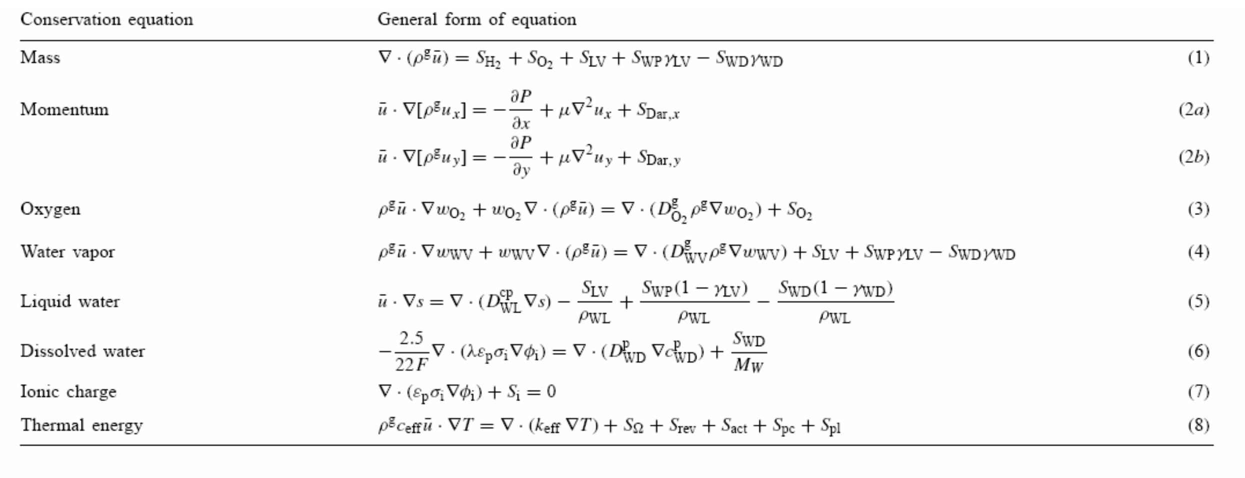

Conservation equation	General form of equation	
Mass	$\nabla \cdot (\rho^{g}\bar{u}) = S_{H_2} + S_{O_2} + S_{LV} + S_{WP}\gamma_{LV} - S_{WD}\gamma_{WD}$	(1)
Momentum	$\bar{u} \cdot \nabla[\rho^{g}u_x] = -\frac{\partial P}{\partial x} + \mu\nabla^2 u_x + S_{Dar,x}$	(2*a*)
	$\bar{u} \cdot \nabla[\rho^{g}u_y] = -\frac{\partial P}{\partial y} + \mu\nabla^2 u_y + S_{Dar,y}$	(2*b*)
Oxygen	$\rho^{g}\bar{u} \cdot \nabla w_{O_2} + w_{O_2}\nabla \cdot (\rho^{g}\bar{u}) = \nabla \cdot (D^{g}_{O_2}\rho^{g}\nabla w_{O_2}) + S_{O_2}$	(3)
Water vapor	$\rho^{g}\bar{u} \cdot \nabla w_{WV} + w_{WV}\nabla \cdot (\rho^{g}\bar{u}) = \nabla \cdot (D^{g}_{WV}\rho^{g}\nabla w_{WV}) + S_{LV} + S_{WP}\gamma_{LV} - S_{WD}\gamma_{WD}$	(4)
Liquid water	$\bar{u} \cdot \nabla s = \nabla \cdot (D^{cp}_{WL}\nabla s) - \frac{S_{LV}}{\rho_{WL}} + \frac{S_{WP}(1-\gamma_{LV})}{\rho_{WL}} - \frac{S_{WD}(1-\gamma_{WD})}{\rho_{WL}}$	(5)
Dissolved water	$-\frac{2.5}{22F}\nabla \cdot (\lambda\varepsilon_p\sigma_i\nabla\phi_i) = \nabla \cdot (D^{p}_{WD}\nabla c^{p}_{WD}) + \frac{S_{WD}}{M_W}$	(6)
Ionic charge	$\nabla \cdot (\varepsilon_p\sigma_i\nabla\phi_i) + S_i = 0$	(7)
Thermal energy	$\rho^{g}c_{eff}\bar{u} \cdot \nabla T = \nabla \cdot (k_{eff}\nabla T) + S_{\Omega} + S_{rev} + S_{act} + S_{pc} + S_{pl}$	(8)

Table 28: Source terms.

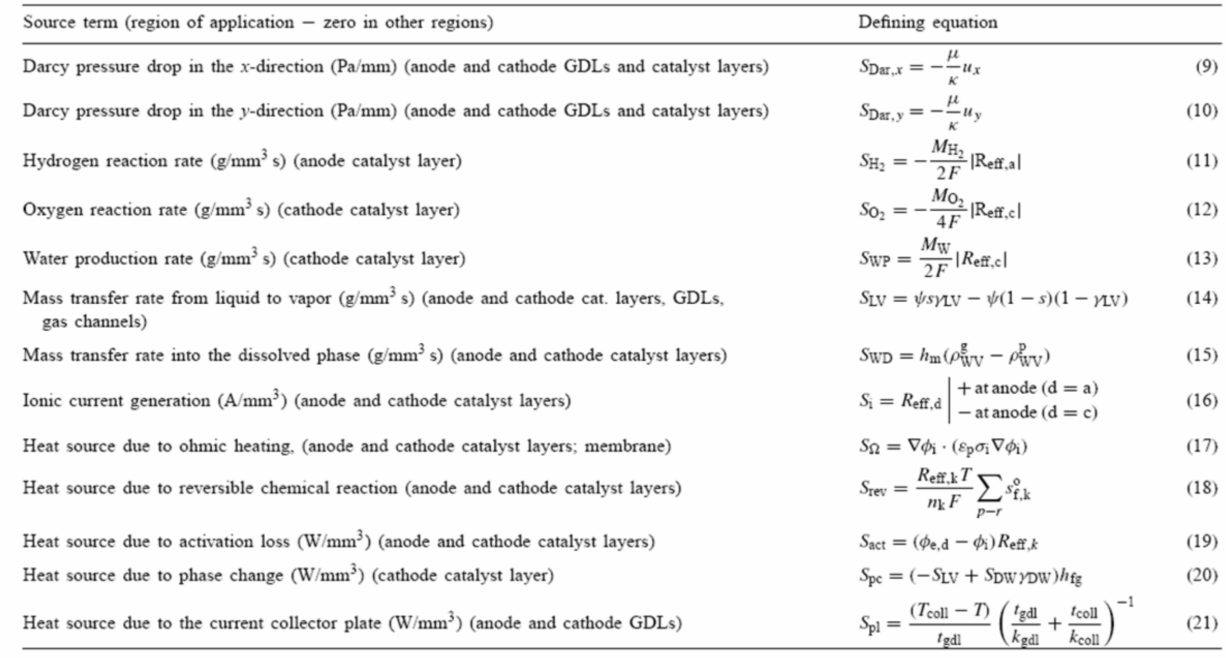

Source term (region of application − zero in other regions)	Defining equation	
Darcy pressure drop in the *x*-direction (Pa/mm) (anode and cathode GDLs and catalyst layers)	$S_{\mathrm{Dar},x} = -\frac{\mu}{\kappa} u_x$	(9)
Darcy pressure drop in the *y*-direction (Pa/mm) (anode and cathode GDLs and catalyst layers)	$S_{\mathrm{Dar},y} = -\frac{\mu}{\kappa} u_y$	(10)
Hydrogen reaction rate (g/mm^3 s) (anode catalyst layer)	$S_{\mathrm{H_2}} = -\frac{M_{\mathrm{H_2}}}{2F} \lvert \mathrm{R}_{\mathrm{eff,a}} \rvert$	(11)
Oxygen reaction rate (g/mm^3 s) (cathode catalyst layer)	$S_{\mathrm{O_2}} = -\frac{M_{\mathrm{O_2}}}{4F} \lvert \mathrm{R}_{\mathrm{eff,c}} \rvert$	(12)
Water production rate (g/mm^3 s) (cathode catalyst layer)	$S_{\mathrm{WP}} = \frac{M_{\mathrm{W}}}{2F} \lvert R_{\mathrm{eff,c}} \rvert$	(13)
Mass transfer rate from liquid to vapor (g/mm^3 s) (anode and cathode cat. layers, GDLs, gas channels)	$S_{\mathrm{LV}} = \psi s \gamma_{\mathrm{LV}} - \psi(1-s)(1-\gamma_{\mathrm{LV}})$	(14)
Mass transfer rate into the dissolved phase (g/mm^3 s) (anode and cathode catalyst layers)	$S_{\mathrm{WD}} = h_{\mathrm{m}}(\rho_{\mathrm{WV}}^{\mathrm{g}} - \rho_{\mathrm{WV}}^{\mathrm{p}})$	(15)
Ionic current generation (A/mm^3) (anode and cathode catalyst layers)	$S_{\mathrm{i}} = R_{\mathrm{eff,d}} \left\vert \begin{array}{l} + \text{at anode (d = a)} \\ - \text{at anode (d = c)} \end{array} \right.$	(16)
Heat source due to ohmic heating, (anode and cathode catalyst layers; membrane)	$S_{\Omega} = \nabla\phi_{\mathrm{i}} \cdot (\varepsilon_{\mathrm{p}} \sigma_{\mathrm{i}} \nabla\phi_{\mathrm{i}})$	(17)
Heat source due to reversible chemical reaction (anode and cathode catalyst layers)	$S_{\mathrm{rev}} = \frac{R_{\mathrm{eff,k}} T}{n_{\mathrm{k}} F} \sum_{p-r} s_{\mathrm{f,k}}^{\mathrm{o}}$	(18)
Heat source due to activation loss (W/mm^3) (anode and cathode catalyst layers)	$S_{\mathrm{act}} = (\phi_{\mathrm{e,d}} - \phi_{\mathrm{i}}) R_{\mathrm{eff},k}$	(19)
Heat source due to phase change (W/mm^3) (cathode catalyst layer)	$S_{\mathrm{pc}} = (-S_{\mathrm{LV}} + S_{\mathrm{DW}} \gamma_{\mathrm{DW}}) h_{\mathrm{fg}}$	(20)
Heat source due to the current collector plate (W/mm^3) (anode and cathode GDLs)	$S_{\mathrm{pl}} = \frac{(T_{\mathrm{coll}} - T)}{t_{\mathrm{gdl}}} \left(\frac{t_{\mathrm{gdl}}}{k_{\mathrm{gdl}}} + \frac{t_{\mathrm{coll}}}{k_{\mathrm{coll}}} \right)^{-1}$	(21)

Table 29: Closure relations.

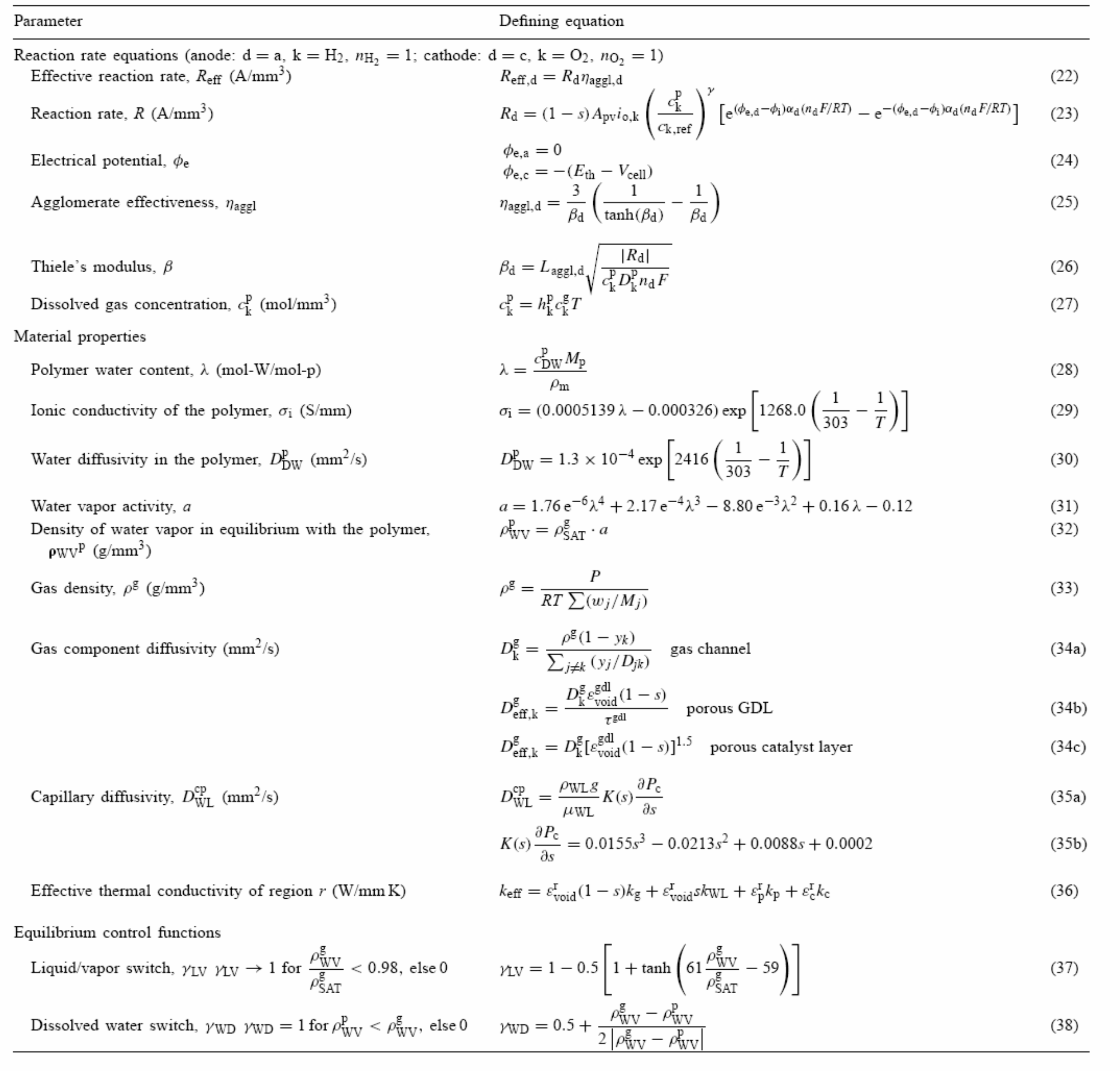

Parameter	Defining equation	
Reaction rate equations (anode: d = a, k = H_2, $n_{H_2} = 1$; cathode: d = c, k = O_2, $n_{O_2} = 1$)		
Effective reaction rate, R_{eff} ($\mathrm{A/mm^3}$)	$R_{\mathrm{eff,d}} = R_{\mathrm{d}} \eta_{\mathrm{aggl,d}}$	(22)
Reaction rate, R ($\mathrm{A/mm^3}$)	$R_{\mathrm{d}} = (1-s) A_{\mathrm{pv}} i_{\mathrm{o,k}} \left(\frac{c_{\mathrm{k}}^{\mathrm{p}}}{c_{\mathrm{k,ref}}} \right)^{\gamma} \left[\mathrm{e}^{(\phi_{\mathrm{e,d}} - \phi_{\mathrm{i}}) \alpha_{\mathrm{d}} (n_{\mathrm{d}} F/RT)} - \mathrm{e}^{-(\phi_{\mathrm{e,d}} - \phi_{\mathrm{i}}) \alpha_{\mathrm{d}} (n_{\mathrm{d}} F/RT)} \right]$	(23)
Electrical potential, ϕ_{e}	$\phi_{\mathrm{e,a}} = 0$ $\phi_{\mathrm{e,c}} = -(E_{\mathrm{th}} - V_{\mathrm{cell}})$	(24)
Agglomerate effectiveness, η_{aggl}	$\eta_{\mathrm{aggl,d}} = \frac{3}{\beta_{\mathrm{d}}} \left(\frac{1}{\tanh(\beta_{\mathrm{d}})} - \frac{1}{\beta_{\mathrm{d}}} \right)$	(25)
Thiele's modulus, β	$\beta_{\mathrm{d}} = L_{\mathrm{aggl,d}} \sqrt{\frac{\lvert R_{\mathrm{d}} \rvert}{c_{\mathrm{k}}^{\mathrm{p}} D_{\mathrm{k}}^{\mathrm{p}} n_{\mathrm{d}} F}}$	(26)
Dissolved gas concentration, $c_{\mathrm{k}}^{\mathrm{p}}$ ($\mathrm{mol/mm^3}$)	$c_{\mathrm{k}}^{\mathrm{p}} = h_{\mathrm{k}}^{\mathrm{p}} c_{\mathrm{k}}^{\mathrm{g}} T$	(27)
Material properties		
Polymer water content, λ (mol-W/mol-p)	$\lambda = \frac{c_{\mathrm{DW}}^{\mathrm{p}} M_{\mathrm{p}}}{\rho_{\mathrm{m}}}$	(28)
Ionic conductivity of the polymer, σ_{i} (S/mm)	$\sigma_{\mathrm{i}} = (0.0005139\,\lambda - 0.000326) \exp \left[1268.0 \left(\frac{1}{303} - \frac{1}{T} \right) \right]$	(29)
Water diffusivity in the polymer, $D_{\mathrm{DW}}^{\mathrm{p}}$ ($\mathrm{mm^2/s}$)	$D_{\mathrm{DW}}^{\mathrm{p}} = 1.3 \times 10^{-4} \exp \left[2416 \left(\frac{1}{303} - \frac{1}{T} \right) \right]$	(30)
Water vapor activity, a	$a = 1.76\,\mathrm{e}^{-6} \lambda^4 + 2.17\,\mathrm{e}^{-4} \lambda^3 - 8.80\,\mathrm{e}^{-3} \lambda^2 + 0.16\,\lambda - 0.12$	(31)
Density of water vapor in equilibrium with the polymer, $\rho_{\mathrm{WV}}{}^{\mathrm{p}}$ ($\mathrm{g/mm^3}$)	$\rho_{\mathrm{WV}}^{\mathrm{p}} = \rho_{\mathrm{SAT}}^{\mathrm{g}} \cdot a$	(32)
Gas density, ρ^{g} ($\mathrm{g/mm^3}$)	$\rho^{\mathrm{g}} = \frac{P}{RT \sum (w_j / M_j)}$	(33)
Gas component diffusivity ($\mathrm{mm^2/s}$)	$D_{\mathrm{k}}^{\mathrm{g}} = \frac{\rho^{\mathrm{g}} (1 - y_k)}{\sum_{j \neq k} (y_j / D_{jk})}$ gas channel	(34a)
	$D_{\mathrm{eff,k}}^{\mathrm{g}} = \frac{D_{\mathrm{k}}^{\mathrm{g}} \varepsilon_{\mathrm{void}}^{\mathrm{gdl}} (1 - s)}{\tau^{\mathrm{gdl}}}$ porous GDL	(34b)
	$D_{\mathrm{eff,k}}^{\mathrm{g}} = D_{\mathrm{k}}^{\mathrm{g}} [\varepsilon_{\mathrm{void}}^{\mathrm{gdl}} (1 - s)]^{1.5}$ porous catalyst layer	(34c)
Capillary diffusivity, $D_{\mathrm{WL}}^{\mathrm{cp}}$ ($\mathrm{mm^2/s}$)	$D_{\mathrm{WL}}^{\mathrm{cp}} = \frac{\rho_{\mathrm{WL}} g}{\mu_{\mathrm{WL}}} K(s) \frac{\partial P_{\mathrm{c}}}{\partial s}$	(35a)
	$K(s) \frac{\partial P_{\mathrm{c}}}{\partial s} = 0.0155 s^3 - 0.0213 s^2 + 0.0088 s + 0.0002$	(35b)
Effective thermal conductivity of region r (W/mm K)	$k_{\mathrm{eff}} = \varepsilon_{\mathrm{void}}^{\mathrm{r}} (1 - s) k_{\mathrm{g}} + \varepsilon_{\mathrm{void}}^{\mathrm{r}} s k_{\mathrm{WL}} + \varepsilon_{\mathrm{p}}^{\mathrm{r}} k_{\mathrm{p}} + \varepsilon_{\mathrm{c}}^{\mathrm{r}} k_{\mathrm{c}}$	(36)
Equilibrium control functions		
Liquid/vapor switch, γ_{LV} $\gamma_{\mathrm{LV}} \to 1$ for $\frac{\rho_{\mathrm{WV}}^{\mathrm{g}}}{\rho_{\mathrm{SAT}}^{\mathrm{g}}} < 0.98$, else 0	$\gamma_{\mathrm{LV}} = 1 - 0.5 \left[1 + \tanh \left(61 \frac{\rho_{\mathrm{WV}}^{\mathrm{g}}}{\rho_{\mathrm{SAT}}^{\mathrm{g}}} - 59 \right) \right]$	(37)
Dissolved water switch, γ_{WD} $\gamma_{\mathrm{WD}} = 1$ for $\rho_{\mathrm{WV}}^{\mathrm{p}} < \rho_{\mathrm{WV}}^{\mathrm{g}}$, else 0	$\gamma_{\mathrm{WD}} = 0.5 + \frac{\rho_{\mathrm{WV}}^{\mathrm{g}} - \rho_{\mathrm{WV}}^{\mathrm{p}}}{2 \lvert \rho_{\mathrm{WV}}^{\mathrm{g}} - \rho_{\mathrm{WV}}^{\mathrm{p}} \rvert}$	(38)

Liquid water transport within the cell is modeled with Eq. (5). The variable that describes liquid water is the saturation, *s*, which is the volume fraction of liquid water relative to the pore volume in the porous sections of the fuel cell, i.e. *s* ≡ *V*WL *V*pore (39)

Within the porous electrodes, liquid water is transported by capillary pressure and interphase mass transfer. The bulk flow term is neglected. The diffusion coefficient for liquid water, *D* cp WL, accounts for water motion via capillary pressure and is based on a semi-empirical relation between capillary pressure and saturation [16]. Within the gas channels, capillary effects are neglected and the liquid is assumed to travel as droplets of negligible volume with a velocity that is equal to the bulk gas velocity. Water is exchanged with the liquid phase, due to evaporation into the vapor, as given by Eq. (14); production from the cathode reaction as given by Eq. (13) if the adjacent vapor is saturated; and transfer into the liquid from the dissolved phase as given by Eq. (15). Equilibrium between the various water phases is described in more detail in Section 2.2. Water in the dissolved form is transported within the polymer membrane and the polymer phase of the catalyst layer as described by Eq. (6). The transport mechanisms include diffusion, electro-osmotic drag, and inter-phase mass transfer as defined by Eq. (15). An advective term would be required if the gas pressure in the anode differed significantly from that in the cathode. For this model, the anode and cathode pressures are assumed to be equal and so the convective transport of water through the MEA is neglected. The transport of ions in the polymer regions of the fuel cell is described by Eq. (7), where the source term, Eq. (16), represents the production/consumption of protons via the electrochemical reactions in the catalyst layers. The rate of the electrochemical reaction is described by Eqs. (22) and (23) which represent a form of the Butler–Volmer relation modified by an effectiveness factor to account for the effect of diffusion through the agglomerate structures in the catalyst layer and multiplied by the term $(1 - s)$ to account for the occlusion of reaction sites due to the accumulation of liquid water within the cell [17]. The effectiveness term, given by Eq. (25), is a measure of how readily reactants diffuse through the spherical agglomerates. An effectiveness of 1.0 indicates that reactants diffusing through the agglomerates encounter no resistance. An effectiveness less than 1.0 indicates that the agglomerate offers resistance to reactant diffusion thereby limiting the reaction rate. The rate of reaction is controlled by the reactant concentration in the polymer at the interface with the reactant gas as given by Henry's law, Eq. (27), and by the local activation overpotential given by $(\varphi \mathrm{e,d} - \varphi \mathrm{i})$. The electrical potential is assumed to be constant over each electrode (catalyst and GDL). As indicated by Eq. (24), the electrical potential is set to zero on the anode side and to the negative of the total overvoltage on the cathode side. Conservation of thermal energy is expressed by Eq. (8) and reflects heat transfer by conduction and convection as well as source terms for Ohmic heating due to ionic resistance as given by Eq. (17), reversible heat as defined by Eq. (18), heat produced via activation losses as given by Eq. (19), and the latent heat associated with the phase change of water as given by Eq. (20). In this model, the collector plates are not included in the solution domain. In an actual fuel cell, the shoulder of the plates would be in contact with the MEA and provide a low-resistance pathway for heat. The source term, $S\mathrm{pl}$, which is given by Eq. (21) approximates the heat transfer through the collector plates had they been part of the solution domain.

Mass transfer between dissolved, liquid, and vapor phases

The model presented here assumes that the three phases in which water can exist—liquid, vapor, and dissolved—are in equilibrium. With this assumption, the model does not address the actual rate of transport between the three phases or the actual path the water follows in moving among the phases. Instead, the phases are simply assumed to be connected by at least one transport path with the mass transfer coefficients along this path sufficiently large to ensure equilibrium. The water in the dissolved phase is assumed to be exchanged with the vapor phase. For convenience and numerical stability, it is assumed that water *leaving* the dissolved phase passes through the vapor phase and goes directly into the liquid phase. Water *entering* the dissolved phase comes directly from the vapor phase. Water is exchanged freely between the liquid and vapor phases, thus maintaining all three phases in equilibrium. Mass transfer among the phases and equilibrium constraints are implemented by the source terms of Eqs. (14) and (15) and switch functions given by Eqs. (37) and (38). The equilibrium between liquid and vapor phases is maintained by Eq. (14) which yields a large positive value for the term $S\mathrm{LV}$

(corresponding to rapid evaporation) if liquid is present and the adjacent vapor exists at a pressure below saturation. Conversely, if the pressure of the vapor phase exceeds the saturation pressure, the term SLV exhibits a large negative value (corresponding to rapid condensation). The dissolved phase is maintained in equilibrium by Eq. (15) which transfers water from the dissolved phase to the vapor phase in proportion to the difference between the vapor density, ρ G WV and the density of the vapor in equilibrium with the dissolved phase, ρ p WV. Water evaporating from the dissolved phase passes directly through the vapor phase and into the liquid as reflected by the term SWD(1−γWD)/ρWL in Eq. (5). Water enters the dissolved phase from the vapor phase as reflected by the term γWDSWD in the conservation equations for overall mass, Eq. (1) and water vapor, Eq. (4). The variable γWD is a switch term, defined by Eq. (38) that has a value of 1 when water is leaving the dissolved phase and zero otherwise. Finally, water entering or leaving the dissolved phase is reflected by the term SWD/Mw in the equation for dissolved water transport, Eq. (6).2 The mass transfer coefficients that permit exchange between the phases and the parameters for the gradual switch function, γLV, were chosen so that the three phases remain near equilibrium with one another. Numerical tests were conducted to verify that near-equilibrium conditions were maintained among the three phases and that the vapor pressure at which evaporation/condensation occurred was within ±2.5% of the saturation vapor pressure at the local temperature.

Table 30: Boundary conditions.

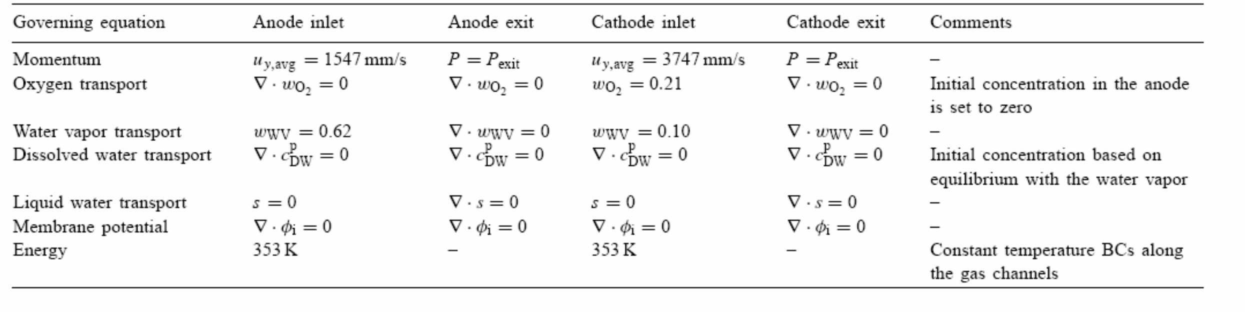

Governing equation	Anode inlet	Anode exit	Cathode inlet	Cathode exit	Comments
Momentum	$u_{y,\mathrm{avg}} = 1547\,\mathrm{mm/s}$	$P = P_{\mathrm{exit}}$	$u_{y,\mathrm{avg}} = 3747\,\mathrm{mm/s}$	$P = P_{\mathrm{exit}}$	–
Oxygen transport	$\nabla \cdot w_{\mathrm{O}_2} = 0$	$\nabla \cdot w_{\mathrm{O}_2} = 0$	$w_{\mathrm{O}_2} = 0.21$	$\nabla \cdot w_{\mathrm{O}_2} = 0$	Initial concentration in the anode is set to zero
Water vapor transport	$w_{\mathrm{WV}} = 0.62$	$\nabla \cdot w_{\mathrm{WV}} = 0$	$w_{\mathrm{WV}} = 0.10$	$\nabla \cdot w_{\mathrm{WV}} = 0$	–
Dissolved water transport	$\nabla \cdot c_{\mathrm{DW}}^{\mathrm{p}} = 0$	$\nabla \cdot c_{\mathrm{DW}}^{\mathrm{p}} = 0$	$\nabla \cdot c_{\mathrm{DW}}^{\mathrm{p}} = 0$	$\nabla \cdot c_{\mathrm{DW}}^{\mathrm{p}} = 0$	Initial concentration based on equilibrium with the water vapor
Liquid water transport	$s = 0$	$\nabla \cdot s = 0$	$s = 0$	$\nabla \cdot s = 0$	–
Membrane potential	$\nabla \cdot \phi_{\mathrm{i}} = 0$	$\nabla \cdot \phi_{\mathrm{i}} = 0$	$\nabla \cdot \phi_{\mathrm{i}} = 0$	$\nabla \cdot \phi_{\mathrm{i}} = 0$	–
Energy	353 K	–	353 K	–	Constant temperature BCs along the gas channels

Boundary conditions

Table 30 contains the boundary conditions and the starting solution used in the model. Since the model is solved by an iterative solution technique, the choice of a starting solution can affect convergence and solution time. The starting solution for the species was set equal to their respective inlet boundary values.

Physical property evaluation

In addition to governing equations and boundary conditions, the numerical model incorporates a number of parameters some of which are fundamental physical properties and others which may be chosen by the fuel cell designer. Table 31 indicates values for properties such as the viscosity of the reactant gases, the exchange current density on bright platinum, etc. that are not design variables. In general, the values in Table 5 were determined from the literature. Values for the exchange current density, transfer coefficient, number of electrons in the rate limiting step, solubility of oxygen in Nafion, and the diffusion coefficient for oxygen in Nafion were estimated from data presented by Zhang et al. [19]. The estimation of these properties was required given that that data in [19] is presented over a temperature range of 303–343 K, and the base case model was run at a temperature of 353 K. In addition, the value used for the diffusion coefficient of oxygen through Nafion is about one half of that reported in [19].

This was done because the diffusion coefficient in recast Nafion is smaller than in Nafion membranes [5]. Additional properties for Nafion were taken from Zawodzinski et al. [23]. Table 32 indicates values for parameters that can be specified by the fuel cell designer. Values in Table 32 were generally determined by direct measurements or specifications for the base case fuel cell that was used for validation of the numerical model. The base case fuel cell used for validation consisted of a 5 cm2 fuel cell assembly, carbon flow field plates, ELAT® GDLs, and a catalyzed Nafion 112 membrane. Geometric properties of the fuel cell assembly were measured directly. In the assembled cell, GDL thickness is non-uniform as it is highly compressed under the flowfield shoulders, but not under the gas channels. The thickness of the GDL was calculated as the average of the uncompressed GDL thickness and the compressed thickness, which was set by the gasket material. The porosity of the uncompressed GDL was assumed to be 0.6. This value was then adjusted to account for a decrease in void volume due to GDL compression. The tortuosity factor that modifies the gas species diffusion coefficients in the GDL was estimated from the work of Springer et al. [22].

Table 31: Physical properties.

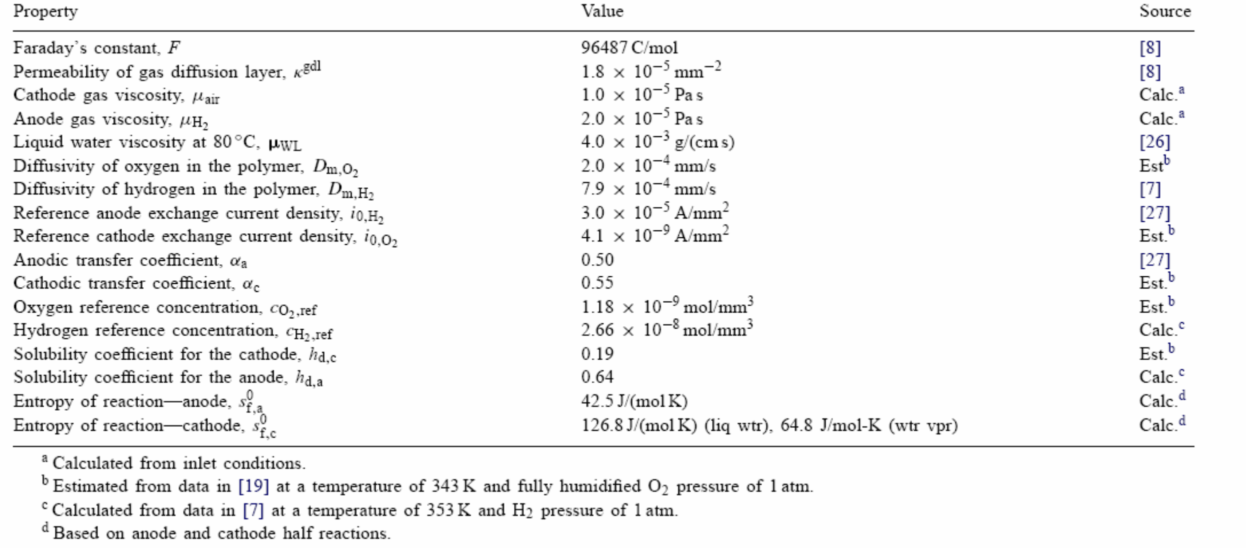

Property	Value	Source
Faraday's constant, F	96487 C/mol	[8]
Permeability of gas diffusion layer, κ^{gdl}	1.8×10^{-5} mm^{-2}	[8]
Cathode gas viscosity, μ_{air}	1.0×10^{-5} Pa s	Calc.[a]
Anode gas viscosity, μ_{H_2}	2.0×10^{-5} Pa s	Calc.[a]
Liquid water viscosity at 80 °C, μ_{WL}	4.0×10^{-3} g/(cm s)	[26]
Diffusivity of oxygen in the polymer, D_{m,O_2}	2.0×10^{-4} mm/s	Est[b]
Diffusivity of hydrogen in the polymer, D_{m,H_2}	7.9×10^{-4} mm/s	[7]
Reference anode exchange current density, i_{0,H_2}	3.0×10^{-5} A/mm^2	[27]
Reference cathode exchange current density, i_{0,O_2}	4.1×10^{-9} A/mm^2	Est.[b]
Anodic transfer coefficient, α_a	0.50	[27]
Cathodic transfer coefficient, α_c	0.55	Est.[b]
Oxygen reference concentration, $c_{O_2,ref}$	1.18×10^{-9} mol/mm^3	Est.[b]
Hydrogen reference concentration, $c_{H_2,ref}$	2.66×10^{-8} mol/mm^3	Calc.[c]
Solubility coefficient for the cathode, $h_{d,c}$	0.19	Est.[b]
Solubility coefficient for the anode, $h_{d,a}$	0.64	Calc.[c]
Entropy of reaction—anode, $s^0_{f,a}$	42.5 J/(mol K)	Calc.[d]
Entropy of reaction—cathode, $s^0_{f,c}$	126.8 J/(mol K) (liq wtr), 64.8 J/mol-K (wtr vpr)	Calc.[d]

[a] Calculated from inlet conditions.
[b] Estimated from data in [19] at a temperature of 343 K and fully humidified O_2 pressure of 1 atm.
[c] Calculated from data in [7] at a temperature of 353 K and H_2 pressure of 1 atm.
[d] Based on anode and cathode half reactions.

The catalyst layer for the base case cell was prepared using a catalyst ink composed of carbon supported catalyst (20 wt.% Pt on Vulcan XC-72R) dispersed in a 5 wt.% Nafion® 1100 solution. The fabrication technique was similar to the decal method given in Wilson et al. [20] with the exception that the ink was applied in the protonated, not TBA+ form. The mass and composition of the catalyst layer were recorded and used to determine the volume fraction of the various constituents and the overall catalyst layer porosity. The thickness of the catalyst layer was determined from SEM images of the MEA cross-section such as the one presented in Fig. 96. The catalyst layer porosity was determined by evaluating the solid volume of the catalyst layer based on its mass and composition and the total volume of the catalyst layer based on its thickness. The mass of the catalyst layer was determined by weighing the catalyst layer after it had been painted onto a Teflon decal and dried to remove all of the solvent. The solid volume of the catalyst layer, Vs, was then be determined by

$$V\mathrm{s} = m\mathrm{cat}x\mathrm{p}\ \rho\mathrm{p} + m\mathrm{cat}x\mathrm{C}x\mathrm{Pt}\ \rho\mathrm{Pt} + m\mathrm{cat}x\mathrm{C}(1 - x\mathrm{Pt})\ \rho\mathrm{C} \quad (40)$$

where $m$cat is the mass of the catalyst layer, xp the mass fraction of polymer in the catalyst, xC the mass fraction of carbon supported catalyst, xPt the mass fraction of platinum in the carbon supported catalyst, ρp the density of the polymer, ρC the density of the carbon support, ρPt the density of platinum. The total volume of the catalyst layer including the pores, Vtot, can be estimated from the SEM images. From these two volumes the porosity, εcat void, which is the volume fraction of pores in the catalyst layer relative to the total layer volume, can be calculated and is expressed as

εcat void = Vtot − Vs Vtot (41)

This approach for determining porosity assumes that the Nafion and carbon phases do not coexist (i.e. the Nafion does not fill the micropores in the activated carbon). This assumption is consistent with the work of Uchida et al. [24] who concluded that the Nafion only exists in the larger pores such as those between particles or agglomerates. Cyclic voltammetry (CV) was used to determine the active catalyst area, Aact, within the catalyst layer. The CV tests were conducted using an approach similar to that described by O'Hayre et al. [25]. With this approach, the electrical potential applied to the catalyst layer is varied from −0.1 to 1.0V and back in a triangle waveform while the current is recorded. The current is integrated over time to determine the charge transferred during the adsorption and desorption of a monolayer of hydrogen on the active catalyst surface. The active area of the catalyst can be then be calculated from

Aact = QA QPt (42)

where QA is the amount of charge (_C) transferred during adsorption (or desorption) and QPt the charge transferred during the adsorption of a monolayer of hydrogen on atomically smooth platinum (210 _C/cm2).

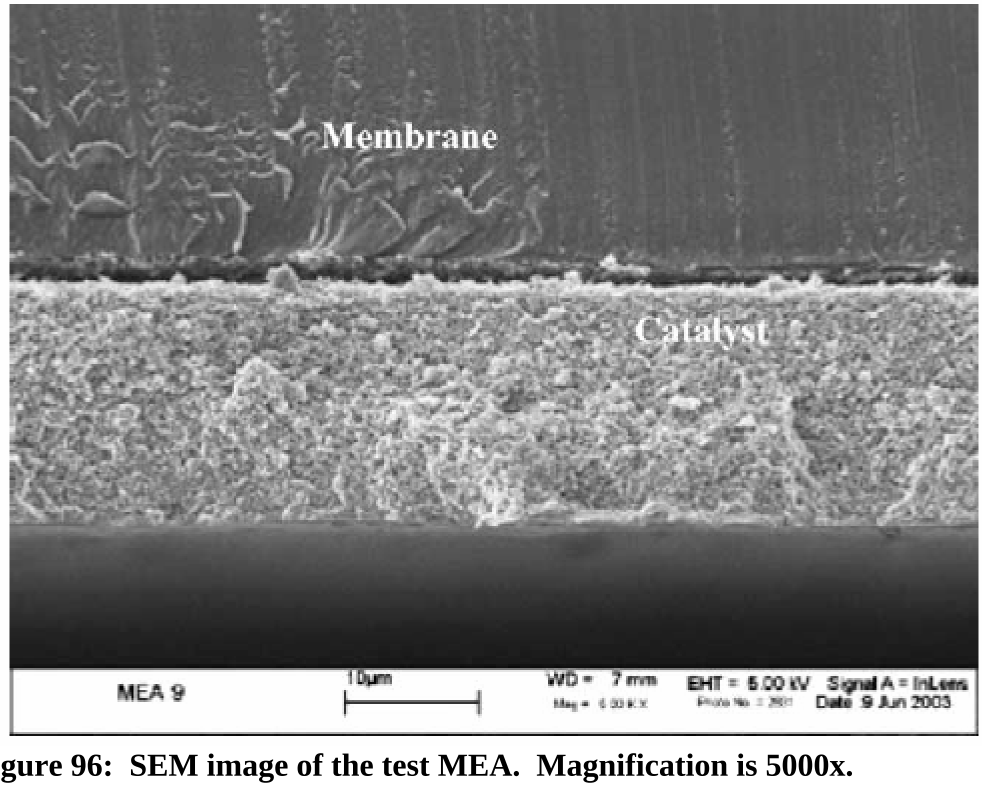

Figure 96: SEM image of the test MEA. Magnification is 5000x.

Table 32: Design and operating parameters for validation study.

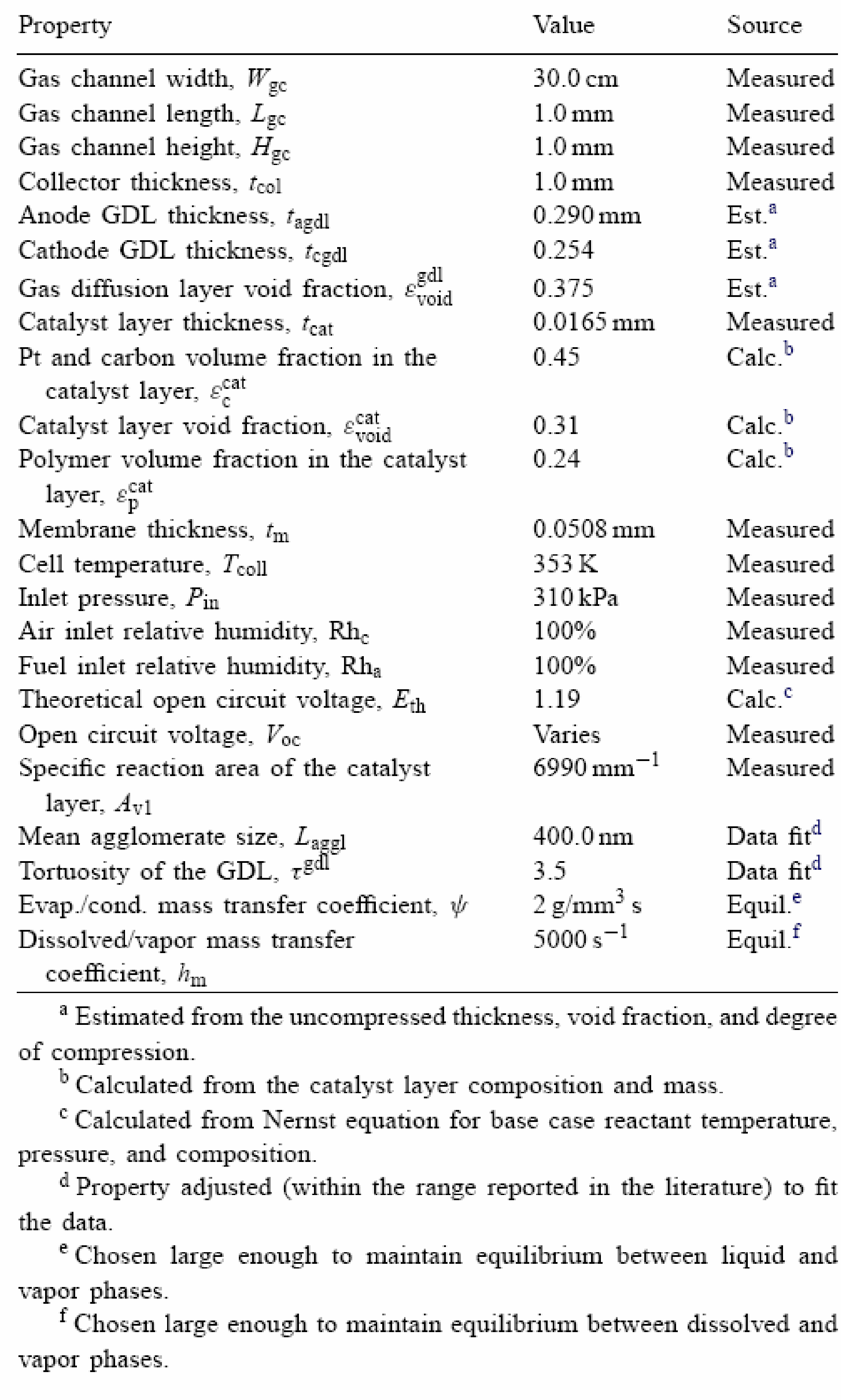

Property	Value	Source
Gas channel width, W_{gc}	30.0 cm	Measured
Gas channel length, L_{gc}	1.0 mm	Measured
Gas channel height, H_{gc}	1.0 mm	Measured
Collector thickness, t_{col}	1.0 mm	Measured
Anode GDL thickness, t_{agdl}	0.290 mm	Est.[a]
Cathode GDL thickness, t_{cgdl}	0.254	Est.[a]
Gas diffusion layer void fraction, ε_{void}^{gdl}	0.375	Est.[a]
Catalyst layer thickness, t_{cat}	0.0165 mm	Measured
Pt and carbon volume fraction in the catalyst layer, ε_{c}^{cat}	0.45	Calc.[b]
Catalyst layer void fraction, ε_{void}^{cat}	0.31	Calc.[b]
Polymer volume fraction in the catalyst layer, ε_{p}^{cat}	0.24	Calc.[b]
Membrane thickness, t_m	0.0508 mm	Measured
Cell temperature, T_{coll}	353 K	Measured
Inlet pressure, P_{in}	310 kPa	Measured
Air inlet relative humidity, Rh_c	100%	Measured
Fuel inlet relative humidity, Rh_a	100%	Measured
Theoretical open circuit voltage, E_{th}	1.19	Calc.[c]
Open circuit voltage, V_{oc}	Varies	Measured
Specific reaction area of the catalyst layer, A_{v1}	6990 mm^{-1}	Measured
Mean agglomerate size, L_{aggl}	400.0 nm	Data fit[d]
Tortuosity of the GDL, τ^{gdl}	3.5	Data fit[d]
Evap./cond. mass transfer coefficient, ψ	2 g/mm^3 s	Equil.[e]
Dissolved/vapor mass transfer coefficient, h_m	5000 s^{-1}	Equil.[f]

[a] Estimated from the uncompressed thickness, void fraction, and degree of compression.

[b] Calculated from the catalyst layer composition and mass.

[c] Calculated from Nernst equation for base case reactant temperature, pressure, and composition.

[d] Property adjusted (within the range reported in the literature) to fit the data.

[e] Chosen large enough to maintain equilibrium between liquid and vapor phases.

[f] Chosen large enough to maintain equilibrium between dissolved and vapor phases.

Numerical methods

The outer surfaces of the gas channels shown in Fig. 95 are bounded by the collector plates (not shown) and are impermeable to gases. As part of the single domain formulation, each governing equation is solved throughout the entire domain, even if the equation is not physically valid in every region. This is accomplished using a variety of numerical techniques [8,21]. For instance, to eliminate the diffusive flux of the gas species through the membrane, which is assumed impermeable to gases, the diffusivities of all gas species are set to zero within the membrane region of the model. The domain is divided into 64×121 elements. Mapped meshing is used to maintain a sufficient mesh density throughout the model domain. In regions of large gradients, such as at interfaces and in the catalyst layers, mesh size is decreased, while in the gas channels and other regions of relatively small gradients, it is much coarser. A sensitivity analysis was conducted by doubling the numberof elements in the mesh. The solution changed on average by less than 2.0% and so was assumed to be mesh independent. The equations are solved with the commercial CFD solver, CFDesign®.

Results and discussion

The numerical model is validated by comparing model results to experimental data. The base case cell was run at a cell temperature of 80 ◦C with the inlet reactant gases on both the anode and cathode sides maintained at a temperature of 80 ◦C, a pressure of 30 psig, and a relative humidity of 100%. The mass flow rate, at both the anode and cathode, corresponded to a stoichiometric ratio of 6 at a current density of 1 A/cm2. A comparison of model results with experimental data at 30 psig (base case) and 20 psig is shown in Fig. 97a and b, respectively.

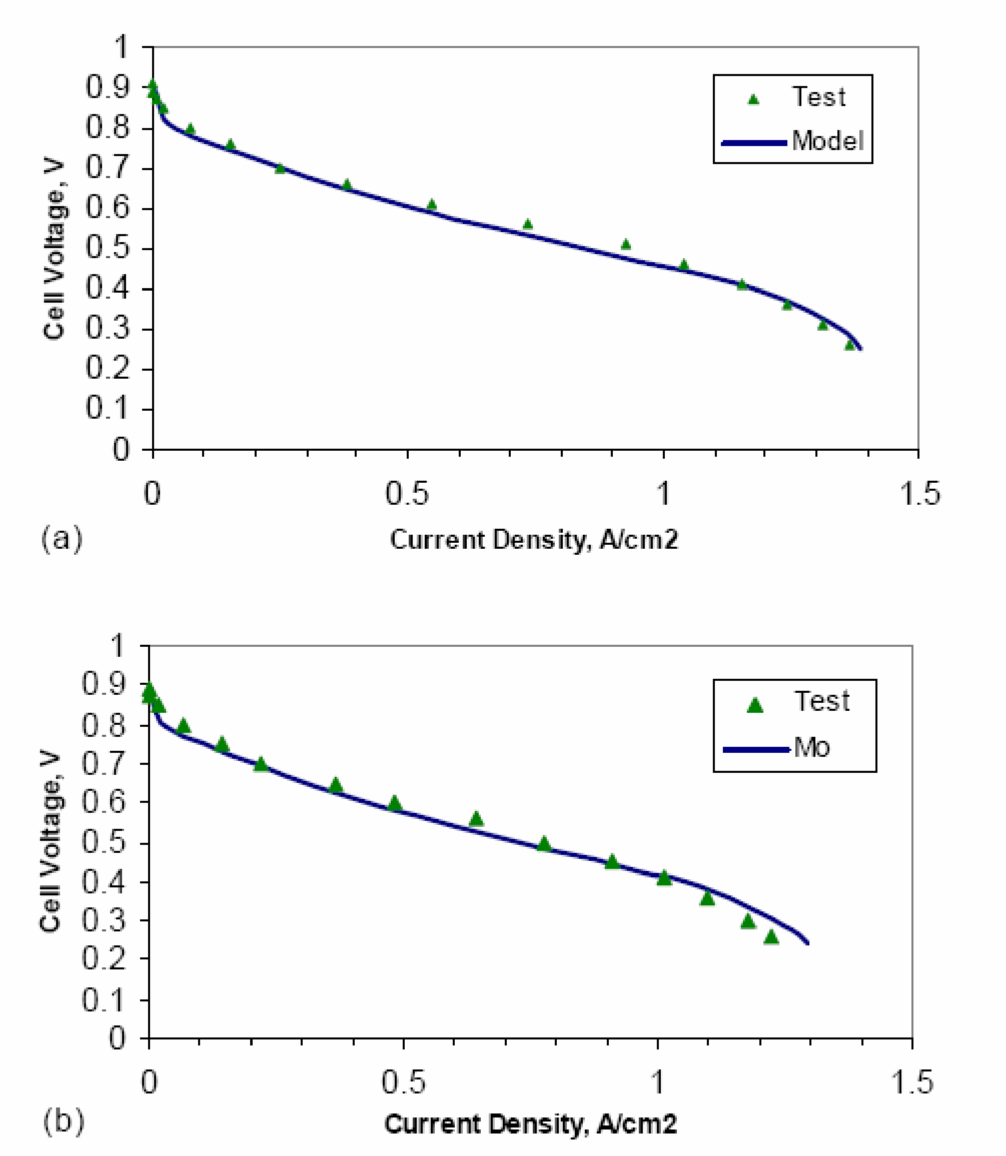

Figure 97: (a) Model comparison with test data at 30 psig (base case). (b) Model comparison with test data at 20 psig.

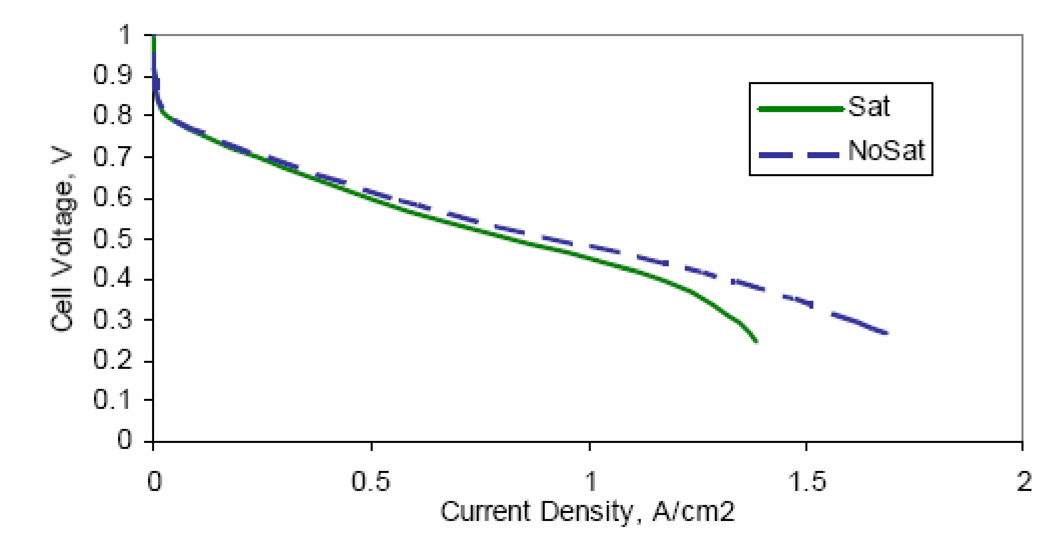

Figure 98: Effect of liquid water buildup on cell performance.

Some of the modeling parameters were estimated by adjusting their values until good agreement was achieved between the test results and the model output. This was done only once, for the 30 psig case. The results shown in Fig. 97b for 20 psig indicate that, without further adjustment, the model is able to accurately predict performance when the cell is running under conditions that differ from the base case. Of particular interest in Figs. 97a and b is the loss in performance due to mass transfer limitation at high current density. The increasingly steep drop in performance as the cell approaches its limiting current density is attributable to the saturation of the cathode GDL and catalyst layer with water and the corresponding restriction in reactant transport. Previous efforts [3,12] to explain limiting current behavior based solely on diffusive resistance in the agglomerates led to a more abrupt drop in performance. By including the effects of liquid water transport, the current model is able to more closely simulate performance in the region where mass transport effects begin to dominate. The importance of liquid water transport to the accurate modeling of fuel cell performance is further illustrated in Figs. 98 and 99. Performance curves with and without liquid water transport are shown for the base case conditions in Fig. 98. The curve labeled "NoSat" does not include the effect of liquid water accumulation on gaseous reactant transport. The predicted performance when liquid water effects are neglected is much better than for the case labeled "Sat", which does include the effect of liquid water accumulation on reactant transport. Comparison of the two curves demonstrates that the effects of liquid water accumulation become apparent even at relatively low values of current density. Furthermore, when liquid water effects are not included in the model, the cell voltage does not exhibit an increasingly steep drop as the cell approaches its limiting current density. This drop off in performance is clearly demonstrated by experimental data, but cannot be accurately modeled without the incorporation of liquid water transport. The variation of current density along the channel for the same two cases at a cell voltage of 0.4V is shown in Fig. 99. In the case where liquid water does not impede reactant transport ("NoSat") the current density produced in the cell is greater in magnitude down the channel relative to the more physically realistic case ("Sat"). In the absence of liquid water, the drop in current density as the reactants are depleted down the channel is more pronounced. When saturation is considered, a decrease in current density in the flow direction reduces the water production rate and leads to a lower degree of saturation of the cathode GDL and catalyst layer at the exit to the cell. With less accumulated water, the GDL and catalyst layer are more open to reactant flow, thus counteracting the effect of reactant depletion and leading to more uniform current density along the gas channel. Fig. 100 shows a contour plot of liquid water saturation for the base case conditions in the cathode GDL and catalyst layer at an average current density of 1.18 A/cm2. The model predicts that the level of saturation decreases along the flow direction. The decrease in saturation is due to the reduced reaction rate (associated with the drop in reactant concentration along the flow direction) and a corresponding drop in the amount of water produced as well as the amount of water dragged across the membrane from the anode. Results from the model also demonstrate the signifi- cance of water transport from the anode to the cathode by electro-osmotic drag. This water transport reduces the performance of the cell both by dehydrating the anode, thereby decreasing its conductivity, and by increasing the accumulation of liquid water at the cathode, which decreases its permeability to reactant gas flow.

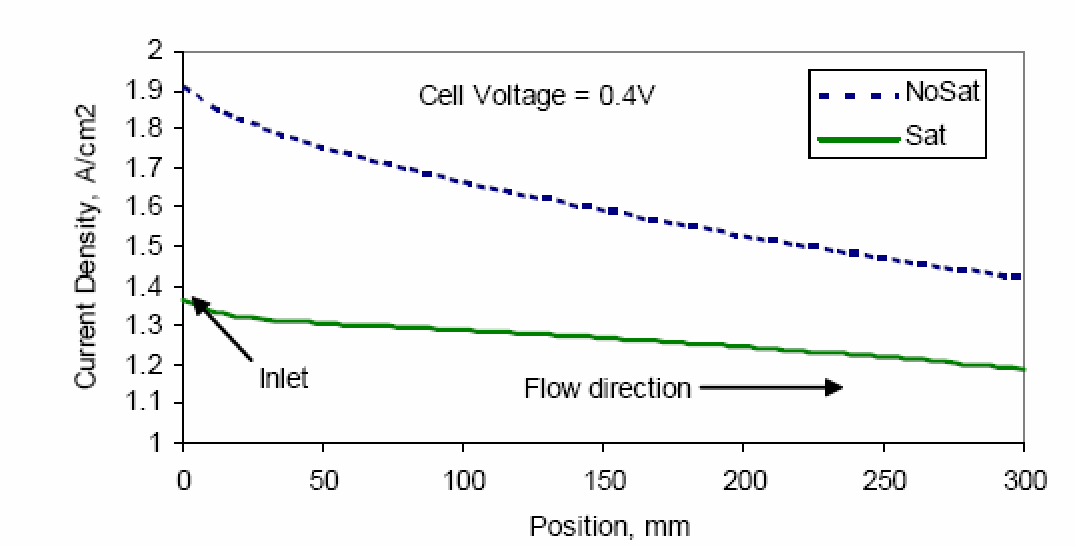

Figure 99: Influence of liquid water on current density variation along the flow direction.

Fig. 101 shows profiles for polymer water content in the catalyst layers and membrane as a function of the local current density and position through the thickness of the MEA at a point halfway down the channel for the base case conditions. The influence of electro-osmotic drag is readily apparent from these results. At low current density, there is very little change in water content across the MEA. This is due to a relatively low amount of drag and to the fact that the vapor activity at the anode and cathode is nearly identical. As current density is increased, the water content profile becomes steeper as the anode dehydrates and the cathode water content increases. The results shown in Fig. 101 also indicate that as current density increases, the total amount of water contained in the MEA decreases. This occurs because the vapor activity of the anode stream has dropped due to water removal upstream leaving less water available to hydrate the anode.

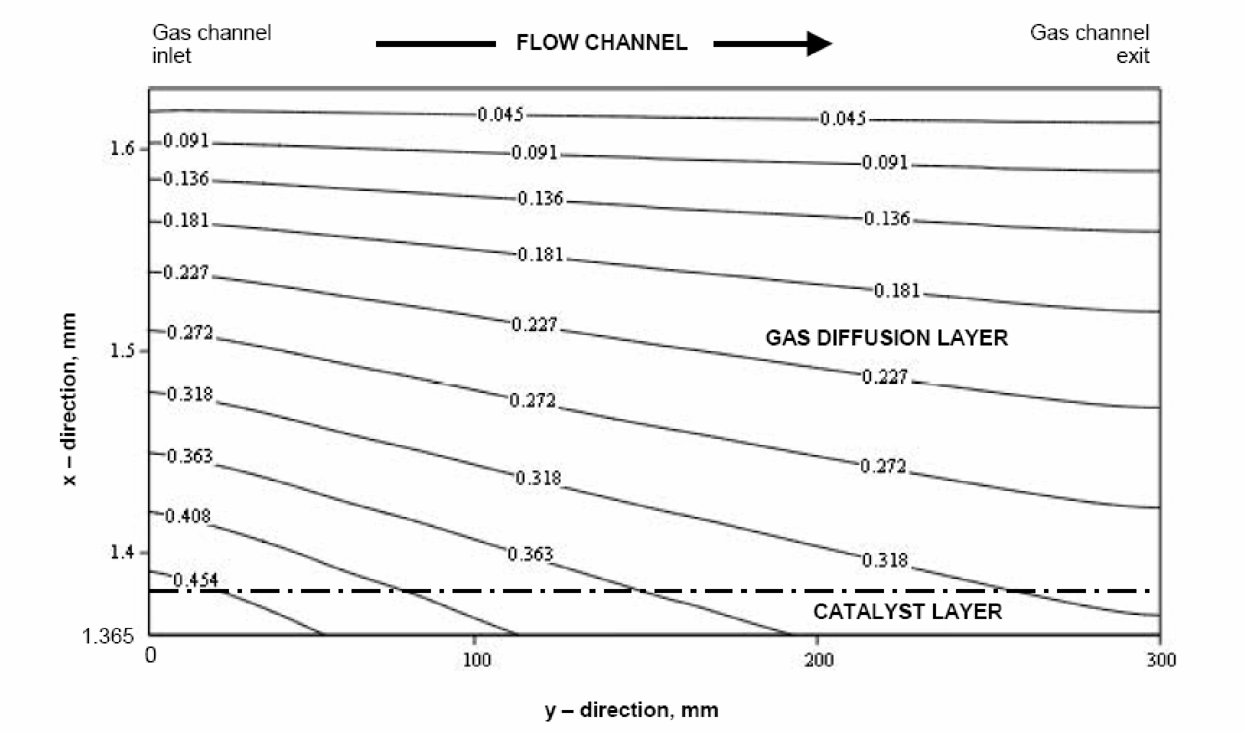

Figure 100: Saturation profiles in the cathode.

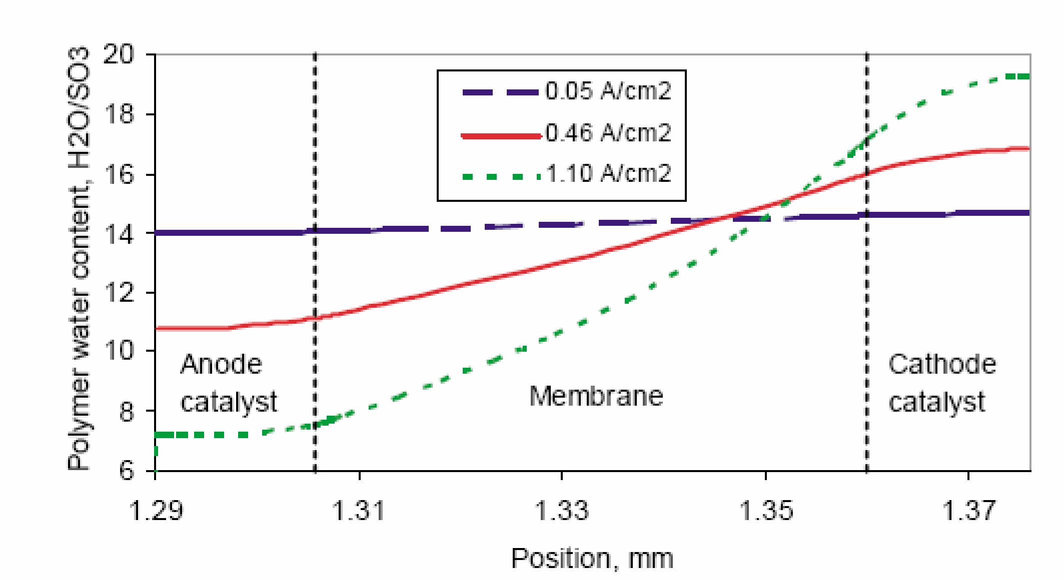

Figure 101: Variation of polymer water content through the MEA.

Table 33: Water transport through the MEA.

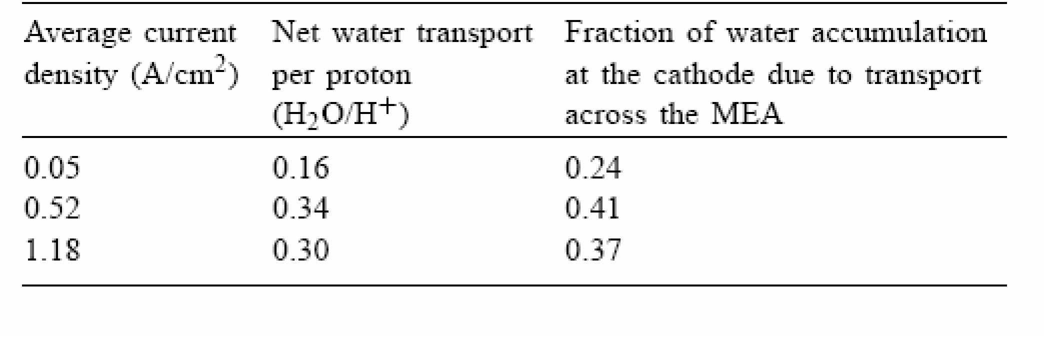

Average current density (A/cm^2)	Net water transport per proton (H_2O/H^+)	Fraction of water accumulation at the cathode due to transport across the MEA
0.05	0.16	0.24
0.52	0.34	0.41
1.18	0.30	0.37

The effect of the water content gradient as well as the significance of the electro-osmotic drag are further illustrated by the data in Table 33. Considering electro-osmotic drag alone, the amount of water moved from the anode to the cathode for fully hydrated Nafion® would be between 2.0 and 2.9 water molecules per proton at 30 ◦C [23]. Due to operation with a partially hydrated membrane and catalyst layers as well as back diffusion of water from the cathode to the anode, the net amount of water moved per proton predicted by the model is between 0.16 and 0.34, which is consistent with the modeling results presented by others [6,7]. It is interesting to note that the water transported across the MEA, from the anode to the cathode, makes up between 20 and 40% of the total amount of water accumulation at the cathode (transport and electrochemical production). This indicates that in addition to limiting cell performance by way of anode dehydration, water transport by electro-osmotic drag is responsible for a significant fraction of the liquid water buildup at the cathode and the resulting reactant transport limitations.

Conclusions

A comprehensive, steady state, two-dimensional model including liquid water transport has been developed and validated with experimental data. Results from the model show that, in order to accurately simulate fuel cell operation, liquid water transport within the cell must be considered as it results in a loss of performance even at relatively low current density. In addition, water transport through the polymer portion of the catalyst layer and the membrane plays an important role with respect to both Ohmic losses and reactant transport restrictions at the cathode. The model predicts a net amount of water transport across the membrane of between 0.16 and 0.34 mole of water per mole of protons transported from the anode to the cathode. This accounts for 20–40% of the total amount of water accumulation at the cathode, which is a combination of water produced electrochemically and water transported by electro-osmotic drag. When operating at high inlet humidity, any water accumulating at the cathode remains in the liquid phase and fills the porous regions of the catalyst layer and the GDL. The fraction of pores filled with liquid water is highest within the catalyst layer near the inlet to the cell.

References

[1] P.C. Sui, L.D. Chen, J.P. Seaba, Y. Wariishi, Modeling and Optimization of a PEMFC Catalyst Layer, SAE Congress, 1999-01-0539, 1999, pp. 61–70.

[2] C. Marr, X. Li, Composition and performance modeling of catalyst layer in a proton exchange membrane fuel cell, J. Power Sources 77 (1999) 17–27.

[3] K. Broka, P. Ekdunge, Modelling the PEM fuel cell cathode, J. Appl. Electrochem. 27 (1997) 281–289.
[4] D. Genevey, M.R. von Spakovsky, M.W. Ellis, D.J. Nelson, B. Olsommer, F. Topin, N. Siegel, N. Montel, Transient Model of the Heat, Mass and Charge Transfer as well as Electrochemistry in the Catalyst Layer of a PEMFC, International Mechanical Engineering Congress and Exposition—IMECE'2002, ASME IMECE Paper No. 33322, New York, NY, November 2002.
[5] F. Jaouen, G. Lindbergh, G. Sundholm, Investigation of mass-transport limitations in the solid polymer fuel cell cathode, J. Electrochem. Soc. 149 (4) (2002) A437–A447.
[6] T.E. Springer, T.A. Zawodzinski, S. Gottesfeld, Polymer electrolyte fuel cell model, J. Electrochem. Soc. 138 (8) (1991) 2334–2341.
[7] D.M. Bernardi, M.W. Verbrugge, A mathematical model of the solid-polymer-electrolyte fuel cell, J. Electrochem. Soc., vol. 139, no. 9, pp. 2477–2490.
[8] S. Um, C.Y. Wang, K.S. Chen, Computational fluid dynamics modeling of proton exchange membrane fuel cells, J. Electrochem. Soc. 147 (12) (2000) 4485–4493.
[9] V. Gurau, H. Liu, S. Kakac, Two-dimensional model for proton exchange membrane fuel cells, J. AIChe, vol. 44, pp. 2410–2422.
[10] T. Zhou, H. Liu, 3-D model of proton exchange membrane fuel cells, Proceedings ASME Heat Transfer Division HTD 366-1 (2000) 43–49.
[11] S. Dutta, S. Shimpalee, J.W. Van Zee, Numerical prediction of mass-exchange between cathode and anode channels in a PEM fuel cell, Int. J. Heat Mass Transfer 44 (2001) 2029–2042.
[12] N.P. Siegel, M.W. Ellis, D.J. Nelson, M.R. von Spakovsky, Single domain PEMFC model based on agglomerate catalyst geometry, J. Power Sources 115 (2003) 81–89.
[13] A. Parthasarathy, S. Srinivasan, A.J. Appleby, C.R. Martin, Temperature dependence of the electrode kinetics of oxygen reduction at the platinum/Nafion® interface—a microelectrode investigation, J. Electrochem. Soc. 139 (9) (1992) 2530–2537.
[14] J. Ihonen, F. Jaouen, G. Lindbergh, A. Lundblad, G. Sundholm, Investigation of mass-transport limitations in the solid polymer fuel cell cathode, J. Electrochem. Soc. 149 (4) (2002) A448–A454.
[15] W. He, J.S. Yi, T. Van Nguyen, Two-phase flow model of the cathode of PEM fuel cells using interdigitated flow fields, AIChI J. 46 (10) (2000) 2053–2064.
[16] D. Natarajan, T. Van Nguyen, A two-dimensional, two-phase, multicomponent, transient model of the cathode of a proton exchange membrane fuel cell using conventional gas distributors, J. Electrochem. Soc. 148 (12) (2001) A1324–A1335.
[17] Z.H. Wang, C.Y. Wang, Two-phase flow and transport in the interdigitated air cathode of proton exchange membrane fuel cells, Proceedings

ASME Heat Transfer Division HTD 366-1 (2000) 27–33.
[18] J.J. Baschuk, X. Li, Modeling of polymer electrolyte membrane fuel cells with variable degrees of water flooding, J. Power Sources 86 (2000) 181–196.
[19] L. Zhang, C. Ma, S. Mukerjee, Oxygen permeation studies on alternative proton exchange membranes designed for elevated temperature operation, Electrochimica. Acta 48 (2003) 1845–1859.
[20] M.S. Wilson, J.A. Valerio, S. Gottesfeld, Low platinum loading electrodes for polymer electrolyte fuel cells fabricated using thermoplastic ionomers, Electrochim. Acta 40 (3) (1995) 355–363.
[21] S. Patankar, Numerical Heat Transfer and Fluid Flow, Hemisphere, Washington, DC, 1980.
[22] T.E. Springer, T.A. Zawodzinski, M.S. Wilson, S. Gottesfeld, Impedance sectroscopy, J. Electrochem. Soc. 143 (2) (1996) 587–599.
[23] T.A. Zawodzinski, T.E. Springer, J. Davey, R. Jestel, C. Lopez, J. Valerio, S. Gottesfeld, A comparative study of water uptake by and transport through ionomeric fuel cell membranes, J. Electrochem. Soc. 140 (7) (1993) 1981–1985.
[24] M. Uchida, Y. Aoyama, N. Eda, A. Ohta, Investigation of the microstructure in the catalyst layer and effects of both perfluorosulfonate ionomer and Ptfe-loaded carbon on the catalyst layer of polymer electrolyte fuel cells, J. Electrochem. Soc. 142 (12) (1995) 4143–4149.
[25] R. O'Hayre, S. Lee, S. Cha, F. Prinz, A sharp peak in the performance of sputtered platinum fuel cells at ultra-low platinum loading, J. Power Sources, 109, 483–493.
[26] R. Fox, A. McDonald, Introduction to Fluid Mechanics, Wiley, New York, 1992.
[27] J. Larminie, A. Dicks, Fuel Cell Systems Explained, Wiley, West Sussex, 2003.

Influence of Temperature on PEM Fuel Cell Operation

Introduction

The proton exchange membrane fuel cell has been the subject of an ever increasing number of modelling efforts for the past fifteen year. Undoubtedly, this growing interest has been caused by increasing concerns about pollution and possible anthropogenic global warming and the consequent research for alternative energy systems that could satisfy the energy demands in a cleaner way, such as those based on hydrogen. Because hydrogen must be produced from other chemical species, the devices that use it to generate electric power must be highly efficient in order to make the entire process energy and cost effective. Accurate numerical models represent a powerful tool for improving fuel cell design, and they have been growing in complexity and accuracy as cheap computational power and better cell understanding has become available. A number of one- and two- dimensional computational models were developed [6-12] but, although they represent significant advances in fuel cell modelling, it has been shown [3] that transport processes occurring in a PEM fuel cell are intrinsically three-dimensional. As a result, it is not possible to accurately predict cell performance unless a realistic, 3D description of the cell geometry is considered. Two-dimensional models are inadequate because they only consider areas where cell efficiency is the largest, thus, strongly overestimating the limiting current unless heavy model tuning is performed. Obviously, this impedes their use as design tools. Moreover, most models do not include the description of the two-phase flow that takes place in the gas distributor channels. However, the advective removal of liquid water from the GDL surface has been shown to affect the saturation level of the gas diffusion electrode [3], thus, strongly affecting mass transport related voltage losses. Physical properties of electrodes and gas species and their dependence on temperature also significantly affect cell performance. Probably for this reason, most works presenting cell models, even three dimensional ones [13,14], show comparisons between experimentally measured and numerically obtained data for only one temperature level. In the present work a, three-dimensional model of a proton exchange membrane fuel cell was used to investigate the effect of operating temperature on cell performance. The model includes a description of two-phase flow in the gas flow channels along with physical property temperature dependencies.

Mathematical Model Development

In order to obtain a fully three-dimensional implementation of the cell model previously developed [1,2], an adequate description of the water removal process occurring at the interface between the GDL and GFC was required. For this reason, a means for calculating the liquid water velocity field in the gas distributor channels without solving a second momentum conservation equation was devised. It was assumed that, in terms of direction, both phases shared the same velocity field but had different magnitudes (i.e. the liquid phase could move slower than the gas phase). Furthermore, a simple mechanical model was used to evaluate the interaction between the gas stream and the liquid water droplets at the GDL/GFC interface. The model uses one of two types of transport process depending on the flow regime. When the flow surrounding the droplet is laminar, no transverse velocity is present. In this regime, water droplets move along the GDL surface as a result of forces acting on the droplets due to viscous drag and surface tension. The viscous drag and surface tension forces can be expressed in terms of the droplet diameter, drag coefficient, gas and liquid velocity, surface tension, and the contact angle. An expression for the ratio of the liquid phase and gas phase velocities can then be obtained by imposing mechanical equilibrium on the forces acting on the droplet. This expression is called the advection coefficient, ψ, and has the form

$$\psi = 1 - 2\sqrt{\frac{2\sin\theta}{WeC_D}} \qquad (1)$$

where the contact angle (θ), drag coefficient, and Weber number depend on, or contain properties that depend on temperature. The last two terms are also functions of gas velocity, which varies with temperature for constant mass flow rate conditions, while the water contact angle was shown to be temperature dependent in tests carried out at the Politecnico di Torino [3] using digital image analysis techniques. It was found that for the GDL material (E-TEK1 ELAT HT 1400-W) used in MEA fabrication at Virginia Tech, the following correlation relating temperature to contact angle held:

$$\theta = -0.9444\left(\frac{T}{T_o}\right) + 3.422 \qquad (2)$$

where To = 298 K and the contact angle is expressed in radians[2]. When the droplet on the GDL surface is exposed to turbulent flow, it is assumed that local gas phase velocity fluctuations are sufficient to dislodge the droplet from the GDL surface. In the absence of a surface tension force to balance the viscous drag, the droplet accelerates until it reaches the gas phase velocity. Under these conditions the advection coefficient ψ approaches unity. Having defined the liquid phase velocity field, it is possible to solve the liquid water transport equation in all of the regions of the fuel cell. The transport equation for liquid water is solved in terms of the liquid water saturation, which is the ratio of the local liquid water volume to local pore volume. The mathematical model is completed with the addition of a series of closure relations, which include a correlation for the flow of liquid water by capillary action through the porous media (represented as a diffusive process although it is in fact advective) as well as relations for physical properties such as density, viscosity, and surface tension. The electrochemical characteristics of carbon supported platinum electrodes with a Nafion electrolyte, were obtained from [15] for several temperature levels.

Experimental Setup and Model Validation

The cell used to obtain experimental data for model validation had a single pass serpentine flow field and an active area of 5 cm^2. A three-dimensional computational domain was defined by neglecting the bends in the serpentine channel while preserving the total length, as shown in Figure 102. An MEA was fabricated and tested to characterise its performance at different temperatures and gas inlet conditions as well as to evaluate certain geometric and physical properties. The mathematical model was then validated experimentally and some of the results of the validation process are summarised in Figure 103, which shows a series of polarisation curves taken over a range of temperatures. The predicted curves are in good agreement with experimental data across the entire operating range. Furthermore, it should be noted that, once the model was tuned for the base case conditions (T = 333 K), it was not adjusted further, i.e. no ‘knobs’ were turned in order to match the experimental data at other temperature levels. A similar figure showing good agreement between predicted and experimental changes in performance due to variations in cathode inlet relative humidity is given in [3]. These validation cases serve to establish confidence in the ability of the model to accurately predict the performance of the test cell under a variety of conditions, making it possible to use the model as a design tool and as a means of studying the effects that contribute to cell performance and how these effects are related to cell temperature. In order to emphasize the fact that the phenomena that govern fuel cell operation are intrinsically three-dimensional, and, thus, only a 3D model can correctly repoduce them, the same mathematical model was run on both a 2D and a 3D computational domain. From Figure 104, it is evident that the 2D model greatly overestimates cell performance, since such a model only considers phenomena occurring on a “slice” of cell cut halfway through the channel height. It has been shown [3,5] that this is the region of highest current production and that, departing from it, cell current decreases, especially in the zones under the channel walls. As a result, 2D models fail to correctly estimate cell performance, unless strong parameter tuning is adopted3, because such models evaluate performance only at the “best conditions”. This, of course, is not the case for welldeveloped 3D models such as the one used here which quite accurately reproduces the experimental data, as shown in Figures 103 and 104.

Results: Temperature Effects

As it can be seen from Figure 103, temperature influences the polarization curve over the entire operating range of the cell. However, as current increases the main cause of voltage loss changes, so that, for low currents, (0<J<0.2 A/cm2) reaction activation losses dominate, in the intermediate range of currents (0.2<J<0.7 A/cm2), ohmic losses are preponderant, and finally, for higher currents, mass transport losses prevail. Furthermore, it follows that temperature influences cell performance in these three regimes to the extent that it affects the leading loss phenomenon. For this reason, in the following discussion, temperature effects on the polarisation curve will be studied separately for each operating regime. However, before proceeding, it is useful to recall the relations that describe the physical phenomena that are relevant to this analysis. The model used here to relate cell current and cathode overpotential (voltage losses) is, essentially, the Butler-Volmer model for reaction kinetics in which an effectiveness term, $c\ \Pi$, has been introduced. For the cathode catalyst layer,

$$j_c = \Pi_c (1-s) A j_c^{ref} \left(\frac{c_{O_2}^{p}}{c_{O_2}^{ref}} \right)^{\gamma_c} \left[\exp\left(\frac{\alpha_c F}{RT} \eta_c \right) - \exp\left(-\frac{\alpha_c F}{RT} \eta_c \right) \right] \qquad (3)$$

The effectiveness accounts for the resistance to oxygen diffusion posed by the polymer material surrounding the reaction sites within the agglomerate structures of the catalyst layer [2]. An additional term, (1-s), where s represents liquid water saturation, accounts for the deactivation of reaction sites due to local pore flooding. In the following discussion, we will be studying the effect of temperature on each term that appears in equation (3), and, thus, its effect on cell voltage.

The diffusion characteristics of the porous media do not change with temperature but, because they affect the relative importance of each (temperature dependent) transport phenomenon, it is interesting to see how temperature effects on the polarisation curve change as the porous medium structure does. Thus, in the following analysis, the parameter

$$GDP = \frac{\varepsilon}{\tau L} \frac{\tau_0 L_0}{\varepsilon_0} \text{ in the GDL} \qquad (4)$$

$$\text{or} \quad GDP = \frac{\varepsilon^{1.5}}{L} \frac{L_0}{\varepsilon_0^{1.5}} \text{ in the CCL} \qquad (5)$$

is defined and used to characterize the porous media. The *GDP* (Gas Diffusion Parameter) is a function of porosity (ε), tortuosity (τ), and layer thickness (L). A reference value of GDP, characteristic of the diffusion medium, was used in the experiments as well as a lower one, characteristic of media with worse gas diffusion properties.

Finally, liquid water transport primarily influences cell operation in the high current region of the polarization curve. In the present model, equation (6) is used to calculate the distribution of liquid water in the gas channels and porous electrodes. Its solution yields the pore saturation, s.

$$\frac{\partial s}{\partial t} + \vec{\nabla} \cdot \left(\vec{u}_l s \right) - \vec{\nabla} \cdot \left(D_{H_2O}^{l} \vec{\nabla} s \right) = \frac{S_s}{\rho_{H_2O}^{l}} \qquad (6)$$

It is worth noting that in porous media the gas phase velocity becomes so small as not to influence the liquid phase, due to the negligible amount of momentum exchanged between the phases. Thus, the advective term drops off, as water flow is driven by capillary pressure only. At these conditions, it is possible to treat this as a diffusive process, defining a suitable diffusion coefficient for liquid water such as

$$D_{H_2O}^{l(\theta>90°)} = \frac{\Sigma s^3 \sqrt{\varepsilon K}\cos\theta}{\nu_{H_2O}^{l}\rho_{H_2O}^{l}}\left(1.417 + 4.240s + 3.789s^2\right) \qquad (7)$$

This was obtained by using Leverett's equation to characterise capillary pressure as a function of saturation so that its diffusivity actually depends on saturation, giving equation (6) a nonlinear nature.

Activation regime

In the activation region, cell current density is low so that both mass transport losses due to limited oxygen diffusivity and electrode saturation are negligible. As a result, diffusion effectiveness is also relatively high and constant with temperature. It follows that higher temperature affects the shape of the polarisation curve mainly through higher values of both reference exchange current density and charge transfer coefficient, as well as directly by appearing in the exponential part of the reaction kinetics model. Despite the fact that we can neglect changes in oxygen concentration across the GDL due to low current production, we must take into account the fact that temperature influences the fraction of water in the gas mixture, and, thus, that of oxygen. As a result, the concentration dependent term plays a relevant role in this region too.

Table 34: Activation overpotential dependence on temperature.

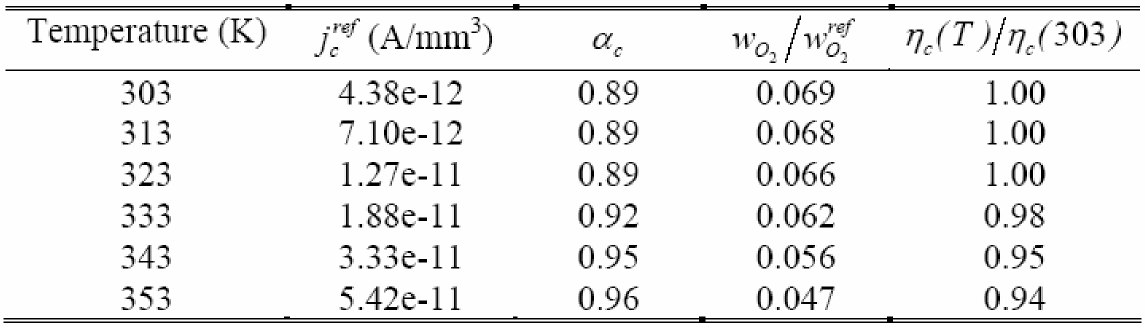

Temperature (K)	j_c^{ref} (A/mm^3)	α_c	$w_{O_2}/w_{O_2}^{ref}$	$\eta_c(T)/\eta_c(303)$
303	4.38e-12	0.89	0.069	1.00
313	7.10e-12	0.89	0.068	1.00
323	1.27e-11	0.89	0.066	1.00
333	1.88e-11	0.92	0.062	0.98
343	3.33e-11	0.95	0.056	0.95
353	5.42e-11	0.96	0.047	0.94

By inverting equation (3) and considering, for our purposes, a value of current density typical of the activation loss region (J=0.05 A/cm2), one can estimate the cathode activation overpotential variation with temperature. In order to do so, values of electrode properties at various temperature levels are required. These are obtained from [15]. Table 34 presents the results of this analysis in the rightmost column, where the overpotential variation with respect to the reference case (303 K) is reported. As can be seen, temperature causes an increase in kinetic parameters, while it reduces the concentration term, because the oxygen mass fraction decreases at higher temperatures, as more water is present in the gas mixture. The increase in kinetics somewhat offsets the reduction in oxygen concentration, so that the net result is a decrease of the cathode activation overpotential with temperature. In terms of cell performance, this is desirable because lower ovepotentials result in higher cell voltage (and, thus, efficiency). However, this effect is mitigated somewhat by the fact that the open circuit voltage decreases for higher values of temperature.

Ohmic regime

In the ohmic region of the polarisation curve, the total cathode overpotential is primarily a result of ohmic losses in the membrane, particularly on the anode side, due to membrane dryout caused by electro-osmotic drag. As a result, the temperature dependent, loss-controlling parameters in this region are membrane ionic conductivity and dissolved water diffusivity. The latter influences the former because, for the same current density, a higher diffusivity implies a more uniform dissolved water distribution, thus, eliminating zones of very low conductivity.

In order to study how these temperature dependent properties affect ohmic losses in the cell, let us consider that the electro-osmotic drag is mainly dependent on current density. Hence, for a given value of current density, it follows from the dissolved water transport equation that the water content gradient will increase as the relative diffusion coefficient decreases. Thus, by solving this equation, one obtains the polymer water content profiles for each temperature level. With this, one can estimate membrane conductivity and, ultimately, ohmic overpotential. Table 35 presents the results of this analysis, obtained by applying the procedure defined above and simulating cell operation at 0.5 A/cm^2.

Table 35: Ohmic overpotential dependence on temperature.

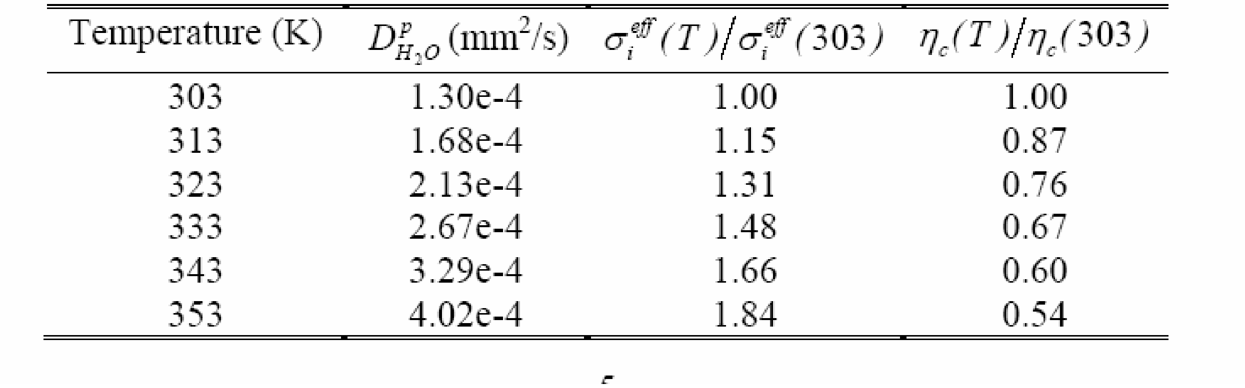

Temperature (K)	$D^{p}_{H_2O}$ (mm^2/s)	$\sigma_i^{eff}(T)/\sigma_i^{eff}(303)$	$\eta_c(T)/\eta_c(303)$
303	1.30e-4	1.00	1.00
313	1.68e-4	1.15	0.87
323	2.13e-4	1.31	0.76
333	2.67e-4	1.48	0.67
343	3.29e-4	1.66	0.60
353	4.02e-4	1.84	0.54

The results clearly show the benefits of higher operating temperatures when the cell is working in the ohmic region of its polarisation curve, because the portion of the open circuit voltage lost to driving the flow of ions almost halved when increasing the temperature from 303 K to 353 K. The reason behind this can be more effectively understood by looking at Figure 105. It is clear that membrane conductivity increases not only because of its own dependence upon temperature [16], but also because the increased diffusion coefficient of dissolved water (which, for a given membrane, is mainly function of temperature, as shown in Figure 105) allows a more uniform distribution of water in the membrane, and, thus, eliminates zones of high resistance to ion transport. In addition, the ability of the membrane to uptake water increases with temperature, which leads to a greater overall water content and a corresponding increase in ionic conductivity.

Mass transport limited regime

In the mass transport limited region, in addition to ohmic and activation losses, cell voltage is strongly affected by resistance to reactant transport, given the high mass flow rate required to sustain the electrochemical reactions at such a high rate. Temperature effects on this region and, in particular, on the limiting current, are some of the most difficult to explain because of the many phenomena that interact with and influence each other at high current density. In order to understand the mechanisms by which temperature influences limiting current, its influence on each phenomenon and parameter affecting maximum current density was analyzed.

Oxygen transport

Oxygen transport limitations affect the limiting current due to the diffusion resistance of the

GDL, since the flow rate necessary to produce an ever higher current is generated by increasing the concentration gradient across the GDL, assuming, of course, that the fraction of oxygen at the channel inlet is fixed. Oxygen mass transport becomes limiting with respect to the reaction rate when its concentration reaches very small values in the catalyst layer. The current at which this happens depends on the oxygen diffusion resistance and the initial value of concentration at the cell inlet, both of which are temperature dependent. As can be seen in Figure 106, oxygen diffusivity increases with temperature. The GDP does not affect the relative change of this parameter with temperature, because porosity, tortuosity, and GDL thickness do not vary with temperature, and the dependence upon saturation has been removed in order to study oxygen transport only. In this same figure, the actual-to-reference mass fraction ratio is both temperature and GDP dependent since, with fully humidified gases, the higher the temperature is, the higher the water vapor mass fraction and the lower the oxygen value while the lower the GDP is, the lower the oxygen effective diffusion coefficient and consequently the lower the oxygen concentration in the CCL. Figure 106 presents two trends of the oxygen mass fraction in the CCL and the ratio of mass fractions appearing in the Butler-Volmer equation, because these quantities also depend on GDP. The continuous lines refer to quantities evaluated using the reference value of GDP, while the dashed lines demonstrate the effect of a reduction of GDP on these variables. Furthermore, the reported value of oxygen mass fraction in the CCL was divided by the value at the channel inlet. Thus, one can see that *in the absence of liquid water* in the electrodes, despite the increase in oxygen diffusivity with temperature, the concentration ratio that influences reaction kinetics decreases with temperature. The reason is that the beneficial effects of higher temperature on diffusivity are offset by the detrimental ones due to higher water content in the gas stream, and thus reduced oxygen concentration at the cell inlet.

Kinetic parameters

The temperature effects on reaction kinetic parameters such as the reference exchange current density (*jref*), the charge transfer coefficient (α), and the diffusion effectiveness (Π) are shown in Figure 107. Little change in the transfer coefficient is observed while exchange current density shows a 6-fold increase in the range of 303 K to 353 K. The behavior of the effectiveness is interesting because its trend changes based on the GDP. This is explained by the fact that, if GDP is high, then the oxygen concentration remains relatively high in the catalyst layer even at high temperatures due to modest gradients, since the controlling diffusion phenomenon (i.e. the one showing the highest resistance) becomes oxygen transport in the polymer of the agglomerate. The result is a higher effectiveness. However, after a certain temperature threshold (343 K in the above figure), oxygen transport in the gas phase is so affected by the reduced inlet mass fraction that effectiveness again decreases. A discussion of how the temperature dependence of oxygen transport and reaction kinetics affects cathode overpotential and, consequently, cell voltage, is reported in [3].

Liquid water transport

In what has been presented to this point, liquid water in the electrode (GDL/CCL) has so far been neglected. However, it does play a significant role in determining cell voltage and limiting current. In our model, water transport in the porous media has been modelled as capillary pressure driven flow. Thus, it is possible to describe it as a diffusive process by defining a suitable diffusivity in the liquid water transport equation (saturation equation). This diffusivity depends nonlinearly on the transported variable (saturation) as well as on surface tension, contact angle, kinematic viscosity, and porosity. Thus, studying the effects of only temperature on water transport required splitting the definition of the liquid water diffusivity into a term containing only functions of saturation, and another containing only physical properties. All the latter vary with temperature, and their combined effect on the saturation-independent part of the diffusivity is presented in Figure 108. It is interesting to note that the trends reported vary according to the value of contact angle used. The green lines (both continuous and dashed) refer to contact angle values which vary as in equation (2) above. The same trend was also shifted down so that the highest value (at lowest temperature) of θ was about 110°. This allowed investigation of the effect on liquid water transport of a less hydrophobic porous medium. The result as seen in Figure 108 is that highly hydrophobic porous materials (the green lines) show values of water diffusivity that monotonically increase within the temperature range considered, while less hydrophobic porous media present a maximum value of diffusivity in the middle of the temperature range. These results show the importance of accurately characterising the surface properties of diffusion media as the temperature varies. Now, if one assumes that the liquid water source in the cathode catalyst layer (due to production by reaction, transport by electro-osmotic drag, and diffusion through the polymer) does not depend upon temperature, then an increase in the diffusivity is followed by a decrease in the saturation gradient so as to keep the water flux constant. As the temperature rises, contact angle and surface tension decrease as does the kinematic viscosity. The trends reported in Figure 108 suggest that the latter presents the largest variations, causing the diffusivity to increase so that for a given cell current, the saturation gradient over the GDL decreases. Assuming for the sake of clarity that saturation in the channel equals zero at a short distance from the interface with the GDL, a smaller saturation gradient implies a smaller absolute value in the CCL, which, in turn, results in an enhancement of oxygen diffusivity and reaction kinetics at higher temperatures and a detriment of the same properties if temperature is reduced. Of course, since the liquid water diffusivity is a function of saturation as well, the resulting trend of water content in the pores is non-linear, which means that the actual value of saturation affects its gradient. This, in turn, is a function of water flux into the CCL as well as the flux out of the GDL/gas channel interface. The latter, as mentioned earlier, is defined by the interaction of water droplets with the gas stream in the gas channels and, as shown in [3], can be described as a function of an appropriate advection coefficient with a strong dependence upon temperature, i.e. increasing two orders of magnitude in the range from 333 K to 353 K. The result is that the flux out of the GDL is greatly enhanced by an increase in temperature, leading to saturation levels in the GDL which are lower, and in turn benefiting not only oxygen gas diffusion in the pores but in thepolymer phase of the agglomerates as well. The result is a greater effectiveness.

Thus, if both reaction kinetics and mass transport effects that include liquid water transport are taken into account when predicting cell behaviour, the most noticeable effect is a more pronounced increase in oxygen diffusivity with temperature when no liquid water is present (compare Figure 109 with Figures 106 and 107 above). This in turn contributes to an increase of oxygen mass fraction in the CCL over most of the temperature range and an increase in the concentration dependent term of the Butler-Volmer equation. In contrast, the effect of saturation is to invert the trends (at least for a large part of the temperature range) seen previously in Figures 106 and 107 for dry electrodes. Furthermore, comparing the effectiveness curves, one notes that saturation affects oxygen diffusivity in the polymer so strongly as to double the effectiveness in the range from 303 K to 343 K, while the dry electrode trends show only a 20% increase. It is also interesting to note that the combined effect of liquid water and lower electrode GDP is that of reducing the oxygen concentration in the CCL and, thus, effectiveness, as well as shifting the peak values of both of these variables to lower temperatures. Thus, as one would expect, at lower temperature and GDP the cell performs badly since as the peak values of oxygen concentration in the CCL and effectiveness shift to lower temperatures as well as lower values, the optimal operating temperature decreases a bit as GDP decreases. This can be explained by the fact that the concentration gradient will be steeper for a lower GDP, and, thus, the benefit of starting with higher concentration in the gas channel (which happens at lower temperatures) offsets the decreased ability to get rid of water from the GDL, resulting in a decrease in the value of the optimal operating temperature. Finally, the effects of liquid water and advection coefficient on fuel cell performance are seen with the polarization curves given in Figures 110 and 111. The results, for example, in Figure 110 show that when liquid water diffusivity is reduced by 25% the limiting current decreases by 7.1% and 5.1% at 333 K and 353 K, respectively. Conversely, at these same temperatures, when the diffusivity is increased by 50%, the limiting current increases by 9.5% and 6.2%, respectively. These trends can also be analyzed in terms of GDL hydrophobic effects on cell performance. In fact, the required reduction and increase in diffusivity were obtained by varying the contact angle θ, i.e. the 25% reduction in liquid water diffusivity was achieved by reducing the contact angle by 9%, while the 50% increase was obtained by increasing contact angle by 13%. Figure 111 shows the effects of changes in the advection coefficient, indicating that these effects are more marked at lower temperatures (± 6% at 333 K versus ± 3% at 353 K), since water transport inside the GDL is less efficient and the gas velocity is lower. This allows the formation of bigger droplets on the surface of the GDL/gas channel interface and in turn causes saturation to increase in the GDL, reducing reactant diffusivity. The significant effect on polarization seen in this figure demonstrates the need for accurately characterizing two-phase mass transport phenomena at the interface between the gas channel and GDL. Any model that does not is bound to be incomplete, since not only would water removal be incorrectly estimated, but so would the estimation of limiting current and cell performance.

Conclusions

The improved liquid water transport model, along with the characterisation of physical properties dependence upon temperature, and the effects on oxygen diffusion of a catalyst layer made up of agglomerates, has helped obtain a good agreement between model predictions and experimentally measured cell performance over a wide temperature range. This has made it possible to trust our model predictions and, thus, use them to investigate how temperature dependent parameters affect cell operation. Some of the conclusions drawn from our study include the following:

- Despite its presence in the denominator of the kinetics equation, higher temperature positively affects reaction kinetics by strongly increasing the reference exchange current density and weakly increasing the charge transfer coefficient.
- In the ohmic region of the polarisation curve, benefits of running the cell at higher temperature can be explained with the higher membrane ionic conductivity caused both by temperature itself and by an increase in membrane water content as well as the diffusivity of water within the membrane, which results in an increased and more homogeneous membrane hydration level.
- Higher temperatures also enhance oxygen diffusivity both in the GDL pores and in the ion conducting polymer. However, because hotter air needs to absorb more water vapour to become saturated, the oxygen fraction at the cell inlet is reduced as temperature is increased. This causes the oxygen concentration in the cathode catalyst layer to be lower at higher temperatures, despite the higher diffusivity. If liquid water presence in the cell electrodes is not taken into account, this reduction is found to offset all the beneficial effects of higher temperatures on

kinetic parameters, resulting in a cell that shows a decrease in performance at higher temperatures.

- The liquid water diffusion coefficient is coupled to temperature through the kinematic viscosity, contact angle, and surface tension, since the values of these properties decrease as the water temperature increases. The level of hydrophobicity of the GDL material affects how liquid water diffusivity changes with temperature, because for slightly hydrophobic materials ($100° < \theta < 110°$), the decrease in contact angle causes its cosine to vary considerably so that in combination with a decrease in surface tension, it counterbalances the decrease in kinematic viscosity, thus, keeping diffusivity practically constant with temperature. However, if a highly hydrophobic material ($135° < \theta < 150°$) is used as in our case, then a reduction in kinematic viscosity prevails at higher temperatures; and the result is a 1.7-fold increase in diffusivity when temperature varies from 303 K to 353 K.
- Water removal by advection at the GDL / GC interface is increased at higher temperatures for two reasons. First of all, gas velocity increases with temperature because in order to keep the stoichiometric ratio constant, the dry air mass flow rate is kept constant. This means that at higher temperatures, the higher water vapour content of fully humidified air causes a higher mass flow rate (and, thus, velocity) in the bipolar plate channels. The second effect is related to the magnitude of the advection coefficient, ψ. This is strongly temperature dependent; and it reaches unity at 353 K, because the flow in the channels becomes turbulent, and liquid water is transported as finely dispersed droplets in the gas stream.
- The result of an increased liquid water diffusivity and a higher advective flux out of the GDL is a lower saturation level in the cathode pores. Since both oxygen effective diffusivity and the reaction kinetics increase as the amount of liquid water within the electrode decreases, it can be said that temperature has a significant impact on these parameters as well.
- Oxygen diffusivity, which is already lower for cooler air, is further reduced by high saturation, and further increased at high temperature by low saturation. It follows from our work here that, for a dry electrode, oxygen diffusivity shows a 1.5-fold increase from 303 K to 353 K. If liquid water effects are taken into account, then the oxygen diffusivity shows a 2.7-fold increase in the same temperature interval.

Higher diffusivity causes a lower concentration gradient, which results in a higher concentration of oxygen in the catalyst layer, despite the lower concentration of oxygen in the gas channel at higher temperature. The result of all of these effects is a reduction of the cathode overpotential as temperature increases, thus, increasing the limiting current.

Finally, it should be emphasized that even though the conclusions just listed apply specifically to the PEMFC modelled and experimentally measured here, they are probably nonetheless more broadly applicable, i.e. to, at the very least, other PEMFCs with similar configurations and material characteristics which fall within the range of values considered here. Thus, we believe that our results provide both a qualitative and quantitative basis for drawing needed insights into the behaviour of these devices, providing guidance for model development and implementation which can move models similar to ours into the realm of general applicability necessary for their use as design tools.

Acknowledgements

The authors would like to thank Prof. Dongiovanni at the Politecnico di Torino for his technical help with regards to the optical technique used for measuring the contact angle and for his financial support in providing a fast computer at the Politecnico in Italy for our 3D model simulations. Similarly, the authors are grateful to Dr. Schnipke at Blue Ridge Numerics Inc. (BRNI), for providing us with a CFDesign® license and working with us to modify BRNI's commercial code in order to accommodate our fuel cell modelling.

Nomenclature

Symbol	*Description*	*Unit*
A	Electrode active area	1/mm
c	Molar concentration	mol/mm^3
C_D	Drag coefficient	-
D	Diffusion coefficient	mm^2/s
F	Faraday's constant	C/mol
j	Volumetric/exchange current density	A/mm^3
J	Superficial current density	A/mm^2
K	Hydraulic permeability	mm^2
L	Length	mm
R	Universal gas constant	J/molK
S	Volumetric source term	g/mm^{3}s
s	Pore saturation	-
T	Temperature	K
u	Velocity	mm/s
We	Weber number	-
w	Mass fraction	-
α	Charge transfer coefficient	-
γ	Concentration ratio exponent	-
ε	Porosity	-
η	Overpotential	V
θ	Water contact angle	rad
λ	Membrane water content	-
ν	Kinematic viscosity	mm^2/s
Π	Diffusion effectiveness	-
ρ	Density	g/ mm^3
Σ	Surface tension	µN/mm
σ	Conductivity	S/mm

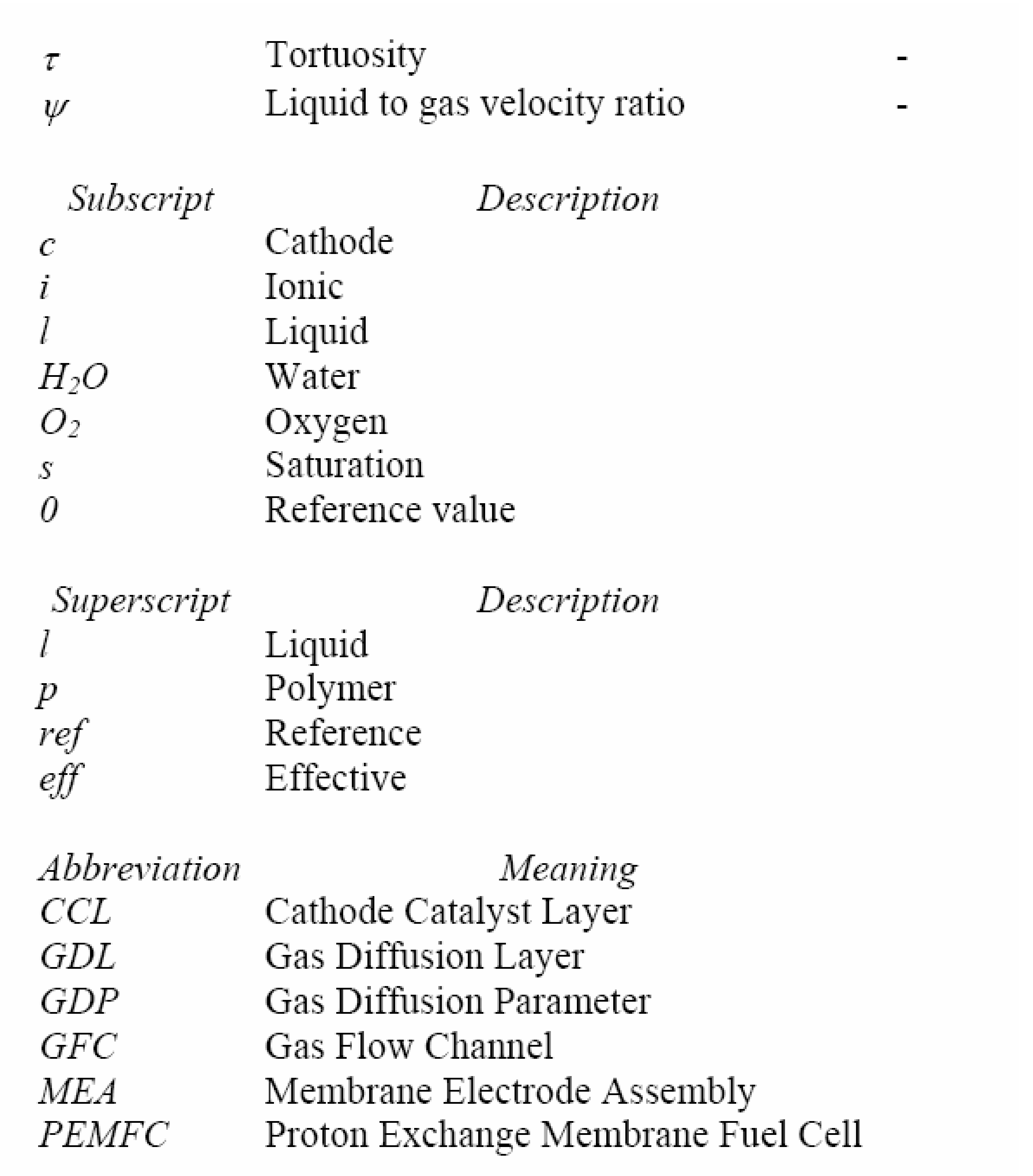

τ	Tortuosity	-
ψ	Liquid to gas velocity ratio	-

Subscript	*Description*
c	Cathode
i	Ionic
l	Liquid
H_2O	Water
O_2	Oxygen
s	Saturation
0	Reference value

Superscript	*Description*
l	Liquid
p	Polymer
ref	Reference
eff	Effective

Abbreviation	*Meaning*
CCL	Cathode Catalyst Layer
GDL	Gas Diffusion Layer
GDP	Gas Diffusion Parameter
GFC	Gas Flow Channel
MEA	Membrane Electrode Assembly
PEMFC	Proton Exchange Membrane Fuel Cell

References

[1] Siegel, N.P., Ellis, M.W., Nelson, D.J., von Spakovsky, M.R., 2004, "A Two-Dimensional Computational Model of a PEMFC with Liquid Water Transport," *Journal of Power Sources*, vol. 128, issue 2, pp. 173-184.

[2] Siegel, N.P., Ellis, M.W., Nelson, D.J., von Spakovsky, M.R., 2003, "Single Domain PEMFC Model Based on Agglomerate Catalyst Geometry," *J. Power Sources*, Vol. 115: pages 81–89.

[3] Coppo, M., 2005, "CFD Analysis and Experimental Investigation of Proton Exchange Membrane Fuel Cells", Ph.D. dissertation, Politecnico di Torino, Turin, Italy.

[4] CFDesign® V5.1, Blue Ridge Numerics, 2003.
[5] Siegel, N.P., 2003, "Development and Validation of a Computational Model for a Proton Exchange Membrane Fuel Cell," Ph.D. dissertation, Virginia Polytechnic Institute and State University, Blacksburg, VA.
[6] Bernardi, D.M., Verbrugge, M.W,1992, "A Mathematical Model of the Solid-Polymer-Electrolyte Fuel Cell", J. Electrochemical Society, Vol. 139, No. 9: pages 2477–2491.
[7] Um, S., Wang, C.Y., Chen, K.S., 2000, "Computational Fluid Dynamics Modeling of Proton Exchange Membrane Fuel Cells", J. Electrochemical Society, Vol. 147, No.12: pages 4485–4493.
[8] Rowe, A., Li, X., 2001, "Mathematical Modeling of Proton Exchange Membrane Fuel Cells", J. Power Sources, Vol. 102: pages 82–96.
[9] Wang, Z.H., Wang, C.Y., Chen, K.S., 2001, "Two-Phase Flow and Transport in the Air Cathode of Proton Exchange Membrane Fuel Cells", J. Power Sources, Vol. 94: pages 40–50.
[10] Berning, T., Lu, D.M., Djilali, N., 2002, "Three-Dimensional Computational Analysis of Transport Phenomena in a PEM Fuel Cell", J. Power Sources, Vol. 102: pages 284–294.
[11] Yan, W.M., Soong, C.Y., Chen, F., Chud., H.S.,2004, "Transient Analysis of Reactant Gas Transport and Performance of PEM Fuel Cells", J. Power Sources, Vol. 143:pages 48–56.
[12] Shan, Y., Choe, S.Y., 2005, "A High Dynamic PEM Fuel Cell Model with Temperature Effects", J. Power Sources, Vol. 145: pages 30–39.
[13] Berning, T., Djilali, N., 2003, "Three-Dimensional Computational Analysis of Transport Phenomena in a PEM Fuel Cell - a Parametric Study", J. Power Sources, Vol. 124: pages 440–452.
[14] Guvelioglu, G.H., Stenger, H.G., 2005, "Computational Fluid Dynamics Modeling of Polymer
Electrolyte Membrane Fuel Cells", J. Power Sources, Vol. 147: pages 95–106.
[15] Zhang, L., Ma, C., Mukerjee, S., 2003, "Oxygen Permeation Studies on Alternative Proton Exchange Membranes Designed for Elevated Temperature Operation," *Electrochimica Acta*, Vol. 48: pages 1845–1859.
[16] Springer, T.E, Zawodzinski, T.A., Gottesfeld, S., 1991, "Polymer Electrolyte Fuel Cell Model", Journal of the Electrochemical Society, Vol. 138, N. 8: pages 2334-2341.

Figure 102: Three-dimensional computational domain.

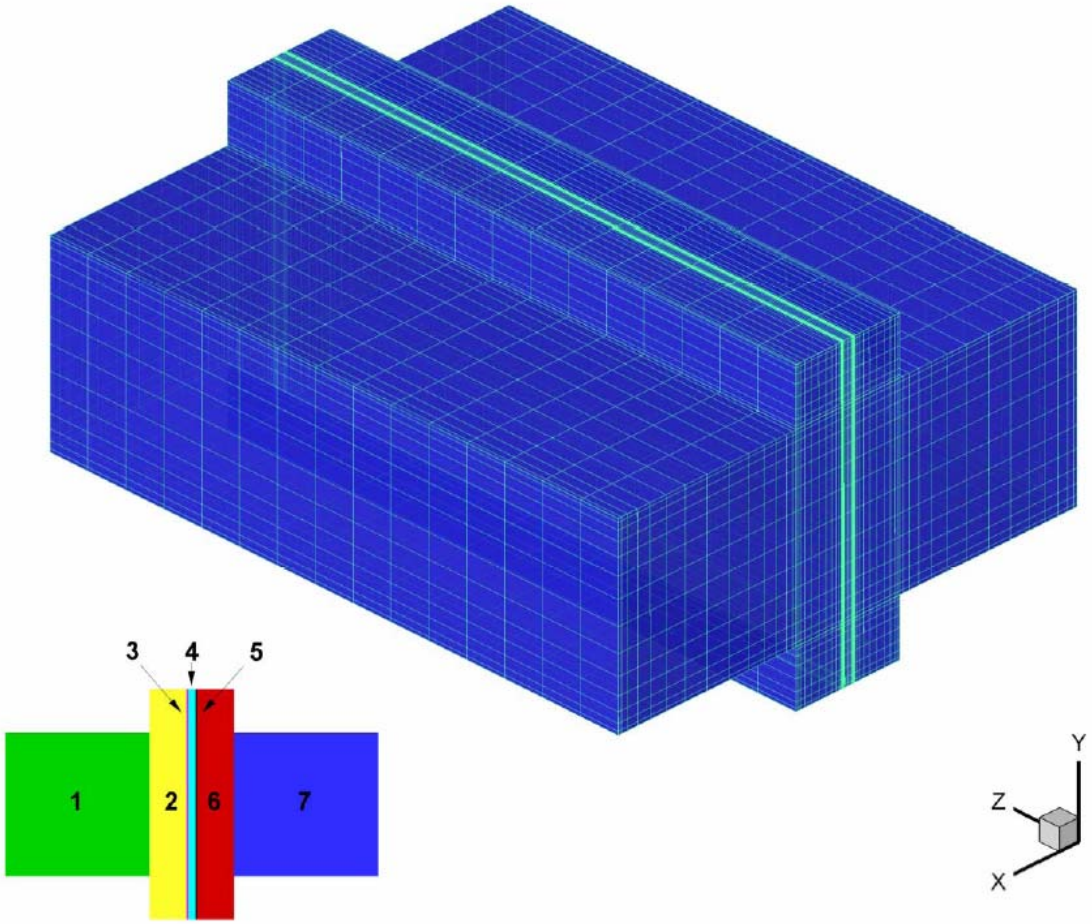

1	Anode gas channel	5	Cathode catalyst layer
2	Anode gas diffusion layer	6	Cathode gas diffusion layer
3	Anode catalyst layer	7	Cathode gas channel
4	Polymer electrolyte membrane		

Figure 103: 3D model validation at different temperature levels.

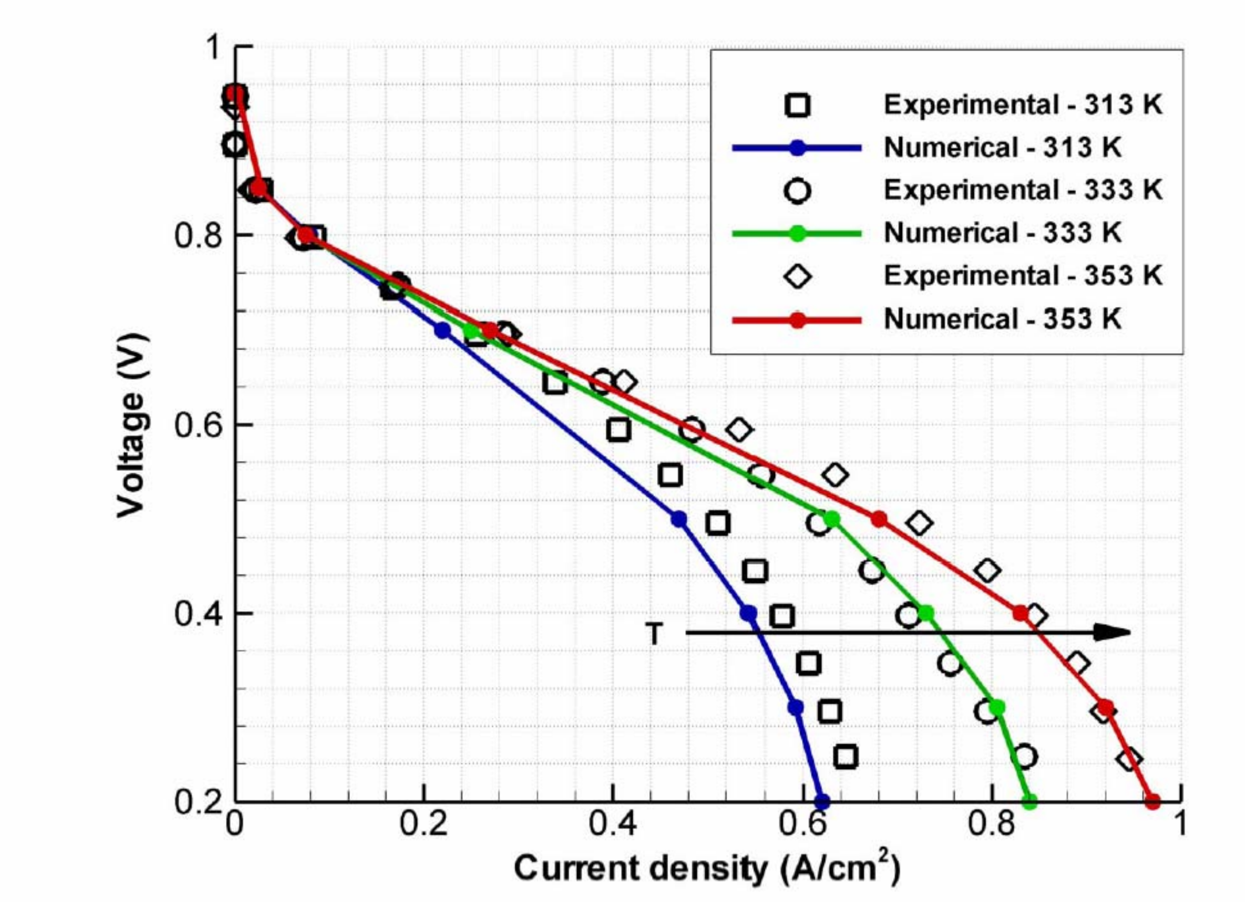

Figure 104: Effect of three versus two dimensions on model predications.

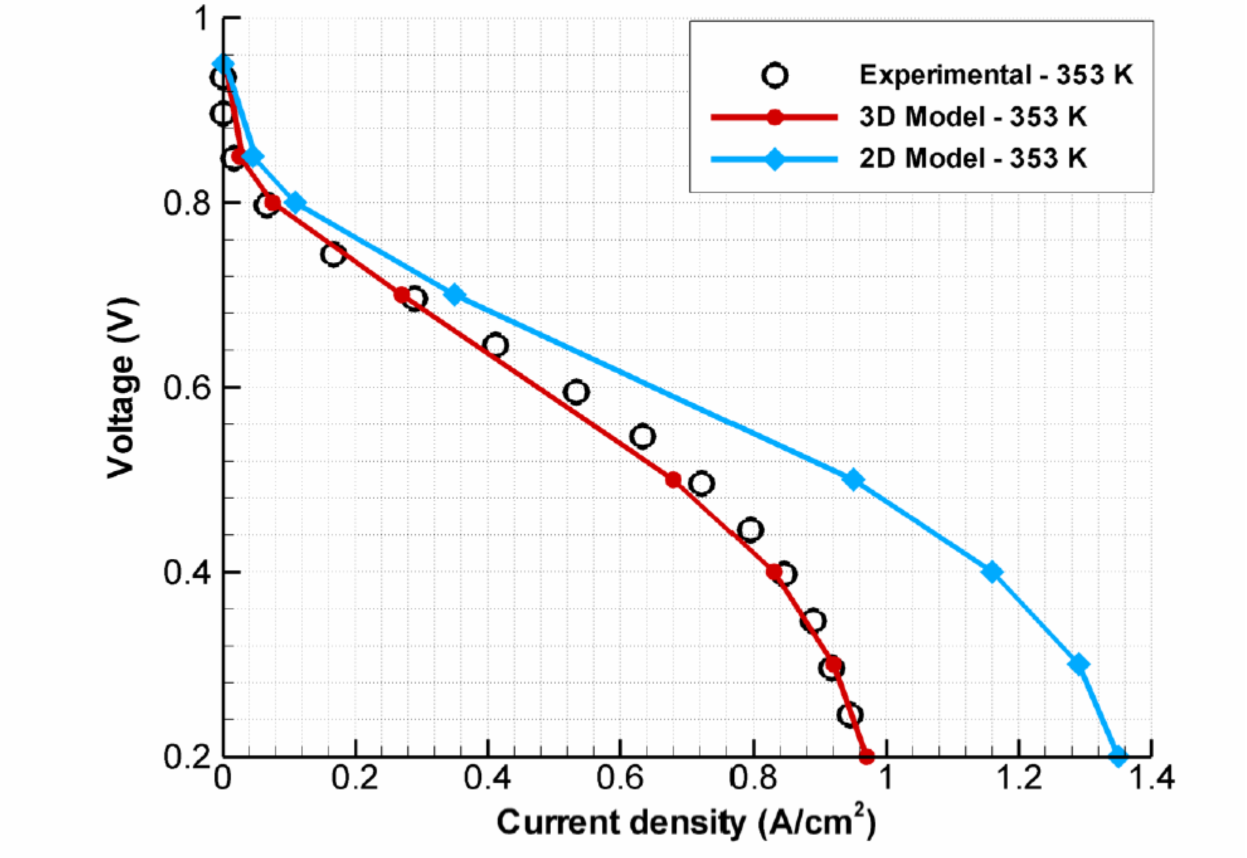

Figure 105: Temperature dependence of dissolved water diffusivity and membrane ionic conductivity; continuous lines were obtained with a reference value of membrane water content (λ=16) while dashed lines show the effect of a 50% reduction in λ on the same variables.

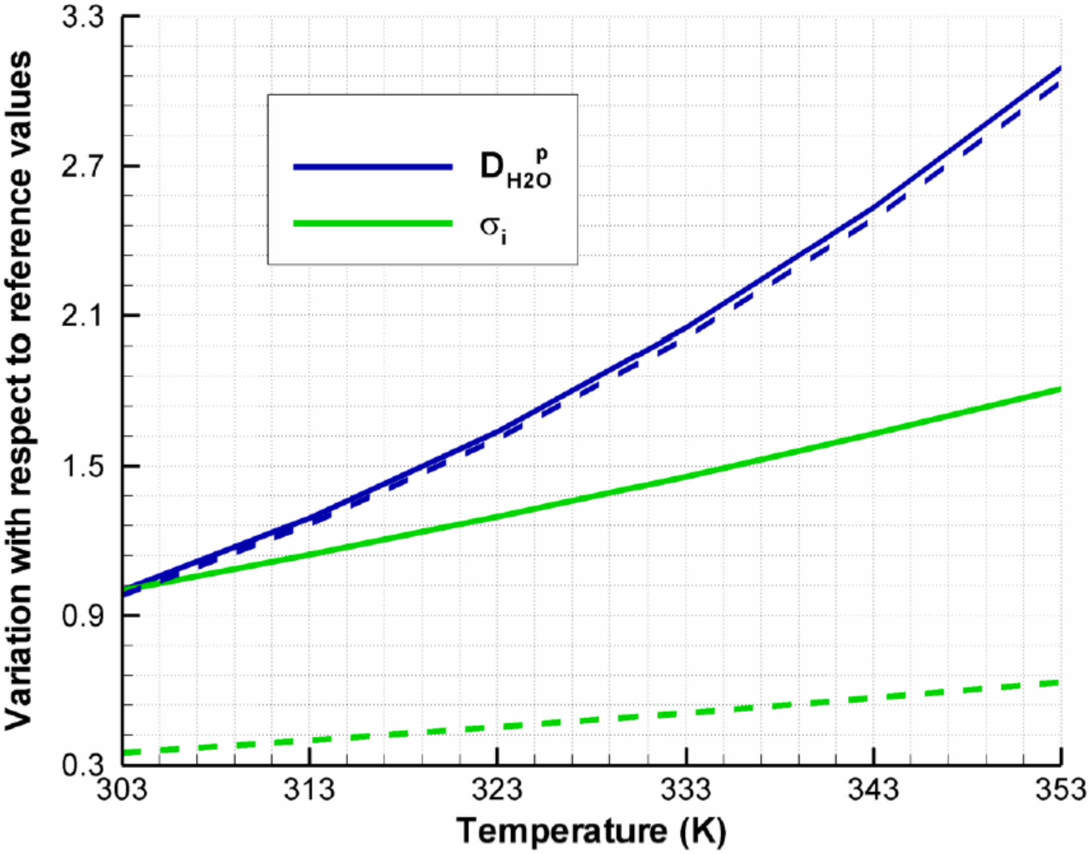

Figure 106: Temperature dependence of oxygen mass fraction and diffusivity for oxygen diffusion in both the GDL and CCL; continuous lines are based on a reference value of GDP while dashed lines are based on a 44% reduction in GDP.

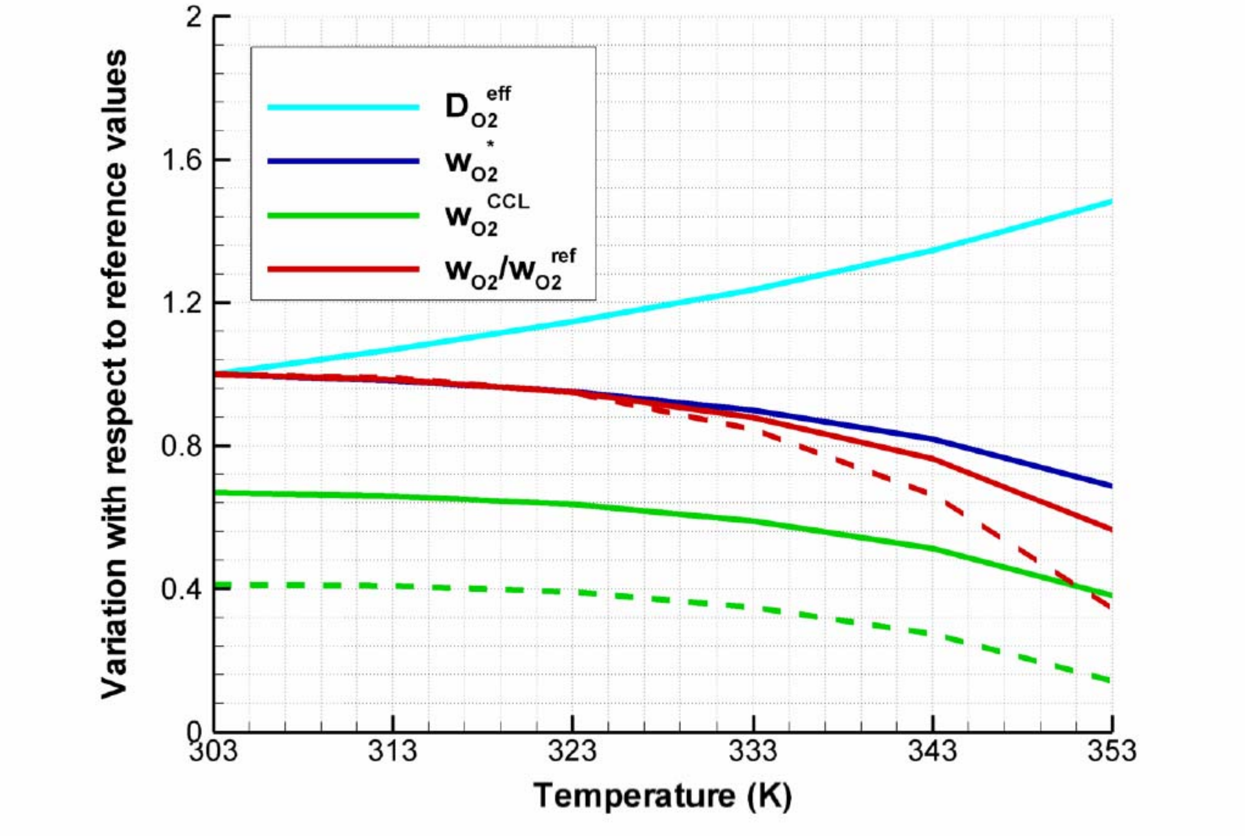

Figure 107: Temperature dependence of kinetic and diffusion-in-polymer parameters; as before, since effectiveness depends on GDP, two trends are reported: continuous lines are based on a reference value of GDP and dashed lines based on a 44% reduction in GDP.

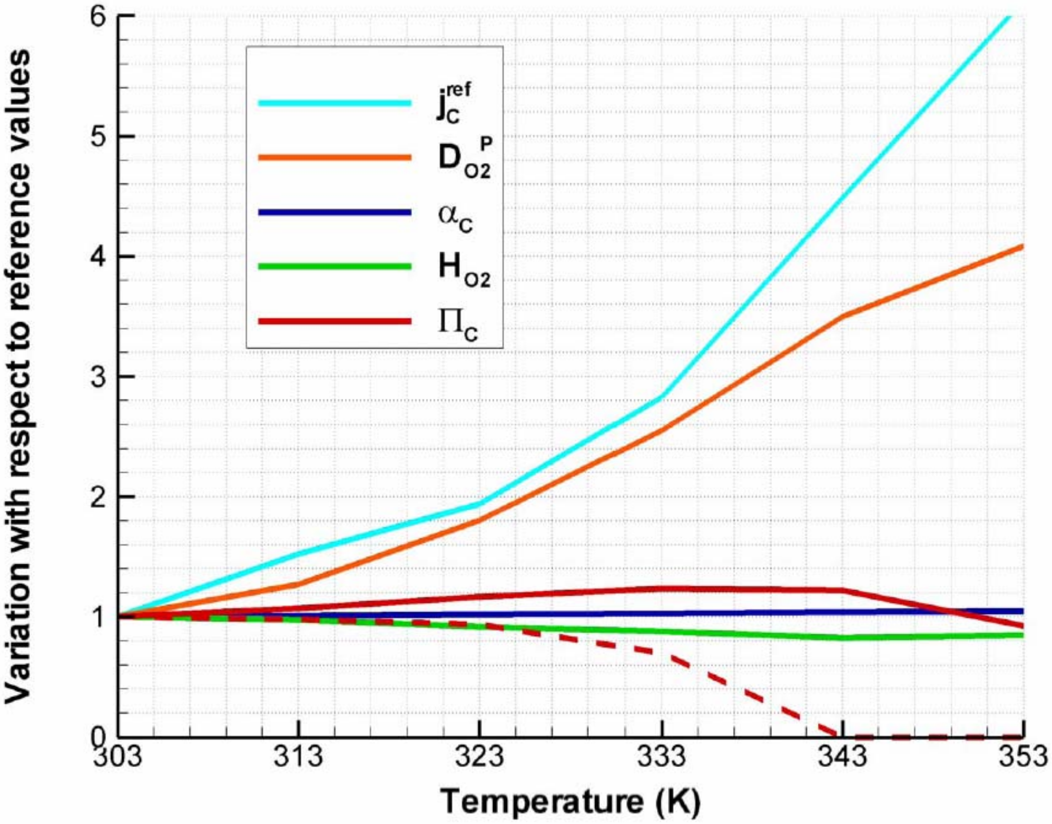

Figure 108: Liquid water diffusivity dependence upon temperature and contact angle; as before, since the diffusivity depends on GDP, two trends are reported: continuous lines based on a reference value of GDP and dashed lines based on a 44% reduction in GDP.

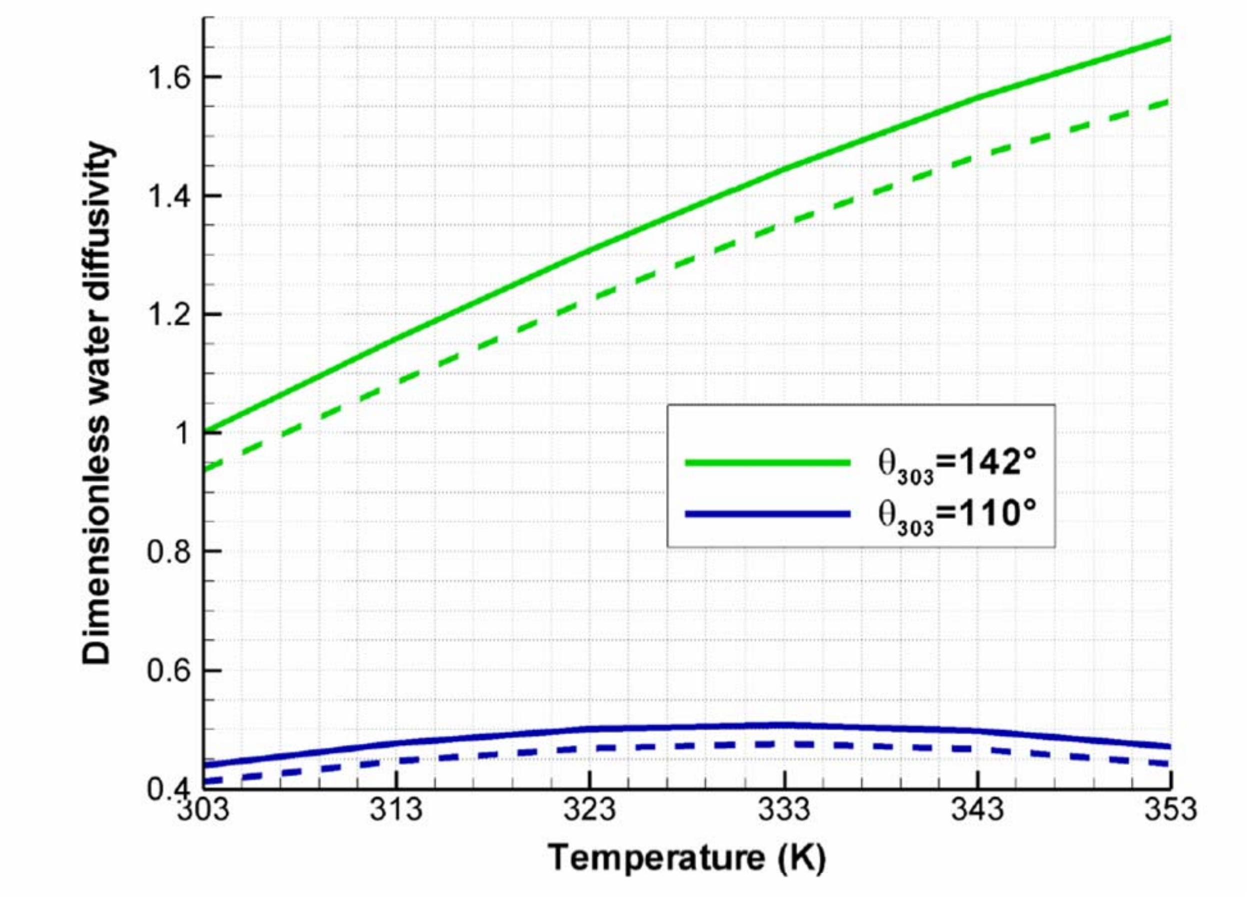

Figure 109: Temperature dependence of quantities related to oxygen diffusion, affected by the presence of liquid water in the diffusion media; as before, due to GDP dependence, two trends are reported: continuous lines based on a reference value of GDP and dashed lines based on a 44% reduction in GDP.

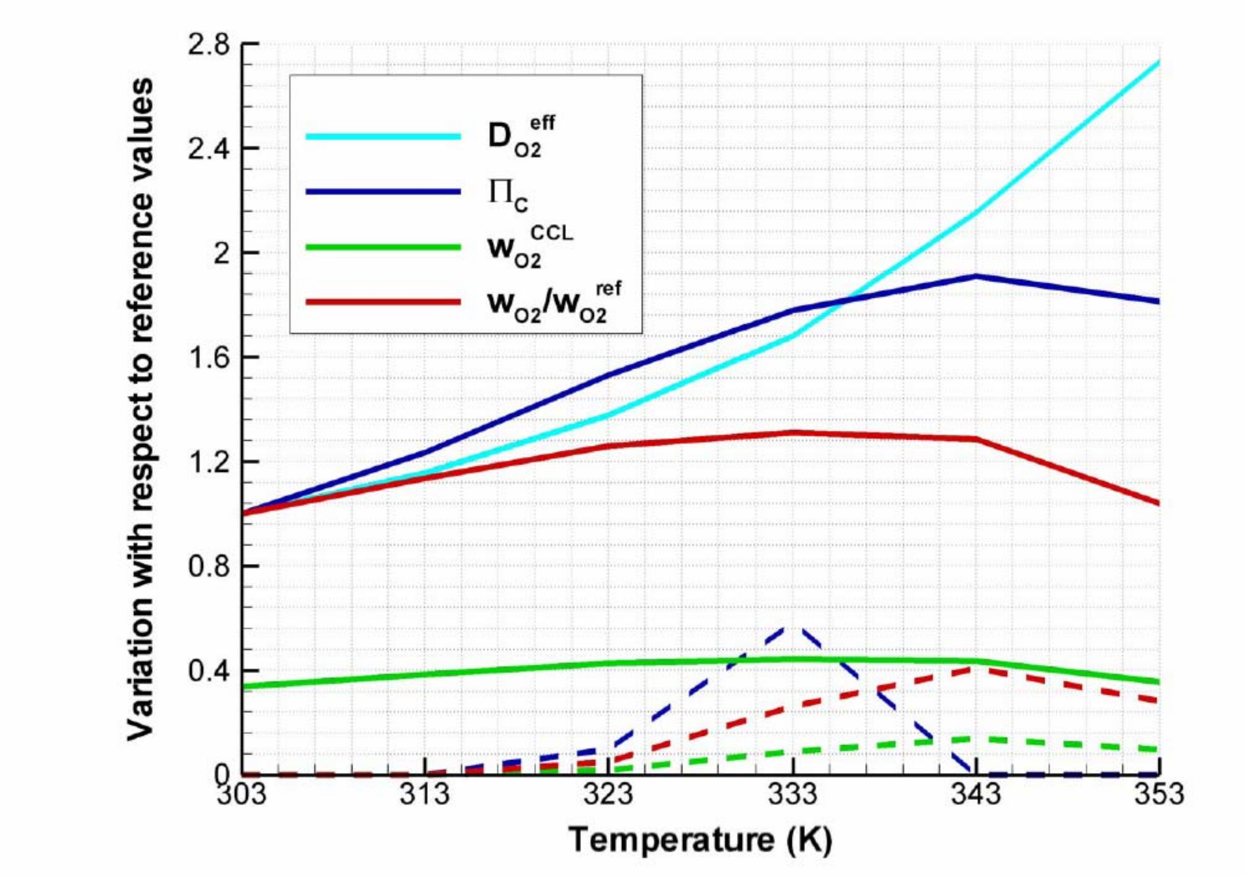

Figure 110: Effect of liquid water presence in the GDP on cell performance.

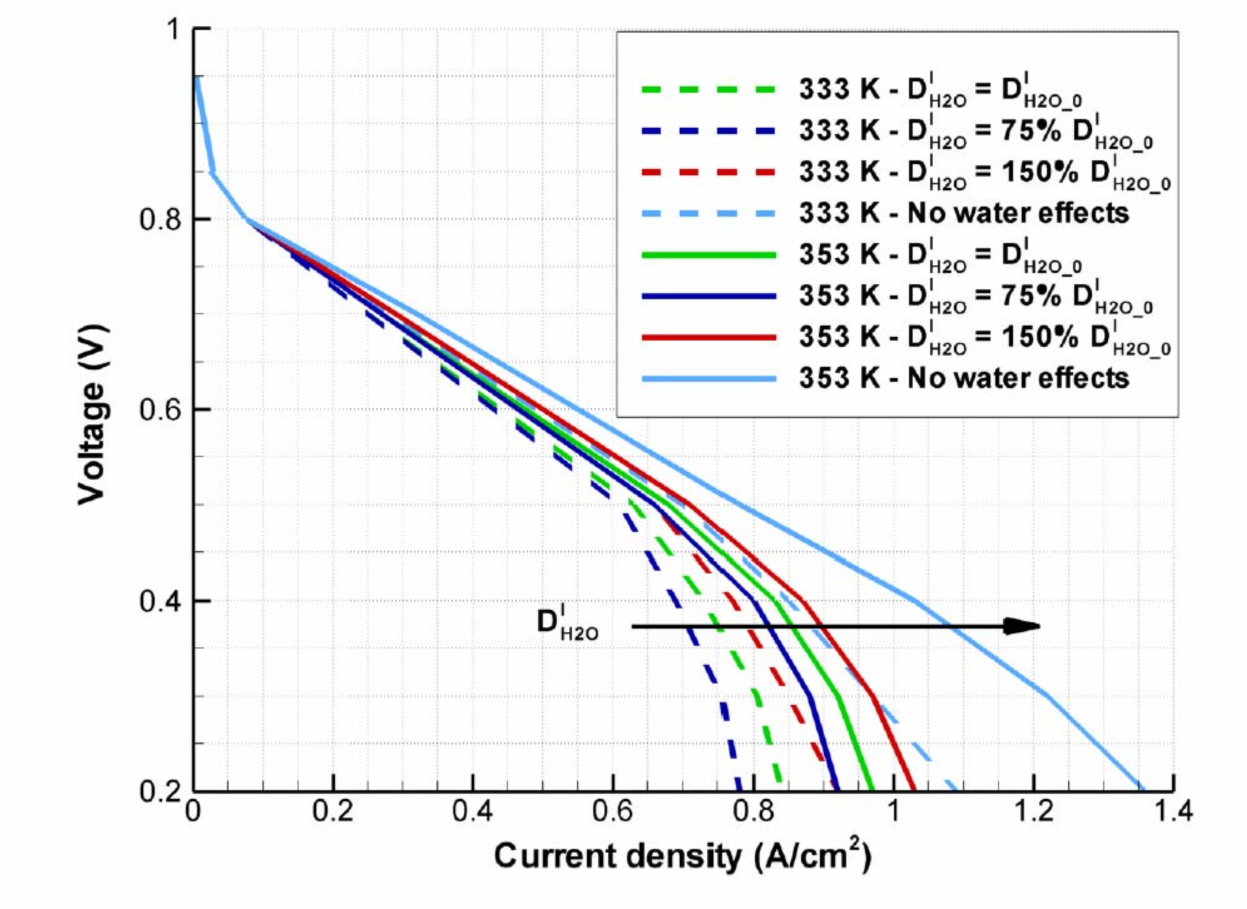

Figure 111: Effect of advection coefficient on cell performance.

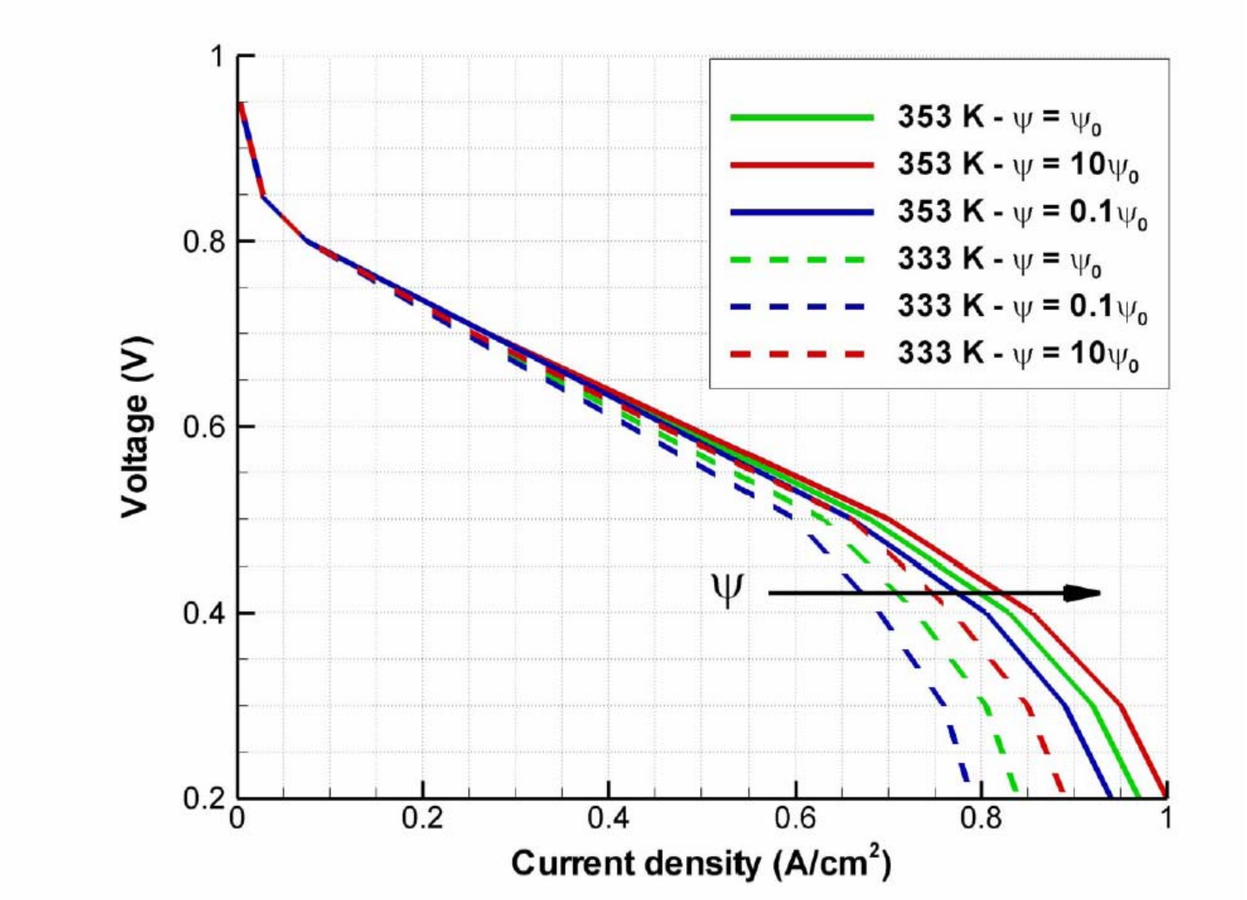

Knowledge Transfer

Refereed Publications

1. J. Huang, D.G. Baird, and J.E. McGrath, "Development of Fuel Cell Bipolar Plates from Graphite Filled Wet-Lay Thermoplastic Composite Materials," *J. Power Sources* 150 (2005) 110-119.
2. F. Wang, M. Hickner, Q. Ji, W. Harrison, J. Mecham, T.A. Zawodzinski, and J.E. McGrath, "Synthesis of Highly Sulfonated Poly(arylene ether sulfone) Random (Statistical) Copolymers via Direct Polymerization," *Macromol. Symp.* 175 (2001) 387-395.
3. F. Wang, M. Hickner, Y.S. Kim, T.A. Zawodzinski, and J.E. McGrath, "Direct Polymerization of Sulfonated Poly(arylene ether sulfone) Random (Statistical) Copolymers: Candidates for New Proton Exchange Membranes," *J. Mem. Sci.* 197(1-2) (2002) 231-242.

4. Y.S. Kim, F. Wang, M. Hickner, T.A. Zawodzinski, and J.E. McGrath, "Fabrication and Characterization of Heteropolyacid (H3PW12O40)/Directly Polymerized Sulfonated Poly(arylene ether sulfone) Copolymer Composite Membranes for Higher Temperature Fuel Cell Applications," *J. Mem. Sci.* 212(1-2) (2003) 263-282.
5. Y.S. Kim, L. Dong, M.A. HIckner, T.E. Glass, V. Webb, and J.E. McGrath, "State of Water in Disulfonated Poly(arylene ether sulfone) Copolymers and a Perfluorosulfonic Acid Copolymer (Nafion) and Its Effect on Physical and Electrochemical Properties," *Macromolecules* 36(17) (2003) 6281-6285.
6. Y.S. Kim, F. Wang, M. Hickner, S. McCartney, Y.T. Hong, T.A. Zawodzinski, and J.E. McGrath, "Effect of Acidification Treatment and Morphological Stability of Sulfonated Poly(Arylene Ether Sulfone)s for Proton Exchange Membranes at Elevated Temperature Operation of Fuel Cell," *J. Polym. Sci., Part B: Polym. Phys.* 41(22) (2003) 2816-2828.
7. W.L. Harrison, F. Wang, J.B. Mecham, V.A. Bhanu, M. Hill, Y.S. Kim, and J.E. McGrath, "Influence of the Bisphenol Structure on the Direct Synthesis of Sulfonated Poly(arylene ether) Copolymers. I.," *J. Polym. Sci., Part A: Polym. Chem.* 41(14) (2003) 2264-2276.
8. Y.S. Kim, L. Dong, M.A. Hickner, B.S. Pivovar, and J.E. McGrath, "Processing Induced Morphological Development in Hydrated Sulfonated Poly(arylene ether sulfone) Copolymer Membranes," *Polymer* 44(19) (2003) 5729-5736.
9. B.R. Einsla, Y.-T. Hong, Y.S. Kim, F. Wang, N. Gunduz, and J.E. McGrath, "Sulfonated Naphthalene Dianhydride Based Polyimide Copolymers for Proton Exchange Membrane Fuel Cells. I. Monomer and Copolymer Synthesis," *J. Polym. Sci., Part A: Polym. Chem.* 44(2) (2004) 862-874.
10. M.J. Sumner, W.L. Harrison, R.M. Weyers, Y.S. Kim, J.E. McGrath, J.S. Riffle, A. Brink, and M.H. Brink, "Novel Proton Conducting Sulfonated Poly(arylene ether) Copolymers Containing Aromatic Nitriles," *J. Mem. Sci.* 239(2) (2004) 199-211.
11. M.A. Hickner, H. Ghassemi, Y.S. Kim, B.R. Einsla, and J.E. McGrath, "Alternative Polymer Systems for Proton Exchange Membranes (PEMs)," *Chemical Reviews* 104(10) (2004) 4587-4611.
12. H. Ghassemi and J.E. McGrath, "Synthesis and Properties of New Sulfonated Poly(*p*-Phenylene) Derivatives for Proton Exchange Membranes. I," *Polymer* 45(17) (2004) 5847-5854.
13. H. Ghassemi, G. Ndip, and J.E. McGrath, "New Multiblock Copolymers of Sulfonated Poly(4'-Phenyl-2,5-Benzophenone) and Poly(Arylene Ether Sulfone) for Proton Exchange Membrane. II," *Polymer* 45(17) (2004) 5855-5862.
14. M. Andrew, T. Mukundan, and J.E. McGrath, "Sulfonated Poly(arylene ether sulfone) Copolymers – Acid and Salt Form: Potential Biofunctional Polymers," *J. Bioactive and Compatible Polym.* 19(4) (2004) 315-329.
15. Y.S. Kim, M.A. Hickner, L. Dong, B.S. Pivovar, and J.E. McGrath, "Sulfonated Poly(arylene ether sulfone) Copolymer Proton Exchange Membranes: Composition and Morphology Effects on the Methanol Permeability," *J. Mem. Sci.* 243(1-2) (2004) 317-326.

16. Y.S. Kim, M.J. Sumner, W.L. Harrison, J.S. Riffle, J.E. McGrath, and B.S. Pivovar, "Direct Methanol Fuel Cell Performance of Disulfonated Poly(arylene ether benzonitrile) Copolymers," *J. Electrochem. Soc.* 151(12) (2004) A2150-A2156.
17. B.R. Einsla, Y.S. Kim, M.A. Hickner, Y.-T. Hong, M.L. Hill, B.S. Pivovar, and J.E. McGrath, "Sulfonated Naphthalene Dianhydride Based Polyimide Copolymers for Proton Exchange Membrane Fuel Cells. II. Membrane Properties and Fuel Cell Performance," *J. Mem. Sci.* 255(1-2) (2005) 141-148.
18. W.L. Harrison, M.A. Hickner, Y.S. Kim, and J.E. McGrath, "Poly(arylene ether sulfone) Copolymers and Related Systems from Disulfonated Monomer Building Blocks: Synthesis, Characterization, and Performance – A Topical Review," *Fuel Cells* 5(2) (2005) 201-212.
19. K.B. Wiles, F. Wang, and J.E. McGrath, "Directly Copolymerized Poly(arylene sulfide sulfone) Disulfonated Copolymers for PEM-Based Fuel Cell Systems. I. Synthesis and Characterization," *J. Polym. Sci., Part A: Polym. Chem.* 43(14) (2005) 2964-2976.
20. Y.J. Kim, B.R. Einsla, C.N. Tchatchoua, and J.E. McGrath, "Synthesis of High Molecular Weight Polybenzoxazoles in Polyphosphoric Acid and Investigation of Their Hydrolytic Stability Under Acidic Conditions," *High Performance Polymers* 17(3) (2005) 377-401.

Preprints

1. J.B. Mecham, F. Wang, T.E. Glass, J. Xu, G.L. Wilkes, and J.E. McGrath, "Sulfonated Poly(arylene ether)-b-Poly(imide) Segmented Copolymers," Abstracts of Papers, PMSE, 221st American Chemical Society National Meeting, San Diego, CA, April 1-5, 2001.
2. W.L. Harrison, F. Wang, J.B. Mecham, T.E. Glass, M.A. Hickner, and J.E. McGrath, "Influence of Bisphenol Structure on the Direct Synthesis of Sulfonated Poly(arylene ethers," Abstracts of Papers, PMSE, 221st American Chemical Society National Meeting, San Diego, CA, April 1-5, 2001.
3. W.D. Polk, S. Wang, Y. Kim, M. Sankarapandian, H.K. Shobha, T.E. Glass, and J.E. McGrath, "Synthesis and Characterization of Segmented Poly(arylene ether phosphine oxide)-B-Poly(dimethylsiloxane) Copolymers," Abstracts of Papers, PMSE, 221st American Chemical Society National Meeting, San Diego, CA, April 1-5, 2001.
4. N. Gunduz, T.Y. Inan, E. Yildiz, and J.E. McGrath, "Sulfonated Six-Membered Ring Polyimides as Proton Exchange Membranes: Synthesis and Characterization," Abstracts of Papers, PMSE, 221st American Chemical Society National Meeting, San Diego, CA, April 1-5, 2001.
5. F. Wang, J. Mecham, W. Harrison, M. Hickner, Y. Kim, and J.E. McGrath, "Synthesis of Sulfonated Poly(arylene ether phosphine oxide sulfone)s via Direct Polymerization," Abstracts of Papers, PMSE, 221st American Chemical Society National Meeting, San Diego, CA, April 1-5, 2001.
6. F. Wang, Y. Kim, M. Hickner, T.A. Zawodzinski, and J.E. McGrath, "Synthesis of Polyarylene Ether Block Copolymers Containing Sulfonate Groups," Abstracts of Papers, PMSE, 222nd American Chemical Society National Meeting, Chicago, IL, August 26-30, 2001.
7. Y.S. Kim, F. Wang, M.A. Hickner, T.A. Zawodzinski, and J.E. McGrath, "Heteropolyacid/Sulfonated Poly(arylene ether sulfone) Composites for Proton Exchange

Membranes Fuel Cells," Abstracts of Papers, PMSE, 222nd American Chemical Society National Meeting, Chicago, IL, August 26-30, 2001.

8. M.A. Hickner, F. Wang, Y.S. Kim, B. Pivovar, T.A. Zawodzinski, and J.E. McGrath, "Chemistry-Morphology-Property Relationships of Novel Proton Exchange Membranes for Direct Methanol Fuel Cells," Abstracts of Papers, PMSE, 222nd American Chemical Society National Meeting, Chicago, IL, August 26-30, 2001.
9. M. Hickner, Y.S. Kim, F. Wang, T.A. Zawodzinski, and J.E. McGrath, "Proton Exchange Membrane Nanocomposites for Fuel Cells," International SAMPE Technical Conference, 33 (2001) 1519-1532.
10. Y.S. Kim, F. Wang, M. Hickner, J.E. McGrath, and T.A. Zawodzinski, "Heteropolyacid/Sulfonated Poly(Arylene Ether Phosphine Oxide) Copolymer Composite Membranes," Polymer Preprints (American Chemical Society, Division of Polymer Chemistry) 43(1) (2002) 342-343.
11. F. Wang, T. Glass, X. Li, M. Hickner, Y.S. Kim, and J. McGrath, "Synthesis and Characterization of Controlled Molecular Weight Poly(arylene ether sulfone) Copolymers Bearing Sulfonate Groups by End-Group Analysis," Polymer Preprints (American Chemical Society, Division of Polymer Chemistry) 43(1) (2002) 492-493.
12. Y.-T. Hong, B. Einsla, Y. Kim, and J.E. McGrath, "Synthesis and Characterization of Sulfonated Polyimides Based on Six-Membered Ring as Proton Exchange Membranes," Polymer Preprints (American Chemical Society, Division of Polymer Chemistry) 43(1) (2002) 666-667.
13. W. Harrison, F. Wang, Y.S. Kim, M. Hickner, and J.E. McGrath, "Synthesis, Characterization, and Morphological Influence of Bisphenol Structure on the Direct Synthesis of Poly(arylene ether sulfone) Copolymers," Polymer Preprints (American Chemical Society, Division of Polymer Chemistry) 43(1) (2002) 700-701.
14. M.A. Hickner, Y.S. Kim, F. Wang, J.E. McGrath, and T.A. Zawodzinski, "Proton Exchange Membrane Nanocomposites," Proceedings of the American Society for Composites (2001) 323-336.
15. W.L. Harrison, K. O'Connor, N. Arnett, and J.E. McGrath, "Homogeneous Synthesis and Characterization of Sulfonated Poly(arylene ether sulfone)s via Chlorosulfonic Acid," Polymer Preprints (American Chemical Society, Division of Polymer Chemistry) 43(2) (2002) 1159.
16. K.B. Wiles, V.A. Bhanu, F. Wang, and J.E. McGrath, "Synthesis and Characterization of Sulfonated Poly(arylene sulfide sulfone) Copolymers as Candidates for Proton Exchange Membranes," Polymer Preprints (American Chemical Society, Division of Polymer Chemistry) 43(2) (2002) 993-994.
17. H. Ghassemi and J.E. McGrath, "Proton-Conducting Polymers Derived from Poly(p-phenylene)s," Polymer Preprints (American Chemical Society, Division of Polymer Chemistry) 43(2) (2002) 1021-1022.
18. L. Dong, Y.S. Kim, F. Wang, M. Hickner, T.E. Glass, and J.E. McGrath, "Self-Diffusion of Water in Sulfonated Poly(arylene ether sulfone) Copolymers by Pulse Field Gradient NMR," Polymer Preprints (American Chemical Society, Division of Polymer Chemistry) 44(1) (2003) 355-356.
19. H. Ghassemi, G. Ndip, and J.E. McGrath, "New Multiblock Copolymers of Sulfonated Poly(4'-phenyl-2,5-benzophenone) and Poly(arylene ether sulfone) for Proton Exchange

Membrane," Polymer Preprints (American Chemical Society, Division of Polymer Chemistry) 44(1) (2003) 814-815.

20. W.L. Harrison, F. Wang, K. O'Connor, N.Y. Arnett, Y.S. Kim, and J.E. McGrath, "Sulfonated Poly(arylene ether sulfone)s Containing Hexafluoroisopropylidene Unit: Influence of Sulfonic Acid Position on Stability and Other Properties," Polymer Preprints (American Chemical Society, Division of Polymer Chemistry) 44(1) (2003) 849.
21. M. Sankir, V.A. Bhanu, H. Ghassemi, K.B. Wiles, M.L. Hill, W. Harrison, M. Sumner, T.E. Glass, J.S. Riffle, and J.E. McGrath, "Systematic Study of the Synthesis and Characterization of 3,3'-sulfonylbis(6-chlorobenzenesulfonic acid) Disodium Salt Monomer for Proton Conducting Polymeric Membranes in Fuel Cell Applications," Polymer Preprints (American Chemical Society, Division of Polymer Chemistry) 44(1) (2003) 1079-1080.
22. K.B. Wiles, V.A. Bhanu, F. Wang, M.A. Hickner, and J.E. McGrath, "Poly(arylene thioether sulfone) Copolymers for PEM-Based Fuel Cell Systems," Polymer Preprints (American Chemical Society, Division of Polymer Chemistry) 44(1) (2003) 1089-1090.
23. Y.S. Kim, L. Dong, M. Hickner, B. Pivovar, and J.E. McGrath, "Methanol Permeation of Sulfonated Poly(arylene ether sulfone) Block Copolymers," Polymer Preprints (American Chemical Society, Division of Polymer Chemistry) 44(1) (2003) 1254-1255.
24. B. Einsla, C.N. Tchatchoua, Y.J. Kim, and J.E. McGrath, "Disulfonated Polybenzoxazoles for Proton Exchange Membrane Fuel Cell Applications," Polymer Preprints (American Chemical Society, Division of Polymer Chemistry) 44(2) (2003) 645-646.
25. W.L. Harrision, M.J. Sumner, M. Hill, Y.S. Kim, M. Hickner, C.N. Tchatchoua, J.S. Riffle, J.E. McGrath, and L. Dong, "Influence of Polar Groups in Sulfonated Poly(arylene ether) Copolymers as Proton Exchange Membranes," Polymer Preprints (American Chemical Society, Division of Polymer Chemistry) 44(2) (2003) 647-648.
26. C.G. Cho, Y.S. Kim, M. Hill, and J.E. McGrath, "Synthesis and Characterization of Poly(arylene ether sulfone) Copolymers with Sulfonimide Side Groups," Polymer Preprints (American Chemical Society, Division of Polymer Chemistry) 44(2) (2003) 649-650.
27. H. Ghassemi, W. Harrison, T.A. Zawodzinski, and J.E. McGrath, "New Multiblock Copolymers Containing Hydrophilic-Hydrophobic Segments for Proton Exchange Membranes," Polymer Preprints (American Chemical Society, Division of Polymer Chemistry) 45(1) (2004) 68-69.
28. K.B. Wiles, C.M DeDiego, and J.E. McGrath, "Poly(arylene sulfide sulfone) Copolymer Composites for Proton Exchange Membrane Fuel Cell Systems: Extraction and Conductivity," Polymer Preprints (American Chemical Society, Division of Polymer Chemistry) 45(1) (2004) 724-725.
29. M. Sankir, W.L. Harrison, K.B. Wiles, Y. Li, and J.E. McGrath, "Proton Exchange Membrane Fuel Cells: I. Synthesis and Characterization of Disulfonated Poly(arylene ether benzonitrile) Copolymers," Preprints of Symposia (American Chemical Society, Division of Fuel Chemistry) 49(2) (2004) 526-527.
30. Y. Li, T. Mukundan, W. Harrison, M. Hill, M. Sankir, J. Yang, and J.E. McGrath, "Direct Synthesis of Disulfonated Poly(arylene ether ketone)s and Investigation of Their Behavior as Proton Exchange Membrane (PEM)," Preprints of Symposia (American Chemical Society, Division of Fuel Chemistry) 49(2) (2004) 536-537.
31. K.B. Wiles, C.M. DeDiego, and J.E. McGrath, "Disulfonated Poly(arylene ether phenyl phosphine oxide sulfone) Terpolymers for PEM Fuel Cell Systems," Preprints of Symposia (American Chemical Society, Division of Fuel Chemistry) 49(2) (2004) 538-540.

32. M.L. Hill, B.R. Einsla, Y.S. Kim, and J.E. McGrath, “Synthesis and Characterization of Sulfonated Poly(arylene ether sulfone)/Zirconium Phenylphosphonate Composite Membranes for Proton Exchange Membrane Fuel Cell Applications,” Preprints of Symposia (American Chemical Society, Division of Fuel Chemistry) 49(2) (2004) 584-585.
33. H. Wang, W. Harrison, J. Yang, and J.E. McGrath, “Synthesis of Substituted Poly(p-phenylene)s by Nickel(0) Catalyzed Coupling Reaction and Derived Multiblock Copolymers for Proton Exchange Membrane Fuel Cells,” Preprints of Symposia (American Chemical Society, Division of Fuel Chemistry) 49(2) (2004) 586-587.
34. C. Tchatchoua, W. Harrison, B. Einsla, M. Sankir, Y.S. Kim, B. Pivovar, and J.E. McGrath, “Novel Sulfonated Proton Exchange Membranes for Fuel Cell Applications: Partially Fluorinated Copolymers,” Preprints of Symposia (American Chemical Society, Division of Fuel Chemistry) 49(2) (2004) 601-602.
35. A. Roy, B.R. Einsla, W.L. Harrison, and J.E. McGrath, “Synthesis and Characterization of Hydroquinone Based Disulfonated Poly(arylene ether sulfone)s Via Direct Copolymerization,” Preprints of Symposia (American Chemical Society, Division of Fuel Chemistry) 49(2) (2004) 614-615.
36. B.R. Einsla and J.E. McGrath, “Synthesis and Characterization of Hydroxy-Functionalized Poly(arylene ether sulfone)s and Conversion to Proton Conducting Membranes for Fuel Cells,” Preprints of Symposia (American Chemical Society, Division of Fuel Chemistry) 49(2) (2004) 616-618.
37. J.E. McGrath, “Advances in Proton Exchange Membranes for Fuel Cells,” Preprints of Symposia (American Chemical Society, Division of Polymeric Materials: Science and Engineering) (2005) 92.
38. N.Y. Arnett, W.L. Harrison, L. Dong, and J.E. McGrath, “Hydrocarbon and Partially Fluorinated Sulfonated Copolymer Blends as Functional Membranes for Fuel Cells,” Preprints of Symposia (American Chemical Society, Division of Fuel Chemistry) 50(2) (2005) 534-535.
39. M. Sankir, Y.S. Kim, W.L. Harrison, A.S. Badami, and J.E. McGrath, “Proton Exchange Membrane for DMFC and H2/Air Fuel Cells: II. Synthesis and Characterization of Partially Fluorinated Disulfonated Poly(arylene ether benzonitrile) Copolymers,” Preprints of Symposia (American Chemical Society, Division of Fuel Chemistry) 50(2) (2005) 568-570.
40. B.R. Einsla, L.A. Harris, M.L. Hill, and J.E. McGrath, “Direct Copolymerization of Wholly Aromatic and Partially Fluorinated Disulfonated Poly(arylene ether sulfone)s,” Preprints of Symposia (American Chemical Society, Division of Fuel Chemistry) 50(2) (2005) 571-572.
41. Y. Li, J. Yang, A. Roy, B. Einsla, F. Wang, and J.E. McGrath, “Partially Fluorinated Disulfonated Poly(arylene ether sulfone) Copolymers with Controlled Molecular Weights and Their Applications to Proton Exchange Membrane Fuel Cells,” Preprints of Symposia (American Chemical Society, Division of Fuel Chemistry) 50(2) (2005) 573-574.
42. X. Yu, A. Roy, and J.E. McGrath, “Synthesis and Characterization of Multiblock Copolymers for Proton Exchange Membranes,” Preprints of Symposia (American Chemical Society, Division of Fuel Chemistry) 50(2) (2005) 577-578.
43. H.-S. Lee, B. Einsla, and J.E. McGrath, “Synthesis and Characterization of Segmented Sulfonated Poly(arylene ether)-B-Polyimide Copolymers as Proton Exchange Membranes,” Preprints of Symposia (American Chemical Society, Division of Fuel Chemistry) 50(2) (2005) 579-580.

44. H. Wang and J.E. McGrath, “Synthesis of (Poly(arylene ether sulfone)-Substituted Poly(p-phenylene)) Multiblock Copolymers for Proton Exchange Membrane,” Preprints of Symposia (American Chemical Society, Division of Fuel Chemistry) 50(2) (2005) 581-582.
45. M.L. Hill, B.R. Einsla, and J.E. McGrath, “Partially Fluorinated Poly(arylene ether sulfone) Copolymers Modified with Zirconium Hydrogen Phosphate for Proton Exchange Membranes,” Preprints of Symposia (American Chemical Society, Division of Fuel Chemistry) 50(2) (2005) 652-653.
46. A. Roy, M. Hickner, T. Glass, Y. Li, B. Einsla, K.B. Wiles, and J.E. McGrath, “States of Water – Investigating the Water-Polymer Interactions and Transport Phenomenon in Proton Exchange Membranes,” Preprints of Symposia (American Chemical Society, Division of Fuel Chemistry) 50(2) (2005) 699-700.
47. J. Yang, Y. Li, H. Wang, M. Hill, X. Yu, K.B. Wiles, H.-S. Lee, and J.E. McGrath, “Viscometric Behavior and Molecular Weight Characterization of Sulfonated Poly(arylene ether sulfone) Copolymers,” Preprints of Symposia (American Chemical Society, Division of Fuel Chemistry) 50(2) (2005) 701-702.
48. A.S. Badami, B. Einsla, M. Hill, K.B. Wiles, and J.E. McGrath, “Morphological Analysis by Atomic Force Microscopy (AFM) of Partially Fluorinated Disulfonated Poly(arylene ether sulfone) Copolymers,” Preprints of Symposia (American Chemical Society, Division of Fuel Chemistry) 50(2) (2005) 703-704.

Patents

1. J.E. McGrath, M. Hickner, F. Wang, and Y.S. Kim, “Ion-Conducting Sulfonated Polymeric Materials,” (2002), Patent Number WO0225764.
2. J.E. McGrath and M. Hickner, “Sulfonated Polymer Composition for Forming Fuel Cell Electrodes,” (2003), Patent Number WO03082956.
3. W. Harrison, H. Ghassemi, T.A. Zawodzinski, and J.E. McGrath, “Multiblock Copolymers Containing Hydrophilic-Hydrophobic Segments for Proton Exchange Membrane Fuel Cells,” (2005), Patent Number WO2005053060.